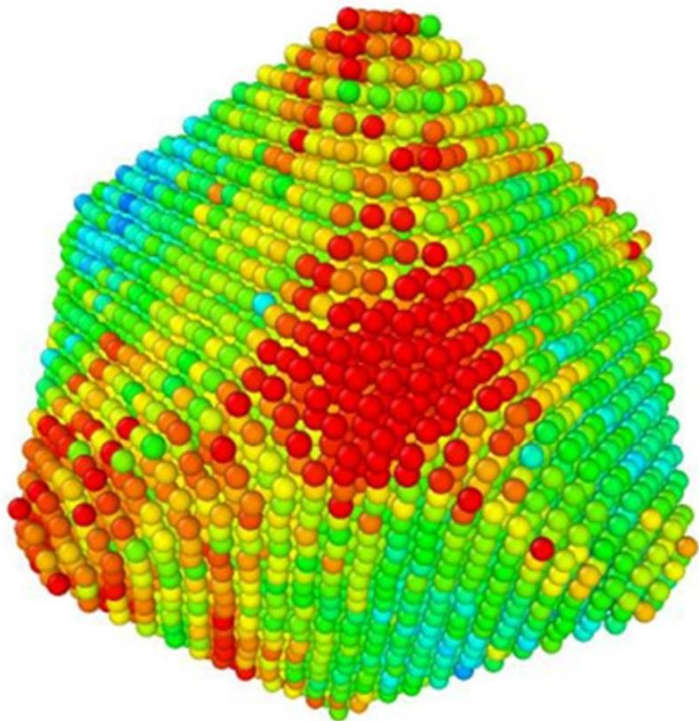


Curriculum 3. Modelling and Simulation

Binayak Mukherjee

**Disorder at the
nanoscale**

A computational study



UNIVERSITY OF TRENTO - Italy

Department of Civil, Environmental
and Mechanical Engineering



Doctoral School in Civil, Environmental and Mechanical Engineering
Topic 3. Modelling and Simulation - 34^o cycle 2018/2022

Doctoral Thesis - February 2022

Binayak Mukherjee

Disorder at the nanoscale

A computational study

Supervisors
Prof. Paolo Scardi, University of Trento
Prof. Stefano Siboni, University of Trento

Cover image taken from “*Effect of oxygen adsorption and oxidation on the strain state of Pd nanocrystals*” by B Mukherjee, A Flor, and P Scardi, Applied Surface Science 541, 148508, 2021



Contents on this book are licensed under a Creative Common Attribution
Non Commercial - No Derivatives
4.0 International License, excepts for the parts already published by other publishers.

University of Trento
Doctoral School in Civil, Environmental and Mechanical Engineering
<http://web.unitn.it/en/dricam>
Via Mesiano 77, I-38123 Trento
Tel. +39 0461 282670 / 2611 - dicamphd@unitn.it

*Dedicated
to my mother,
for gifting me the superpower of reading;
to my father,
for teaching me to be a physicist and a man;
and to my wife,
whose sacrifices and contributions toward this thesis are at least as great as mine*

“But the physical world is quantum mechanical, and therefore the proper problem is the simulation of quantum physics”

Richard Feynman,

Simulating Physics with Computers

International Journal of Theoretical Physics, Vol. 21, Nos. 6/7, 1982

Abstract

Disorder is an inherent component of real materials, with significant implications for their application in functional devices. Despite this, the theoretical modelling of disorder remains restricted, primarily due to the large simulation cells required to adequately represent disordered systems, and the associated computational costs. This has been remedied in part by the increased availability of resources for high performance computing. In this thesis, using a combination of computational techniques, primarily density functional theory and ab initio as well as classical molecular dynamics, we investigate disorder in two broad categories – physical and chemical disorder, in three distinct classes of materials: palladium nanoparticles, the negative thermal expansion cuprite Ag_2O and the complex quaternary chalcogenide $\text{Cu}_2\text{ZnSnS}_4$, known commonly as kesterite.

The ‘physical’ disorder discussed in the thesis constitutes shape- and adsorption-induced mechanical softening on the surface of Palladium nanocrystals used for nanocatalysis. This includes one study on the adsorption of organic capping agents, and another on the adsorption of oxygen molecules and the subsequent oxidation of Pd. In the former, it was observed that the strain effect due to adsorption-induced surface disorder is significantly greater than that due to variations in surface termination, i.e. nanoparticle shape. Moreover in the latter case, different crystallographic facets with different degrees of disorder were found to affect the spin-flip induced activation of oxygen atoms, relevant to the catalytic oxygen reduction reaction in hydrogen fuel cells. In each case, the computational results were combined with a sophisticated, phenomenological whole powder pattern modeling of X-ray diffraction data primarily from synchrotron radiation, leading to an accurate characterization of the Debye-Waller coefficient, which was established as a reliable metric for disorder in crystalline systems. In the case of Ag_2O instead, we demonstrated that the large experimental Debye-Waller coefficient was due to thermal diffuse scattering arising from the strong distortion of the Ag_4O coordination tetrahedra.

The second form of disorder which was investigated is ‘chemical’ disorder, which refers to cation disorder in the quaternary chalcogenide $\text{Cu}_2\text{ZnSnS}_4$ studied for its performance as a thermoelectric material. Similar to the studies on palladium, the disorder was quantified through the Debye-Waller coefficient using molecular dynamics simulations, this time from ab initio methods, and compared with X-ray diffraction data from a synchrotron source. The ordered phase of CZTS is known to crystallize in a tetragonal phase, with alternating Cu-Zn and Cu-Sn cation layers sandwiched between sulfur layers. Two forms of cation disorder were studied: disorder only in the Cu-Zn layer, leading to a disordered tetragonal phase, and full cation site randomization, leading to a disordered cubic polymorph. In the former case, it was found that the higher symmetry of the disordered tetragonal structure led to an average symmetrization of the nearest neighborhood of each individual cation, as a result of which there was a convergence of bands at the valence band maximum, leading to an experimentally observed increase in p-type carrier concentration. In the case of CZTS with full cation disorder, inhomogenous bond led to favorable modifications of the electronic and phonon properties, allowing for a simultaneous improvement of the experimentally measured electrical and thermal conductivities as well as the Seebeck coefficients. Finally, by studying the atypical electronic band structure of this cubic polymorph, we were able to identify topologically non-trivial behavior evidence of bulk band inversion, robust surface states, and an adiabatically continuous connection to a known TI phase. As such, we were able predict disordered cubic CZTS to be the first disorder-induced topological Anderson insulator in a real material system.

Acknowledgements

This thesis, on paper, encapsulates much of the research I have performed at the University of Trento from late 2018 to early 2022, yet in spirit it is a significant milestone on a list of aspirations I have held for as long as I can remember.

First and foremost, thanks are due to my principal supervisor Prof. Paolo Scardi, whose role during my stay in Trento has gone above and beyond that of a supervisor; and on whom I was always able to count, for a steady stream of guidance, motivation and support.

Thanks are due also to my co-supervisor Prof. Stefano Siboni, for following my progress closely, and his availability, patience and kind suggestions.

This thesis was made possible due to the efforts of Dr. Luca Rebuffi, under whose guidance and advice I took up this position, whose ties with me extend beyond the academic domain, and on whose constant moral and emotional support I could rely on, when they were frequently needed.

I would also like to thank Prof. Rosa di Maggio, Prof. Claudio della Volpe, and Prof. Matteo Calandra at the University of Trento, and Prof. Dario Narducci of the University of Milan Bicocca for their useful comments on my work, and Dr. Carlo Fanciulli at CNR-ICMATE, Lecco for several fruitful collaborations.

I am deeply indebted to Prof. Robert Dinnebier and Dr. Sebastian Bette at the Max-Planck Institute for Solid State Research, Stuttgart, for enabling access to high performance computing resources without which a large amount of work for this thesis would not have been possible.

Thanks are also due to our Dr. Mirco d'Incau and Sergio Setti, whose efforts keep our laboratories running.

Special thanks are in store for my friends and colleagues in Trento: Eleonora I. and Matteo, Narges, Syafiq and Haziqah, Alberto, Ketan, Himanshu, Salman, Eleonora T., and Marcelo; and Arko, Rajanya and Subhankar. Thank you for the many, many discussions, both enlightening and pleasurable, and the timely assistance which made my stay in Trento, during trying global times, enjoyable.

My journey to this PhD was enabled through the timely guidance and interventions of some of my teachers in India, in chronological order: Prof. Krishnapada Sarkar, Prof. Keka Basu Choudhury, Prof. Dipanjan Rai Chaudhuri, Dr. Asheesh Raturi and Prof. S.C. Bhatt.

Thanks also go out to the friends who have made life worth living: Samman, Sankalita, Anish, and the whole family from Dehradun: Dharmendra, Sayan, Rituraj and Ankur, and to my niece Anusree.

This thesis, in a sense is a fulfillment of dreams older than me, those of my parents; and expressing gratitude in this context is overwhelming. Suffice to say that everything I am today is because of them.

Finally, to Sheekha, my best friend and wife, thank you for suffering me, and making all of this worth doing.

Index

| | |
|---|----|
| Introduction | 5 |
| 1 Surface softening and disorder in Palladium nanoparticles | 19 |
| 1.1 Surface softening in palladium nanoparticles`: effects of a capping agent on vibrational properties | 19 |
| Abstract | 19 |
| 1.1.1 Introduction | 19 |
| 1.1.2 Experimental and computational methodology | 22 |
| 1.1.3 Experimental results | 25 |
| 1.1.4 Effect of nanoparticle morphology on surface vibrations | 31 |
| 1.1.5 Deformation of surface layers due to adsorption | 35 |
| 1.1.6 Conclusions | 39 |
| Appendix | 40 |
| Author contributions | 46 |
| Acknowledgements | 46 |
| 1.2 Effect of oxygen adsorption and oxidation on the strain state of Pd nanocrystals | 47 |
| Abstract | 47 |
| 1.1.1 Introduction | 47 |
| 1.2.2 Experimental and computational methodology | 50 |
| 1.2.3 Experimental results..... | 53 |
| 1.2.4 Progression of oxidation on Pd nanocube..... | 58 |
| 1.2.5 Surface deformation with oxygen adsorption..... | 64 |
| 1.2.6 Conclusion..... | 68 |
| Appendix..... | 70 |
| Author contributions..... | 75 |
| Acknowledgements..... | 76 |

| | | |
|-------|---|-----|
| 2. | Bulk disorder in negative thermal expansion cuprite Ag_2O | 77 |
| | Abstract | 77 |
| 2.1 | Introduction | 77 |
| 2.2 | Materials, synthesis and methodology | 80 |
| 2.3 | X-ray diffraction and data modeling | 82 |
| 2.4 | Atomistic picture of disorder in the crystalline structure | 85 |
| 2.5 | Conclusions | 91 |
| 3. | Disorder in thermoelectric $\text{Cu}_2\text{ZnSnS}_4$ and its effect on transport properties | 93 |
| 3.1 | Static and dynamic components of Debye-Waller coefficients in the novel cubic polymorph of low-temperature disordered $\text{Cu}_2\text{ZnSnS}_4$ | 93 |
| | Abstract | 93 |
| 3.1.1 | Introduction | 93 |
| 3.1.2 | Methods | 98 |
| 3.1.3 | Results and discussion | 100 |
| 3.1.4 | Conclusion | 105 |
| | Appendix | 106 |
| | Acknowledgements | 108 |
| 3.2 | Order–Disorder Transition in Kesterite $\text{Cu}_2\text{ZnSnS}_4$: Thermopower Enhancement via Electronic Band Structure Modification | 109 |
| | Abstract | 109 |
| 3.2.1 | Introduction | 109 |
| 3.2.2 | Methods | 110 |
| 3.2.3 | Results and discussion | 112 |
| 3.2.4 | Conclusions | 117 |
| | Acknowledgements | 118 |

| | | |
|-------|---|-----|
| 3.3 | Origin of a Simultaneous Suppression of Thermal Conductivity and Increase of Electrical Conductivity and Seebeck Coefficient in Disordered Cubic Cu ₂ ZnSnS ₄ | 119 |
| | Abstract | 119 |
| 3.3.1 | Introduction | 119 |
| 3.3.2 | Methods | 120 |
| 3.3.3 | Results and discussion | 124 |
| 3.3.4 | Conclusions | 137 |
| | Appendix | 138 |
| | Acknowledgements | 152 |
| | Author Contributions | 152 |
| 4. | Disorder induced topological Anderson insulator in Cu ₂ ZnSnS ₄ | 153 |
| | Abstract | 153 |
| 4.1 | Introduction | 153 |
| 4.2 | Computational methodology | 155 |
| 4.3 | Results and discussion | 157 |
| 4.4 | Conclusions | 166 |
| | Appendix | 167 |
| | Author contributions | 176 |
| | Acknowledgements | 176 |
| 5. | Conclusion, perspectives, and ongoing activities | 177 |
| 6. | Appendix | 183 |
| 6.1 | List of publications | 183 |
| 6.2 | Participation in schools and conferences | 184 |
| 6.3 | Grants for computational time | 185 |
| | References | 187 |

Introduction

Materials in the solid state are broadly divided into two categories – amorphous and crystalline. The latter is distinguished from the former by the presence of order – the periodic repetition in space of a single formula unit, or group of atoms, known as the unit cell. As such, order is generally considered to be the defining feature of crystalline materials, and it plays a central role in both the experimental characterization as well as theoretical analysis of this class of material. Examples of the former include the constructive interference of X-rays, electrons and neutrons from the periodic lattice structure of a crystalline material, which gives rise to diffraction patterns; examples for the latter include Bloch's theorem, which allows to find the energy level of electrons in a crystalline system by solving the Schrödinger equation within a periodic potential^{1,2}.

In light of this inherent connection between crystalline matter and order, it appears almost non-intuitive that such systems should host disorder. Nevertheless, disorder in crystalline systems is well known in the field of material science, and a large amount of research has been directed towards characterizing, understanding, and possibly exploiting such disorder.

Types of disorder

Disorder in crystalline materials takes many forms. The most ubiquitous example of this is the thermal vibration of atoms. While these vibrations are generally harmonic oscillations of atoms about their ‘ideal’ crystalline lattice position and thus are cancelled out over long time-periods, a snapshot at any point in time naturally still reveals a displacement of the atoms from their ideal position. Additionally, in many materials, these vibrations are anharmonic in nature, further contributing to disorder. Such anharmonic vibrations constitute a departure from a simple ball-and-spring model, with the so-called ‘phonon spring constant’ no longer a constant, but rather varying as a function of the displacement of the atom from its ideal position. This thermal or dynamic disorder, particularly coupled with

strong anharmonicity, can be connected to several variations in mechanical, elastic and thermal properties and phase transitions in materials. For example, it is known to be responsible for negative thermal expansion in several compounds, such as SnSe, ScF₃, CaZrF₆ and Ag₂O³. Additionally, vibrational anharmonicity leads to a suppression in the lattice (or phonon) contribution to the thermal conductivity of a material, a feature which is found to be beneficial for applications in insulating and refractory materials^{4–6} and thermoelectrics⁷.

Apart from this dynamic disorder due to temperature, a further, static, disorder exists in most crystalline systems. This is surface disorder, the consequence of translational symmetry breaking as a result of the termination of the crystal. This termination gives rise to unsaturated dangling bonds in the material, leading to a rearrangement of surface atoms to minimize the surface energy. In fact, the thermodynamics for particles at this length scale dictates that the energetically stable shape of nanocrystals be in a class of multifaceted polyhedra, the so-called Wulff solids⁸, and significant morphological changes are expected as a consequence of the reduction in particle size⁹. The rearrangement of surface atoms, also known as surface reconstruction, naturally involves a departure from the bulk atomic lattice, thus introducing disorder into the system^{10,11}. As such, it is the finite size of the particle itself which is responsible for this disorder, and as a consequence, its effects are most pronounced at the nanoscale, in the domain of high surface-to-volume ratios. This kind of disorder holds particular significance in the field of nanocatalysis, with surface modifications promoting or inhibiting bond formation and breaking in adsorbed molecules, thus modifying the reaction kinetics of certain kinds of industrially significant chemical reactions¹².

The types of disorder discussed above are inherent, in varying degree, to all materials. Specific kinds of materials often have other, more specific local interruptions to the regular crystalline symmetry. These crystallographic defects can be of various types: point defects, such as vacancies, interstitials, impurities, antisites and topological defects; line defects such as dislocations and cracks, and planar defects such as stacking faults, twins, antiphase boundaries and grain boundaries. These defects play a central role in the behavior of various functional materials, by modifying their electrical, vibrational and mechanical properties. These include changes to fundamental material

characteristics, such as electronic band structures, phonon modes and dispersions, chemical bonding, and band topologies, which affect a wide range of physical properties. As such, the study of these defects plays a central role in materials science and engineering. Indeed, while defects are naturally present to varying degree within virtually all materials, it has been found that *engineering* specific kinds of defects in different functional crystalline materials can be used to leverage an improvement in certain properties. Such defect engineering is at the forefront of materials research, and has been used to improve the performance of photovoltaic^{13–15}, thermoelectric^{16,17} and electronic devices¹⁸, catalysts^{19,20}, batteries²¹, hydrogen fuel cells²² and various other technologies.

The types of disorder discussed above, by no means constitute an exhaustive list of disorder in crystalline systems; rather, they generally correspond to the kind of disorder we study in this thesis. In fact, there are several ways in which crystalline materials can be disordered, particularly when the structure has an internal degree of freedom. An example of such disorder is the case of the chemically complex semiconductor alloys which we study, where the crystalline structure remains positionally ordered but compositionally disordered, the inner degree of freedom being the chemical composition of the atomic species. Other examples are paramagnetic crystals with disordered dipole moments, as well as molecular crystals where the molecular center-of-mass lies on a periodic lattice, but the orientation of the molecules might be disordered²³. In the present thesis however, we will restrict ourselves to the study of two broad categories of disorder: ‘physical’ or ‘structural’ disorder, and chemical or compositional disorder. The former includes surface disorder from adsorption as well as bulk disorder from anisotropic interactions between atoms, while the latter consists of the randomization of the atomic specie at the cation lattice sites in a quaternary compound.

Quantifying disorder

In order to study the role of disorder in functional materials, a way to measure disorder is required. One such standard measure is the Debye-Waller (DW) factor, also known as temperature factor. Introduced first by Peter Debye in 1913²⁴, and subsequently modified by Ivar Waller in 1923²⁵, the DW factor is a measure of the

attenuation of the intensity of a Bragg peak in a diffraction pattern, due to phonons². This attenuation increases in temperature due to thermal diffuse scattering (TDS), but does not completely eliminate the peaks as far as long-range order is retained within the system²⁶. The intensity scattered by a powder sample is the product of two terms: the Bragg scattering or diffraction term, and a diffuse scattering term. Compared to the diffracted signal from a powder of perfect crystalline domains, the Bragg term is decreased in intensity by the Debye-Waller (DW) factor, which is multiplied to the atomic scattering factor. This reduction in intensity of the Bragg peak thus corresponds to the diffuse scattering term. The Debye-Waller coefficient B_{iso} is the isotropic, scalar part of the DW-factor, and is considered an adequate approximation, particularly for powder diffraction experiments. The B_{iso} , which is directly proportional to the atomic (or ionic) mean square displacement (MSD), is given by²⁷

$$B_{iso} = \frac{8\pi^2}{3} \langle u^2 \rangle$$

The B_{iso} is commonly obtained by fitting neutron diffraction data, simply because of the large interaction cross-section of neutrons with phonons, compared to that of X-rays. This situation can be partially remedied using high brilliance synchrotron radiation sources, where the large flux of photons compensates for the lower X-ray – phonon cross-section. Besides using neutrons instead of X-rays, the best experimental condition is one where single crystals can be studied, most often by X-ray scattering. A sophisticated, phenomenological modelling of the peak-broadening from size and strain effects allows for a more realistic estimation of the B_{iso} . This approach, called whole powder pattern modelling (WPPM)^{28,29}, seeks to model the entire peak profile based on the convolution of the different components responsible for peak broadening. Each component is represented by a theoretically derived expression accounting for different sources of broadening, and is not just restricted to size and strain effects, but can also account for other features such as the instrumental profile of the diffractometer, as well as microstructural effects such as dislocations and faulting. Since the peak broadening is correctly accounted for by the other terms, the value of B_{iso} is explicitly due to the attenuation in intensity from disorder and is proportional to the atomic MSD. It thus serves as a connection between the macroscopic and microscopic features of the material. To understand the microscopic underpinning

of the measured disorder, we resort to molecular dynamics (MD) simulations, to study the evolution of an atomistic system under various external conditions such as temperature, pressure, etc. Based on statistical mechanics, this computational technique allows us to obtain trajectories of the atomistic system, from which many properties, including thermal/vibrational, elastic and thermodynamic, can be calculated. One of these properties is the atomic MSD, this time computed directly from the displacement of individual atoms. This is particularly useful, given that it allows a direct comparison with the experimental B_{iso} , and serves to explain the atomistic origin of the disorder. Additionally, MD trajectories allow for a visualization of the systems being simulated, and the color mapping of various properties onto these visualizations helps to paint a clear picture of structural changes in the material. The central function of molecular dynamics is an integration of the equations of motion for the system, using various algorithms, of which the most famous is Verlet integration³⁰. This then allows the calculation of atomic trajectories for consecutive timesteps, which are used to study the time-evolution of the system within the predetermined external conditions and constraints. MD simulations can be of two types - classical MD and *ab initio* MD. In the former case, the potential within which the equations of motion are solved is provided externally in the form of a forcefield with certain parameters³⁰, with many different forcefields available for different kinds of systems; these include simple potentials such as Lennard-Jones and Buckingham, useful for simulating inert gases and ionic compounds respectively, the Stillinger-Weber potentials for covalent materials³⁰, embedded atom model (EAM) forcefields for bulk metals³¹, reactive force fields (ReaxFF) for chemical reactions³², and specific forcefields for polymers^{33–35}. While a large variety of forcefields are available, oftentimes their parameterization does not extend to chemically complex systems, or even simple systems with complicated structural behavior. These limitations are partially resolved using *ab initio* molecular dynamics (AIMD), where the forces on atoms are instead calculated quantum mechanically from scratch, through the Hellmann-Feynman theorem³⁶. This allows for the simulation of more complicated materials, *without* the need for predetermined forcefields, and as such, can be used for a wider range of materials. AIMD, however, has its own drawbacks. The most efficient way of computing the Hellmann-Feynman forces is generally

using density functional theory (DFT), a computational technique which scales (with the number of particles in the simulations, n) as $O(n^3)$, an order of magnitude greater than classical MD, which scales as $O(n^2)$. This means that simulations with AIMD simply take longer than those with classical MD, in turn restricting both the system size as well as timescales (\sim picoseconds rather than \sim nanoseconds), which can be reasonably probed. Therefore, the simulation technique used needs to be carefully decided based on the problem.

Beyond its application in AIMD, DFT provides significant information on phonon, and particularly electron properties, the latter being inaccessible to classical simulation methods. Conceived originally by Enrico Fermi³⁷, DFT was given much of it's current formalism through the seminal work of Walter Kohn^{38,39}. DFT allows an investigation of the ground state electronic structure of materials, using simply the material geometry as input, and solving the Kohn-Sham (KS) equations. The KS equations are a set of Schrödinger-like equations, with a mean-field (single particle) approximation to the many-body problem, i.e., instead of accounting for individual electron-electron interactions, each electron is approximated to exist in a mean field from all the others. This allows the calculation of various properties: most importantly the electronic charge density, band structure, and density of states, as well phonon dispersion and vibrational density of states, and as such, it has become the workhorse theory in materials modelling. However, apart from the aforementioned constraints due to computational speed, which makes calculations for larger systems or longer timescales unfeasible, DFT suffers from several other limitations. The most infamous is the underestimation of the band gap of semiconducting materials – the result of an inadequate approximation to the many body electron-electron exchange and correlation energies⁴⁰. This implies that DFT cannot account for effects due to the strong correlation between electrons, and therefore cannot predict phenomena such as Mott insulators or superconducting behavior. Nevertheless, DFT still provides qualitatively reliable results for a large range of materials, and despite the band-gap problem, describes other features of semiconducting materials reasonably well^{41,42}. With the advent of modern high performance computing (HPC) facilities (which enable simulations of larger systems), as well as the development of hybrid functionals⁴³ (which improve, though do not fix, the band-gap

problem) and post-DFT techniques (which allow for the reliable calculation of excited states)⁴⁴, this electronic structure method remains a centerpiece in materials theory.

Applications

The study of nanocrystalline disorder presented in this thesis was performed primarily within the context of materials engineering for sustainable and renewable energy applications. It is estimated that by the year 2050, the global demand for energy will reach 260 PWh per year, making this one of the stiffest challenges humanity must overcome in the 21st century^{45,46}. It is also abundantly clear that this energy demand must be met *while* drastically reducing and eventually phasing out the use of fossil fuels, so as to mitigate rising temperatures and prevent irreversible and disastrous climate change events world wide⁴⁷. In this thesis, we discuss how disorder occurs in certain energy materials, and how it affects their physical properties and ultimately their functionality, primarily in the two areas of nanocatalysis and thermoelectrics. The materials in question are Palladium (Pd) nanoparticles in the first case, used as nanocatalysts for the oxygen reduction reaction, and Cu₂ZnSnS₄ (CZTS) nanoparticles in the second, well known within the field of photovoltaics, but studied here for their performance as thermoelectric materials. Additionally, we also study Ag₂O, which has antibacterial properties, and is the primary component of silver oxide batteries.

Catalysis may be defined as the process of increasing the rate of a chemical reaction through the addition of a substance known as a catalyst, which itself remains generally unchanged in the process^{48,49}. Instead, the catalyst presents an alternative route between the reactants and products with a lower activation energy barrier compared to the uncatalyzed reactions. It is estimated that the manufacturing of up to 90% of all commercial chemical products involve catalysts in some step of the process, with the global market for catalysts in 2014 standing at US\$33.5 billion. The catalytic properties of small particles have been studied for a long time, primarily as a means of maximizing the surface area exposed to the reactants. Given that catalysts are normally produced from expensive materials, maximizing their usage efficiency through higher surface-to-volume ratios is naturally

beneficial. As such, the development of nanoscience has had a significant impact on the field of catalysis. Nanoparticles, by virtue of where they exist on the length scale, show behavior which lies at the interface of bulk and molecular materials. As a result of the large surface-volume ratio, a significant fraction of atoms on the surface are undercoordinated in comparison to the bulk configuration, with greater steric freedom, which promotes the formation of non-equilibrium, metastable structural modifications in nanostructured materials during the chemical reaction. This is particularly prevalent at rough or stepped surfaces, edges and vertices, where the undercoordination of atoms is specially prominent⁵⁰. These metastable modifications then affect the binding, modification and transport of surface species such as electrons and adsorbent molecules, with the goal of catalyst design being to enhance the reaction activity, selectivity and stability of the catalyst-reactant system.

Since the majority of catalytic activity takes place on the surface of the catalyst, it becomes essential to understand the nature of disorder on the nanocatalyst surface. In the absence of bonding partners, the dangling bonds of undercoordinated surface atoms can only bond with similarly undercoordinated neighbors through a drastic rearrangement. This causes significant rebonding, with the associated disorder penetrating several layers into the bulk¹².

In general, this surface reconstruction takes the form of an inward relaxation of the atoms on the surface, thus shortening the interlayer spacing. This has been found to be proportional to the roughness of the surface^{51,52}, with the atoms moving inwards to smoothen out the roughness. Both clean metal and semiconductor surfaces are known to reconstruct significantly⁵³, the most famous being the reconstruction of the Si (111) surface. Additionally, surfaces also reconstruct due to the adsorption of molecules. Similar to clean surfaces, adsorption induces relaxation and buckling of the surface layers, with the adsorbates forming clusters on the substrate. It is interesting to note that the bonding between adsorbate and surface atoms primarily affects only nearest-neighbor atoms of the substrate¹², and the local nature of this interaction is prominently reflected in the atomic mean square displacement. Surface reconstruction due to adsorption is directly connected to the enhanced catalytic activity of rough surfaces with low coordination sites^{54,55}. The binding energy of chemisorbed molecules at these steps and kinks are higher than on flat surface sites,

so bond breaking at these sites require lower activation energy. This leads to a certain contradiction: higher binding energies suggest that the adsorbed species remain at the defect sites for longer periods, which corresponds to a lower turnover rate; in contrast to the clearly observed high turnover rate associated with higher catalytic activity. This can be explained using a dynamic reconstruction picture – chemisorbed species create catalytically active sites by reconstructing the substrate, which then rapidly undergoes periodic restructuring with cycles of desorption and readsorption, which leads to high turnovers¹². As such, obtaining an atomic level understanding of these processes through computational techniques coupled with precise experimental characterisation opens the way for a better understanding of these structural modifications, and how they affect the relevant chemical reactions, from a microscopic perspective.

In that context, the Pd nanoparticles studied in this thesis plays an important role in ‘green’ or sustainable energy sources – they are an important component of hydrogen fuel cells, where they catalyze the oxygen reduction reaction (ORR), which combines oxygen and hydrogen to produce water and clean energy.

Thermal gradients exist all around us – sometimes naturally, sometimes as a consequence of human activity – and their exploitation offers another source for clean energy. A large component (more than 60%) of the energy generated in typical energy conversion processes are lost as dissipated heat^{56,57}. The recovery of this waste heat can increase the global efficiency of processes, reduce primary fuel consumption and lower emissions⁵⁸, and reduce the heat discharged into the atmosphere⁵⁹. Alternatively, electrical power may be harnessed from ambient energy, which consists of low intensity, distributed sources⁶⁰. These include solar power, fluid flows, vibrational energy, electromagnetic radiation, and low-temperature heat sources⁶¹. Harnessing of energy from these ambient sources can be used to power small electronic devices, particularly those physically embedded deep within larger integrated technologies, *without* the additional encumbrance and cost associated with an external power source⁶². Thermoelectrics has been suggested as a solution to both these problems of waste heat recovery and energy harvesting. Loosely defined as the direct conversion of a thermal gradient into electric voltage and vice-versa via a thermocouple, the

‘thermoelectric effect’ is actually a combination of three interrelated effects – the Seebeck effect, the Peltier effect and the Thomson effect. The Seebeck effect is the generation of a voltage across a material in the presence of a heat gradient, while in the Peltier effect heat flows in the presence of a current through a material, in the direction of the charge flow. The third effect, known as the Thomson effect, is the absorption or release of heat at the two ends of a material in the simultaneous presence of a current and temperature gradient⁶³. Thermoelectric (TE) materials, which display these effects, are generally narrow-band semiconductors such as the bismuth chalcogenides. The voltage due to the Seebeck effect is generated in the same direction of the thermal gradient for p-type semiconductors and in the opposite direction for n-type materials. The objective in the design of TE materials is to maximize a dimensionless quantity known as the thermoelectric figure of merit, which is given by $ZT = \sigma S^2 / \kappa T$ where σ , S , and κ are the three TE parameters: electrical conductivity, Seebeck coefficient and thermal conductivity respectively, and T is the absolute temperature. The simultaneous improvement of all three parameters is considered to be one of the primary challenges in TE material design, however, there are several interdependencies between the parameters. The most common strategy is to independently decrease the lattice part of the thermal conductivity without significantly affecting the electrical conductivity. This is achieved using the so-called ‘phonon-glass electron-crystal’ (PGEC) model⁶⁴, which is a material framework which allows for the conduction of electrons as in a crystal, while at the same time blocking the conduction of phonons as in a glass. There are several (possibly concurrent) ways in which this kind of behavior may be achieved in a crystalline material, all of which rely on introducing certain kinds of disorder into the system. One method is through defect engineering, through the creation of point defects, vacancies or rattling structures with heavy ions, all of which allow for the scattering of phonons from the defect site⁶⁵. Another strategy is the use of complex disordered crystals with large unit cells. In such materials, the network which is responsible for electron transport, i.e. the electron crystal, is separated from the phonon glass which incorporates various disordered structures⁶⁶. And finally, as with catalysis, nanostructuring and the use of 2-dimensional structures have been found to be viable solutions^{67,68}, with phonon scattering from grain boundaries and interfaces. While

disorder generally leads to flatter phonon dispersion relations, indicating a lower phonon group velocity and thus a low thermal conductivity, additional reductions in the value can be obtained through soft phonon modes arising from impurities and rattling ions^{6,69,70}. Nevertheless, separating the electrical and thermal conductivities remain an active research problem in TE materials.

Another strategy to improve the TE performance of a material is instead to improve the power factor σS^2 , which makes up the numerator of the TE figure of merit ZT. This, once more, is a challenging objective, given that the electrical conductivity is directly proportional to the mobility of charge carriers, whereas the Seebeck coefficient is inversely proportional. As such, a simultaneous increase in the two parameters can be obtained through an increase in the carrier concentration, which can be achieved either by introducing degeneracy in the electronic band extrema, or by injecting charge carriers through doping, all the while ensuring that there is no significant reduction in carrier mobility^{71,72}. Overall, the introduction of disorder and nanostructuring to improve the TE performance of a crystalline material is considered to be a generally successful strategy, and as such, motivates a careful study of the effects of disorder on the electron and phonon transport properties of established, *as well as* potential TE materials.

Perhaps more a result of coincidence than causality, the best thermoelectric materials such as Bi₂Te₃, Bi₂Se₃, Sb₂Te₃ and SnTe are also found to be topological insulators (TI's)^{73–79}. TI's are a kind of quantum matter, characterised by an insulating bulk coupled to a highly conducting surface. This overlap between TE and TI materials is primarily the result of similar properties, such as the presence of heavy elements and a narrow band gap, being favorable both for good TE performance *and* TI behavior. The bulk electronic band structure of TI's generally shows anti-crossing features (a departure from the parabolic band model) at the band extrema, along with band inversion (inverted ordering of orbital contributions to bands), at certain high symmetry points in the Brillouin zone. The surface band structure, instead, shows gapless surface states, most commonly associated with a linear band dispersion (Dirac points), though gapless states with parabolic dispersions are also known. These topologically protected surface states are perhaps the most interesting feature of TI's, due to

their quantum mechanically guaranteed absence of electron backscattering from non-magnetic disorder, such as impurities or defects. This opens the way for the high-mobility transport of charge carriers on the surface of TI's, a feature which remains to be significantly exploited. The fact that topological surface states offer high mobility conduction channels for electrons, but *not* phonons, hints at a possible realization of the PGEC model^{77,79–82}. However, in TI nanostructures, the boundary states from opposite surfaces of adjacent particles exist in close proximity to each other, leading to a possible hybridization of these surface states⁸³. This opens up a hybridization gap in the gapless surface states, potentially destroying their topological protection, but at the same time leading to an improvement in the Seebeck coefficient. Indeed, studies have shown that topological surface states (or edge states in 2D materials) can still act as high-mobility electron transport channels despite the presence of a hybridization gap, thus leading to an overall enhancement in the ZT. Thus, in addition to the aforementioned reduction of the thermal conductivity, nanostructuring in TE materials which are also TI's can be potentially beneficial for their performance.

While topological insulators (and their surface states) are known to be robust to weak disorder, strong disorder is known to destroy this topological protection⁸⁴. However, there exists a class of topological insulator, known as the topological Anderson insulator (TAI)⁸⁵, where disorder-induced Anderson localization leads to a renormalization of the topological mass of the charge carriers via the band structure, causing a transition from a topologically trivial phase to a TI⁸⁶. TAI phases are therefore expected to manifest in materials which, in their ordered form, are topologically trivial, but close to a topological phase. As such, Sb₂Se₃ was proposed as a possible candidate TAI material, given that the closely related Bi₂Te₃, Bi₂Se₃ and Sb₂Te₃ have all been demonstrated to be TI's⁸⁷. Nevertheless, to the best of our knowledge, neither experimental nor theoretical studies have shown a rigorous TAI behavior in any real material compound. Given the strong overlap between TI's and TE materials, and the important role of disorder in TE materials, the role of disorder in TI's and TAI's need to be thoroughly examined. In this context, we study disorder in Cu₂ZnSnS₄, to understand how it affects electron and phonon transport properties, and finally the topological classification of it's electronic band structure.

The remainder of this thesis is structured in the following way. The first chapter is on surface softening and disorder in Pd nanoparticles due to adsorption and the subsequent modification of the surface strain state. This chapter is divided into two subsections: the former deals with the adsorption of an organic capping agent, and demonstrates that the disorder due to adsorption dominates over the effect of nanoparticle shape; the latter studies oxygen adsorption and oxidation, and its effect in modifying the Pd nanoparticle morphology, and also predicts a variation across different surface facets for the spin-flip induced oxygen activation process, with possible implications in the catalytically important oxygen reduction reaction. The second chapter concerns the large thermal diffuse scattering as a consequence of structural distortion in Ag_2O , an oxide which displays negative thermal expansion. The third chapter deals with the substitutional and antisite defects in the chemically complex quaternary chalcogenide $\text{Cu}_2\text{ZnSnS}_4$ (CZTS), and its effect on the thermoelectric performance of this compound. It is subdivided into three parts, the first of which is a structural study of disorder in CZTS; the second deals with the effects of Cu-Zn disorder and the consequent modification of its electronic band structure, which results in an improved thermopower; the third subsection studies inhomogeneous bonding in full cation disordered CZTS, which leads to a simultaneous improvement of the electrical conductivity and Seebeck coefficient, coupled with ultra-low thermal conductivity. The fourth chapter studies the atypical electronic band structure of full-cation-disordered CZTS, and makes a prediction for a disorder induced topological Anderson insulator phase, the first such prediction in a real material system. In the fifth and final chapter, we draw conclusions on the work done in the thesis, provide some perspectives, and briefly describe the state of continuing activities on the topics covered.

1 Surface softening and disorder in palladium nanoparticles

1.1 Effects of a capping agent on the vibrational properties of Pd nanoparticles

This section is taken from: Rebuffi, L., Mukherjee, B., Siboni, S., Young, A.P., Williams, B.P., Tsung, C.K. and Scardi, P., 2020. “*Surface softening in palladium nanoparticles: effects of a capping agent on vibrational properties*”. *Nanoscale*, 12(10), pp.5876-5887.

DOI: <https://doi.org/10.1039/D0NR00182A>

Abstract

The presence of a capping agent (CTAB) on Pd nanoparticles produces a strong static disorder in the surface region. This results in a surface softening, which contributes to an overall increase in the Debye–Waller coefficient measured by X-ray powder diffraction. Molecular dynamics and density functional theory simulations show that the adsorption-induced surface disorder is strong enough to overcome the effects of nanoparticle size and shape.

1.1.1 Introduction

Palladium (Pd) is one of the most studied and used noble transition metals for catalysis at the industrial level, with applications in chemical synthesis¹, fuel cells²⁻⁴, hydrogen storage⁵, and the oxygen reduction reaction (ORR)⁶, to name a few. In recent years, the ability to chemically synthesize crystalline nanoparticles (NPs) of Pd enclosed by well-defined facets has been established, driven by an improved understanding of NP growth dynamics and its connection to the morphology of the NP's⁶. Pd NPs have been synthesized in a shape-controlled manner through various techniques, such as by using selective capping ligands⁷⁻⁹, seeded growth^{8,10-13}, heteroepitaxial growth¹⁴⁻¹⁶, and electrochemical methods^{17,18}. Shape-controlled growth has been demonstrated to enhance catalytic activity^{10,14} of Pd NPs. Shao et al have shown that Pd nanocubes enclosed by {100} facets exhibit catalytic activity comparable to Pt nanocatalysts⁶, an

order of magnitude higher than Pd nano-octahedra enclosed by {111} facets. Long et al have demonstrated that the {100} facet in Pd nanocubes preferentially forms singlet O₂, due to a charge transfer from the Pd surface to O₂ resulting in a spin-flip process in the O₂ molecules. This leads to a more efficient activation of molecular oxygen, a feature which proves beneficial for organic oxidation¹⁹. It has also previously been shown for the case of hydrogenation reactions^{20,21} that the nanoparticle shape affects not just efficiency but also selectivity of the catalytic activity. As such, it is essential to recognize the importance of producing NPs with desired shapes and a narrow size distribution.

Capping agents play a central role in achieving this remarkable control on the size and morphology of NPs. Yet rather paradoxically, it has been argued that growing nanoparticles either entirely without capping agents^{22,23}, or with removal of the capping agent after synthesis^{24,25} can be of great benefit to catalysis applications.. There have also been several studies which have highlighted the beneficial role of capping agents in catalysis, through the process of selective poisoning^{26–28}, though a knowledge deficiency of the behaviours of capping agents on a metal surface makes it a challenging task to rationally take advantage of capping agents in nanocatalysis. Ab initio simulations can prove extremely useful in this regard, to find out more about the mechanism of selective poisoning. As such, our understanding of the behaviour of capping agents on NP surfaces still remains very limited²⁶, and it is of critical importance to understand the effect of adsorption in general, and of capping agents in particular on the surface of Pd NPs in terms of the underlying mechanisms at the atomic and electronic scales.

To this end, the Debye-Waller coefficient (B) proves to be a convenient experimental measure of the vibrational properties of atoms, not just in the bulk of a material, but also – as demonstrated in this study – on or close to the surface. Traditionally, B has been used to describe the attenuation of X-ray or coherent neutron scattering caused by thermal motion. It is directly related to the atomic mean square displacement (MSD)²⁹, and has been shown to be connected to the phonon “spring constant” of a nanocrystalline atomic system³⁰. In the present article we show how the atomic disorder induced at the NP surface due to surface termination as well as adsorption significantly affects the measured value of B of the entire nanocrystalline powder.

Characterization techniques^{31–34} for nanoparticles are keeping pace with the advances in synthesis techniques. These methods include a combination of scanning tunnelling microscopy (STM) and transmission electron microscopy (TEM)³¹, a combination of X-ray photoelectron spectroscopy (XPS) and atomic force microscopy (AFM)³², as well as the more traditional X-ray powder diffraction (XRPD)^{35,36}. XRPD in particular can offer some specific advantages in extracting information from nanocrystalline systems, compared to other techniques. Historically, the most important advantage for XRPD has been in its versatility, low cost of usage and easy availability, and as a direct result, in the ability to extract data in both in-situ and in-operando experiments. Compared to microscopy and imaging techniques such as STM, TEM or coherent diffraction imaging (CDI), which provide information only from a small cross-section of the sample, XRPD provides information averaged over the whole system. This advantage also holds true in the comparison with low energy electron diffraction (LEED), a favored technique for nanoparticles, with the additional factor that electron diffraction must always be performed in vacuum, which often adds further complications. Neutron diffraction, widely used in the study of vibrational properties of atoms, is compromised by the need for large sample volumes making it rather unsuitable for studying nanoparticles, while perpetually suffering from a scarcity of neutron sources. On the other hand, spectroscopic techniques such as XPS which provide reliable information on the chemical properties of the sample, are effectively snapshots in time, and capture none of the dynamical effects resulting in the vibration of atoms.

This article thus demonstrates the efficacy of the traditional XRPD technique combined with modern synchrotron radiation sources and an improved diffraction data analysis paradigm like the Whole Powder Pattern Modelling (WPPM) method³⁷. On the theoretical side, multiscale simulations in the form of classical molecular dynamics (MD) and density functional theory (DFT) provide an insight at the atomic and electronic levels respectively. Brought together, this combination proves a unique asset in obtaining reliable information about the size, microstructure and vibrational properties of the entire nanocrystalline powder sample, while still making a distinction between the bulk and surface contributions to the overall effects.

1.1.2 Experimental and computational methodology

Materials, synthesis and characterization

The Pd nano-octahedra were synthesized in a 3 step process. In the first step, small Pd seeds were formed. In a 20 mL vial, 30 mg of cetyltrimethylammonium bromide (CTAB) was dissolved in 9.3 mL of deionized water through sonication. 250 μ L of a 0.01 M solution of dihydrogen tetrachloropalladate (II) (H_2PdCl_4) was added and gently stirred. 450 μ L of 0.02 M sodium borohydride ($NaBH_4$) was added, turning the solution brown. The solution was then left stirring for 1 hour. The second step involved the formation of intermediate sized Pd nanocubes. In a 20 mL vial, 100 mg of CTAB was dissolved in 9.3 mL of deionized water through sonication. 500 μ L of 0.01 M H_2PdCl_4 was added. The solution was heated, under gentle stirring, in an oil bath at 60 °C. After 5 min, 100 μ L of 0.04 M ascorbic acid was added, followed immediately by 50 μ L of the smaller Pd seed solution. The resulting solution was heated for 2 h. For use in the larger nano-octahedra synthesis, eight solutions were combined and re-dispersed in 10 mL of deionized water. In the final step, the large (50-55 nm) Pd nano-octahedra were formed. In a 20 mL vial, 364.5 mg of CTAB was dissolved in 10 mL of deionized water through sonication. The solution was then gently stirred in an oil bath at 30 °C. 250 μ L of 0.01 M solution of H_2PdCl_4 and 50 μ L of a 1 mM solution of KI were added to the solution, which was left to heat for 5 min. 200 μ L of the previously prepared intermediate sized Pd nanocube solution was then added to the reaction solution. 100 μ L of a 100 mM solution of ascorbic acid was immediately added to the solution, which was left to heat for 40 h. The vial was removed from the oil bath and cooled for 10 min. The particles were centrifuged at 9000 rpm for 15 min and re-dispersed three times. Discarding the final clear supernatant, the particles were re-dispersed in a final volume of 1 mL in deionized water.

The smaller (~ 25 nm) nanocubes were prepared according to a recipe described in previous publications^{11,38,39} in a procedure somewhat different to the nano-octahedra, but still involving the reduction of H_2PdCl_4 by ascorbic acid in the presence of CTAB. Crucially, these nanoparticles were then cleaned of the capping agent CTAB before measurements were made. The capping agent was cleaned using the

techniques described in Vidal-Iglesias et al³⁸. The process involves centrifuging the sample twice and redispersing in water, followed by adding NaOH (one NaOH pellet per 50 ml solution), and finally washing 3-4 times with ultrapure water (Millipore Milli-Q).

The diffraction data for this study was obtained from the synchrotron radiation beamline at the advanced photon source (APS) of the Argonne National Laboratory (ANL, Lemont, IL, USA). Kapton capillaries (0.8 nm diameter) were loaded with a concentrated dispersion of nanoparticles, dried and then sealed with epoxy. Data collection at the 11-BM beamline was performed in the traditional Debye-Scherrer geometry, using radiation at 30 keV (Si powder calibrated wavelength); further operational details may be found in the references⁴⁰ and the website of the facility. The capillary was rotated on the 11-BM spinner at 4200 rpm, and measurements were made at three different temperatures: 100 K, 200 K and 300 K, for both cubic and octahedral nanoparticles. The XRD patterns were analyzed with the WPPM method using the PM2K software (University of Trento, Italy, Scardi et al⁴¹ and references therein). The instrumental profile was modelled using a standard LaB₆ powder pattern, while the pattern from the sample holder was modelled using pseudo-Voigt curves over the pattern from an empty kapton capillary⁴². The size and strain broadening models were the same for both shapes, and for the three temperatures. The domain shapes were taken from the microscopy images as octahedron and truncated cube, with WPPM allowing for the refinement of the degree of truncation alongside the mean and variance for the particle edge length, as given by a lognormal distribution. The strain broadening was also modelled with the WPPM approach, where the inhomogeneous atomic displacement caused by the surface of the NPs was taken into account³⁵, which together with the shape and the reduced dimensions of the crystalline domains leads to the broadening of the diffraction peaks³⁷. While the background was treated using a Chebyshev polynomial, the Pd unit cell parameter and Debye-Waller coefficients were also refined independently to account for the temperature, with the simple scalar form B_{iso} of the traditional Debye-Waller factor B introduced to account for the decrease in the Bragg scattering intensity. Similarly the decrease in intensity due to thermal motion of the atoms was accounted for by freely refining the temperature diffuse scattering (TDS)⁴³.

The TEM images of the Pd nano-octahedra were obtain using a JEOL JEM2010F instrument, operated at 200 kV, with the samples being

dropcast onto a carbon-coated copper grid. SEM images were obtained on a JEOL JSM6340F, with the samples being dropcast on a cleaned silicon wafer for SEM treatment. The TEM images for the Pd nanocubes were instead obtained on a JEOL 3010 microscope operating at 300 kV. Further details on these image can be found in the work by Solla-Gullon et al³⁹.

Classical molecular dynamics

The classical molecular dynamics simulations were performed using the large-scale atomic/molecular massively parallel simulator (LAMMPS) ⁴⁴. The interactions between the Pd atoms were modelled using the embedded atom method (EAM)⁴⁵⁻⁴⁷. The EAM potentials have previously been shown to agree quite well with experimental characterizations of strain using XRPD³⁵. The integration time step in the simulation for the larger particles (> 60000 atoms) was set to be 1.5 femtoseconds (fs), while for the smaller particles it was set to 1 fs. For thermalization calculations, the total potential energy of each NP was first minimized as a function of the atom coordinates, using a Hessian-free truncated Newton (HFTN) algorithm. The system was then allowed to evolve in a canonical ensemble (constant particle number N, system volume V and temperature T) until an appropriate thermal equilibrium was reached at T = 300K. The isothermal condition was reached using a chain of 100 Nosé-Hoover thermostats with a 5.0 picosecond damping parameter and implementing the MTK corrections⁴⁸ to the equations of motion. Subsequently, the temperature constraint was removed, and the system was allowed to evolve in the microcanonical (constant N, V and total energy E) ensemble until the mean square displacement of the system (MSD $\langle u^2 \rangle$), calculated using the software VMD⁴⁹ was seen to stabilize. To simulate the melting of the nanoparticles the energy of the NP's is minimized and they are equilibrated at 300K, then the simulation cell is connected to a chain of 1000 Nosé-Hoover thermostats with a damping parameter of 10 ps and MTK corrections implemented. The thermostats are fixed 1800 K, close to the bulk melting point of Pd.

Density functional theory

The geometry optimization for surface regions was performed with DFT using the plane wave basis set implemented in Quantum Espresso^{50,51}. The electron-exchange correlation functional was approximated using the Perdew-Burke-Ernzerhof (PBE)⁵² functional, with the scalar-relativistic PBEsol pseudopotentials⁵³ which use the

projector augmented wave (PAW) method, and have been shown to be highly effective in calculating the elastic and mechanical properties of solids^{54–56}. Corrections for the van der Waals interaction were implemented using the Grimme-D2⁵⁷ method. The integration in the irreducible Brillouin zone was performed with sampling using a fine 4x4x1 Monkhorst-Pack k-mesh centered at the Γ point, with Marazari-Vanderbilt charge smearing of the order of 0.001 Rydberg (Ry). The cutoffs used for the kinetic energy and the charge density were 60 and 480 Ry respectively. The Pd 111 surface was modelled using 3x3 surface slabs with a thickness of 5 atomic planes. A vacuum layer of 15 Å was introduced in the Z-direction to prevent any interaction between periodic copies. Once the Hellmann-Feynman forces on all atoms were converged below 0.01 eV/Å, the surface geometry was visualized and the relative displacements of the surface atoms from their ideal positions after adsorption were calculated using the Open Visualization Tool (OVITO)⁵⁸.

1.1.3 Experimental results

Some of the results of the WPPM analysis of the diffraction data are presented in Figure 1.1.1 (see SI for completed set of patterns). The insets in Figure 1.1.1(a) and (c) show data and modelling in logarithmic intensity scale to highlight the details of the peak tail regions. From this, we can get a clear idea about the high quality of the fit for the data, which gives us a reliable Debye-Waller coefficient, the value of which is refined as a free parameter in the fitting model. WPPM includes a model for the TDS contribution to the measured pattern, so that Debye-Waller coefficient is not only determined by the decay of Bragg peak intensities with the diffraction angle, but also by the diffuse scattering caused by dynamic (temperature) and static disorder. The insets in Figure 1.1.1(b) and (d) show the lognormal distribution of the nanoparticle edge size, providing an idea of the limited dispersion of nanoparticle sizes, which makes it possible to refer disorder to the nanoparticle of mean size, and allowing us to construct a sufficiently representative atomistic model considering only an average particle size. For the octahedral nanoparticles the average particle edge length was determined to be 52.954 nm. Similarly, the cubic nanoparticles were found to have an average edge length of 23.061 nm.

As can be seen from the transmission (TEM) and scanning (SEM) electron microscopy results in Figure 1.1.2 and Figure 1.1.3,

respectively, the octahedral nanoparticles display a narrow size and shape distribution. Overall, the shapes of the Pd nano-octahedra are fairly sharp, with only a small amount of truncation at the tips.

From the TEM images in Figure 1.1.4 we again observe a narrow size and shape distribution with a few multiply-twinned particles with the “non-crystallographic” shapes (Figure 1.1.4(a), circled in red)³⁹. In general, we observe that the nanocubes are somewhat truncated at the corners and edges, more so than the octahedral particles, exposing {111} and {110} facets in addition to the {100} surface from the cube face. Therefore, the WPPM analysis included an

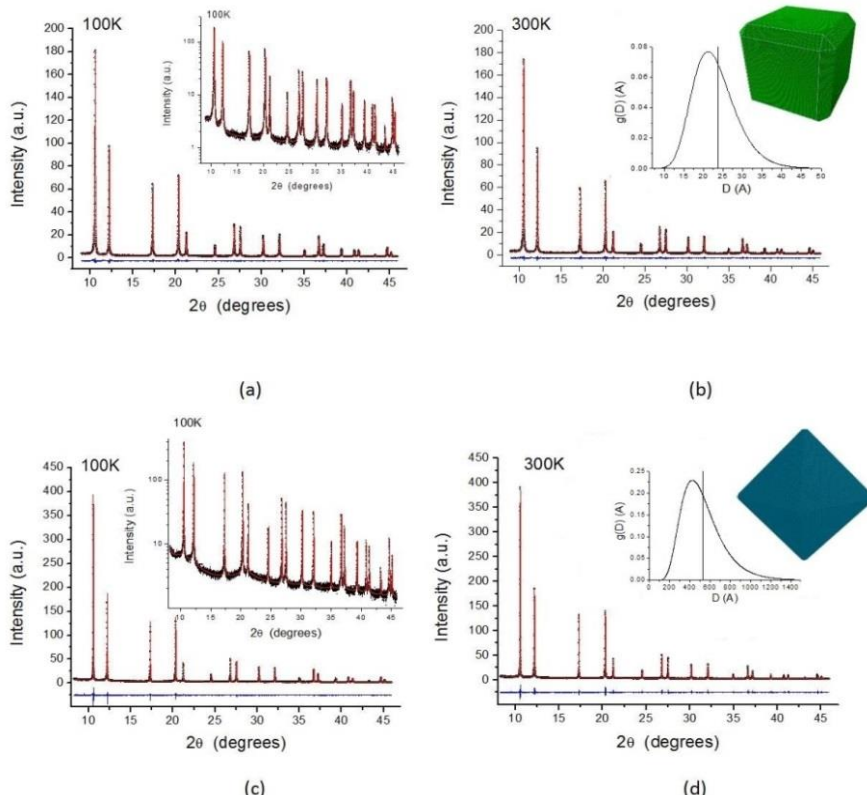


Figure 1.1.1. Whole Powder Pattern Modelling of XRPD data: (a) and (b) show data (circle) and modelling (line) with their difference (residual, line below) for the truncated cubes at 100K and 300K, respectively (reproduced with permission from Flor et al. (2018)); (c) and (d) show analogous results for the nano-octahedra at 100K and 300K, respectively. Insets show: log scale data and modelling at T=100K in (a) and (c); size (edge length) distributions for truncated cubes (b) and nano-octahedra (d) with indication of the mean value (vertical bar) and a model of the refined shape

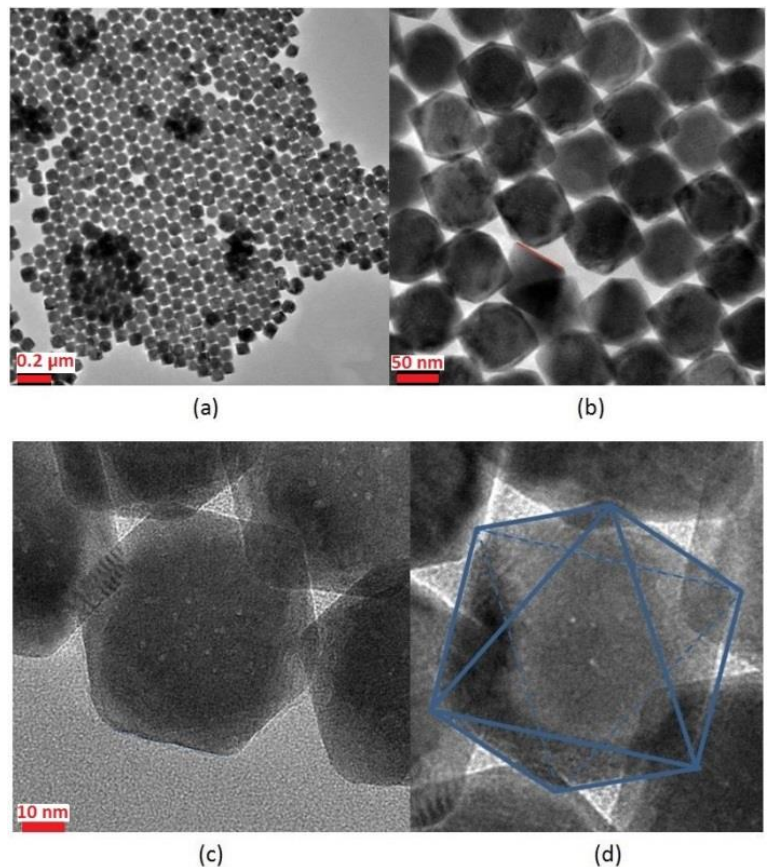


Figure 1.1.2. Transmission electron microscopy (TEM) images of Pd nano-octahedra, with progressive increase in magnification from (a) to (d)

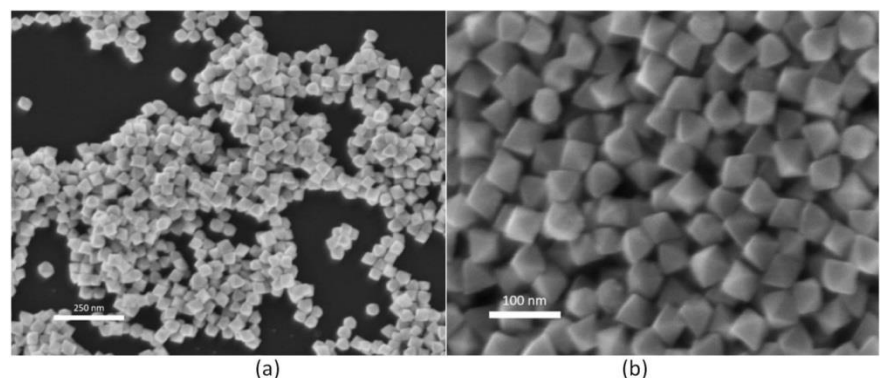


Figure 1.1.3. Scanning electron microscope (SEM) images of Pd nano-octahedra, with progressive increase in magnification from (a) to (b)

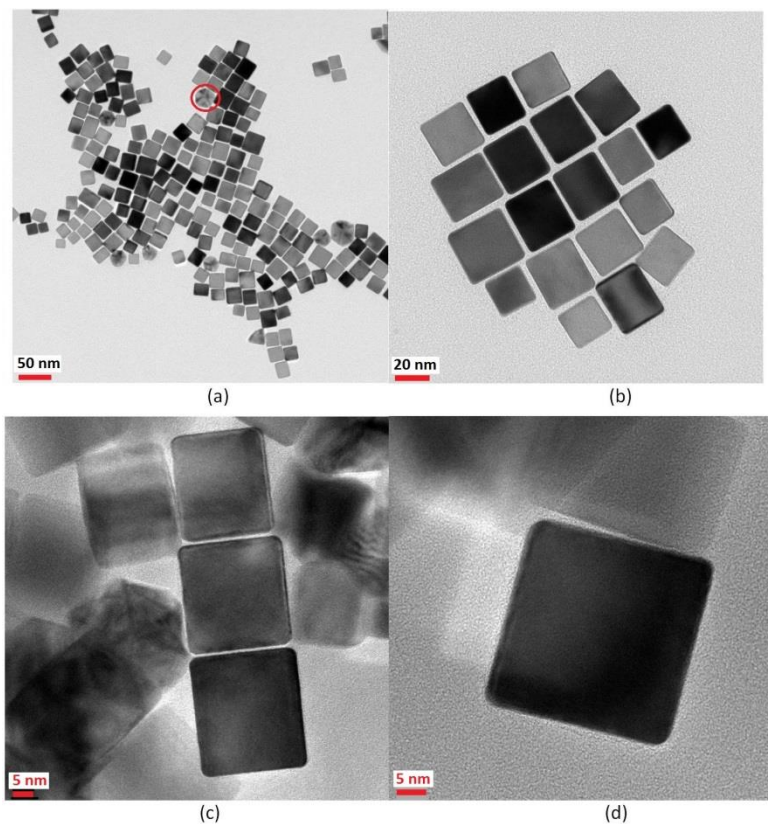


Figure 1.1.4. TEM images of Pd nanocubes, with progressive increase in magnification from (a) to (d)

additional parameter for the degree of truncation³⁵, leading to the average shape shown in the inset of Figure 1.1.1(b). In both cases the agreement between XRPD and microscopy on the size of the NPs is quite satisfactory. Figure 1.1.5 shows the Warren plot⁵⁹ for the larger octahedral particles and the smaller truncated cubes, obtained from the WPPM modelling of the strain broadening. This diagram shows the standard deviation of the distribution of atomic displacements between scattering centres along the given crystallographic directions, as a function of the distance L between them; as such, the Warren plot provides a measurement of the long-range strain within the crystalline domain. In our specific case, Figure 1.1.5 shows that the nano-octahedra have a higher level of inhomogeneous atomic displacement compared to the nanocubes along all three main crystallographic directions [h00], [hh0] and [hhh]. Additionally, we see that the [hhh] direction is, for both shapes, below the [h00] direction, as a consequence of the elastic anisotropy of the metal, which for Pd

results from the [hhh] being the stiff (less deformable) and [h00] the soft (more deformable) directions.

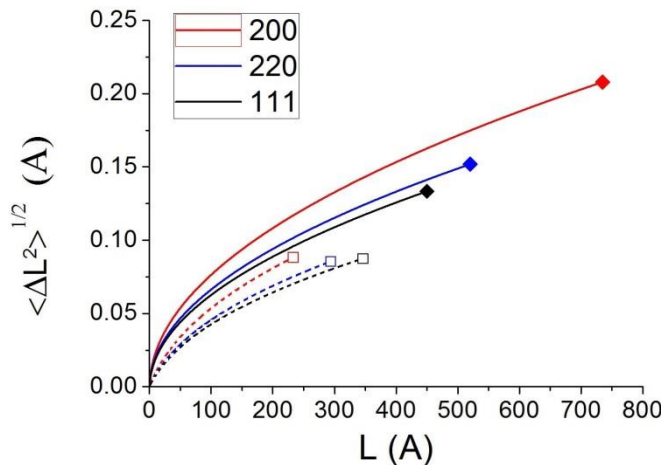


Figure 1.1.5. Warren plot for smaller cubes vs larger octahedra. The octahedra (solid lines) are represented as diamonds (\blacklozenge) while the cubes (dashed lines) are denoted using squares (\square)

The strain as shown in the Warren plot (Figure 1.1.5) demonstrates the overall strain inside the nanoparticle (L along the x-axis being the distance between any two points in the crystalline domain), along different crystallographic directions. The Debye-Waller factor contributes to this overall strain, in particular accounting for strain due to short-range disorder, both static (due to deformation of the crystal structure) and dynamic (due to thermal vibrations of crystal atoms). The Debye-Waller factor in turn is related to the MSD through the relation $B_{iso} = \frac{8\pi^2}{3} \langle u^2 \rangle$. Indeed, it has been shown that B_{iso} increases considerably from the bulk form of most materials to the corresponding nanocrystals; this is true both in plastically deformed aggregates⁶⁰ and in isolated metal nanocrystals⁶¹, with B_{iso} representing the static and dynamic disorder in the local atomic environment. This is mostly a property of each single atom, with a limited but measurable effect of the innermost coordination shells⁴².

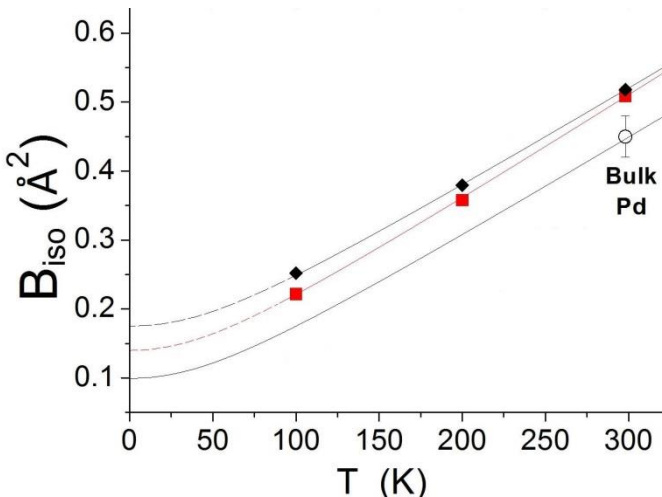


Figure 1.1.6. Variation in Debye-Waller coefficient (B_{iso} , left axis) with the measurement temperature. Black diamonds (\blacklozenge) represent nano-octahedra, and red squares (\blacksquare) nanocubes; open circle (\circ) for B_{iso} of bulk Pd. Trends for B_{iso} refer to a Debye model (see text for details).

As can be clearly observed in Figure 1.1.6, values for both shaped nanoparticles lie significantly above the B_{iso} for bulk Pd, a feature which is explained both qualitatively and quantitatively through fitting the data points using the Debye model along with an additional term for the static disorder, B_s ⁶²:

$$B_{\text{iso}}(T) = B_s + \frac{6h^2}{mk_B\Theta_D} \frac{1}{4} + \frac{6h^2}{mk_B\Theta_D} \left(\frac{T}{\Theta_D}\right)^2 \int_0^{\Theta_D/T} \frac{\xi}{e^\xi - 1} d\xi \dots \quad (1.1.1)$$

where T is the temperature of the system, Θ_D is the Debye temperature, m is the mass of an atom and the integral represents the (third) Debye function. The numerical values of B_s and Θ_D are discussed later, and compared with values obtained from MD and DFT simulations.

Even if the quantitative description is somewhat restricted due to the presence of only three experimental data points, the comparison between the nano-octahedra and the nanocubes, clearly shows that the former have consistently higher values of B_{iso} .

It may be argued that in the core of a NP the strain is similar to that present in the bulk material. This would imply that any difference in B_{iso} for nanoparticles of different shapes of the same material is due to a different surface strain, as a result of surface termination by different planes. Thus, particles with a higher B_{iso} could be expected to have a larger surface-to-volume ratio, conversely, it could be expected that smaller NPs (with a higher surface-to-volume ratio) would have a larger value of B_{iso} compared to larger NPs. This makes the experimental results in Figure 1.1.5 and Figure 1.1.6 rather counterintuitive, and worthy of further investigation.

1.1.4 Effect of nanoparticle morphology on surface vibrations

To verify the overall contribution of nanoparticle morphology to the Debye-Waller factor, we performed classical MD simulations. It must be considered that the effectiveness of EAM potentials used in these simulations is somewhat limited at smaller particle sizes. These potentials, designed to accurately describe Pd atoms in the bulk, are known to be less reliable in surface regions. Therefore, for extremely small NPs with a high surface-to-volume ratio, the application of EAM potentials becomes questionable^{36,63}. Despite these caveats, previous research³⁵ has reported reasonably good matching of MD predictions with experimental results for shaped Pd nanoparticles of intermediate sizes. A set of Pd nanoparticles with the two shapes in our experimental sample (octahedron and truncated cube) was chosen, ranging in size from 110905 atoms to 891 atoms for the octahedron and from 108471 to 911 atoms for the truncated cube. Additionally, a single simulation for the truncated cube with 840405 atoms, comparable in size to the experimental cube (edge length ~ 23 nm) was performed, to confirm the veracity of the estimates and extrapolations made with NP's of smaller size. A comparison of the B_{iso} for the different shaped NPs can be seen in Figure 1.1.7, where it is evident that the B_{iso} for the Pd octahedra remain consistently lower than for the truncated cubes, with the values generally increasing as the size of the nanoparticle decreases. Fluctuations appear in the trends for the individual shapes – this is to be expected due to the random nature of the microcanonical ensemble in which the thermalization is simulated and as is visible, these fluctuations have no bearing on the general trend in the B_{iso} for the different shapes.

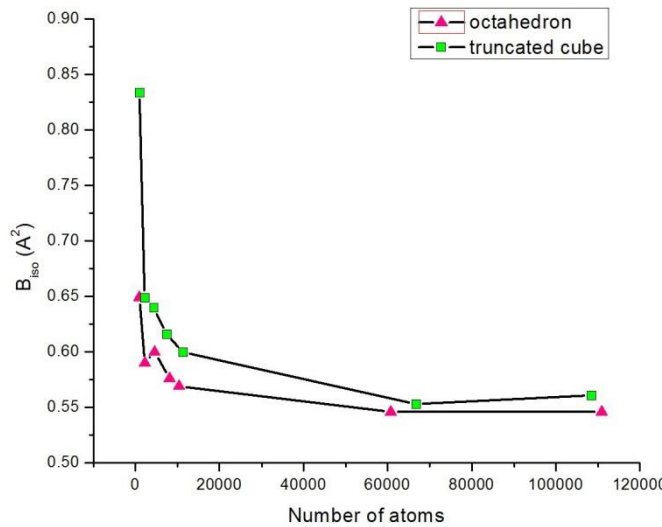


Figure 1.1.7. Comparison of B_{iso} from MD simulations for truncated cubes and octahedra over a range of sizes

It is evident from comparing the two curves in Figure 1.1.7 that, contrary to the results obtained from XRPD, the octahedral shape is more resistant to thermal vibrations (i.e., lower B_{iso}) than truncated cubes.

This is further confirmed through the simulated melting of two NP's of different shapes. For this purpose, two medium-sized particles are chosen – an octahedron with 60735 atoms and a truncated cube with 66711 atoms.

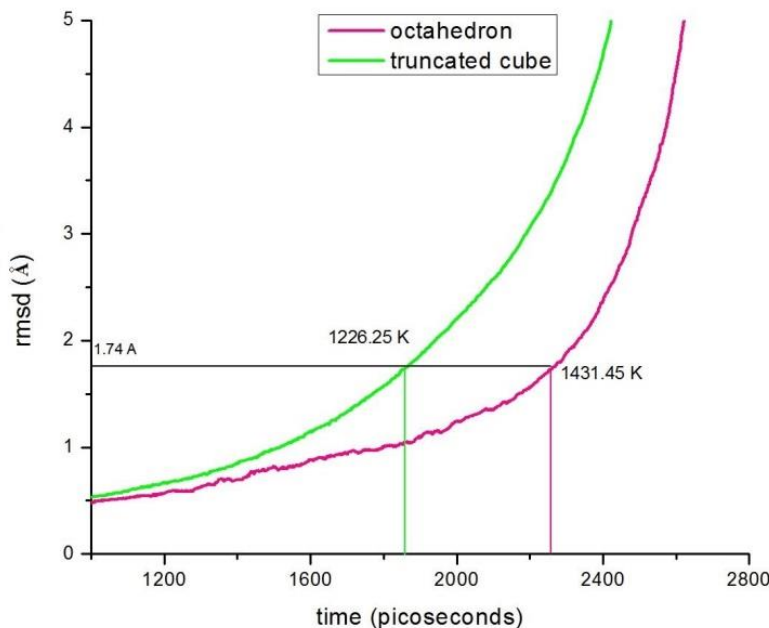


Figure 1.1.8. Simulated melting of nano-cube and nano-octahedron of similar size. Root mean squared displacement (RMSD) is shown as a function of the MD simulation time, which corresponds to increasing temperature. Melting point, indicated for each shape, is defined according to the Lindemann criterion (see text for details).

It is a well-known feature of nanoparticles that they melt at temperatures much lower than the bulk, the melting point decreasing with the reduction in size of the nanoparticle⁶⁴. For this reason, the two NPs in this simulation were chosen with a small but distinct difference in size – the octahedron having around 10% fewer atoms than the truncated cube. Despite this, from Figure 1.1.8 it is clear that the cube-shaped NP starts melting earlier, with a lower melting point (1226 K) compared to the octahedron (1431 K). For the purpose of this article we treat melting using the Lindemann criterion²⁹, which defines the melting point as the temperature at which the MSD ($\langle u^2 \rangle$) of each atom about its equilibrium position in the system exceeds a fraction of about 0.2 times the square of the interatomic spacing, which in the case of Pd is about 3.89 Å.

It is evident from the above discussion on melting points that the shape of the particle directly influences the vibrational properties of nanoparticles, particularly at the surface. We propose to make a

simple assessment of the surface contribution to the MSD, in order to qualitatively understand the results.

We separate out the surface vibrations from the bulk, by writing the total MSD as the sum of surface and bulk contributions,

$$\langle u^2 \rangle = \langle u^2 \rangle_{surf} f_{surf} + \langle u^2 \rangle_{bulk} (1 - f_{surf}) \dots (1.1.2)$$

f_{surf} being the fraction of atoms considered to be in the surface region.

Within the limits of this simplified estimate, the MSD at any given temperature T may be written as a function of the Debye temperature Θ_D as

$$\langle u^2 \rangle \approx \frac{9\hbar^2 T}{Mk_B \Theta_D^2} \dots (1.1.3)$$

where M is the mass of an atom in the NP and \hbar is the reduced Planck's constant. We can then rewrite equation 1.1.2 as,

$$\langle u^2 \rangle \approx \frac{9\hbar^2 T}{Mk_B} \left[\frac{f_{surf}}{\Theta_{D, surf}^2} + \frac{(1 - f_{surf})}{\Theta_{D, bulk}^2} \right] \dots (1.1.4)$$

where $\Theta_{D, bulk}$ and $\Theta_{D, surface}$ are the Debye temperatures for the bulk material and the surface region respectively. The surface Debye temperature can then be written as,

$$\Theta_{D, surf} \approx \left[\frac{1}{f_{surf}} \left(\frac{Mk_B}{9\hbar^2 T} \langle u^2 \rangle - \frac{(1 - f_{surf})}{\Theta_{D, bulk}^2} \right) \right]^{-\frac{1}{2}} \dots (1.1.6)$$

Using the values of the MSD obtained from the simulation of the smaller nanoparticles to calculate $\Theta_{D, surf}$ and then substituting this value into equation 1.1.4 for the full sized experimental nanoparticles, we can extrapolate a value of the MSD and by extension both the Debye temperature and the Debye-Waller factor of the experimental NP's.

Fitting the experimental data points in Figure 1.1.6 using the correlated Debye model⁶², we obtain different values of the Debye temperature for the octahedron (273 K) and the cube (266 K) as seen from the difference in slopes of the fitted curves for the two different shapes. Comparing these values to the numbers obtained from

simulation and extrapolation, we see a reasonable qualitative agreement, in that the nano-octahedron is predicted to have a higher Debye temperature ($\Theta_{D,\text{octahedron}} = 264$ K) compared to the nanocube ($\Theta_{D,\text{cube}} = 252$ K). The quantitative discrepancies arise less from a deficiency in the extrapolation model, and more from the somewhat inadequate description of systems at the nanoscale by the EAM potentials used in MD simulations – the value of Θ_D calculated directly from the simulation of the experimental sized nanocube (249 K) matches closely the value obtained by extrapolating from the smaller cube, but less so the value obtained from fitting the experimental data.

From the above discussion, we make a theoretical proposition on the nature of the dependence of the Debye-Waller coefficient on NP morphology. Through the principle of elimination, it is evident that the shape alone cannot be responsible for the difference in the experimentally observed B_{iso} ; it appears therefore that the presence of adsorption on the NP surface is ultimately responsible for the elevation in the B_{iso} as seen from experiment, which we attempt to prove conclusively with DFT simulations.

1.1.5 Deformation of surface layers due to adsorption

It has been recently demonstrated by Bozyigit et al³⁰ using ab initio MD simulations that the RMSD (and therefore the B_{iso}) at nanoparticle surfaces is significantly larger compared to the bulk, due to the mechanical ‘softness’ of the surface region which leads to a reduced phonon spring constant. In this article we propose an extension to this model, making the argument that adsorption of various molecules on a NP surface leads to a further mechanical ‘softening’ of the surface region, which causes the increase in B_{iso} observed with XRPD. This ‘softening’ of the surface region is demonstrated by comparing the geometries, obtained with DFT, of the Pd surface in the presence and absence of adsorption.

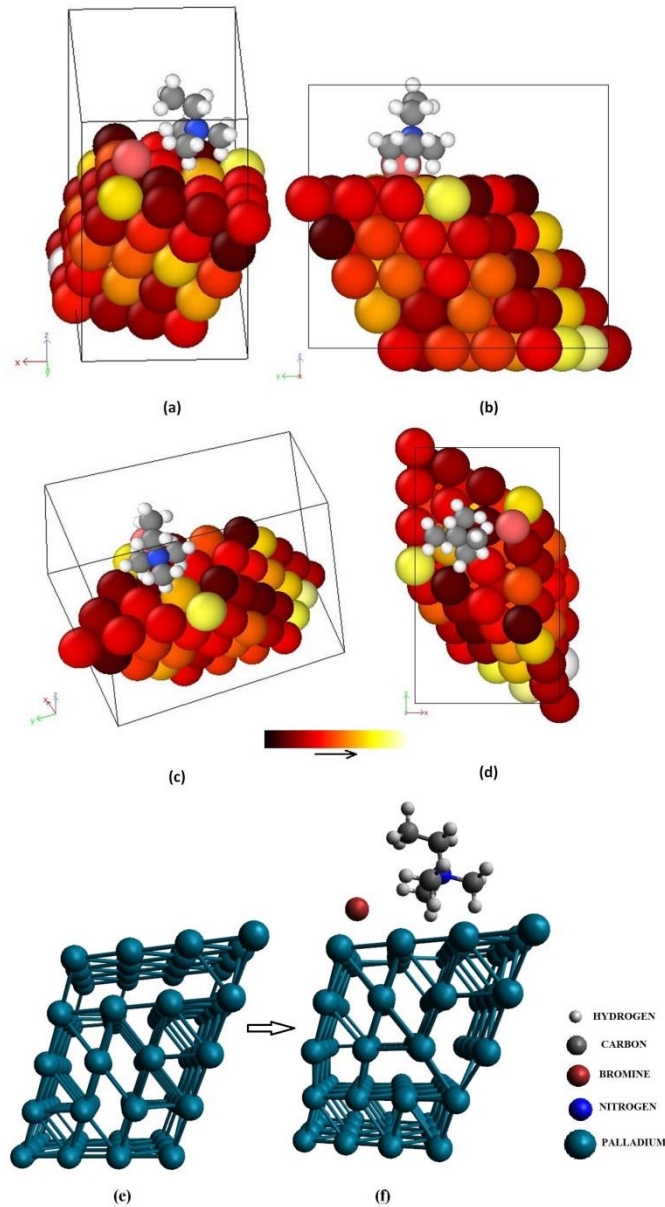


Figure 1.1.9. Adsorption of CTAB head on Pd 111 surface: The displacement of individual atoms of the Pd 111 surface due to adsorption of CTAB are shown from different perspectives in (a) to (d). The original and distorted structures are shown in (e) and (f) respectively

The octahedral NP covered with CTAB is modelled by the adsorption of a single truncated CTAB head on a Pd 111 surface, using a variable-cell relaxation to obtain a suitable convergence of Hellmann-Feynman forces. The CTAB head consists of a large positively charged centre with a single nitrogen atom in the middle surrounded by three saturated carbon atoms, coupled electrostatically to a single external bromine atom. As expected, the softening effect of the adsorption of a large zwitterionic surfactant head on a closely packed 111 surface produces an extremely large deformation of the surface layers (see **Error! Reference source not found.**1.1.9), which also penetrates a significant depth into the subsurface.

As demonstrated clearly through our classical MD calculations, the total measured Debye-Waller coefficient for nanostructured objects

is a weighted sum of surface and bulk contributions. From our DFT calculations of the surface regions in the presence of an adlayer, we demonstrate a large deformation of surface regions compared to the clean surfaces. This introduces a distinct mechanical softening of the nanoparticle surface which would, in accordance with Bozyigit et al³⁰ produce a strong increase of Debye-Waller coefficient, which convincingly explains the seemingly paradoxical disparity in the experimentally observed values of B_{iso} for the octahedral NPs in a capping agent in comparison to the cubic NPs with a clean surface.

In Flor et al³⁶ the authors have introduced a formalism to separate out 'dynamic' and 'static' components of the MSD of atoms in a nanoparticle. The former is the well-known effect of the thermal vibration of atoms, while the latter is shown to be a distinct feature arising as a result of the displacement of atoms from their ideal positions due to both long- and short-range strain. Using our DFT calculations, we show that adsorption of atoms on the surface leads to a large increase in the static component of the MSD, corresponding to B_s in Equation 1.1.1 and calculated from the curve in Figure 1.1.6, and as a consequence, the Debye-Waller coefficient as measured with XRPD.

Since DFT calculations are made at 0 K, thermal vibrations are non-existent. Therefore, we can calculate the static MSD simply by comparing the position of surface atoms in an ideal configuration, with their positions obtained using DFT after relaxing the clean surface followed by adsorption. For the adsorption of CTAB on the Pd 111 surface with periodic boundary conditions to model the surface of

the Pd nano-octahedron, we obtain an MSD of 0.218, corresponding to a value of 1.2508 \AA^2 for the B_{iso} .

We attempt to extrapolate the experimental B_{iso} values by considering the fraction of ‘bulk’ having a bulk-like value of B_{iso} , and adding to it the fraction of surface, with the value of surface B_{iso} as indicated by simulations run for smaller systems. For our purposes here, we define the surface as the first 3 atomic layers, since from the DFT simulations we can see (Figure 1.1.9 (e) and (f)) that most of the MSD increase due to capping molecules extends to that depth and not strongly beyond. Additionally, we have verified that a reasonable change of the number of surface layers does not significantly alter the qualitative results, justifying this seemingly arbitrary definition of surface.

Then, using the approximate relation

$$B_{\text{iso},\text{full}} \approx B_{\text{iso},\text{surface}} \times f_{\text{surf}} + B_{\text{iso},\text{bulk}} \times (1 - f_{\text{surf}})$$

we can provide a quantitative estimate for the Debye-Waller coefficient in the experimental NPs.

In the octahedron, we consider that the presence of the capping agent makes a strong enough contribution to the static disorder of the surface, to make the increase of the dynamic contribution possibly negligible. Then, using a surface static B_{iso} from DFT and a surface dynamic B_{iso} from the classical MD, and the experimental B_{iso} value for bulk Pd, we estimate B_{iso} as 0.523 \AA^2 for the nano-octahedron compared to the experimentally observed value of 0.522 \AA^2 , and as 0.5003 \AA^2 for the smaller truncated nanocubes as compared to 0.509 \AA^2 from experiment (details of calculation in supplementary information).

It is then clear from the arguments above that the static component of the MSD resulting from the adsorption of the CTAB molecule on the surface of the octahedral NPs is involved in raising the total B_{iso} for the octahedron to above that of the smaller nanocubes, in agreement with what is seen from our experimental results. While the high quantitative agreement of our multiscale model to experimental numbers is potentially a coincidence, given that the model involves several approximations and multiple simulation techniques with their own individual drawbacks, the qualitative description is consistent with, and clearly explains the experimental trend.

1.1.6 Conclusions

Through the discussions above we conclusively show, using both experiment and theoretical modelling, that the presence of capping agents on a nanoparticle surface significantly alters the properties of the NP surface. It is clear that the Debye-Waller coefficient, as obtained from X-ray powder diffraction using an advanced data-analysis paradigm, can serve as a sensitive measure of disorder. We identify the effect of shape on the overall vibrational properties of nanoparticles and demonstrate through simulations that the octahedral shape is inherently more stable against thermal vibrations in comparison to the cubic shape, likely due to the higher coordination number of the [111] facet enclosing its surface, compared to the [100] facet for the cube. Our results indicate, for the first time in the literature, a direct qualitative understanding of fluctuations of the Debye-Waller coefficient in the presence or absence of capping agents on nanoparticle surfaces. We argue that the adsorption of the capping agent introduces a strong static disorder at the surface region of the nanoparticle as a consequence of surface softening, a hypothesis which is borne out by our findings, both theoretical and experimental. This adsorption-induced surface disorder is strong enough to overcome the effects of a lower surface-to-volume ratio, causing the Debye-Waller coefficient of a larger NP to become greater than that of a much smaller one, a concept which potentially has many far-reaching implications in the field of nanocatalysts. As such our work opens up a new window to further multiscale investigations in order to better understand the nature of the interaction of the capping agent and other adsorbates with nanoparticle surfaces, and the significant effects this might have on the catalytic action of metal nanoparticles.

Appendix

1. X-ray diffraction data and modelling

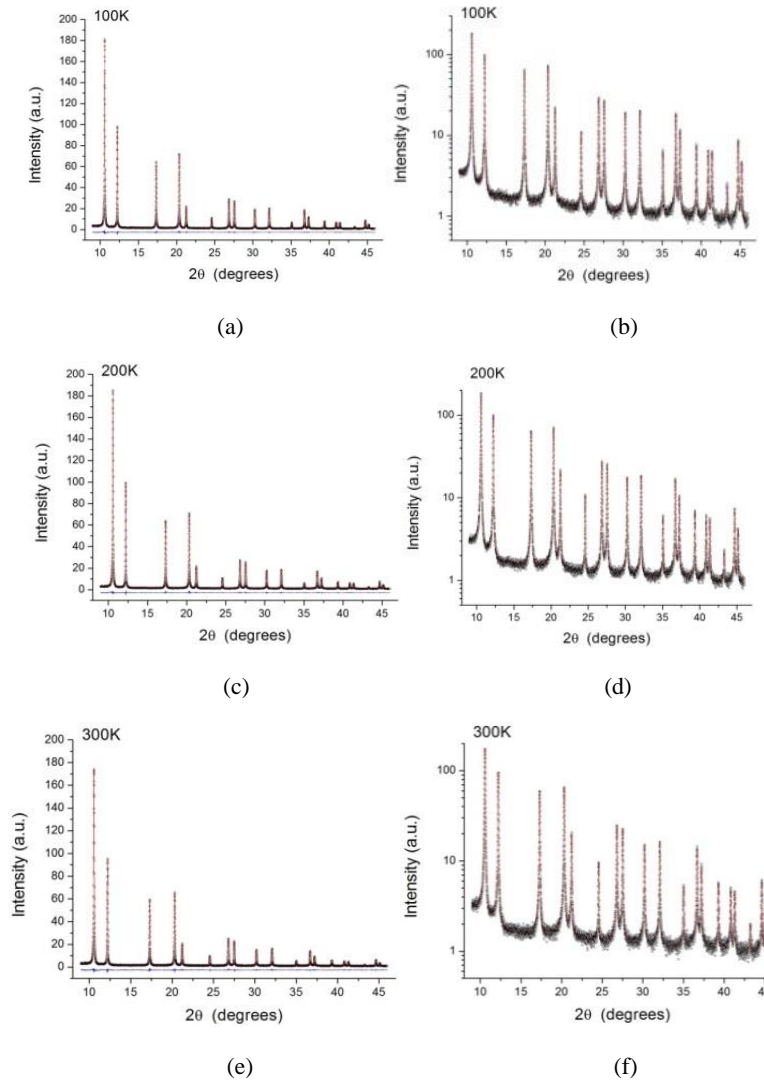


Figure S1.1.1: Whole Powder Pattern Modelling of XRPD data: (a), (c) and (e) show data (circle) and modelling (line) with their difference (residual, line below) for the truncated cubes at 100 K, 200 K and 300 K respectively (reproduced with permission from Flor et al. (2018); while (b), (d) and (f) show the corresponding data, with X-axis in a log scale

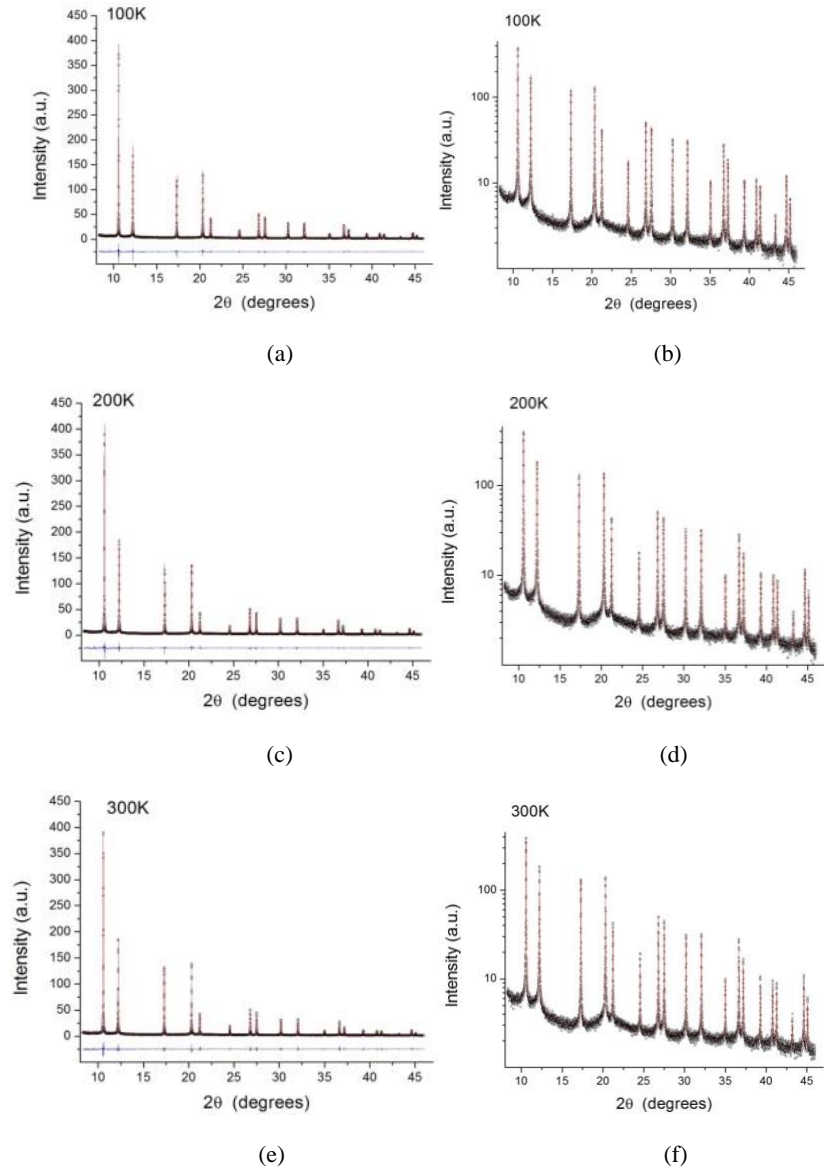


Figure S1.1.2. Whole Powder Pattern Modelling of XRPD data: (a), (c) and (e) show data (circle) and modelling (line) with their difference (residual, line below) for the octahedra at 100 K, 200 K and 300 K respectively; while (b), (d) and (f) show the corresponding data, with X-axis in a log scale

3. Variation in lattice parameter

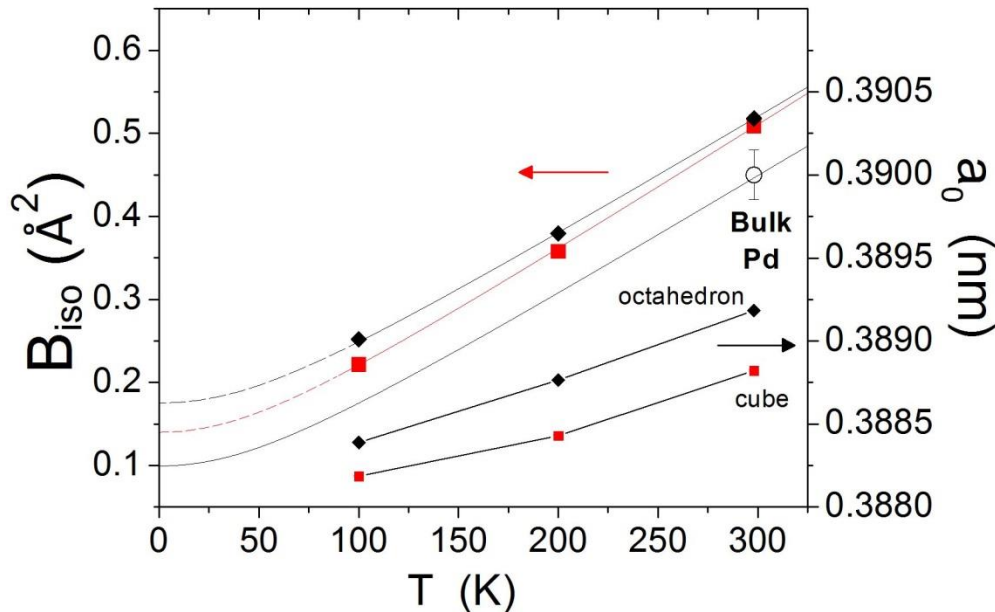
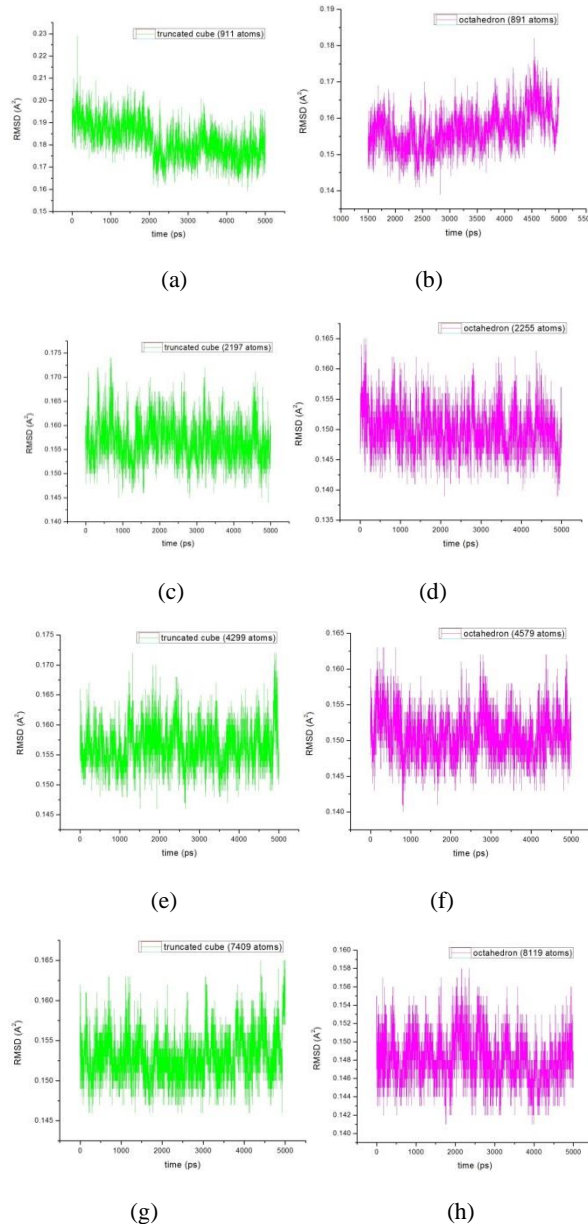


Figure S1.1.3. Variation in Debye-Waller factor (B_{iso}) and unit cell parameter (a_0) with the measurement temperature. The change in B_{iso} (shown by the 3 upper curves) is represented on the left axis, while the change in a_0 (shown by the 2 lower curves) is on the right axis. Black diamonds (\blacklozenge) for nano-octahedra, and red squares (\blacksquare) for nanocubes; open circle for B_{iso} of bulk Pd. Trends for B_{iso} refer to a Debye model (see text for details).

Aside from the different values of B_{iso} , we also observe a slightly lower ($\sim 0.003 \text{ \AA}$) lattice parameter for the octahedron compared to the cube. This is likely the result of the higher coordination number of the closely packed 111 surfaces enclosing the octahedron, compared to the 100 surfaces enclosing the cube, which being more tightly bound possibly exert a squeezing effect on the octahedral NPs.

2. Root mean square displacement of simulated particles



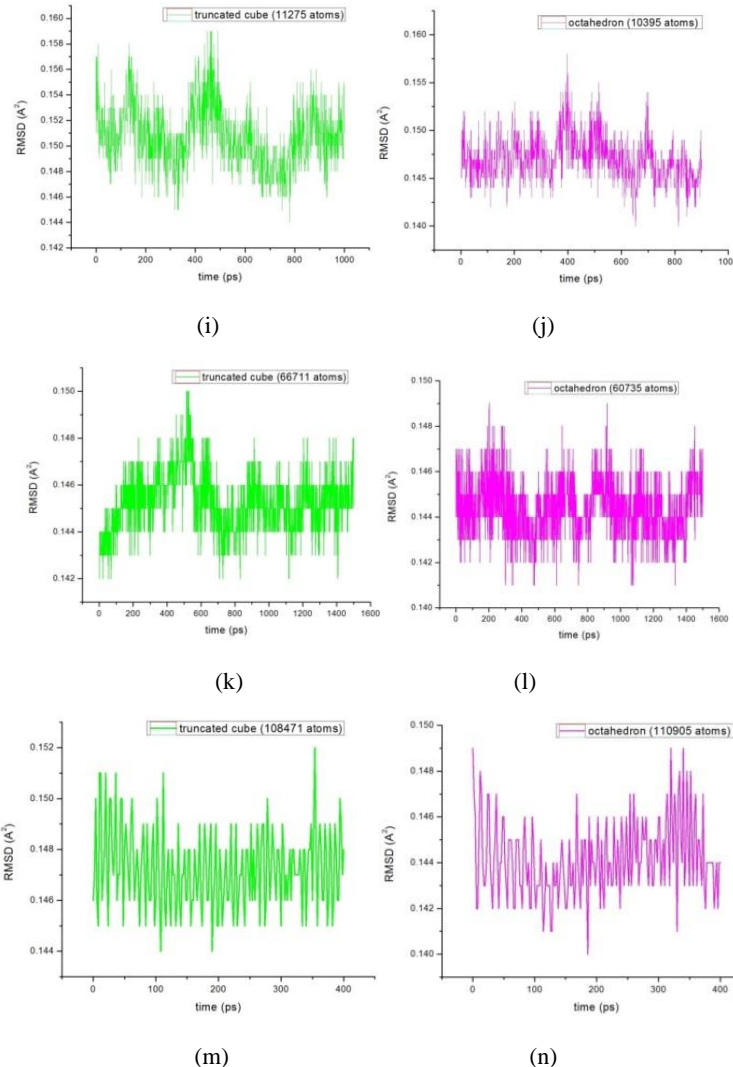


Figure S1.1.4. Stable RMSD for the NP's thermalized with MD. The figures in green represent the truncated nanocubes, while the figures in magenta correspond to the nano-octahedra. The number of atoms for each case is provided in the inset legend

3. Estimation of B_{iso} for experimental cube and octahedron

MD and DFT simulation were not made to provide exact values of MSD/B_{iso} ; more than absolute values, the simulations are intended to explain the effect of nanocrystal size and shape and of capping agents, in particular on the static disorder of the nanocrystal surface. This is particularly useful in the comparison of our studied systems: Pd octahedra capped by CTAB, and truncated Pd nanocubes virtually ‘clean’, i.e., measured after careful removal of any capping agent.

As indicated by MD, one would expect the B_{iso} to be smaller for the octahedral than the cubes; this is partly due to the size, as octahedral are bigger than the cubes, and

B_{iso} decreases with size, toward the bulk value (0.45 \AA^2); but is also an apparently intrinsic feature of the shape, as the octahedral are enclosed by $\{111\}$ facets, with higher coordination than the $\{100\}$ facets of cubes. One way and/or the other octahedral should give a lower B_{iso} .

An estimate can be obtained by MD simulations, but the size of the crystals requires quite long calculations, and in any case we know that MD potentials cannot be exact or give values directly comparable with experiments. So we can make an assessment of B_{iso} values by considering the fraction of ‘bulk’, with $B_{iso} = 0.45 \text{ \AA}^2$, and add the fraction of surface, considered here as made of the three outermost layers, with the B_{iso} indicated by MD simulations run for smaller systems.

This corresponds to make (surface dynamic) + bulk, and gives 0.468 for octahedral, and 0.5003, that is $B_{iso}(\text{cubes}) > B_{iso}(\text{octahedra})$. $B_{iso}(\text{cubes})$ is in good agreement with the experimental value of 0.509(4) at $T=300\text{K}$. Concerning the octahedral, we put forward that the capping agent gives a rather strong contribution to the static disorder of the surface. This is indicated to be of the order of 1.25 \AA^2 for CTAB on (111) Pd. This makes the dynamic contribution of the surface (made of the three outermost layers in our models) probably negligible. Indeed, if we add the DFT value for the static disorder effect of CTAB, correctly weighted for the fraction of surface atoms in the octahedral, we obtain, (surface static, due to adsorption) + bulk = 0.523 \AA^2 . More than the good match with the experimental value, 0.522(3), which is probably coincidental, here the relevant result is that MD and DFT simulations explain the higher B_{iso} of the octahedral with respect to the cubes, caused by the strong contribution of the capping agent to the surface static disorder.

Octahedron (experimental)

Approximate no. of atoms (from fitting XRD data) = 4,780,000

Approximate size (from fitting XRD data) = 53 nm

Surface static B_{iso} due to CTAB = 1.2508 \AA^2

Estimated no. of surface atoms (3 outermost layers) = 435,000

Fraction of surface atoms, $f_{surf} = 435000/4780000 = 0.091$

Estimated $B_{iso} = (\text{surface static, due to adsorption}) + \text{bulk}$

$$= (0.114 + 0.409) \text{ \AA}^2$$

$$= 0.523 \text{ \AA}^2 \text{ (compared to } 0.522 \text{ \AA}^2 \text{ from experiment)}$$

Cube (experimental)

Approximate no. of atoms (from fitting XRD data) = 781,000

Approximate size (from fitting XRD data) = 23 nm

Estimated no. of surface atoms (3 outermost layers) = 142,700

Fraction of surface atoms, $f_{surf} = 142700/781000 = 0.1827$

Surface dynamic B_{iso} from MD (3 layers, calculated on smaller cube with 66711 atoms) = 0.725 Å²

$$\begin{aligned}B_{iso} &= \text{surface dynamic + bulk} \\&= (0.1325 + 0.3678) \text{ Å}^2 \\&= 0.5003 \text{ Å}^2 (\text{compared to } 0.509 \text{ Å}^2 \text{ from experiment})\end{aligned}$$

Author contributions

Luca Rebuffi was primarily responsible for sample handling, the experimental setup and data reduction. Binayak Mukherjee was primarily responsible for making the MD and DFT simulations and for writing the article, and contributed to the analysis of the experimental data and theoretical modelling of the bulk and surface, with equal contribution as first author. Stefano Siboni was primarily responsible for the theoretical modelling of the nanoparticle bulk and surface. Allison P. Young, Benjamin P. Williams, Chia-Kuang Tsung were primarily responsible for the synthesis of the Pd nano-octahedra. Paolo Scardi was primarily responsible for conceiving the work, analyzing the experimental data, and contributed to the collection of experimental data, theoretical modelling of the nanoparticle and the writing of the article.

Acknowledgements

The work carried out at Argonne National Laboratory was supported by the US Department of Energy, Office of Science, Office of Basic Energy Sciences, under contract DE-AC02- 06CH11357. We acknowledge the CINECA award under the ISCRA initiative, for the availability of high performance computing resources and support in making DFT calculations. BM would like to acknowledge Dr. Alberto Flor for discussions and help in carrying out molecular dynamics simulations.

1.2 Effect of oxygen adsorption and oxidation on the strain state of Pd nanocrystals

This section is taken from: Mukherjee, B., Flor, A. and Scardi, P., 2021. “Effect of oxygen adsorption and oxidation on the strain state of Pd nanocrystals”. Applied Surface Science, 541, p.148508.

DOI: <https://doi.org/10.1016/j.apsusc.2020.148508>

Abstract

X-ray powder diffraction using a synchrotron light source reveals significant modifications to both morphology and strain state in Palladium nanocubes after oxidation. Short-range strain measured by the static component of the Debye-Waller coefficient is observed to be higher in the oxidized nanoparticles; while long-range strain related to the line broadening of the diffraction peaks is seen to decrease. Using multiscale modelling with classical molecular dynamics and density functional theory, we connect the decrease in long-range strain to the increased truncation of the oxidized nanocubes, while the higher short-range strain is shown to be due to surface softening from oxygen adsorption. Different surface disorder on different crystallographic facets lead to opposing trends for oxygen activation on the different exposed surfaces of the truncated nanoparticles.

1.2.1. Introduction

Palladium nanocrystals (Pd NC's) are well known as catalysts in the chemical industry, with a wide range of applications including oxidation of organic molecules⁶⁵, synthesis of polymeric materials^{3,4}, hydrogenation reactions^{21,66}, and the oxygen reduction reaction in fuel cells⁶⁷. Among organic molecules, the oxidation of methane (CH_4) to carbon dioxide (CO_2) is considered an environmentally sustainable combustion process compared with other hydrocarbon based fuels, due to the comparatively lower carbon-to-hydrogen ratio in CH_4 . However, among all saturated hydrocarbons, methane has the highest carbon-hydrogen bond strength which in turn produces sub-optimal ignition performance for reaction in the gas phase⁶⁸. On the other hand, CH_4 dissociates with low activation energy on several noble metal surfaces, allowing an enhancement of the ignition reaction. Of

these noble metals, Pd is regarded as one of the most promising catalysts for complete, low temperature oxidation of CH₄^{69–72}. The catalytic activity of Pd nanocrystals is known to be a function of size, morphology, synthesis method and oxidation state of the particle, and as such, these factors play an important role in determining the efficiency of the CH₄ oxidation process. Additionally, due to the exposure to ambient oxygen (O₂) throughout the combustion process, Pd-based catalysts are expected to be oxidized and form both surface and possibly some bulk oxide, a phenomenon which has been shown to measurably affect the catalytic process^{73–75}. Reports in the literature suggest that PdO is the more catalytically active phase⁷⁶ at lower temperatures, while at higher temperatures metallic Pd dominates catalytic activity⁷⁷. Compared to pure metallic Pd, coincident Pd and PdO phases have been shown to be more active catalysts for the combustion reaction of CH₄⁷⁸.

Another industrially important catalytic process which involves the adsorption of O₂ on Pd surfaces is the oxygen reduction reaction (ORR). Pd has been used as the cathode material for ORR in electrochemical applications such as fuel cells. ORR has been studied in alkaline media using anion exchange membranes (AEMs). A significant motivation to change the electrolyte membrane from acidic (mainly in proton exchange membranes (PEMs)) to alkaline is the improved electrokinetics of ORR in an alkaline environment, in contrast to the excessive corrosion in acidic media^{79,80}. In this regard, several cathode electrocatalysts have been proposed, among which Pd-based NC's are an important candidate⁸¹.

Several reports in the literature have addressed the adsorption of oxygen and/or subsequent oxidation of the metal surface of Pd NC's. Collins et al (2014)⁸² have studied the oxidation of Pd NC's using a combination of transmission electron microscopy (TEM) and x-ray photoelectron spectroscopy (XPS). They have demonstrated that oxidation of the NC starts from edge and corner sites, leading cubic NC's to evolve towards a rounded shape, whereas octahedral particles tend to maintain their morphology. Using density functional theory (DFT) calculations alongside high performance liquid crystallography (HPCL) and near-edge X-ray absorption fine structure (NEXAFS) experiments, Long et al (2013)¹⁹ have shown that the activation of O₂ for catalytic processes by Pd NC's is strongly dependent on the corresponding crystallographic facet. They have identified the 100 surface of the NC to be the most efficient in inducing a spin-flip

process in the O₂ molecule via a transfer of charge from the Pd surface to the molecule, thereby activating the inert ground-state O₂ molecule to a highly reactive singlet O₂. Using molecular dynamics (MD) simulations with a reactive force-field (ReaxFF), Mao et al (2016)⁸³ have studied the role of Pd NC's in the combustion of methane. The authors have predicted that O₂ molecules block the active sites for the adsorption of CH₄, and are less likely to dissociate on oxygen-coated Pd surfaces. Significantly however, these same oxygen-coated NC surfaces induce the dissociation of CH₄ at a lower temperature compared to bare NC's. Most recently, Zhang et al (2017)⁸⁴ have confirmed using high-resolution TEM studies that oxidation of Pd NC's starts from active sites present at the edge and corners of the particle, and have shown that the oxide phase starts by forming small, island-like clusters on the NC surface.

While these aforementioned studies and others⁸⁵ have thoroughly characterized the kinetics of oxygen adsorption on the surface of Pd and other NC's, they remain conspicuously silent on the matter of strain generated due to the presence of oxygen on the NC surface. Surface lattice strain is well known for being a crucial factor which may be tuned in order to enhance catalytic performance in NC's⁸⁶. Lattice distortion due to surface strain is known to modify the electronic structure of the metal NC surface by inducing a shift in the surface d-band center⁸⁶. As a result, strain-engineering of the NC surface can be effectively used to optimize the sorption energies of molecules for a particular chemical reaction⁸⁶. Combining coherent diffraction imaging (CDI) with reactive MD and finite elements modelling, Kim et al (2018)⁸⁷ have studied the role of oxygen adsorption in modifying the strain-state of Pt nanocatalysts during CH₄ oxidation. In a recent publication, Rebuffi et al (2020)⁸⁸, through a combination of X-ray powder diffraction (XRPD) experiments and MD and DFT simulations, have studied the role of capping agent-induced disorder on a Pd NC surface. They have conclusively shown that the short-range strain developed on the surface of a Pd NC due to surface softening induced by the adsorption of the capping agent CTAB is significant enough to overcome the strain-effects associated with both size and shape of the nanoparticle. As such, the question of how the strain-state of a Pd NC is affected by the presence of oxygen is highly relevant for understanding the effects of oxygen adsorption and oxidation on the catalytic performance of Pd NC's.

In this article, we aim to answer this question through a combination of experimental results from XRPD, and theoretical modelling in the form of multiscale simulations using MD with reactive potentials, as well as DFT. The tried-and-tested XRPD technique, with high quality data obtained from synchrotron light sources and analysed using advanced data analysis paradigms such as the whole powder pattern modelling (WPPM) approach³⁷, can prove a unique asset in characterizing strain in a NC. XRPD provides average information over the entire powder sample, in comparison to microscopy and imaging techniques such as scanning tunneling microscopy, transmission electron microscopy, or coherent diffraction imaging, which are able to probe only a small cross-section of the sample at a time. By completely and accurately fitting high quality diffraction data, the short- and long-range strain effects in Pd NC's have been effectively quantified in the past via the Debye-Waller coefficient (DW)⁸⁸ and the Warren plots³⁵ respectively. These experimental results, along with the use of DFT and MD simulations with state-of-the-art reactive forcefields, allow us to present a complete qualitative account for the modification of the strain-state in Pd NC's as a result of O₂ adsorption.

1.2.2. Experimental and computational methodology

Materials, synthesis and characterization

The Pd nanocubes were synthesized following a recipe extensively described in the literature^{35,89}. The process was started by dissolving 105 mg of the capping agent polyvinylpyrrolidone (PVP), 600 mg of potassium bromide(KBr), and 60 mg of L-ascorbic acid in a ~20 ml glass scintillation vial in a total volume of 8.0 ml of deionized water. This was then equilibrated by stirring for around 10 minutes at a rate of 500 rpm inside an oil bath set at 373 K. A separate solution containing 57 mg sodium tetrachloropalladate (Na₂PdCl₄) dissolved in 3.0ml deionized water was then injected rapidly into the already prepared solution. The reaction was then allowed to continue for 3 hours, after which the particles were precipitated by adding a 10:1 acetone:water solution and centrifuging at 8000 rpm. The collected particles were then rinsed and similarly brought down twice more before being redispersed in 100 µl water as the final volume of solution used in the XRPD experiments. The samples were oxidized by leaving them exposed to ambient conditions.

The XRPD data was acquired at the powder diffraction beamline (11-BM) of the Advanced Photon Source at the Argonne National Laboratory. The capillary containing the Pd NC's were mounted on the beamline spinner and operated at 4200 rpm to ensure uniform collection of data and statistical consistency. Three measurements, 1 hour each, were performed at 100 K, 200 K and 300 K, with radiation of wavelength 0.0413874 nm, and the data was collected over a 2θ range of 0 to 60. The XRPD patterns thus obtained were then analyzed according to the WPPM method using the PM2K software (University of Trento, Italy, Scardi et al.⁴¹ and references therein). Effects on the pattern due to the sample holder was modelled using pseudo-Voigt curves over the pattern from an empty Kapton capillary, while the instrumental profile was modelled using a standard LaB₆ powder pattern. The size and strain-broadening models were the same for all three temperatures. The initial size and shape of the NC was obtained from previously TEM images (see supplementary Figure S1.2.3), some of which are also found in previous publications³⁵, with a subsequent refinement of the mean and variance of the particle edge length (defined by a lognormal distribution), as well as the degree of truncation being performed by the WPPM algorithm. The strain broadening in particular is phenomenologically modelled with the WPPM approach, which accounts for the inhomogenous atomic displacement due to the surface of the NC's³⁵. This effect, coupled with the shape and the truncation of the crystalline domain within the surfaces of the NC leads to anisotropic broadening of the diffraction peak³⁷. The background was treated using a Chebyshev polynomial and the Pd unit cell parameter and Debye-Waller coefficients were independently refined to account for the effect of temperature, with the decrease in Bragg scattering intensity being accounted for with the simple scalar form B_{iso} of the traditional Debye-Waller factor. Additionally, temperature diffuse scattering (TDS) is used in order to account for the local atomic displacement due to thermal (dynamic) as well as disorder (static) effects⁴³. The phase analysis to separate the PdO phase from the metallic Pd was instead performed using the software Topas^{41,90}.

Classical molecular dynamics

The large-scale atomic/molecular massively parallel simulator (LAMMPS)⁴⁴ was used to perform classical MD simulations. To study the long-range strain we use Pd NC's modelled using embedded atom method (EAM) potentials⁴⁵⁻⁴⁷. It has been demonstrated in the

literature³⁵ that these potentials produce a description of strain in reasonable overall qualitative agreement with experimental observations from XRPD, thus being quite adequate for modelling the long range strain generated due to a rounding of the Pd NC. The time step for the Verlet integration was taken as 1.5 femtoseconds (fs). The energy of the NC's was first minimized using a Hessian-free truncated Newton (HFTN) algorithm. The NC's were then thermalized by allowing them to evolve in a canonical ensemble (constant particle number N, system volume V and temperature T) until an appropriate thermal equilibrium was reached at T=300K. A chain of 100 Nosé-Hoover thermostats with a 5.0 picosecond damping parameter with MTK corrections⁴⁸ implemented on the equations of motion was used to reach the isothermal condition. Subsequently the constant temperature condition was removed, and the system was allowed to evolve in the microcanonical ensemble (constant N, V and total energy E). The simulation trajectories were visualized with Ovito⁵⁸ and the mean square displacement ($\langle u^2 \rangle$) of the system was then calculated using the software VMD⁹¹.

On the other hand, to study the oxidation of Pd NC's and the short-range strain developed thereof, the ReaxFF forcefield developed by Senftle et al⁷⁵ was used. This forcefield describes coulombic, covalent and van der Waals interactions using bond-length/bond-order combined with polarizable charge⁹². The force field has been trained against ab initio data sets and can therefore accurately model bond breaking and formation in chemical reactions, and has been used in the past to model oxygen adsorption on Pd nanoparticles^{93,94}. The Pd NC's of different size were first equilibrated at 300 K for 50 picoseconds (ps), and subsequently heated up to 600 K in another 50 ps using a chain of 100 Nosé-Hoover thermostats. Subsequently, in different simulations, they were either allowed to evolve at 600 K in a microcanonical (NVE) ensemble for 50 ps, or heated up again to 900 K in the same time. A significant difference in the ReaxFF-MD simulations compared to MD with EAM potentials, is the use of a much smaller integration timestep of 0.2 fs, since to smoothly model chemical reactions the timestep needs to be an order of magnitude lower than the smallest time-period for a molecular oscillation (~1 fs)^{95,96}.

Density functional theory

The initial step of the DFT calculations involved the relaxation of the geometry of the different Pd surface facets using the electronic structure calculation package Quantum Espresso^{50,51}. The Perdew-Burke-Ernzerhof (PBE)⁵² functional was used as an approximation for the exact electron-exchange correlation function, with the scalar-relativistic PBEsol pseudopotentials⁵³ using the projector augmented wave (PAW) method. These pseudopotentials have been reported in the literature⁵⁴⁻⁵⁶ to faithfully reproduce elastic and mechanical properties in solids. Corrections for the van der Waals interaction were implemented using the Grimme-D2⁵⁷ method. A fine 4x4x1 Γ -centered Monkhorst-Pack k-mesh was used to sample the irreducible Brillouin zone, with a Marzari-Vanderbilt charge smearing of 0.001 Rydberg (Ry). The cutoffs used for the kinetic energy and charge density were respectively taken as 60 Ry and 480 Ry. The Pd 111, 110 and 100 surfaces were modelled using 3 x 3 surface slabs. The thickness of the surface slabs were 5 atomic planes in the Z-direction, with a 15 Å vacuum layer introduced to reduce interactions between periodic copies. The convergence thresholds for the energy and Hellman-Feynman forces were set to 0.001 eV and 0.01 eV/Å respectively. Charge and magnetization densities have been visualized using VESTA⁹⁷.

1.2.3. Experimental results

The analysis of the diffraction data using the WPPM approach can be seen in Figure 1.2.1 (a-c) at three different temperatures, with the insets showing the intensity in logarithmic scale in order to highlight the details in the peak tail regions. This serves as an indication of the quality of the fit, allowing us to draw reliable conclusions on the DW coefficient, in terms of B_{iso} values. While the dynamic component of B_{iso} dominates at higher temperatures, the static component due to distortion of the crystal lattice is a temperature-independent feature. The changes in the diffraction pattern due to the onset of oxidation can be clearly seen, most remarkably around the 15° mark on the Bragg angle scale in Figure 1.2.2(e).

Using WPPM of the XRPD data, we study the change in morphology of the Pd NC due to oxidation. The size-broadening effect on the diffraction peaks from the NC's is modelled with a lognormal distribution for the NC edge size, with an additional freely refined

parameter, going from 0 for perfect cubes to 1 for perfect octahedra, being used to quantify the deviation from a perfect cubic shape at the edges and corners of the NC. As is evident from Figure 1.2.2, the nanoparticles have a fairly uniform and homogenous size distribution, corroborated by TEM images (see Figure 1.2.1d inset and supplementary

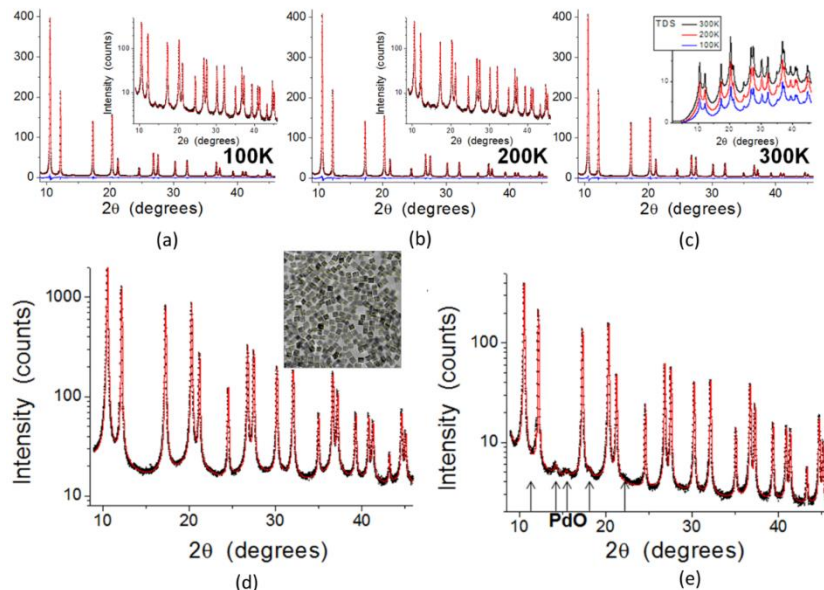


Figure 1.2.1. Whole powder pattern modelling of XRPD data: (a) and (b) and (c) show data (circle) and modelling (line) for the truncated cubes at 100 K , 200 K and 300 K respectively; the corresponding insets in (a) and (b) show the same data with the Y-axis (intensities) in the logarithmic scale for clarity, while the inset in (c) shows the TDS at the three temperatures; inset in (d) shows TEM image of clean nanoparticles attesting to a homogenous distribution of particle shape and size; (e) and (f) show the fitting of the diffraction patterns (300 K, intensities in logarithmic scale) before and after the onset of oxidation respectively. Arrows in (e) point to the PdO peaks.

information file, Figure S1.2.3). Oxidation of the NC leads to a reduction in average particle edge length from 14.23(1) nm to 14.05(1) nm, and an increase in degree of NC truncation from 0.110(2) to 0.163(4), suggesting an overall ~10% decrease in volume of the NC.

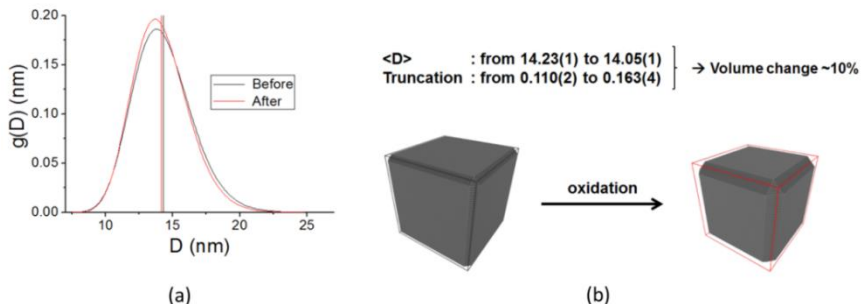


Figure 1.2.2. Change in NC morphology due to oxidation: (a) shows the lognormal distribution for NC edge size from WPPM modelling, while (b) is representative of the increase in truncation of the NC

This conclusion is further supported by performing a phase analysis of the diffraction pattern, which attests to the presence of a secondary nano-polycrystalline phase of around 7 % of palladium(II) oxide (PdO) formed on the Pd NC surface. This indicates that Pd atoms are dislodged from the Pd lattice and form a crystalline PdO phase in-place, leading to the reduction in volume of the pure Pd phase.

The short-range strain developed on the Pd NC surface, both static (deformation of the crystal structure) and dynamic (due to thermal vibrations of crystal atoms), is measured through the DW coefficient (B_{iso}). This is proportional to the mean-square displacement (MSD) of individual atoms in the NC from their ideal crystalline positions, and is connected to the MSD ($\langle u^2 \rangle$) through the expression, $B_{iso} = \frac{8\pi^2}{3} \langle u^2 \rangle$. It is thus a local property, mostly restricted to individual atoms, with a small but measurable effect on their closest coordination shells⁴². The B_{iso} of nanocrystalline materials is known to be considerably higher than their bulk counterparts^{36,60,61}, and in a recent study Rebuffi et al (2020)⁸⁸ have demonstrated that its value for an NC is significantly increased by the surface disorder induced by adsorption of a capping agent.

From fitting the diffraction pattern, the values of B_{iso} obtained for the Pd nanocube both before and after oxidation are observed to lie well above the bulk value for metallic Pd, as seen in Figure 1.2.3. This can be explained by a correlated Debye model⁶², according to which the B_{iso} at a particular temperature T is written as:

$$B_{iso}(T) = B_s + \frac{6h^2}{mk_B\Theta_D} \frac{1}{4} + \frac{6h^2}{mk_B\Theta_D} \left(\frac{T}{\Theta_D}\right)^2 \int_0^{\Theta_D/T} \frac{\xi}{e^\xi - 1} d\xi \dots (1.2.1)$$

where h is Planck's constant, Θ_D is the Debye temperature, m is the mass of an atom, the integral represents the (third) Debye function, and B_s is an additional term which corresponds to static disorder.

While the quantitative description is somewhat restricted by the limited number of data points, it is nevertheless quite clear from the curves in Figure 1.2.3 that the B_{iso} for the Pd nanocubes after oxidation is increased compared to the clean particle before. From these results, it is reasonable to make the assertion that it is in fact the adsorption of O_2 on the surface of the Pd nanocube which is responsible for the increase in B_{iso} , an assertion which we confirm using different simulation methods.

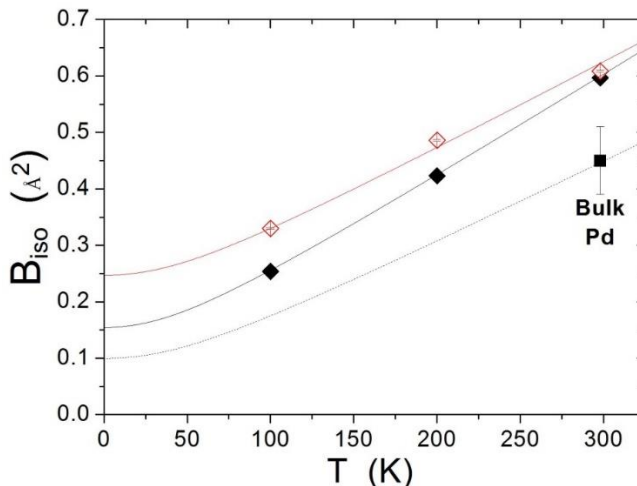


Figure 1.2.3. Increase in Debye–Waller coefficient (B_{iso} , left axis) with the measurement temperature. Solid black diamonds (\blacklozenge) represent nanocubes before oxidation and open red diamonds (\lozenge) after; the solid square (\blacksquare) represents B_{iso} of bulk Pd. Trends for B_{iso} (dotted line) refer to a Debye model (see text for details)

Apart from the information on short-range strain due to oxidation, the long-range strain effects in the nanoparticle can also be quantified from fitting the diffraction pattern, and represented through the Warren plot, as seen in Figure 1.2.4(a). This diagram expresses the long-range strain within a crystalline domain by plotting the standard

deviation of the distance L ($\langle \Delta L^2 \rangle^{1/2}$) between atomic scattering centers along specific crystallographic directions, as a function of L . In our specific case, it can be seen from Fig 4(a) that the ($\langle \Delta L^2 \rangle^{1/2}$) curve in the oxidized NC lies consistently lower compared to the clean particle, across all three main crystallographic directions [h00], [hh0], [hhh], suggesting a reduction in long-range strain in the NC due to oxidation.

The experimental results from Figure 1.2.3 and Figure 1.2.4(a) show that while oxidation leads to an increase in the short-range strain in the NC, as seen through the increase in the B_{iso} , the overall long-range strain represented by the inhomogenous atomic displacement in the Warren plot seems to diminish, compared to the clean particle. In the following sections we seek to further explain these seemingly contradictory changes in the strain-state of the Pd NC due to oxidation, through the application of multiscale modelling techniques.

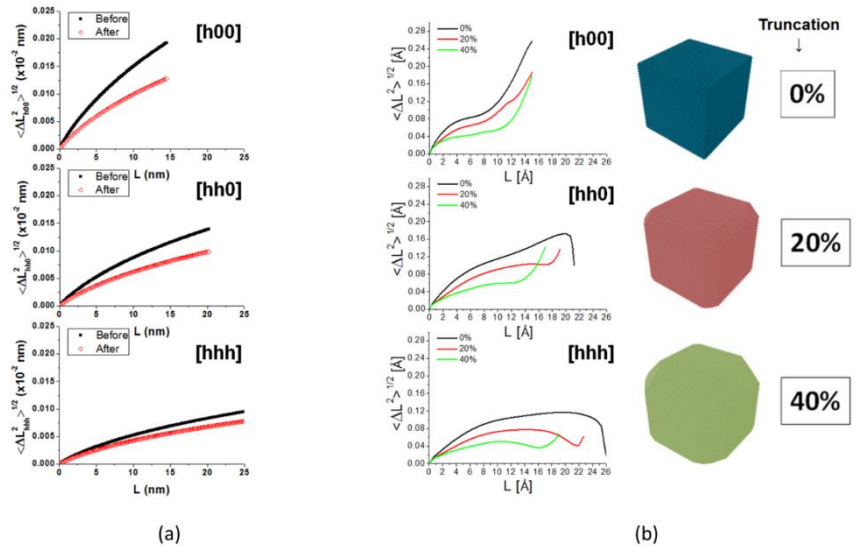


Figure 1.2.4. Warren plot describing long-range strain: (a) shows the experimental Warren plot, obtained from fitting of diffraction data before (black line) and after (green) oxidation, along different crystallographic directions and (b) shows the Warren plot obtained from MD simulations along the corresponding directions, with truncation of 0 (blue), 0.2 (red) and 0.4 (green).

1.2.4. Progression of oxidation on Pd nanocube

In order to study how the kinetics of the oxidation process correlate with the modification of the strain state in the Pd NC's, we have used MD simulations using reactive force fields (ReaxFF), which are significantly more computationally intensive than EAM potentials. In order to perform tractable simulations for the naturally slow oxidation process, we have made the simulations in an oxygen-rich environment, with a tradeoff of particle size in favour of longer simulation timescales. To investigate the kinetics of oxidation, we have used a Pd nanocube with 911 atoms. Figure 1.2.5 (also see supplementary video) shows the progressive oxidation of the NC. Concurrent with previous reports in the literature^{82,84}, we observe that the oxygen adsorption starts preferentially at edge and corner sites. Subsequently, these molecules are seen to split, and individual oxygen atoms can be seen to penetrate into the surface and subsurface layers of the Pd NC. As more and more oxygen penetrates the layers of Pd atoms, the cubic NC starts to lose its shape starting from the edges and corners, leading to the progressive ‘rounding’ of the NC shape, as observed experimentally by Collins et al⁸², as well as our own diffraction results.

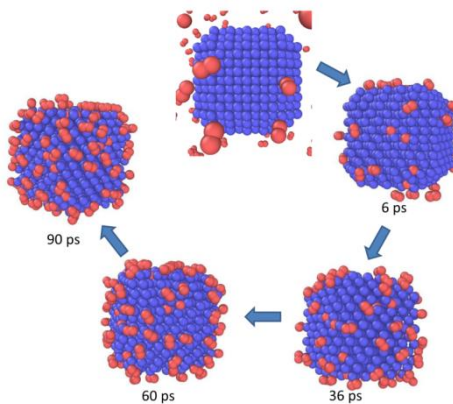


Figure 1.2.5. Oxidation on the Pd NC surface over time, starting from edge and corner sites. Red balls for oxygen atoms, blue for palladium. See supplementary video.

To further characterize the oxidation process, we have calculated the radial pair distribution function (rpdf) of pairs of atomic species in the oxidized nanocube, after 20 ps, 430 ps and 780 ps. in the Pd-Pd rpdf in Figure 1.2.6(a), we notice a shift in the peaks towards higher distances as the simulation progresses, corresponding to a ‘swelling’

of the NC as increasing amounts of oxygen penetrate the surface and subsurface layer and form the PdO phase. This feature is particularly highlighted at longer distances, as seen in the inset of Figure 1.2.6(a). The presence and increase of the PdO phase is confirmed by the evolution of the O-Pd rpdf as shown in Figure 1.2.6(b). The position of this peak, centered close to 2.1 Å, attests to the formation of a partially crystalline phase of palladium oxide which continues to increase, as seen from the increase in peak height over longer simulation times. Fig 1.2.6(c) shows the O-O rpdf, with the two primary peaks showing the contraction and relaxation modes of the oxygen molecules in the atmosphere. The distribution of the O-O rpdf is distinctly asymmetric, with a ‘step’ in the upper tail region of the curve close to 1.3 Å. This step is representative of the oxygen molecules physisorbed on the surface of the Pd NC. It hints at a metastable state for oxygen on the Pd surface before complete dissociation, where the O₂ molecules remain weakly bound, with a higher interatomic separation compared to atmospheric O₂. The increase of the step height at longer time scales corresponds to the increase in the number of oxygen molecules physisorbed on the surface of the NC.

From a visual inspection of the MD trajectories combined with the calculated rpdf, we thus obtain a clear picture of how oxidation proceeds on a Pd NC – forming a layer of physisorbed oxygen on the surface with some molecules subsequently dissociating to form a PdO phase within surface and subsurface layers, with the process starting preferentially from edge and corner sites, thereby leading to a rounding-like modification of the NC shape.

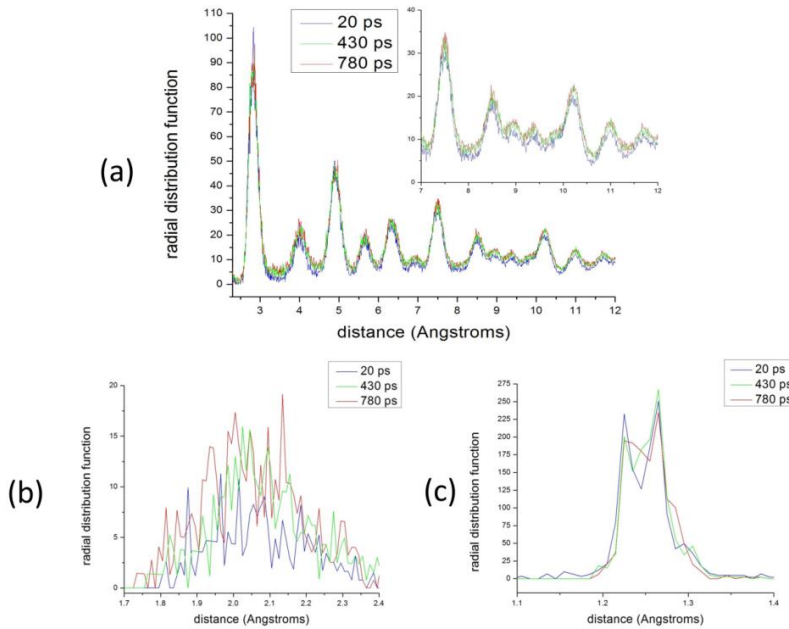


Figure 1.2.6. Radial pair distribution function: (a) denotes the Pd-Pd rpdf, with the inset highlighting the shifting of the peaks over longer distances as oxidation proceeds, (b) represents the O-Pd rpdf, showing the increase in the peak representing PdO at 2.1 Å with increasing oxidation, (c) shows the O-O rpdf, with a ‘step’ around 1.3 Å² denoting the physisorbed oxygen on the Pd surface. Blue, green and red lines correspond to the data at 20 ps, 430 ps and 780 ps of simulation time respectively.

In order to characterize the strain-state of the Pd NC, we have performed simulated oxidation on a larger Pd NC, with 11275 atoms. The increase in size of the simulated particle restricts the degree of oxidation occurring within the simulation timescale, but the larger particle allows for a more faithful representation of the elastic properties of the NC, suitable for a comparison with the significantly larger experimental objects.

Figure 1.2.7 shows the time evolution of atomic displacement magnitude on the surface of the Pd NC undergoing oxidation, given by the displacement of individual atoms from their mean position. As expected, high strain (corresponding to higher atomic displacement, red atoms) is generated at corner sites, due to preferential adsorption of oxygen at these locations and the under-coordination of atoms at these points. Over time, the high strain region expands to edge sites, before spreading to the rest of the NC surface, due primarily to

undercoordination of the atoms at edge and corner sites coupled with the elastic anisotropy in Pd NC's³⁵.

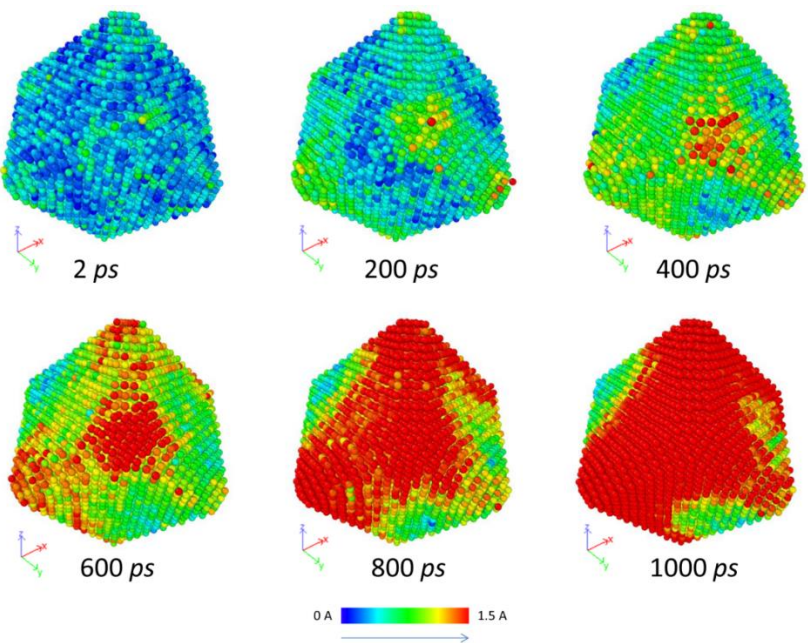


Figure 1.2.7. Increasing disorder on the Pd NC surface: The magnitude of atomic displacement of Pd atoms due to oxygen adsorption, color-mapped to the surface of the Pd NC at six different points in simulation time. Only Pd atoms are shown.

This disorder introduced into the surface region of the NC due to the adsorption of oxygen and the resulting displacement of Pd atoms from their mean positions leads to the generation of short-range strain, which manifests itself in the static component of the Debye-Waller coefficient. This can be directly verified by obtaining the B_{iso} via the mean square displacement (MSD) calculated from the MD trajectories.

Figure 1.2.8 shows a comparison of the B_{iso} for the Pd NC from MD simulations under different conditions. For a clean NC evolving in a microcanonical (NVE) ensemble at 600 K (green line), the value of the B_{iso} remains stable over the simulation time scale. In comparison, the B_{iso} for the same NC evolving at the same temperature under the same NVE conditions in an oxygen atmosphere (blue line), is seen to steadily rise, corresponding to the increase in surface disorder as seen in Figure 1.2.7, as well as the experimental B_{iso} curves obtained from XRPD (Figure 1.2.3). It is important to note here that the experimental conditions differ significantly from the simulation: the experiments

were performed with larger particles oxidized over longer times, with measurements at lower temperatures compared to the MD calculations. All these factors contribute to a significantly higher value for the B_{iso} obtained from the simulations. Nevertheless, the qualitative trend is clear – the presence of adsorbed oxygen on the Pd NC promotes surface disorder, leading to a clear rise in the Debye-Waller coefficient. In order to contrast the oxygen-induced static disorder with the dynamic disorder due to temperature, we show a third simulation, with the oxidation process of the same NC simulated on a temperature ramp from 600 K to 900 K (red line). The B_{iso} in this case is seen to not only be much higher than at 600 K, but also appears to increase at a much faster rate, in contrast with the almost linear increase for the values at lower temperatures.

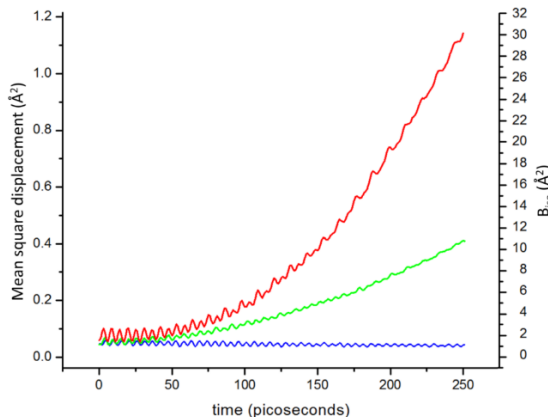


Figure 1.2.8. Time evolution of the Debye-Waller coefficient represented by B_{iso} (right axis) and mean square displacement (left axis), for a clean Pd nanocube at 600 K (green), a Pd nanocube undergoing oxidation at 600 K (blue), and a Pd nanocube undergoing oxidation while on a temperature ramp from 600 K to 900 K (red). All lines refer to both axes, which only differ by a scaling factor of $8\pi^2/3$.

From the above discussion, it is then clear that oxidation in Pd NC's leads to an increased surface disorder as measured through B_{iso} , a distinct static effect clearly separate from the much stronger dynamic effects due to temperature. While the increase in B_{iso} due to oxidation results from the displacement of Pd surface atoms from their mean position due to the interaction with oxygen atoms, the well-known temperature effect is due to the thermal motion of Pd atoms away from their mean positions, throughout the entire NC, causing the larger overall increase in B_{iso} .

As opposed to the increase in short-range strain, the long-range strain is experimentally observed to be lower in the oxidized NC compared to the clean particle as observed from the Warren diagram in Figure 1.2.4(a). To study the decrease in the long-range strain after oxidation, we use MD simulations using EAM potentials, which are more appropriate for simulating thermal/elastic properties.

To model the ‘rounding-out’ effect observed from experiment, we use three similar sized Pd nanocubes with increasing levels of truncation, going from 0 to 0.4. After each NC is thermalized, the Warren plot is calculated from the MD trajectories following the methods described in detail by Flor et al (2019)³⁶. This process involves calculating the mean-square relative displacement (MSRD) from the averaged deviation in the distance between pairs of atoms ($\overrightarrow{r_{ij}}$) in the entire particle over the whole thermalization trajectory. This is then used to calculate the long-range strain leading to the Warren plots in Figure 1.2.4(b), which when compared with Figure 1.2.4(a), are clearly in a good qualitative agreement with experimental observations. We can then safely assert that the truncation of the nanocube due to preferential oxidation at edge and corner sites and the subsequent rounding in its shape, leads to a decrease in long-range strain. This can be explained as a release in strain due to a transition from a sharp to a more rounded morphology, reflected in the lower strain values for the oxidized/truncated particles in Figure 1.2.4 compared to the clean/sharp NC’s.

1.2.5. Surface deformation with oxygen adsorption

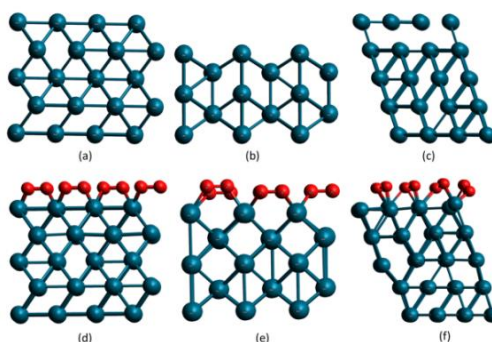


Figure 1.2.9. Deformation of the Pd nanocube surfaces in the presence of oxygen molecules: (a), (b) and (c) show the clean 100, 110 and 111 surfaces respectively; (d), (e) and (f) are the corresponding surfaces deformed in the presence of 1 ML O₂ surface coverage

In a recent study, Rebuffi et al⁸⁸ used DFT to show the deformation of a Pd NC surface region in the presence of a capping agent molecule, and demonstrated a corresponding increase in the Debye-Waller coefficient of the NC due to this surface softening. In a similar manner, we simulate the surface deformation of the Pd surface due to the adsorption of oxygen molecules in order to explain the higher B_{iso} of the oxidized NC. This deformation is demonstrated by comparing the relaxed geometries, of the three main crystallographic facets 100, 110 and 111 of a Pd nanocube surface with 1 ML surface coverage (Figure 1.2.9), and calculating the MSD of the surface atoms with respect to the clean surface. The static component of the B_{iso} ³⁶ is then calculated from the MSD, to provide a measure of surface-strain modification due to adsorption of oxygen.

The lightest deformation is observed on the low-density 100 surface (Figure 1.2.9a and 1.2.9d) which corresponds to the face of the Pd nanocube, with a calculated B_{iso} of 0.318 \AA^2 . The edges of the nanocube are modelled with the 110 surface, and demonstrate a swelling effect (Figure 1.2.9b and 9e) upon oxygen adsorption, with an increased inter-layer separation between the atomic planes constituting the surface region, with a correspondingly high B_{iso} of 4.73 \AA^2 . The 111 surface, corresponding to the corners of the truncated nanocube, shows the strongest deformation of all three surfaces. Deformation on this high-density surface takes the form of disorder in the atomic positions of the surface layers (Figure 1.2.9c and 1.2.9f), in response to the adsorption of O_2 molecules. The static B_{iso} of the 111 surface, 5.67 \AA^2 , is the highest among all three.

The relatively weak deformation of the NC faces (100 surface), coupled with an outward expansion of the edges (110 surface) and strong disorder in the corner facets (111 surface), is congruent with the rounding-out of the cubic NC upon oxidation, as seen from the diffraction peak broadening, and reported in the literature from electron microscopy⁸². Additionally, to compare with our experimental results from XRD, we calculate an estimated B_{iso} for the whole nanocube before and after oxidation, with the assumption that the B_{iso} for the core of the NC corresponds to the bulk value (0.45 \AA^2). The total B_{iso} of the NC can then be approximated as,

$$B_{iso} \approx B_{iso,rfac} \times f_{surf} + B_{iso,bulk} \times (1 - f_{surf})$$

where f_{surf} is the fraction of total atoms estimated to be on the surface. It should be noted that this expression provides only a

qualitative estimate of the B_{iso} for a whole NC from small scale MD and DFT calculations; however, it has been previously used⁸⁸ to calculate the B_{iso} for Pd NC's, with results reasonably comparable to experimental values.

For the clean nanocube, the main surface strain is due to dynamic (temperature related) effects, while after the adsorption of oxygen, the static effects can be considered to be dominant. As such, calculating the $B_{iso, surface}$ for the clean cube from MD and for the oxidized NC from DFT, we estimate $B_{iso, full}$ as 0.5312 \AA^2 and 0.608 \AA^2 respectively, compared to 0.597 \AA^2 and 0.609 \AA^2 from XRD at room temperature (Figure 1.2.3). While the model somewhat overestimates the difference in B_{iso} between the clean and oxidized nanocubes, it is clear on a qualitative level that the surface softening and disorder induced by the adsorption of O_2 is ultimately responsible for the experimentally observed increase in B_{iso} .

Given the clear modification of the strain-state of the Pd nanocatalyst with oxidation as measured through X-ray diffraction, and the subsequent ascription of this effect to surface softening and disorder from O_2 adsorption, it is of some importance to understand how this surface disorder affects the reactivity of the adsorbed molecules.

Catalytic activity is well known¹⁹ to vary on the different surface facets of Pd. Additionally, the variation in the calculated electronic density of states of O_2 molecules adsorbed on the Pd surfaces according to changing surface coverage (supplementary Figure S1.2.3), suggests that this is another factor which plays a role in modifying the catalytic activity. For a low surface coverage (0.25 ML) the average magnetization of O_2 molecules on the 100 surface, as calculated from DFT, is found to be less than half that on the 111 surface, in qualitative agreement with calculations by Long et al¹⁹. Interestingly however, we find that the average magnetization per molecule with surface coverage has opposite trends on the 100 surface, compared to the 111.

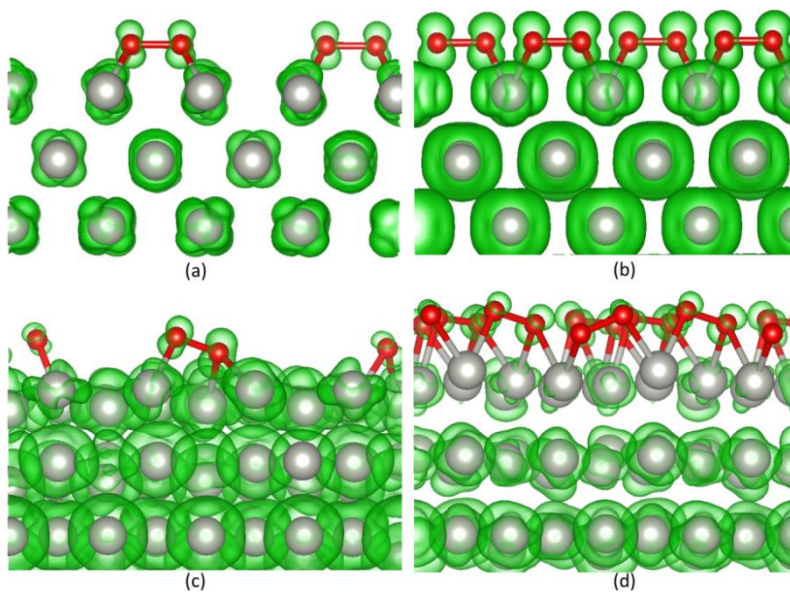


Figure 1.2.10. Magnetization density isosurface of O_2 molecules on Pd surfaces: (a) and (b) show the density on the 100 surface at 0.25 ML and 1 ML surface coverage respectively, while (c) and (d) show the densities for the corresponding surface coverages on the 111 surface. Red balls correspond to oxygen atoms, grey balls palladium.

This effect can be seen clearly from the magnetization density (calculated as the difference in charge densities for spin states with opposite signs) in Figure 1.2.10. While the magnetization of O_2 molecules on the 100 surface is seen to go up with increasing surface coverage (Figure 1.2.10a and 1.2.10b), it appears to decrease for the molecules on the 111 surface (Figure 1.2.10c and 1.2.10d).

The magnetization of O_2 molecules is a critical measure of the catalytic activity of the Pd surface – transfer of charge from the metal surface to the half-filled π^* orbitals of the paramagnetic ground state triplet O_2 molecule (${}^3\Sigma_g$) leads to a reduction in the magnetic moment, and a corresponding increase in reactivity through a transition to the diamagnetic excited singlet states (${}^1\Delta_g$, ${}^1\Sigma_g$). While at lower surface coverage, the 100 surface is predicted to perform better at activating O_2 molecules, it appears to become saturated with increased surface coverage. The 111 surface on the other hand seems to be able to reduce the magnetic moment of oxygen molecules at higher surface coverages.

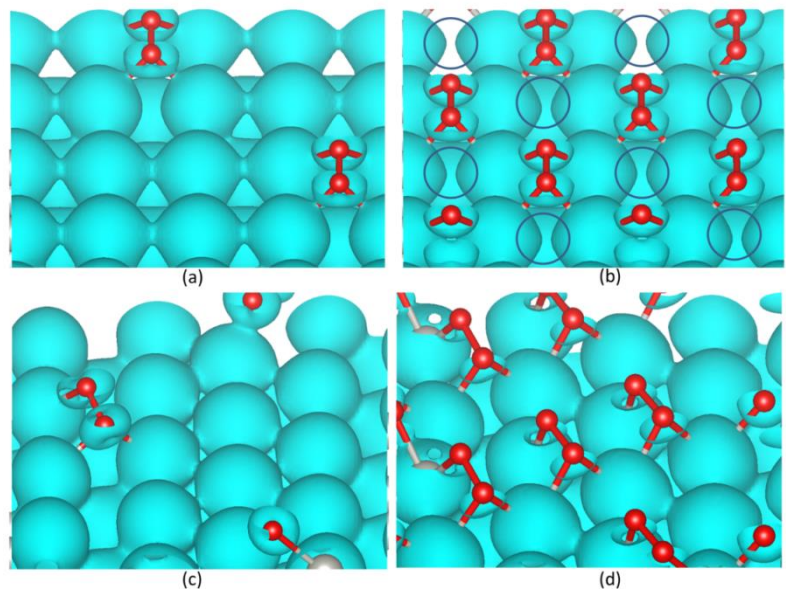


Figure 1.2.11. Partial charge density isosurface of Pd d-electrons: (a) and (b) show the density on the 100 surface at 0.25 ML and 1 ML surface coverage respectively, while (c) and (d) show the densities for the corresponding surface coverages on the 111 surface. Dark blue circles show the depletion in charge density. Red balls correspond to oxygen atoms, the isosurfaces are truncated above the Pd surface for clarity.

This effect can be explained by calculating the partial charge distribution of Pd d-electrons on the respective surfaces (Fig 1.2.11). On the 100 surface, we clearly observe a depletion of charge at higher surface coverage (Figure 1.2.11a and 1.2.11b), a distinct feature absent on the 111 surface. This depletion impedes the charge-transfer induced spin-flip process for the activation of O₂ molecules on the 100 surface at higher surface coverage. The absence of a similar depletion on the denser, disordered 111 surface, supporting a higher distribution of electrons, allows for a greater volume of charge transfer, explaining the decrease in magnetization of O₂ molecules at higher surface coverage. This phenomenon shows the potential for more sustained activation of O₂ molecules at corner sites of truncated Pd nanocubes, and Pd 111 surfaces in general.

1.2.6. Conclusion

Using a coupling of X-ray diffraction and theoretical modelling with classical MD and DFT, we study how the strain-state of cubic Pd nanocatalysts is modified as a result of oxidation. We show that the analysis of XRD data with sophisticated data analysis techniques like WPPM can be used as an accurate measure for strain effects in nanoparticles, both long-range through the Warren plot, and short-range via the Debye-Waller coefficient, even for a kinetic process such as oxidation. In this article, we find that the oxidation of Pd nanocubes leads to a decrease in long-range strain combined with a measurable increase of short-range disorder. Using classical MD simulations with EAM potentials, we show that the decrease in long-range strain is the result of the increasing truncation of the nanocube with oxidation. We analyse the kinetics of the oxidation process using MD simulations with ReaxFF force-fields, and show that the oxidation process and the accompanying local disorder progress from edge and corner sites of the NC, explaining the increased truncation of oxidized Pd nanocubes. From the MD simulations, we compute an increase in the Debye-Waller coefficient of the nanocube with progressing oxidation, in line with what is measured from XRD. Subsequently, we perform DFT calculations of oxygen adsorption on the individual crystallographic surface facets of truncated Pd nanocubes - 100 representing the faces, 110 the edges, and 111 the corners. We find that while the adsorption process has a limited deforming effect on the 100 faces, it leads to an outward expansion on the 110 edges and strong atomic disorder on the 111 surfaces. This combined deformation mechanism leads to a significantly large surface B_{iso} , which in turn leads to the increased B_{iso} for the whole nanocube, in agreement with the XRD measurement, and provides a theoretical explanation for the experimentally observed rounding effect of oxidation. Finally, from the electronic structure calculation with DFT, we find that the different exposed facets have different trends in catalytic activity – while the ordered 100 faces are better at activating O_2 molecules from singlet to triplet states at lower surface coverage, the disordered 111 surfaces have the potential for more sustained O_2 activation at higher surface coverages. Thus, through a combination of multiscale modelling and experimental analyses, we provide a novel understanding of how oxidation modifies the strain-state in Pd NC's, and the potential effects it may have on their catalytic activity.

Appendix

1. X-ray diffraction data and modelling

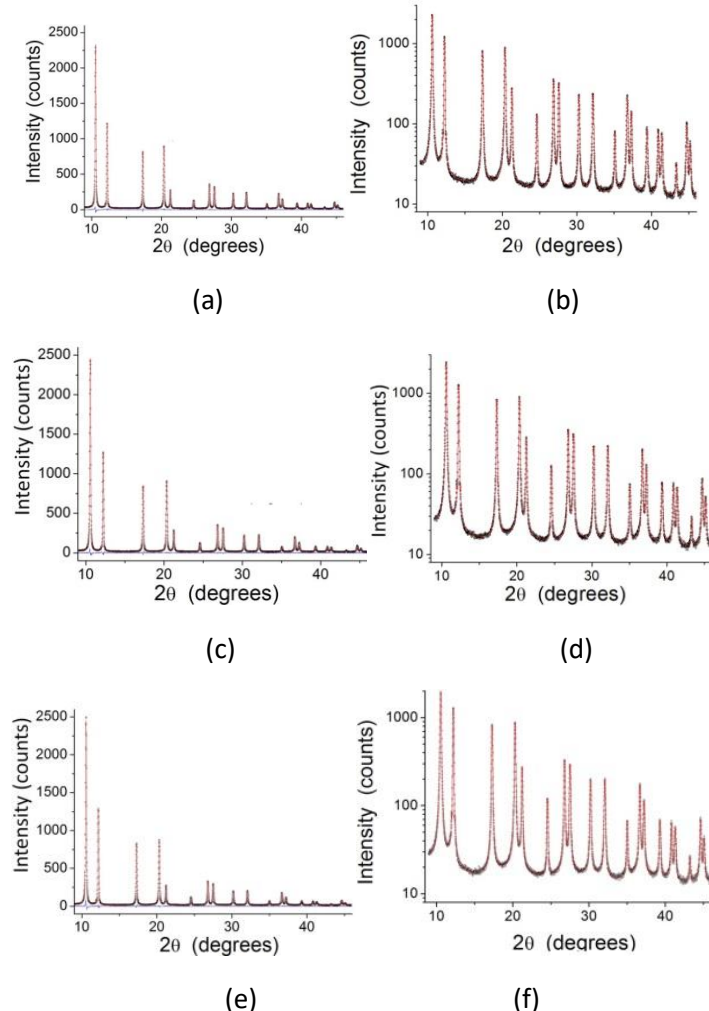


Figure S1.2.1: Whole Powder Pattern Modelling of XRPD data: (a), (c) and (e) show data (circle) and modelling (line) with their difference (residual, line below) for the clean nanocubes at 100 K, 200 K and 300 K respectively; while (b), (d) and (f) show the corresponding data, with X-axis in a log scale.

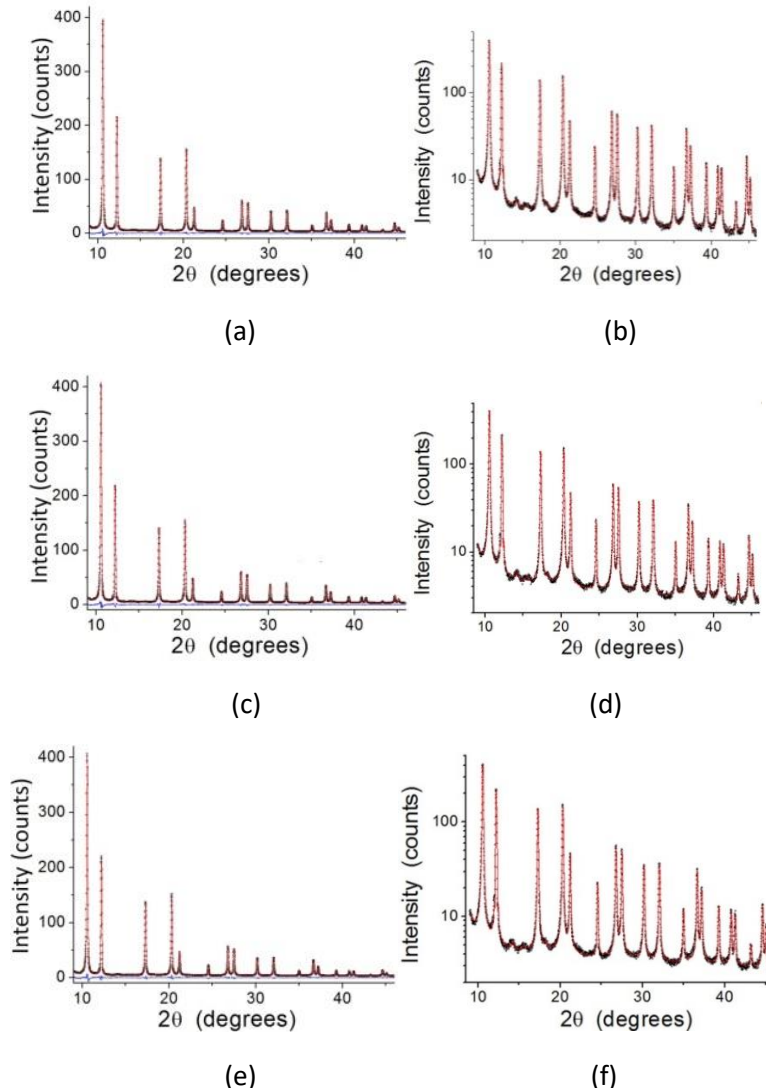


Figure S1.2.2: Whole Powder Pattern Modelling of XRPD data: (a), (c) and (e) show data (circle) and modelling (line) with their difference (residual, line below) for the oxidized nanocubes at 100 K, 200 K and 300 K respectively; while (b), (d) and (f) show the corresponding data, with X-axis in a log scale.

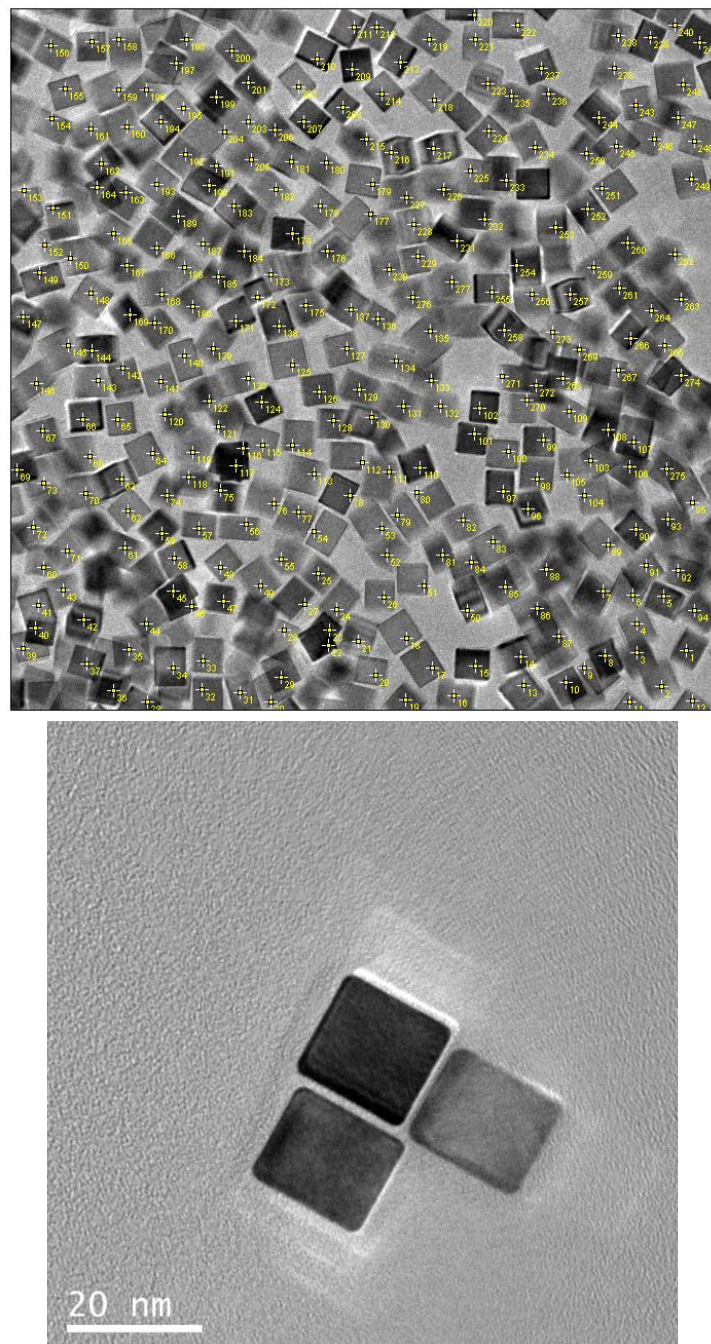


Figure S1.2.3: Transmission electron microscopy (TEM) images of the clean Pd nanocubes, showing a uniform and homogenous size and shape distribution. Figures courtesy Chia-Kuang (Frank) Tsung, Boston College.

2. Estimation of B_{iso} for nanocube before and after oxidation

Clean nanocube (experimental)

Approximate no. of atoms (from fitting XRD data) = 182016

Approximate edge size (from fitting XRD data) = 14.23 nm

Area of 100 surface = 1214.96 nm²

Density of 100 surface = 13.26 atoms/nm²

No of atoms on 100 surface (3 layers) = 48330

Area of 110 surface = 189 nm²

Density of 110 surface = 9.35 atoms/nm²

No of atoms on 110 surface (3 layers) = 5302

Area of 111 surface = 4.25 nm²

Density of 111 surface = 15.05 atoms/nm²

No of atoms on 111 surface (3 layers) = 115

Estimated no. of surface atoms = 48330 + 5302 + 115 = 53747

Fraction of surface atoms, f_{surf} = 53747/182016 = 0.2953

Surface dynamic B_{iso} from MD = 0.725 Å²

Bulk B_{iso} = 0.45 Å²

$$B_{iso} = B_{iso}(surface, dynamic) \times f_{surf} + B_{iso}(bulk) \times (1-f_{surf})$$

$$= (0.725 \times 0.2953 + 0.45 \times 0.7047) \text{ Å}^2$$

$$= 0.2141 + 0.3171$$

$$= 0.5312 \text{ Å}^2 \text{ (compared to } 0.597 \text{ Å}^2 \text{ from experiment)}$$

Oxidized nanocube (experimental)

Approximate no. of atoms (from fitting XRD data) = 181529

Approximate edge size (from fitting XRD data) = 14.05 nm

Area of 100 surface = 1184.42 nm²

Density of 100 surface = 13.26 atoms/nm²

No of atoms on 100 surface (3 layers) = 47115

Area of 110 surface = 272.96 nm²

Density of 110 surface = 9.35 atoms/nm²

No of atoms on 110 surface (3 layers) = 7656

Area of 111 surface = 9.08 nm²

Density of 111 surface = 15.05 atoms/nm²

No of atoms on 111 surface (3 layers) = 408

Fraction of 100 surface atoms, $f_{surf,100}$ = 47115/181529 = 0.2595

B_{iso} (static, 100 surface) = 0.318 Å² (from DFT)

Fraction of 110 surface atoms, $f_{surf,110}$ = 7656/181529 = 0.0422

B_{iso} (static, 110 surface) = 4.73 Å² (from DFT)

Fraction of 111 surface atoms, $f_{surf,111}$ = 408/181529 = 0.0022

B_{iso} (static, 111 surface) = 5.67 Å² (from DFT)

$$B_{iso} = B_{iso}(\text{static, 111 surface}) \times f_{surf,111} + B_{iso}(\text{static, 110 surface}) \times f_{surf,110} + B_{iso}(\text{static, 100 surface}) \times f_{surf,100} + B_{iso}(\text{bulk}) \times (1-f_{surf})$$

$$= (5.67 \times 0.0022 + 4.73 \times 0.0422 + 0.318 \times 0.2953) + (0.45 \times 0.696) \text{ Å}^2$$

$$= 0.0125 + 0.1996 + 0.0825 + 0.3132$$

$$= 0.6078 \text{ Å}^2 \text{ (compared to } 0.609 \text{ Å}^2 \text{ from experiment)}$$

3. Electronic density of states

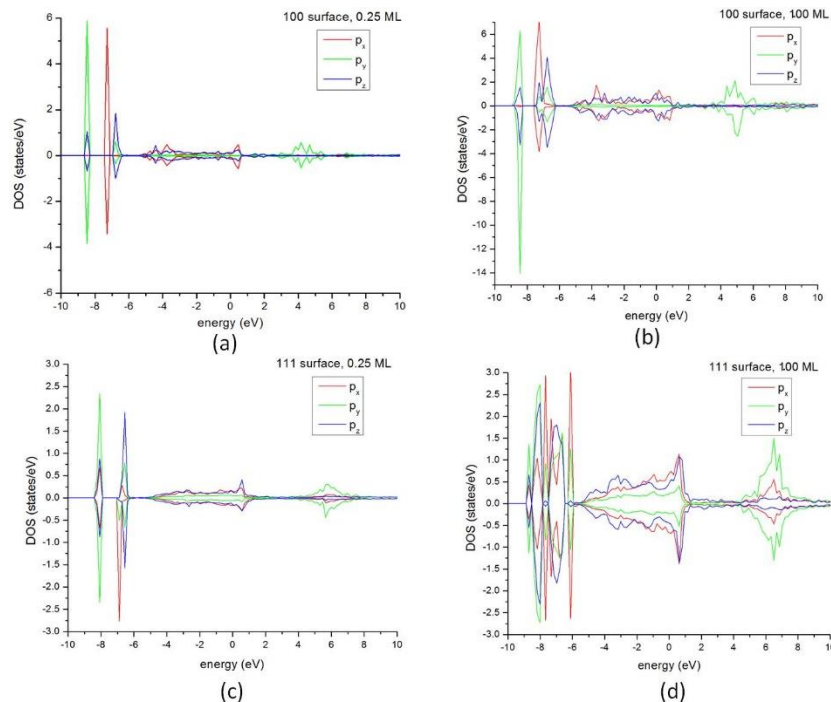


Figure S1.2.4: Orbital projected electronic density of states (DOS) for oxygen molecules on the Pd surface: (a) corresponds to 0.25 ML O₂ on the 100 surface, (b) corresponds to 1.00 ML O₂ on the 100 surface, (c) corresponds to 0.25 ML O₂ on the 111 surface and (d) corresponds to 1.00 ML O₂ on the 111 surface; red, green and blue lines refer to the x, y and z components of the oxygen p-orbital respectively.

Author contributions

BM was primarily responsible for writing the article, making the MD-ReaxFF and DFT simulations and calculating the Debye-Waller coefficient, and contributed to the analysis of the experimental data. AF was primarily responsible for making the MD-EAM simulations and calculating the Warren Plot from these simulations, and contributed to the analysis of the experimental data. PS was primarily responsible for conceiving and supervising the work, analysing the experimental data, and contributed to the collection of experimental data, and supervised the writing of the article.

Acknowledgements

The work carried out at Argonne National Laboratory was supported by the US Department of Energy, Office of Science, Office of Basic Energy Sciences, under contract DE-AC02-06CH11357. We acknowledge the CINECA award under the ISCRA initiative, for the availability of high performance computing resources and support in making DFT calculations. The authors would like to acknowledge Dr. Narges Ataollahi for discussions regarding applications of Pd nanoparticles in catalytic processes.

2 Bulk disorder in negative thermal expansion cuprite Ag₂O

Abstract

Modelling of X-ray powder diffraction data from silver oxide reveals a large diffuse scattering and high Debye-Waller coefficient. Molecular dynamics simulations and density function theory calculations point to large structural distortion, with both static and dynamic components, as the source. Anisotropic forces and displacements of atoms coupled with soft phonon modes are found to be responsible for the structural distortion leading to the high diffuse scattering.

2.1 Introduction

Silver (I) oxide (Ag₂O) has been the subject many investigations, with the main objective being to decipher its unconventional structural behavior, most notably its negative thermal expansion (NTE). It finds applications as a modifier in fast-ion conducting glasses, batteries^{1,2} and biomedical applications³, and its catalytic properties have also drawn attention^{4,5}. Ag₂O crystallizes in the Pn-3m space group with the cuprite structure. However, unlike Cu₂O which shows a small NTE below room temperature, Ag₂O shows negative thermal expansion in the entire temperature range within which it is stable (up to ~500 K)^{6,7}. The mechanism for this atypical behavior has been extensively analyzed with a range of experimental techniques such as extended X-ray absorption fine structure (EXAFS), inelastic neutron scattering (INS) and X-ray powder diffraction (XRPD), as well as theoretical calculations with density functional theory (DFT), ab initio molecular dynamics (AIMD) and quantum chemistry.

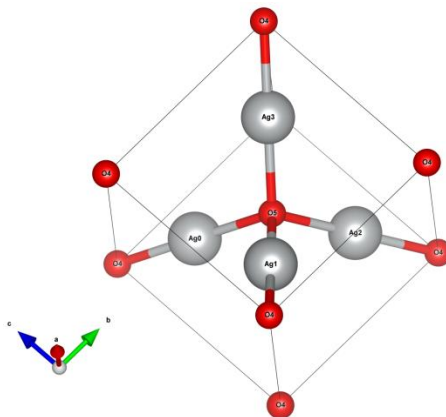


Figure 2.1. Structure of Ag_2O , showing the tetrahedral coordination of O with four Ag ions, and the linear coordination of Ag with two O atoms

Within the cuprite structure of Ag_2O , a single oxygen ion has a tetrahedral coordination with four silver ions, forming Ag_4O tetrahedra, whereas each silver atom has a linear coordination with two oxygen atoms (see Figure 2.1). Investigations with EXAFS^{8–13} have revealed that deformations of these Ag_4O tetrahedra are connected to the mechanism of NTE in Ag_2O . These experiments in fact suggest that the Ag-O nearest-neighbor distance increases slightly with temperature, whereas the Ag-Ag second-nearest-neighbor distance goes down, driving the bulk NTE behavior. Calculations with quantum chemical techniques reveal that only the Ag-O and Ag-Ag interactions are prevalent in Ag_2O , compared to the additional O-O interaction in Cu_2O ¹⁴. DFT calculations instead show that the character of bonding in the two cuprite structures is somewhat different, with the Ag-O bond being more ionic than its Cu-O counterpart, thus allowing for a more significant distortion of the Ag_4O tetrahedra¹⁵. This information on bonding helps to explain the difference in the structural behavior of Cu_2O and Ag_2O , and the strong NTE of the latter.

The anharmonicity of the vibrational modes in Ag_2O are also known to play an important role in the NTE. Inelastic neutron scattering measurements have shown evidence for phonon softening as a consequence of temperature⁷, as have DFT calculations^{6,7,16}. However, these calculations were made within the quasi-harmonic approximation (QHA), which does not account for the higher order terms in the phonon interactions at finite temperature. As such, the results within the QHA fail to predict the entire NTE behavior, only

accounting for half the NTE at low temperatures. Molecular dynamics simulations in temperature allow to overcome the problem. Using AIMD simulations to obtain the vibrational density of states (VDOS) through the Fourier-transformed velocity autocorrelation function, Lan et al¹⁷ demonstrated the presence of strong anharmonic effects in Ag₂O. In particular, they were able to identify the strong interactions between Ag- and O-dominated modes as the driving factor behind the NTE behavior at temperatures above 250 K.

While a significant amount of work has been done to understand the nature and mechanism of NTE in Ag₂O, another structural feature, the Debye Waller coefficient (B_{iso}), has received comparatively little attention. The B_{iso} gives a measure of how much power, in elastic scattering, is transferred from lattice diffraction to diffuse scattering, as a consequence of the displacement of the atoms from the ideal periodic lattice. The main effect of this is the attenuation in the intensity of radiation (X-rays or neutrons) diffracted by a crystalline material. Notably, using diffuse neutron scattering data fitted with a thermal diffuse scattering (TDS) model, Wada et al¹⁸ have shown significantly high values of B_{iso} in Ag₂O, both for the Ag and O species. In that study, the authors argue that there are two factors leading to the high values of B_{iso} – the dynamic thermal vibration of the atoms, and also the static distortion of the crystalline structure; however, they are unable to describe the extent of the relative contributions of these two modes.

In several recent studies, a combination of XRPD measurements and molecular dynamics simulations have shown that increased values of B_{iso} correspond to an increase in static atomistic disorder in various crystalline systems, including metals¹⁹, surface metal oxides²⁰, and chemically complex semiconductors²¹. Atomic disorder is connected to the B_{iso} through the relation

$$B_{iso} = \frac{8\pi^2}{3} \langle u^2 \rangle \dots \quad (2.1)$$

where $\langle u^2 \rangle$ is the mean square displacement (MSD) of individual atoms from their ideal periodic lattice sites. In the present article, using a combination of XRPD data modelling, DFT calculations and molecular dynamics simulations with reactive forcefields, we attempt to describe disorder in Ag₂O, and the role of the static and dynamic contributions to the increased TDS and elevated B_{iso} values.

2.2 Materials, synthesis and methodology

Synthesis of Ag₂O

Silver oxide was produced from the reaction of silver nitrate (AgNO₃) and sodium hydroxide (NaOH) following the reaction mechanism:



Ag₂O reacts with the CO₂ of the environment and forms silver carbonate.



To prevent the carbonation reaction, the preparation of Ag₂O was performed inside of glove box under N₂ gas. 60 mL of Silver nitrate (0.1M) was placed in a beaker on a stirrer and 60 mL of sodium hydroxide (0.5M) was added into the solution. The reaction is fast and the compounds undergo changes in both state and color. The reaction continues for 20 mins until a brown precipitate was completely settled to the bottom of the beaker. The solid silver oxide formed a dull brown clump. The liquid sodium nitrate solution was removed and disposed in a sealed container as it is toxic, and possibly a source of carcinogens. The silver oxide is collected and dried on a hotplate for 2 hr at 70 °C.

XRD characterization and modelling

X-ray diffraction (XRD) patterns were collected using Rigaku PMG diffractometer in Bragg-Brentano geometry, with Cu-K α radiation operated at 40 kV and 30 mA. The sample preparation for XRD measurement was performed entirely inside the glove box.

The sample was exposed to the air for 25 mins (the time that was spent to attach the sample to the instrument and fix the parameters). The XRD pattern of Ag₂O can be indexed to pure cubic phase of Ag₂O (space group Pn-3m(224), PDF#41-1104). The small peak at 2θ angles 29° could be assigned to the hydrated Ag₂O. The sample was handled in a protected atmosphere and measured quickly in air, in order to reduce the tendency to carbonatation, which alters especially the surface of the sample exposed to air (and CO₂).

Rietveld refinements ²² of the XRD data were performed with the software TOPAS 7 ²³. The line profile analysis of the size and strain broadening was performed using macros based on the whole powder

pattern modelling (WPPM)^{24,25} approach, which models the entire peak profile through the convolution of the different components responsible for peak broadening. The size broadening of the profile was modelled with a lognormal distribution of spherical domains. The strain strain broadening instead was treated using the PAH model, which is considered a flexible approach to model a general anisotropic microstrain²⁵. The thermal diffuse scattering is described using the model of Sakuma²⁶, which is discussed in more detail in the following section.

Computational methodology

The density functional theory calculations were performed with the Vienna ab initio simulation package (VASP)²⁷⁻²⁹. In order to account for the large anharmonicity, a 3x3x3 supercell of Ag₂O was used, with 162 atoms. The Perdew-Burke-Ernzerhof (PBE)³⁰ form of the generalized gradient approximation (GGA) was used to approximate the exchange-correlation energy, with scalar-relativistic PBEsol pseudopotentials³¹. An energy cutoff of 400 eV was used for all the calculations, with a Gaussian charge smearing of 0.1 eV. Due to the large size of the supercell, the irreducible Brillouin zone was sampled only at the zone-center (Γ -point). The electronic degrees of freedom are relaxed until the change in the total free energy and energy eigenvalues are both smaller than 10^{-6} eV. Density functional perturbation theory was used to obtain the dynamical matrix. Subsequently, the PHONOPY³² code was used to diagonalize the dynamical matrix and obtain the interatomic force constants, from which the vibrational DOS and phonon dispersion relations were obtained.

The molecular dynamics simulations were performed using the large-scale atomic/molecular massively parallel simulator (LAMMPS)³³, with the Ag/O reactive forcefield developed by Saleh et al³⁴. For these simulations, a 15x15x15 supercell of Ag₂O with periodic boundary conditions was used. The system was first thermalized at 300 K as an isothermal-isobaric (NPT) ensemble for 10 ps, in order to account for the NTE. Subsequently, they were allowed to evolve within a canonical (NVT) ensemble for a further 50 ps. In both cases, a chain of 100 Nose-Hoover thermostats was used, and the integration timestep was set to 0.2 fs. The simulation trajectories were visualized with Ovito³⁵ and the mean square displacement of the system was then calculated using the software VMD³⁶.

2.3 X-ray diffraction and data modeling

The intensity scattered by a powder sample can be written as the sum of two terms, the well-known Bragg scattering, or diffraction term, I_B , and a diffuse scattering term, I_D . Compared to the diffracted signal from a powder of perfect crystalline domains, the Bragg term is decreased in intensity by the Debye-Waller (DW) factor multiplying to the atomic scattering factor f ; this reduction in intensity feeds the diffuse scattering term.

The original expression of the Debye-Waller (DW) factor, still used to date to correct the Bragg term for temperature and in general, atomic static disorder, refers to uncorrelated displacements of single atoms. The most common assumption, following the 1913 work of P.J.W. Debye³⁷, is that each atom behaves as an Einstein oscillator, with a Mean Square Displacement, $MSD = B/(8\pi^2)$, such that:

$$DW(2\theta) = e^{-M} = e^{-B(\sin\theta/\lambda)^2} \dots (2.2)$$

where λ is the wavelength of incident radiation, θ is the angle of incidence, and B (also known as B_{iso} in the scalar form) is the Debye Waller coefficient. While the DW factor scales down Bragg diffraction by multiplying to the atomic scattering factor, the diffuse scattering from such uncorrelated oscillators takes a simple form, in particular for a single-element phase:

$$I_D = k(2\theta)ff^*(1 - e^{-2M}) \dots (2.3)$$

where $k(2\theta)$ includes constants and terms depending on the experimental conditions, like the polarization correction, and f^* is the complex conjugate of f . For the case of Ag_2O , neglecting any correlations, and substituting the value of M from (2.2), this takes the form:

$$I_D = k(2\theta)[f_{Ag}f_{Ag}^*(1 - e^{-2B_{Ag}(\sin\theta/\lambda)^2}) + f_Of_O^*(1 - e^{-2B_O(\sin\theta/\lambda)^2})] \dots (2.4)$$

where f_{Ag} , f_O , B_{Ag} and B_O are the atomic scattering factors and Debye-Waller coefficients of Ag and O respectively.

If correlations in the vibration of atoms are included, at least between the close neighbours in the inner coordination shells, for binary

systems the diffuse scattering intensity is given by the expression due to Sakuma^{18,26}:

$$I_D = k(Q) \left\{ \sum_s n_s f_s f_s^* [1 - e^{-2M_s}] + \sum_s \sum_{s'} n_s f_s f_s^* \left[e^{-(M_s + M_{s'})} (1 - \mu_{ss'}) - e^{-(M_s + M_{s'})} \right] Z_{ss'} \frac{\sin(Qr_{ss'})}{Qr_{ss'}} \right\} \dots (2.5)$$

The above expression (written in reciprocal space where $Q=4\pi\sin\theta/\lambda$) includes the sum over all pairs of sites (s and s'), with n_s being the number of s atoms per unit cell; $Z_{ss'}$ is the number of sites belonging to the s' neighbour around an s site. In the present formulation the expression is written for a stoichiometric compound, but the theory can easily be extended to include partial occupancy of sites. The correlation term, $\mu_{ss'}$, is defined as

$$\mu_{ss'} = \frac{2\langle \Delta r_s \cdot \Delta r_{s'} \rangle}{\langle \Delta r_s^2 \rangle + \langle \Delta r_{s'}^2 \rangle} \dots (2.6)$$

which includes the effect of correlated displacements, $\langle \Delta r_s \cdot \Delta r_{s'} \rangle$. When displacements are uncorrelated, $\mu_{ss'} = 0$, and (2.6) reduces to the equivalent of (2.4). The model described here has been used by Wada et al¹⁸ to account for thermal diffuse scattering in Ag₂O using neutron diffraction, and in the present article we extend its application to X-ray powder diffraction.

The modelling of the data (Figure 2.2) with the thermal diffuse background provides a relatively good fit, with an RWP of 8.1, though with a broad ‘tweak’ peak at $2\theta \sim 34^\circ$. The average crystallite domain size was estimated at around 63 (1) nm, with a standard deviation of around 15 (2) nm, indicating a fairly broad size distribution. The freshly synthesized sample was found to be of high purity, and could be modelled with a single cubic phase with the Pn-3m(224) space group. In agreement with previous studies^{6,18}, large Debye-Waller coefficients were obtained for both atoms, with the value for silver ($B_{Ag} = 4.1$ (1)) half that of oxygen ($B_O = 8.9$ (6)).

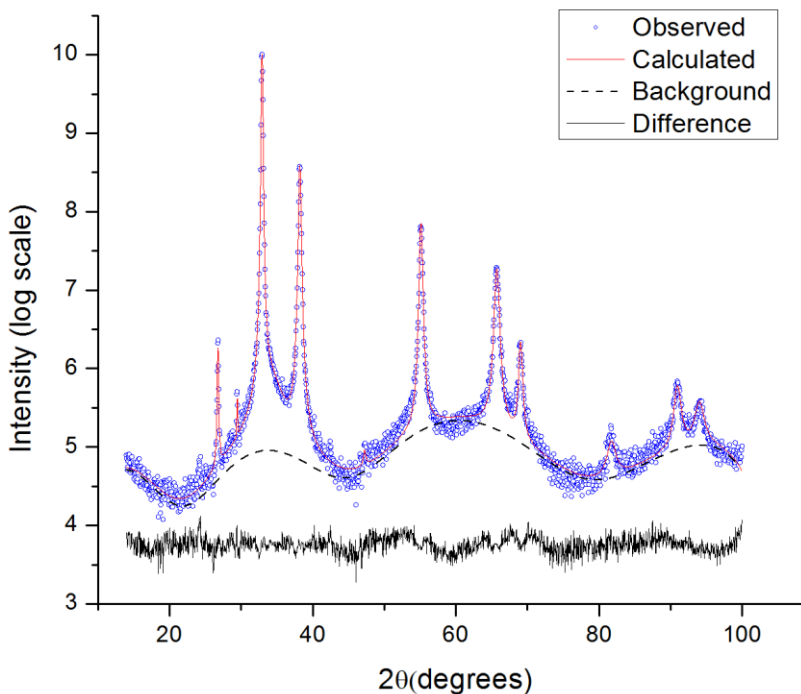


Figure 2.2 WPPM modelling (red line) of the observed diffraction pattern of Ag_2O (blue circles), with a thermal diffuse scattering background (black dashed line)

It should be noted that while the Rietveld refinement with the described TDS model gives a reasonable fit, it nevertheless has certain limitations. The expression (2.5) is obtained by considering only the first four neighbors, with a configurational average of terms (details on the derivation of (2.5) can be found in the cited literature²⁶) with no specific accounting of phonon dispersions. This effectively excludes long-distance correlations, which in terms of normal modes of vibration correspond to phonons of greater wavelength, which would give sharp features around the Bragg peak position. Consequently, (2.5) leads to a very diffused signal, whereas other TDS models, like Warren's³⁸, include phonon dispersion and therefore correlations over different, even much larger distances. Unfortunately, Warren's model is limited to systems with only one type of atom, thus necessitating the use of the present model. Nevertheless, Sakuma's model can capture the main features of the TDS, with the specific correlations in binary systems. Here we follow the work of Wada et al¹⁸, which provides the $\mu_{ss'}$ correlation terms for the innermost neighbours. The TDS expression (2.5) is included through a macro in the software TOPAS, for the modelling of powder patterns with the Rietveld method, with

the DW coefficients shared by the DW factor affecting the Bragg component and the TDS of expression (2.5).

2.4 Atomistic picture of disorder in the crystalline structure

In order to understand the atomistic origin of the high B_{iso} values obtained from the diffraction data, we have performed DFT calculations, as well as MD simulations with a reactive forcefield. From the MD trajectories at 300K, we compute the radial pair distribution function (RPDF), and compare with the RPDF at 0 K, obtained by relaxing the geometry with DFT. As seen from Figure 2.3a, the nearest neighbor Ag-O distance (solid blue peak) is found to increase in temperature, whereas the second neighbor Ag-Ag separation (solid black peak) contracts at room temperature vis a vis its position at 0K. Both these feature are in good agreement with EXAFS measurements in the literature¹⁴, which suggest that the negative thermal expansion in Ag₂O is driven by the contraction of the Ag-Ag distance, while the Ag-O separation increases. Beyond the first two peaks however, the RPDF presents a strongly diffuse nature, suggestive of significant disordering.

The MD trajectories also allow the calculation of the atomic root mean square displacement (RMSD), from which we can obtain a measure of the B_{iso} . As seen in Figures 2.3c and d, the calculated B_{iso} values are somewhat overestimated, particularly for oxygen, when compared to the measured values. Both this, and the diffuse nature of the RPDF can be attributed to the reactive force field used in the simulation, which was originally trained against surface adsorption of oxygen molecules on an Ag substrate, rather than the elastic properties of bulk crystalline Ag₂O³⁴. This then allows for certain extreme distortions of the Ag-O-Ag bonds which are possible for adsorbed surface oxygen, but are less feasible within the Ag₄O tetrahedra in the bulk crystalline phase, leading to the overestimation of the B_{iso} . Nevertheless, the calculated values of the B_{iso} are in qualitative agreement with the experimental values, with $B_{\text{O}} (= 14.8 \text{ \AA}^2)$ being roughly double of $B_{\text{Ag}} (= 7.4 \text{ \AA}^2)$.

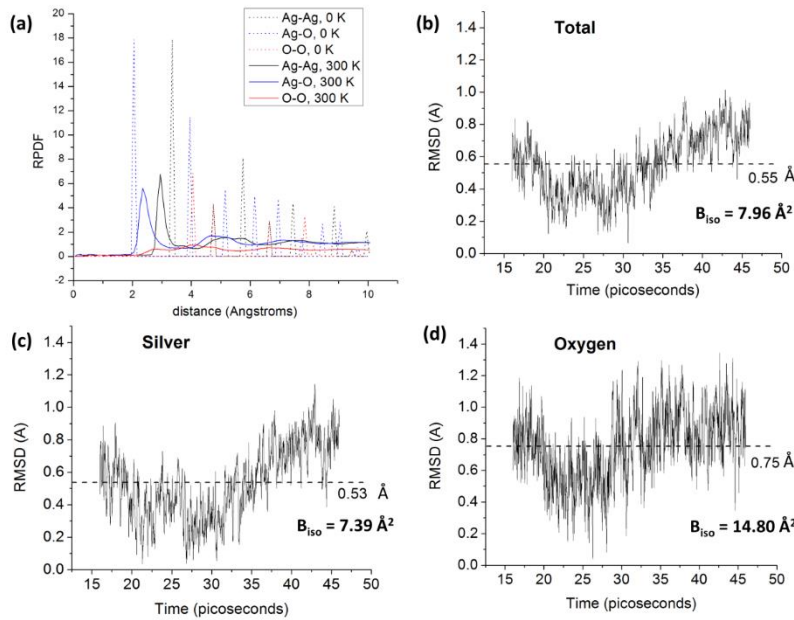


Figure 2.3. (a) Calculated radial pair distribution function of Ag_2O at 0 K (dotted line) and 300 K (solid line), with Ag-Ag (black), Ag-O (blue) and O-O (red) pairs shown; (b) Calculated total RMSD; (c) RMSD of silver atoms; (d) RMSD of oxygen atoms

Given the significantly larger atomic mass of Ag compared to O, and the presence of twice as many Ag ions, the total RMSD, averaged over all atoms gives a value of $B_{\text{tot}} (= 7.96 \text{ \AA}^2)$, close to the value of B_{Ag} . This points to the dominant role of Ag in the large TDS measured in Ag_2O .

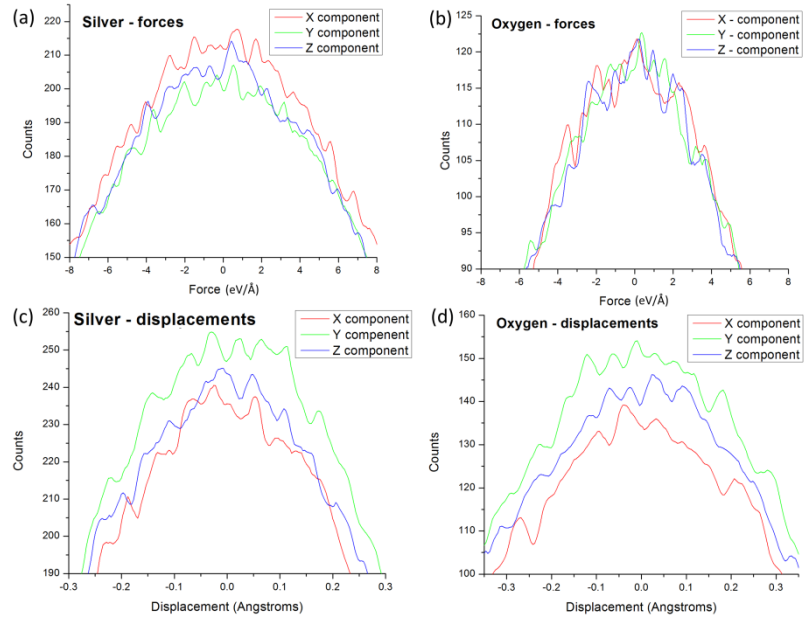


Figure 2.4. Anisotropy of forces and displacements in Ag_2O ; Distribution of X (red), Y (green) and Z (blue) components of (a) forces on Ag atoms, (b) forces on O atoms, (c) displacements of Ag atoms, (d) displacement of O atoms. The Y-axis gives the number of atoms (counts) experiencing the forces/displacements corresponding to the X-axis.

The nature of the distortion of the crystalline lattice can be elucidated by computing the distribution of forces and displacements on the atoms, resolved along the X, Y and Z components, which correspond to the [100], [010] and [001] crystallographic directions respectively, and averaged over the length of the trajectory. Interestingly, the forces on Pd atoms (Figure 2.4a) are significantly anisotropic compared to those on O atoms (Figure 2.4b). The isotropy of forces on O atoms are simple to explain, sitting as they do at the center of the Ag_4O tetrahedra, and interacting mostly with the coordinating Ag ions. Indeed, from DFT calculations, we find that there is little to no overlap of charge densities between adjacent oxygen atoms (Figure 2.5c). This is in contrast to the clear bonding, not just between between adjacent Ag-O pairs (Figure 2.5a) but also between second neighbor Ag-Ag pairs (Figure 2.5b), in agreement with the quantum chemical calculations and EXAFS studies of Artioli et al¹⁴. These interactions, which have been used to explain the NTE behavior in Ag_2O , thus can also be seen as source of the anisotropic forces on Ag atoms. The consequence of this is the anisotropic displacements of

both Ag (Figure 2.4c) and O (Figure 2.4d) atoms, which acts as the source for the large TDS and high B_{iso} values in Ag_2O .

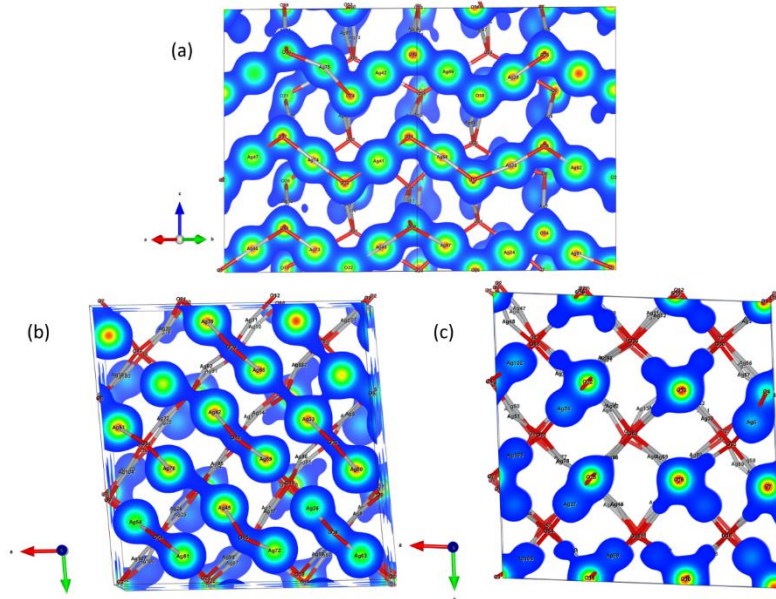


Figure 2.5. Bonding in Ag_2O : (a) Presence of Ag-O bonding; (b) Presence of Ag-Ag bonding; (c) absence of O-O bonding

In order to ascertain the contribution of static and dynamic disorder to these displacements, we turn once more to the calculated RPDF. By sampling the MD trajectory for a number of frames, and taking the average of coordinates of each atom over the frames, we effectively cancel out the thermal vibrations, and count only the purely static displacements. Instead, by generating the RPDF's for each individual frame, and calculating their average, we obtain the full thermally diffuse disorder. The difference between these two averages is then a measure of the dynamic disorder.

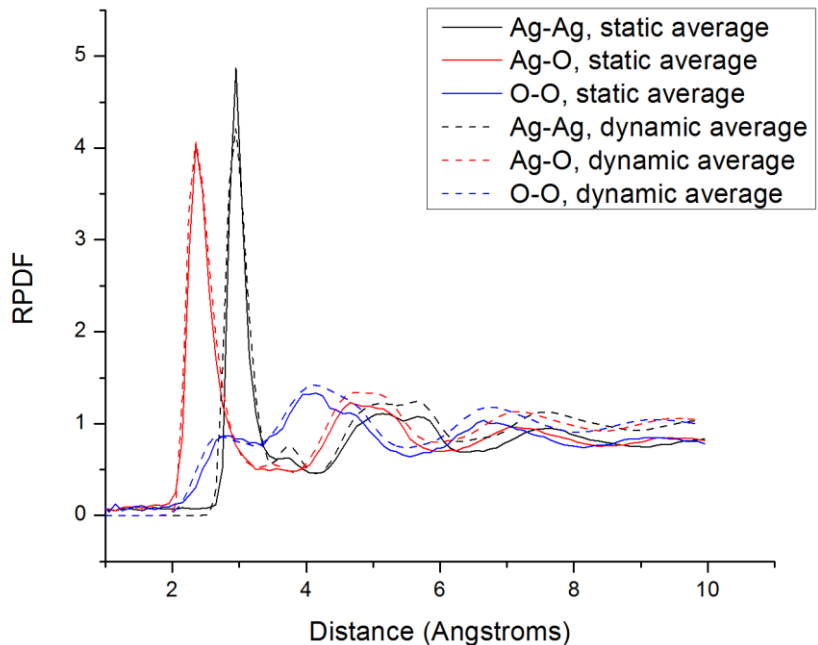


Figure 2.6. Average radial pair distribution function for Ag-Ag (black), Ag-O (red) and O-O (blue) pairs. The solid line gives the RPDF of the averaged coordinates (static average), while the dashed line gives the average over the RPDFs for each sampled frame

Figure 2.6 clearly shows the similarities in the two RPDF's – most prominently for the nearest neighbor Ag-O (red) peak, where the full dynamic average (dashed line) is nearly overlapped by the pure static average (solid line), indicating that the static distortions are dominant in broadening the distribution of nearest neighbor Ag-O pair separations. The greater difference between the two averages in the diffuse tail suggests a dynamic component to the disorder which affects the pair distribution. This, as well as the largely diffuse O-O peaks, are artefacts from the forcefield, which appears to somewhat significantly overestimate the displacement of O atoms.

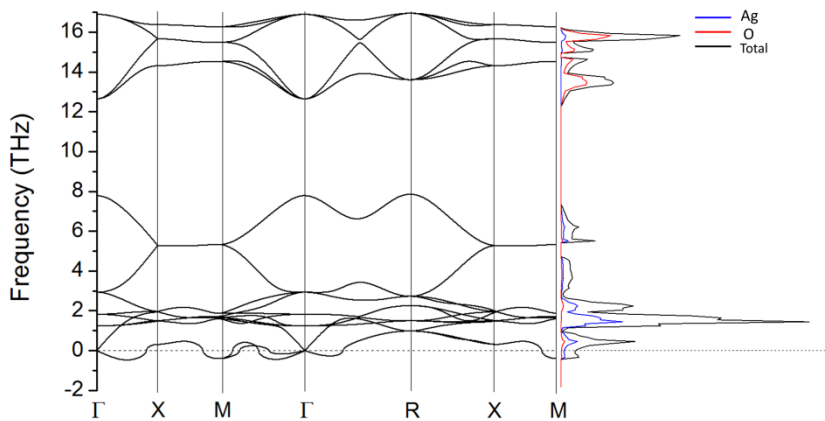


Figure 2.7. Phonon dispersions (left) and their corresponding atom projected vibrational density of states (right); the red curve corresponds to the VDOS projected on Ag, and the blue curve on O; the black curve represents the total VDOS.

The role of static distortions is further supported by the presence of imaginary phonon frequencies in the phonon dispersion and vibrational density of states calculated with DFPT. These soft modes, represented as negative frequencies (Figure 2.7), correspond to non-restorative forces on the atoms, which give rise to dynamical instabilities of the structure. These modes, along with the low frequency region of the VDOS is dominated, as expected, by the heavy Ag ions, and points to a static displacement of these ions. Such imaginary modes in the phonon dispersion have not been reported in the literature, and arise as a consequence of the large 3x3x3 supercell used in the calculations, which accounts well for long-wavelength (low frequency) phonons. These modes in Ag_2O are relatively small compared to the well known soft modes which drive displacive phase transitions – as such, they account for a small distortion of the parent structure rather than complete transition to a different symmetry. It should be noted that these vibrational properties have been calculated within the quasi-harmonic approximation (QHA), which has been shown to be insufficient to describe the full anharmonicity in Ag_2O , and fails to fully account for the NTE at high temperatures¹⁷. However, it is found to be adequate to describe the distortion in Ag_2O which gives rise to high thermal diffuse scattering and B_{iso} .

5. Conclusions

In this article, we have studied the large thermal diffuse scattering in Ag_2O , and investigated its atomistic origin. The approximate correlation-shell theory of Sakuma, used to model TDS in Ag_2O with neutron diffraction, is extended to X-ray powder diffraction. While missing long-range correlations which exclude the sharp Bragg-like features of the TDS, this model accounts reasonably well for the B_{iso} , which is estimated to be quite high. Molecular dynamics simulations reveal that this is connected to a strong disorder in the crystalline structure of Ag_2O , with a complex interplay between static and dynamic components, which arises from anisotropic forces and displacements of atoms and soft phonon modes. While the present treatment well describes the disorder in Ag_2O at a qualitative level, the requirement for a more complete understanding motivates the development of a better theory of thermal diffuse scattering, as well as a more accurate molecular dynamics forcefield, in order to describe this material with complex structural properties.

3 Disorder and transport properties in thermoelectric Cu₂ZnSnS₄

This section is partially taken from: Isotta, E., Mukherjee, B., Bette, S., Dinnebier, R., Scardi, P., 2022. Static and dynamic components of Debye–Waller coefficients in the novel cubic polymorph of low-temperature disordered Cu₂ZnSnS₄. IUCrJ, 9(2).

DOI: <https://doi.org/10.1107/S20522522000239>

3.1 Static and dynamic components of Debye-Waller coefficients in the novel cubic polymorph of low-temperature disordered Cu₂ZnSnS₄

Abstract

Cu₂ZnSnS₄ (CZTS) is an attractive material for sustainable photovoltaics and thermoelectrics, and several properties originate from its marked polymorphism. High-energy mechanical alloying is discovered leading to a disordered phase possessing a sphalerite-like cubic structure. This is investigated in detail with the aid of laboratory and Synchrotron radiation X-ray diffraction and *ab initio* molecular dynamics. The disordered cubic polymorph is preserved below 663 K. With thermal treatments above, the tetragonal kesterite phase forms, used as a reference for structural and microstructural features. The study focuses on Debye-Waller coefficients, which are found considerably larger for the disordered cubic than the tetragonal sample. Indeed, disorder leads to a ~1 Å² upward shift through the temperature range 100–700 K, a feature confirmed by *ab initio* calculations, which point to a particularly high contribution from disordered Sn cations. This supports the general understanding that structural disorder introduces a temperature-independent static contribution to the atomic mean square displacement. Debye-Waller coefficients are found to be a good measure of this disorder, known to critically affect transport properties.

3.1.1 Introduction

Kesterite, with reference formula $\text{Cu}_2\text{ZnSnS}_4$ (CZTS) is a sulphide mineral that has recently been the subject of intense investigation in different fields. It belongs to the family of $A^I_2B^{II}C^{IV}X^{VI}_4$ quaternary compounds, with $A=\text{Cu}$, $B=\text{Zn,Fe}$, $C=\text{Sn}$ and $X=\text{S,Se}$ ¹. The term kesterite is typically used for the mineral, or by extension for the tetragonal $I\bar{4}$ crystal structure first associated to it². CZTS is a semiconducting chalcogenide, with a p-type conductivity arising from frequently occurring acceptor defects, such as Cu_{Zn} (predicted with the lowest formation energy³) and Cu_{Sn} antisites, and Cu vacancies⁴. Owing to the direct band gap of ~1.5 eV and high absorption coefficient in the order of 10^4 cm^{-1} ⁵, CZTS raised attention in the photovoltaic (PV) community as a possible absorber for thin film solar cells. Indeed, it consists of earth-abundant, non-toxic, and low-cost raw elements, thus representing an attractive alternative to other mature PV materials like $\text{Cu}(\text{In,Ga})\text{Se}_2$. These encouraging premises, coupled with theoretical predictions of a conversion efficiency limit of 32.4%⁶, led to an extensive research on this material in the past 20 years⁷. Despite CZTS is deemed the most promising PV material among the emerging critical-raw-material free technologies⁸, to date the improvement has been rather feeble, with the best achieved efficiencies not exceeding 14%^{9–13}.

For the same reasons of sustainability and harmlessness, CZTS has also been explored as a possible thermoelectric (TE) material^{14–27}. Given the large energy gap, CZTS shows an increasing performance with temperature, thus potentially appropriate for applications in the mid-high temperature range (600–800 K)²⁰. Improved TE properties have been obtained when doped with Cu^{15,17} or if S is replaced by Se^{14,28}. Both bulk and thin film^{21,29} TE CZTS have been explored, showing an effective behaviour with particular kinds of defects and disorder^{23,26,27}. Other investigations of CZTS include applications like tandem PVs^{8,30}, photocatalysis³¹, photodetection³², and gas sensing^{33,34}. Recently, it has also been proposed as one of the possible candidates for hybrid thermoelectric-photovoltaic solar harvesting³⁵.

Owing to the chemical complexity, CZTS exhibits a pronounced polymorphism based on a tetrahedral coordination derived from the zinc-blende. The most commonly reported polymorph is the ordered tetragonal (space group s.g. $I\bar{4}$) kesterite-type structure. Another proposed crystallographic arrangement of CZTS is stannite (s.g.

$I\bar{4}2m$). Due to the low energy of formation of the Cu_{Zn} antisites, CZTS can also be found in the disordered tetragonal polymorph (s.g. $I\bar{4}2m$, commonly referred to as disordered kesterite) described by Schorr et Al.³⁶. This has been discovered occurring above 533 K, the order-disorder transition temperature, and frequently for lower temperatures, typically coexisting with the $\bar{I}4$ structure in metastable form, for kinetics reasons³⁶⁻³⁸. Disordered kesterite is characterized by a full occupational disorder of Cu and Zn in the intermediate planes, that transforms 2c and 2d Wyckoff positions of $\bar{I}4$ into the unique 4d site of $I\bar{4}2m$ CZTS. The other Cu-Sn layer is instead identical for ordered and disordered kesterite. Stannite, despite possessing the same space group of disordered tetragonal kesterite, differs in the cation arrangement as it presents, perpendicularly to the **c**-axis, a Cu-only layer alternated by a Sn-Zn one.

Figure 3.1.1 shows the different crystal structures of CZTS and a simulation of their corresponding X-ray diffraction (XRD) patterns with Cu $K\alpha$ radiation. No major difference is observed between stannite, ordered and disordered kesterite. This is expected as they mainly differ in the arrangement of Cu⁺ and Zn²⁺ cations, which, being isoelectronic, are indistinguishable for X-rays. $\bar{I}4$ kesterite has been predicted by first-principle calculations as the most stable among these polymorphs, together with cation disorder in the Cu-Zn layer³⁹. This has been confirmed by neutron scattering measurements^{1,36}, which can instead distinguish the two cations because of the different neutron scattering length. These, and more⁴⁰⁻⁴², results allowed to establish that CZTS commonly arranges in the kesterite structure, ruling out stannite for stoichiometric conditions. CZTS seems more frequently to occur in a mixed ordered-disordered state, with the level of Cu-Zn disorder strongly dependent on the growth conditions and kinetics of thermal treatments. Further modifications of the tetragonal arrangement have been considered in the literature^{1,39,43}.

Another reported polymorph of CZTS is the hexagonal $P6_3mc$, derived from the wurtzite ZnS structure. The phase is described as a hexagonally close packed arrangement of sulphur atoms, with half of the interstitial positions randomly occupied by Cu, Zn and Sn cations. This was first reported in 2011⁴⁴ and synthesized by hot-injection with the use of dodecanethiol (DDT). Several other reports of wurtzite-type CZTS can be found, all reporting the use of DDT in the synthesis⁴⁴⁻⁴⁹ and/or nano-dimension^{50,51}. By cross comparing results

from different works, we notice a general tendency to find a larger amount of wurtzite CZTS when the dimension of grains is nanometric (<30 nm of average dimension)^{44–50}, while for increasing domain size the phase seems to reduce to stacking faults^{45,51–54}, until unobserved.

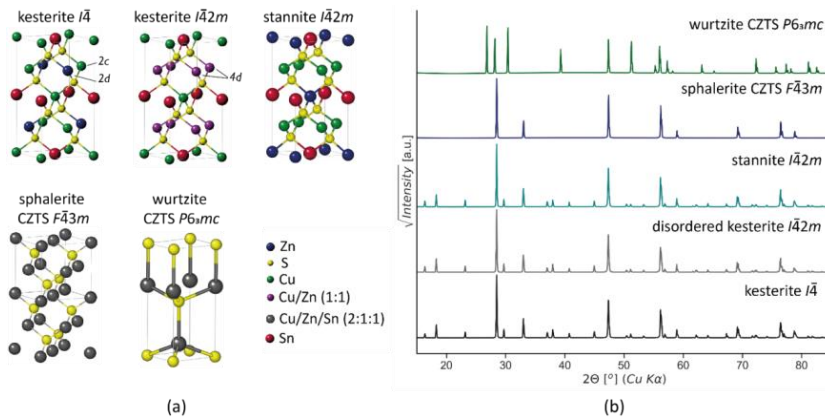


Figure 3.1.1. a) The different crystal structures of $\text{Cu}_2\text{ZnSnS}_4$ (CZTS), from top left: ordered tetragonal kesterite s.g. $\bar{I}4$, disordered tetragonal (commonly called disordered kesterite) s.g. $\bar{I}4\bar{2}m$, stannite s.g. $I\bar{4}2m$, disordered cubic sphalerite CZTS s.g. $F\bar{4}3m$, and hexagonal wurtzite CZTS s.g. $P6_3mc$. b) X-ray Diffraction patterns for the different structures of CZTS, simulated for $\text{Cu K}\alpha 1$ radiation.

A cubic phase of CZTS has also been reported. This, with space group $F\bar{4}3m$, is associated to the Sphalerite-type structure and represented as a cubic stacking of sulphurs in the [111] direction with a random occupation of the cation site by Cu, Zn and Sn. There seem to be two kinds of reports for this polymorph. The first is the high-temperature cubic³⁷, which is the stable form of CZTS above 1156 K. High-temperature transitions to higher-symmetry structures are also found in other compounds of the adamantine family^{55,56}. A second kind is the metastable low-temperature cubic structure, obtained when the sample is synthesized via reactive mechanical alloying^{24,27,57} (e.g. by ball-milling), a production method gaining increasing interest as fast, simple and scalable. The highly disordered but low-temperature environment of high-energy mechanical alloying seems to favour a disordered arrangement of cations. Only few reports on low-temperature cubic CZTS from ball milling can be found^{24,27,57}, although in several works where kesterite was synthesized by mechanical alloying, the XRD patterns of the as-milled powders were clearly missing the tetragonal superstructure reflections^{18,58–63}. This

was typically associated to disorder⁵⁸ and, in rather loose terms, to a low crystallinity^{64–67}. Occasionally low-temperature sphalerite CZTS has been reported from hot injection preparations as well⁶⁸, sometimes mixed with the wurtzite⁵¹ or the kesterite^{54,69} phase. The polymorph is metastable, as it is reported transforming into tetragonal kesterite above ~663K²⁷. Similar low-temperature sphalerite phases were reported for other multinary chalcogenides^{19,70}.

Disorder in kesterite seems to be of particular importance: from a TE perspective, Cu-Zn disorder is found to induce electronic band-degeneracy, remarkably improving the thermopower^{23,26,71}; full cation disorder is instead discovered optimizing all the three TE parameters at the same time²⁷, namely suppressing the thermal conductivity and enhancing the electrical conductivity and Seebeck coefficient. On the other hand, disorder seems to negatively affect the PV performance. Numerous investigations were devoted to the role of Cu-Zn disorder^{36,37,72–76}, while recent studies point to extensive disorder and Sn_{Zn} antisites as the true source of PV efficiency loss⁷⁷. In addition, recent theoretical studies predict that high cation disorder induces a transition to a topologically non-trivial phase, attributing disordered CZTS to the class of Topological Anderson Insulators (TAIs)⁷⁸.

This makes it essential to further study and understand this kind of disorder. The aim of this work is to perform a structural characterization of the low-temperature cubic CZTS phase made by mechanical alloying and compare it with tetragonal kesterite. The temperature stability and evolution of the phases are investigated. A careful experimental and theoretical study of the temperature trend of the Debye-Waller coefficients allows to identify static and dynamic components for the disordered cubic phase. This can contribute to a general understanding of the role of cationic disorder in the thermal behaviour of the material. Advancement in understanding disordered CZTS can shed light on important disorder-induced properties such as the TAI behaviour, as well as the reported critical consequences on TE and PV performance.

3.1.2 Methods

Sample preparation

CZTS powders were synthesized via reactive mechanical alloying in a planetary mill (Fritsch P4 Pulverisette 4). Elemental precursors (Cu powder, <75 µm, 99%; Zn powder, purum, 99%; Sn powder, puriss, 99%, S flakes, purum, 99.5%; all by SigmaAldrich) were weighted in stoichiometric quantity with a ball-to-powder weight ratio of 100:1. The milling was performed with an 80 ml brass jar and 25 brass balls (12 mm in diameter) as milling medium. The whole procedure of vial filling, milling and powder collection was performed in air. 480 µl of ethanol (99.8%, SigmaAldrich) was added to the precursor mixture as lubricant. High energy milling conditions were used, with jar rotation $\omega = -540$ rpm, main disk revolution $\Omega = 300$ rpm, for a fixed ratio $\omega/\Omega = -1.8^{24,79}$, and a milling time of 60 minutes. This milling time has been selected because guaranteeing minimal contamination from the vial and ball material²⁴. Thermal treatments of powders were performed to achieve the cubic or the tetragonal structures. For cubic samples: 60 min at 433 K (heating rate $r = 20$ K/min) followed by 20 min at 573 K ($r = 20$ K/min up to 533 K and 10 K/min from 533 to 573 K); for tetragonal samples: 60 min at 573 K (heating rate $r = 20$ K/min) followed by 20 min at 833 K ($r = 20$ K/min up to 793 K and 10 K/min from 793 to 833 K). After the treatment, the samples were left to naturally cool down to ambient temperature. Thermal treatments were performed in a tubular oven under Ar flux (estimated O₂ level < 10 ppm).

X-ray diffraction

High resolution Synchrotron Radiation X-Ray Diffraction (SRXRD) was performed at the Paul Scherrer Institute (Villigen, Switzerland), MS Beamline X04SA. Data were collected with the Mythen II detector, at a wavelength of 0.5639 Å (~22 keV). Measurements at room temperature and over temperature were performed. For the latter, isothermal measurements every 75 K were performed in the range 323-773 K, or 323-873 K. A temperature ramp of 10 K/min was provided by a hot air blower. Si640d standard patterns were collected to model the instrumental profile. Specimens were sealed in 0.3 mm-diameter quartz glass (for over temperature) and borosilicate glass (for room temperature) capillaries spun during the measurement. For measurements over temperature intended to accurately estimate the Debye-Waller coefficients, samples were diluted with 50% vol glass

powder from ground capillaries. This was applied to decrease the X-ray absorption to the point of making absorption corrections unnecessary (reaching a linear absorption coefficient $\mu^*R \sim 0.3$, such that systematic deviations in intensity between low and high angles are <1%). Low temperature patterns were recorded on a StadiP powder diffractometer (Stoe) using Debye Scherrer geometry and Ag-K_{α1} radiation from a primary Ge(111)-Johann-type monochromator equipped with a triple array of Mythen 1K (Dectris) detectors. The capillaries were heated until 400 K and subsequently cooled to 100 K using a hot and cold air blower (Cobra 700, Oxford Cryosystems) applying heating and cooling rates of 5 K/min. XRPD patterns were taken in 50 K intervals applying a scan range from 0-110° 2θ, a scan time of 8 h and a delay time of 30 min prior to each measurement to ensure thermal equilibration.

Rietveld refinements⁸⁰ of the XRD data were performed with the software TOPAS 7⁸¹. Crystallite size and strain analysis was carried out with the support of macros based on whole powder pattern modelling (WPPM)^{82,83}, directly including microstructural parameters for the refinement of the data. For size broadening a lognormal distribution of spherical domains was considered, from which the arithmetic mean size \bar{D} and standard deviation $\bar{\sigma}$, and volume weighted mean column height D_v were calculated. The choice of a spherical shape for the crystal domain modelling was supported by transmission electron microscopy observations. For strain, the PAH model (from Popa, Adler and Houska, who provided phenomenological observations), deemed a flexible approach to model a general microstrain, was applied⁸². For certain phases, in order to limit the number of free parameters, estimations of mean size and strain were performed with built-in TOPAS macros, based on the double-Voigt method⁸⁴. This approach was applied when the phases were present in small amounts and introducing WPPM would increase the number of refinable parameters making the fit unstable. Built-in TOPAS macros provide, respectively, the volume weighted mean size based on the integral breadth (L_{vol} , calculated assuming spherical domains and conceptually comparable with D_v). To be precise: they share the same definition, but the first is extracted from the modelling of peaks with Voigt functions, the latter introduces a lognormal distribution of spherical domains directly in the model) and average microstrain (e_0) from a combination of Gaussian and Lorentzian strain broadening.

Faulting scenarios on cubic CZTS were evaluated with the software TOPAS 7⁸¹, for the modelling of stacking fault disorder and for the determination of fault probabilities.

***Ab initio* Molecular Dynamics**

The *ab initio* molecular dynamics simulations were performed using the Vienna *ab initio* simulation package (VASP)^{85,86}. A 64-atom supercell was used to represent both the ordered tetragonal and disordered cubic polymorphs of CZTS. The electron-exchange correlation functional was approximated using the Perdew–Burke–Ernzerhof (PBE)⁸⁷ form of the generalized gradient approximation, with the scalar-relativistic PBEsol pseudopotentials⁸⁸, shown to be highly effective in calculating the elastic and mechanical properties of solids^{89–91}. All calculations were performed with an energy cutoff of 400 eV and a Gaussian charge smearing of 0.1 eV. The irreducible Brillouin zone was sampled with a 2x2x2 Monkhorst Pack gamma-centred k-mesh, with electronic degrees of freedom relaxed until the change in the total free energy and energy eigenvalues were both smaller than 10^{-6} eV. The molecular dynamics simulations were performed within a canonical (NVT) ensemble connected to a heat bath with a Nose-Hoover thermostat, set to 10 K, 100 K, 300 K, 500 K and 700 K for multiple trajectories. In each case, the system was allowed to evolve with a timestep of 2 femtoseconds, for 10000 steps, corresponding to a total simulation time of 20 picoseconds. The trajectories were subsequently visualized using OVITO⁹², and the root mean square displacement was calculated from the trajectories using VMD⁹³. In order to measure the anisotropy, we calculated the interatomic force constants from Density Functional Theory (DFT) via the finite difference method, from which we calculated the log-Euclidian anisotropy parameter⁹⁴.

3.1.3 Results and Discussion

A zinc-blende derived disordered phase

High-resolution Synchrotron Radiation X-Ray Diffraction (SRXRD) patterns are collected over the range 293 - 873 K on a sample of as-milled powder and can be seen in Figure 3.1.2. As already pointed out in previous work from some of the authors (Isotta *et al.*, 2020b), mechanical alloying seems to promote a disordered arrangement of the cations leading to a cubic sphalerite-like $F\bar{4}3m$ crystal structure. Peaks are generally broad pointing to small and defected domains, in agreement with TEM observations (see TEM imaging in the Supplementary Note SN 1). This cubic phase seems to be preserved until 673 K, where additional peaks (see black arrows in Figure 3.1.2)

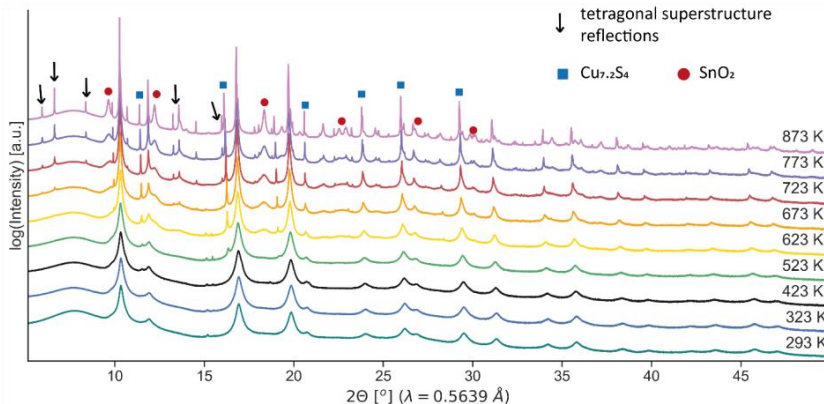


Figure 3.1.2. Synchrotron radiation X-ray diffraction over temperature for an as-milled CZTS sample, with indication of tetragonal superstructure reflections and secondary phases

develop in the XRD patterns, hallmarking the transition to the lower symmetry phase of tetragonal kesterite. Thermal analyses, in (Isotta *et al.*, 2020b), also confirm this observation, locating the cubic to tetragonal CZTS transition at ~663 K. Additional peaks in the higher temperature SRXRD patterns are attributed to SnO₂ and Cu_{7.2}S₄ secondary phases.

To better understand this phase transition and the differences between the cubic and tetragonal phases of CZTS, a detailed structural investigation of two thermally treated samples has been performed.

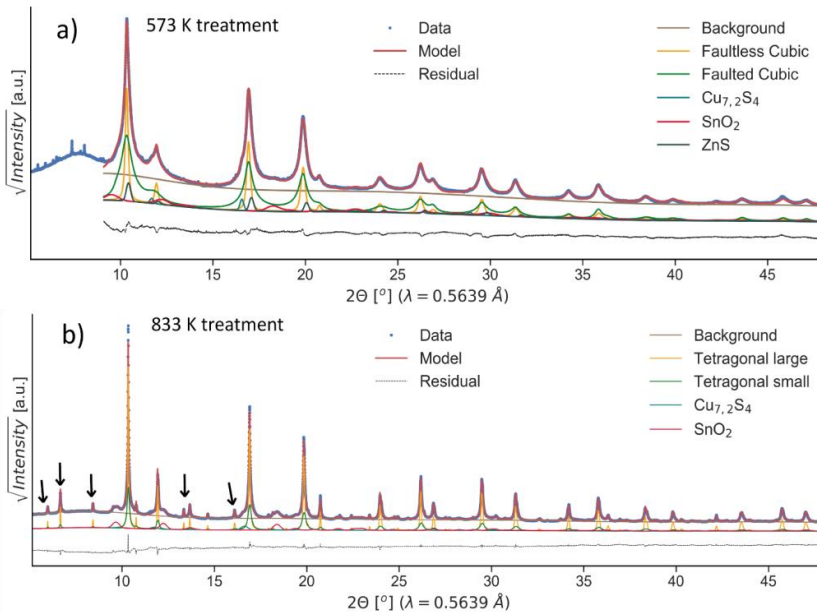


Figure 3.1.3. Synchrotron radiation X-ray diffraction data with Rietveld refinement for CZTS samples from mechanical alloying, thermally treated at 573 K (a) or 833 K (b) to stabilize the cubic or the tetragonal phase, respectively. Data is plotted as dotted blue, modelling as solid red and residual as dashed black. Models of individual phases are shown in coloured solid lines. Some of the most intense tetragonal superstructure reflections are marked by the black arrows.

Treatment temperatures are chosen below, at 573 K, and above, at 833 K, the transition temperature. SRXRD data and modelling with Rietveld refinement are presented in

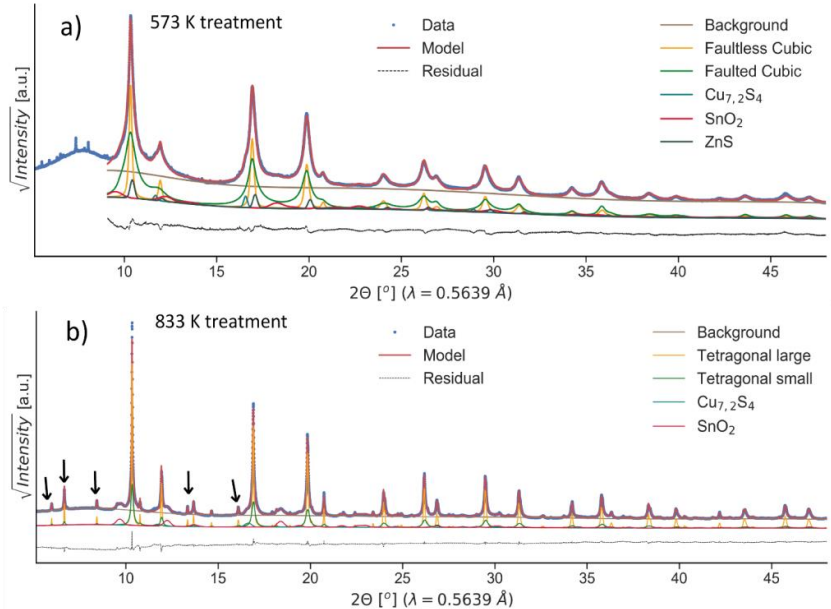


Figure 3, while fit parameters are reported in [Error! Reference source not found.](#) and [Error! Reference source not found.](#) and will be discussed in the next section. A thermal treatment at 573 K (

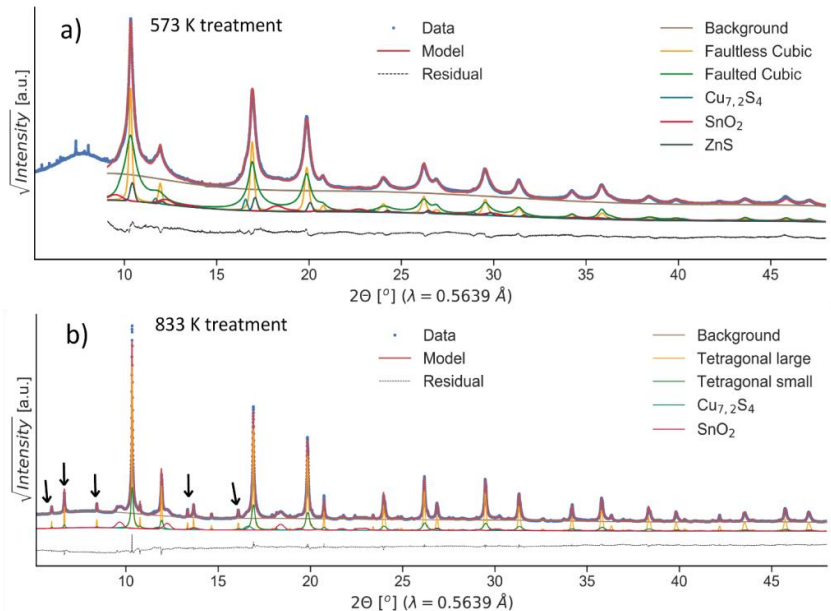


Figure 3a) seems to preserve the disordered cubic CZTS reflections observed for the as-milled powders, whereas at 833 K we observe the development of the tetragonal kesterite phase.

Evolution of atomic mean squared displacement: static and dynamic components

DW coefficients for the samples treated at 573 K and 833 K are visible in Figure 3.1.4a. For the sake of comparison, a unique B_{iso} has been refined for the different cations of tetragonal CZTS. As expected, the values of cation B_{iso} increase with temperature, showing good agreement between the low- and the high-temperature datasets. A linear trend well models the cation DW coefficients for the tetragonal sample, whereas for the cubic above 500 K the B_{iso} grows slower than linear. What is most remarkable, though, is the large offset in the trends of the two samples: all through the temperature range, the cubic sample presents a cation B_{iso} almost 1 Å² higher than the tetragonal. This points to an additional, temperature-independent contribution which is understood to arise from athermal structural disorder. The full cation disorder in the cubic polymorph leads to a randomization of nearest neighbours, giving rise to inhomogenous bonding and consequently, a significant distortion of the coordination tetrahedra. This structural disorder, which exists without temperature, is known to manifest as an increase in the MSD^{95–97}, thus adding a static component to the B_{iso} ⁹⁸, over and above the temperature-dependent vibrational or dynamic contribution. The latter component in fact seems alike for the two samples, as attested by the nearly identical slope of the linear trends. Above 500 K, the downwards deviation from linear of the cation B_{iso} for the nominally cubic sample likely results from a progressive tendency towards order. The DW coefficient of the anion, instead, does not present a systematic trend, with values at times higher or lower than the cations: we believe these results should be taken with precaution, as the ability of diffraction to capture the atomic displacement parameter is reduced with lighter elements. A reliability assessment is presented in the SN 9, showing that the cation's B_{iso} possess higher credibility of values.

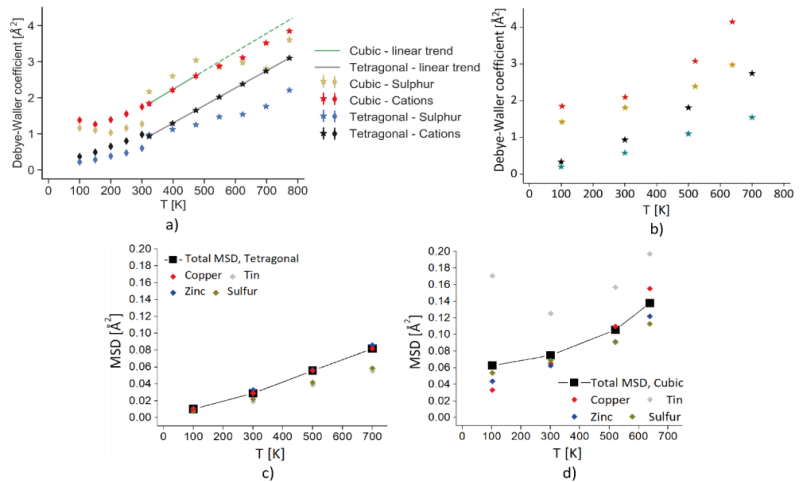


Figure 3.1.4. (a) Temperature evolution of Debye-Waller coefficients B_{iso} from the Rietveld refinement of high-temperature SRXRD data (star markers) and low-temperature XRD data (diamond markers) for a nominally cubic (treated at 573 K) and tetragonal (treated at 833 K) samples. A unique B_{iso} has been refined for the cation site. See main text for further details. (b) B_{iso} for the cubic and tetragonal structures obtained from the MSD calculated from AIMD trajectories. (c) MSD of the different ionic species and their average for the ordered tetragonal structure. (d) MSD of the different ionic species and their average for the disordered cubic structure.

To understand the trends in the B_{iso} from an atomistic point-of-view, we have performed *ab initio* molecular dynamics simulations on both the ordered tetragonal and disordered cubic polymorphs. The MSD of each atomic species is calculated between 100 K and 700 K. The MSDs for the disordered polymorph are found to be generally higher than for the tetragonal. For the latter (Figure 3.1.4.c), the MSDs of the different species cluster together. Cu and Zn ions show slightly higher values, possibly due to their bonding, which is more ionic in nature, and involves lower electron sharing. Sn and S, on the other hand, being strongly covalently bound to each other are expected to move the least, and indeed present a comparatively lower MSD. This behaviour is dramatically reversed for the disordered cubic structure (Figure d), where Sn dominates the MSD. This can be explained by the s^2 lone-pair retention and rattling in certain Sn ions (see Figure c-d), shown to possess low frequency optical modes. These could be responsible for the upward shift in B_{iso} and MSD observed for the cubic polymorph. A deviation from linearity at low temperatures is expected, due to the zero-point energy. The presence of disorder-induced vibrational modes surviving at low temperature might be the

reason why this deviation happens at higher temperatures for the cubic compared to the tetragonal phase.

Obtaining the weighted B_{iso} (Figureb) from the calculated MSD we observe good agreement, qualitatively and even somewhat quantitatively, with experiments (Figurea). In particular, the cubic polymorph shows a $\sim 1 \text{ \AA}^2$ positive offset in the cation's B_{iso} . For the tetragonal polymorph the B_{iso} shows virtually no static disorder, although in the real sample a non-zero (though minimal) value is expected due to frequently occurring antisites, defects, and nanoscale size. From these results, it emerges that the ordered and disordered polymorphs are separated not just by a different vibrational behaviour of the ions (seen in the temperature trend), but also by a distortion of the crystalline lattice due to disorder, seen in the static upward shift in the B_{iso} . The observation of a static component in B_{iso} is a further demonstration of cation disorder in the cubic sample. This can add credibility to the assignment of the phase to the disordered sphalerite structure.

3.1.4 Conclusion

In this work, the novel phase of disordered cubic CZTS from mechanical alloying is carefully studied. The polymorph is metastable at room temperature and is found to transition to tetragonal kesterite above 663 K. Different treatment temperatures are used to produce cubic and tetragonal CZTS samples. Rietveld refinements of SRXRD data allow to analyse and compare structural and microstructural features. In particular, the cubic stacking of disordered CZTS is found possessing a considerable fraction of twin faults. These seem to anneal in tetragonal samples, treated at a higher temperature, pointing to an inverse relationship between faulting and domain size. Temperature-dependent SRXRD measurements allow to observe an upward shift of $\sim 1 \text{ \AA}^2$ in the cation B_{iso} of the cubic sample with respect to the tetragonal counterpart. This is believed arising from disorder, as the softer bonds and distorted crystalline lattice can accommodate larger atomic MSD. As also confirmed by *ab initio* calculations, disorder leads to a static contribution to MSD, whereas the dynamic component does not differ between the ordered and disordered polymorphs. The work brings further advancement in understanding disorder in CZTS, known to significantly affect thermal and electronic transport properties²⁷, as well as induce topologically non-trivial behaviour⁷⁸. DW coefficients obtained from XRD are found to be

good indicators of disorder: B_{iso} can represent a method to quantify disorder and its dynamic behaviour, of crucial interest to predict and adjust the transport properties. Future work will involve the investigation of possible short-range cation motifs in the disordered cubic arrangement through extended X-ray absorption fine structure and the atomic pair distribution function technique, with the support of *ab initio* modelling.

Appendix

Ground-state binding energy for the different structures

| | Binding energy per unit atom [eV] |
|--|-----------------------------------|
| Sphalerite $F\bar{4}3m$ CZTS | -4.02 |
| Wurtzite $P6_3mc$ CZTS | -3.98 |

Table S6. Ground-state binding energies per unit atom calculated *ab initio* for a CZTS cubic sphalerite and a CZTS hexagonal wurtzite structure.

Compliance tensors and anisotropy in CZTS

In order to measure the anisotropy in CZTS, we performed DFT calculations using the finite difference method. This allows us to obtain the compliance tensor for the ordered and disordered polymorphs, which are given respectively as,

$$C_{ordered} = \begin{bmatrix} 97.9 & 59.5 & 58.7 & 0.3 & 0 & 0 \\ 59.5 & 97.9 & 58.7 & -0.3 & 0 & 0 \\ 58.7 & 58.7 & 96.3 & 0 & 0 & 0 \\ 0.3 & -0.3 & 0 & 43.2 & 0 & 0 \\ 0 & 0 & 0 & 0 & 43.8 & 0 \\ 0 & 0 & 0 & 0 & 0 & 43.8 \end{bmatrix}$$

and

$$C_{disordered} = \begin{bmatrix} 55.7 & 40.5 & 41.3 & -2.9 & 4.6 & 3.8 \\ 40.5 & 50.2 & 44.4 & 6.2 & 7.7 & 2.9 \\ 41.3 & 44.4 & 63.9 & -2.4 & 2.1 & 1.5 \\ -2.9 & 6.2 & -2.4 & 12.6 & -1.3 & -2.5 \\ 4.6 & 7.7 & 2.1 & -1.3 & 11.8 & -10.5 \\ 3.8 & 2.9 & 1.5 & -2.5 & -10.5 & 2.8 \end{bmatrix}$$

where all values are in GPa.

It should be noted that to minimize the forces acting on individual ions, the DFT reduces the symmetries of the supercell to triclinic. This leads to small non-zero values of c_{ij} for $i,j > 3$ ($i \neq j$). In addition, given the metastable nature of the disordered polymorph, several negative terms are also introduced. Nevertheless, this does not significantly affect the overall qualitative nature of the anisotropy in the two polymorphs, or their comparison. For the ordered tetragonal polymorph, the compliance matrix is in good agreement with that obtained by He and Shen⁹⁹.

In order to quantify the degree of anisotropy, we use the log-Euclidean anisotropy parameter A^L ⁹⁴, which is valid for all crystalline symmetries. It is an absolute measure of anisotropy, with perfect isotropy yielding a value of zero. This measure of anisotropy is given as,

$$A^L(C^V, C^R) = \sqrt{\left[\ln\left(\frac{\kappa^V}{\kappa^R}\right) \right]^2 + 5 \left[\ln\left(\frac{\mu^V}{\mu^R}\right) \right]^2}$$

where C is the compliance tensor, κ and μ are the bulk and shear moduli respectively, while the superscripts V and R refer to the Voigt and Reuss averages.

For the ordered tetragonal polymorph, this parameter has a value of 0.77 while for the disordered cubic this comes out to 1.12, indicating that the latter polymorph is more anisotropic. This of course is in agreement with the fact that full cation disorder leads to significant inhomogeneous bonding in cubic CZTS. In comparison to SrVO₃, which is the most anisotropic cubic crystal shown in Ref 94, with a value of 5.3, CZTS presents a relatively limited anisotropy.

In order to further understand the nature of the anisotropy, we have calculated the Young's modulus projected along the [hhh] and [h00] family of directions. The reciprocal of Young's Modulus in the direction of the unit vector l_i for the general triclinic system is given by¹⁰⁰,

$$l_1^4 s_{11} + 2l_1^2 l_2^2 s_{12} + 2l_1^1 l_3^2 s_{13} + 2l_1^2 l_2 l_3 s_{14} + 2l_1^3 l_3 s_{15} + 2l_1^3 l_2 s_{16}$$

$$\begin{aligned}
& + l_2^4 s_{22} + 2l_2^2 l_3^2 s_{23} + 2l_2^3 l_3 s_{24} + 2l_1 l_2^2 l_3 s_{25} + 2l_1 l_2^3 s_{26} \\
& + l_3^4 s_{33} + 2l_2 l_3^3 s_{34} + 2l_1 l_3^3 s_{35} + 2l_1 l_2 l_3^2 s_{36} \\
& + l_2^2 l_3^2 s_{44} + 2l_1 l_2 l_3^2 s_{45} + 2l_1 l_2^2 l_3 s_{46} \\
& + l_1^2 l_3^2 s_{55} + 2l_1^2 l_2 l_3 s_{56} \\
& + l_1^2 l_2^2 s_{66}
\end{aligned}$$

where s_{ij} are the elements of the stiffness tensor.

We represent the [hhh] direction by taking the average of all [111] directions, while the [h00] direction is represented by the average of [100], [010] and [001] directions. For the ordered tetragonal, the average reciprocal Young's modulus for the [hhh] directions is obtained as 0.0092 GPa⁻¹ ($E = 108.7$ GPa) while for the [h00] directions the value is 0.019 GPa⁻¹ ($E = 52.6$ GPa). Similarly, for the disordered cubic, along the [hhh] directions we get a value of 0.02 ($E = 50$ GPa), while along the [h00] directions the value is 0.04375 ($E = 22.9$ GPa).

These results indicate that for both the ordered and disordered polymorphs of CZTS, the [hhh] direction is stiffer in comparison to the [h00] direction. This can be explained by the fact that the rigid Sn – S covalent bonds lie along the 111 directions, making deformation along that direction significantly more difficult than in the 100 direction.

Acknowledgements

The authors would like to acknowledge C. Stefani, F. Adams and A. Schulz from the Max-Planck-Institute for solid state research for supporting the collection of laboratory XRD data and Raman spectra, Dr. N. Casati and A. Cervellino of Paul Scherrer Institute for help with SRXRD measurements, Dr. Alan Coelho for suggestions on data modelling, and Dr. G. Ischia for help with TEM measurements. X-ray diffraction beamtime was provided by the Paul Scherrer Institute, with proposal 20191560 and Mesquik proposal 20210241. The simulations were performed on the national supercomputer HPE Apollo Hawk at the High Performance Computing Center Stuttgart (HLRS) under the grant DISKESTE.

3.2 Order–Disorder Transition in Kesterite Cu₂ZnSnS₄: Thermopower Enhancement via Electronic Band Structure Modification

This section is partly taken from: Isotta, E., Mukherjee, B., Fanciulli, C., Pugno, N.M. and Scardi, P., 2020. Order–disorder transition in kesterite Cu₂ZnSnS₄: Thermopower enhancement via electronic band structure modification. *The Journal of Physical Chemistry C*, 124(13), pp.7091-7096.

DOI: <https://doi.org/10.1021/acs.jpcc.0c00886>

Abstract

The order-disorder transition of kesterite (CZTS, Cu₂ZnSnS₄) from I-4 to I-42m crystal structures has a marked effect on Seebeck coefficient, which displays a sharp enhancement at the transition temperature, around 533K. Considered to be detrimental for the performance of photovoltaic kesterite, the order-disorder transition appears to be beneficial for thermopower. Experimental data and ab initio calculations explain the origin of this enhancement: the increase of crystal symmetry in the disordered polymorph leads to a favorable electronic band structure characterized by flat and converged bands. At the transition, a sharp drop in mobility and increase in carrier concentration experimentally prove this mechanism of Seebeck enhancement. This, other than providing a new understanding of the material, can cast light on some profitable mechanisms to enhance the thermoelectric performance. Additionally, the increase in Seebeck provides an efficient tool to observe the transition and possibly to quantify disorder.

3.2.1 Introduction

Kesterite (CZTS) is a p-type chalcogenide material with reference formula Cu₂ZnSnS₄. It has long been studied as absorber in thin film photovoltaic devices,^{1–3} and recently deemed promising as a potential thermoelectric material,^{4–10} valued for its intrinsically low thermal

conductivity⁴ and composition based on non-toxic, abundant and low-cost elements.¹¹ In its ordered and low temperature form, kesterite is reported having a tetragonal *I*-4 crystal structure, while it was recently proved that a cubic *F*-43*m* low-temperature polymorph can be obtained for samples made by high-energy ball-milling, as an effect of a high disorder state of the cations.^{4,12} This appears to be a metastable phase, since it transitions to the tetragonal polymorph on heating, as the temperature activates a reordering of the cations.⁴ At around 533K, tetragonal kesterite faces a reversible order-disorder phase transition: cations in the intermediate Cu-Zn planes of the *I*-4 structure (*2c* and *2d* Wyckoff positions) completely randomize their position (becoming *4d* Wyckoff position) thus transitioning to the tetragonal *I*-42*m* structure.^{5,13–15} This transition has been studied in some detail in recent years, because disorder is considered detrimental for the photovoltaic performance of CZTS, as well as difficult to avoid. In fact, owing to the low formation energy of the Cu_{Zn} and Zn_{Cu} antisite defects,^{16,17} a certain degree of disorder is inevitable in CZTS, even after extensive annealing treatments. Significant efforts have been made to quantify the degree of disorder and the subsequent loss in photovoltaic efficiency, rarely finding an ultimately suitable technique.^{5,14} Nevertheless, for what concerns thermoelectric performance things proved to be different: the order-disorder transition has a marked and beneficial effect on the Seebeck coefficient.⁵

The aim of this work is to demonstrate experimentally and through *ab initio* calculations the physical origin of the increase in thermopower caused by the order-disorder transition of kesterite, which we connect with the crystal-symmetry induced modification of the electronic band structure.

3.2.2 Methods

Experimental

Bulk kesterite sintered disks were produced according to previously described procedures,^{4,5} starting from reactive ball milling of the elementary components, i.e., metals and sulfur in stoichiometric proportions, to obtain kesterite nanometric powders, then cold-pressed and thermally treated. Some of the samples undergone a quenching process in air, either starting from the sintering temperature of 560°C, or from a lower temperature reached with natural cooling, to room

temperature. Absolute Seebeck coefficient measurements have been performed in 4-contact configuration and with Pt standard with a Linseis LZT Meter, in the temperature range 320K-720K, with a temperature gradient of 10K. Carrier density and mobility have been measured with an MMR K-20 and an H-50 measurement systems. Results are obtained by a combined measurement of Hall effect and resistivity as a function of temperature. Resistivity is determined by the Van Der Pauw method using squared shaped samples with thickness below 1 mm, providing an optimal geometrical ratio between surface and thickness. Hall effect measurements have been performed with a permanent-magnet field of 6270±10 G. The currents for testing have been set to values below 10 mA in order to prevent any thermal change in the samples. All the measurements are performed in vacuum, to prevent material degradation, and in the temperature range 300K-620K.

Density Functional Theory (DFT) calculations

The ab initio electronic structure calculations with DFT have been performed using the plane wave basis set implemented in the Vienna ab initio simulation package (VASP).^{18,19} The electron-exchange correlation functional was approximated using the Perdew-Burke-Ernzerhof (PBE)²⁰ form of the generalized gradient approximation (GGA). All calculations were performed with an energy cut-off of 300 eV. The ordered and disordered structures were modelled with 16 and 64 atom supercells respectively, visible in Figure 3.2.1, and the geometry was optimized with an 8x8x8 and 4x4x4 Monkhorst Pack (MP) k-mesh, respectively, centered at the Γ point, with Gaussian charge smearing in the order of 0.01 eV. The electronic degrees of freedom were relaxed until the change in the total free energy and energy eigenvalues were both smaller than 10^{-6} eV. The disordered structure was generated by manually assigning a random Cu/Zn arrangement in the 4d Wyckoff positions of the *I*-42m structure, keeping the overall stoichiometry balanced (Cu:Zn = 1:1 in 4d sites). The bands were calculated along a high-symmetry path in the irreducible Brillouin zone obtained using the SeeK-path²¹ tool, while the electronic density of states (*DoS*) was obtained using a dense 24x24x24 MP k-mesh for the 16-atom supercell and an 8x8x8 MP k-mesh for the 64-atom supercells.

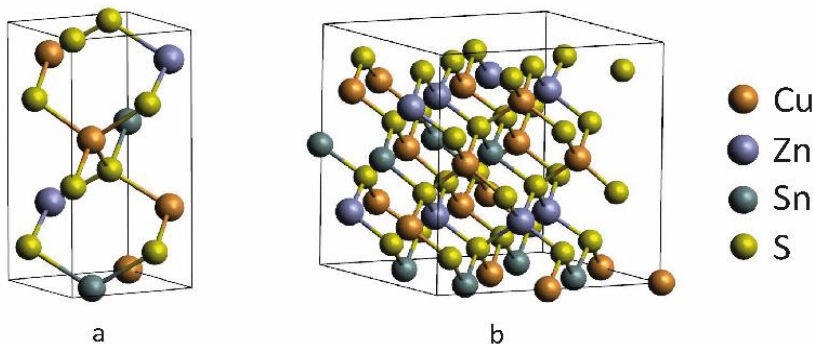


Figure 3.2.1. Supercell crystal structures of kesterite used in DFT calculations: (a) ordered, s.g. $I\bar{4}$ and 16-atom cell; (b) disordered, s.g. $I\bar{4}2m$ and 64-atom supercell.

3.2.3 Results and discussion

Thermoelectric properties

The order-disorder phase transition of kesterite, from the ordered $I\bar{4}$ to the disordered $I\bar{4}2m$ tetragonal structures, has been reported at $533K \pm 10K$.^{13,14} As shown by thermal analyses, it is a second-order and reversible transition,⁵ and it consists of a full occupational disorder of Cu and Zn cations in the $4d$ Wyckoff positions. This transition appears to have a beneficial role for thermoelectric CZTS. Indeed, the measurement of Seebeck coefficient, reproduced in Figure 3.2.2a, displays a sharp increase around the transition temperature.⁵ Insets of Figure 3.2.2a show the ordered $I\bar{4}$ crystal structure for the region below the transition temperature, where Cu and Zn occupy specific positions in the intermediate planes, and the disordered $I\bar{4}2m$ structure for the high-temperature region, where a unique position is considered to account for a mixed and random occupation of the two cations. We have put forward that this enhancement is due to a higher symmetry in the crystal structure of disordered CZTS.⁵ Indeed, due to this loss of specificity in the positions of Cu and Zn, the disordered is a more symmetric structure. This can also be noticed by the additional 2-fold rotation axis and mirror plane specified in the space group $I\bar{4}2m$.

Figure 3.2.2b shows the electrical resistivity measured in Van Der Pauw configuration, while Figure 3.2.2c displays the carrier concentration, measured via Hall effect on the same sample, and the carrier mobility, calculated from resistivity and carrier concentration data. Around the order-disorder transition temperature we notice a substantial increase in carrier concentration, that nearly triples its values, and a corresponding decrease in mobility. We observe a kink in resistivity (Figure 3.2.2b) around the transition temperature. It is worth mentioning that literature data reports a smaller electronic bandgap E_g for disordered kesterite (~ 1.50 eV) with respect to ordered (~ 1.67 eV).^{15,22}

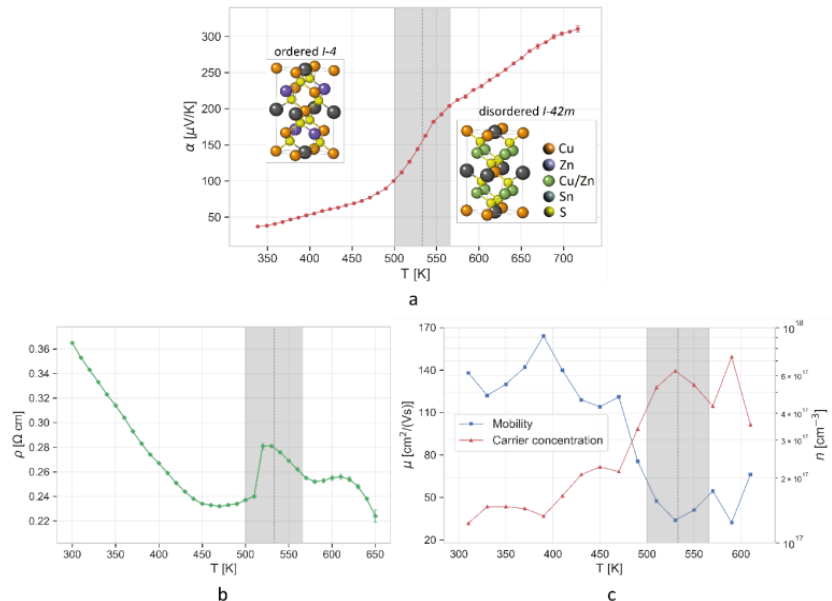


Figure 3.2.2. (a) Absolute Seebeck coefficient α (standard deviation is expressed with error bars) with insets showing the relevant kesterite crystal structures for each temperature region, namely ordered I-4 in the low-temperature and disordered I-42m in the high-temperature zone. Data reproduced from Ref.5 with permission from MDPI. (b) Electrical resistivity ρ (standard deviation is expressed with error bars), (c) and carrier mobility μ and concentration n (in logarithmic scale) measured for a bulk CZTS sample. In the order-disorder transition region (highlighted in grey) it is possible to notice an increase in Seebeck coefficient and carrier concentration, and a corresponding drop in the mobility. This is attributed to band structure modifications: crystal-symmetry induced band convergence and reduction of curvature.

Electronic band structure

In order to provide a theoretical explanation for the experimentally observed changes in thermopower, electrical resistivity, carrier mobility and carrier concentration caused by the order-disorder transition, we performed *ab initio* band structure calculations for ordered (Figure 3.2.3a) and disordered (Figure 3.2.3b) kesterite. From these calculations we observe a threefold effect on the bands caused by the transition from the ordered to the disordered phase. Firstly, we see an increased convergence at the top of the valence band in the disordered phase, with the separation between the top three bands dropping from 0.139 eV ($\sim 5.51 \text{ kT}$, calculated at $T = 298\text{K}$) for the ordered phase to 0.072 eV ($\sim 1.39 \text{ kT}$, calculated at $T = 600\text{K}$) for the disordered. Secondly, we observe a significant reduction in curvature (flattening) at the top of the valence band in the disordered phase compared to the ordered. Finally, we observe a decrease in the band gap going from the ordered to the disordered phase, though it must be considered that the exchange-correlation functional in GGA is known to strongly underestimate the band gap. While more sophisticated calculations using hybrid functionals do provide a better estimation of the band gap, they become prohibitively expensive in terms of computational resources, particularly for larger supercells such as the disordered structures. It may be assumed that the errors for similar systems are similar and cancel out in comparative studies, the accuracy of the calculations being validated by their agreement with experiments. The effect of an increased band convergence and a reduced curvature due to higher disorder in the crystal structure is evidenced also by the density of states (*DoS*), presented in Figure 3.2.3c, which is higher at the top of the valence band, with steeper slope of *DoS* (and of $\ln(\text{DoS})$, in the inset) for the disordered phase with respect to the ordered. The asymmetry of the *DoS* with respect to the Fermi level is consistent with the p character of the material. In the Supporting Information, the extended band structures are visible, as well as the band structures for a partially disordered sample and another configuration of disorder, to confirm and generalize the validity of the DFT results.

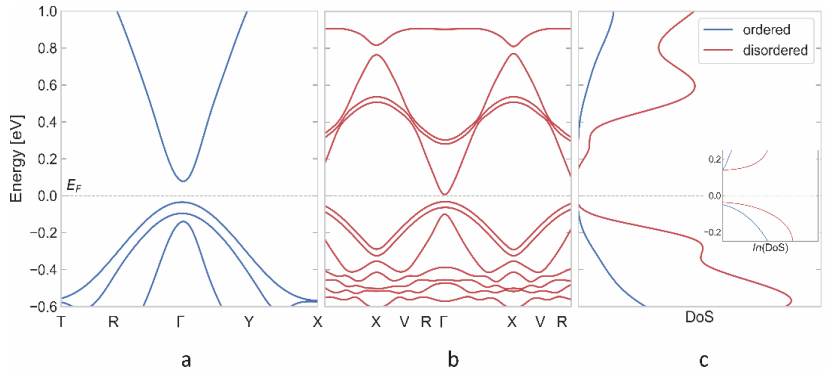


Figure 3.2.3. Band structures for ordered (a), and disordered (b) kesterite. Panel (c) displays the density of states *DoS*, with inset showing the natural logarithm of the *DoS*. With an increase of disorder, the top valence bands tend to converge and reduce their curvature, the bandgap narrows, while *DoS* and *ln(DoS)* get higher and steeper.

We believe this band structure modification is at the origin of the difference in electrical properties. The Fermi energy is set to 0 eV in each case. X-axis is on the same scale in k-space for (a) and (b).

Order-disorder transition: crystal symmetry induces band convergence and flatness

The thermopower is directly proportional to the density of state effective mass $m_{DoS}^* = N_V^{2/3} m_I^*$, where N_V is the band degeneracy and m_I^* is the inertial effective mass of charge carriers along the conduction direction.²³ It has been pointed out in the literature that there may be a connection between an increase in the symmetry of a crystal structure and an improved band convergence.^{24–26} We believe the order-disorder transition of CZTS to be an example of this behavior: the higher crystal symmetry causes an increase in the electronic band degeneracy N_V , as proved by DFT, thus justifying the sharp growth in the experimentally observed Seebeck coefficient. We attribute the observed increase in carrier concentration (Figure 3.2.2b) both to the decrease in E_g and to the convergence of bands. In fact, were it due to a narrower bandgap alone, we would expect a corresponding decrease in thermopower and electrical resistivity, while experimental data shows that thermopower increases with the transition whereas resistivity does not decrease. A higher band convergence could instead explain why we observe an enhancement of Seebeck despite the increase in carrier

concentration. Resistivity displays a sharp upwards kink around the transition temperature, and then smoothly decreases to reach values in the order of those obtained prior to the transition. This is also in contradiction with the increased carrier concentration and can only be explained with the observed sharp drop in mobility, which in this case we associate to a carrier localization due to band convergence. In many literature cases, a pronounced decrease in mobility is associated to an enhancement of thermopower,²⁷ along with a steeper *DoS* as expressed by Mott's formula.²⁸ Moreover, from *ab initio* calculations we observe a reduced curvature in the valence bands, which is in agreement with an increased m_I^* and decreased mobility. Indeed, the movement of cations and the concurring rearrangement of covalent bonds happening during the transition might have promoted a higher number of available energy levels (therefore higher carrier concentration) but more localized (causing the drop in mobility and the increase in Seebeck). This, contrary to what reported for other systems,^{29,30} seems to not extensively penalize electrical resistivity owing to the simultaneous increase in carrier concentration caused by band convergence. The *DoS*, being higher for the disordered phase, highlights the higher availability of valence states close to the Fermi level and their higher occupation, associated to the reduced bandgap. The trend of the logarithm of the density of states (shown in the inset of Figure 3.2.3c) is steeper at the top of the valence band for the disordered polymorph, in agreement with the higher thermopower provided for by Mott's formula.²⁸ Furthermore, a sharper asymmetry of the *DoS* with respect to the Fermi level is found which is consistent with the p-type nature and is typically associated with an increase in Seebeck.²⁸ In general, the DFT calculations are in good agreement with the experimental results. It is evident that the described phenomenon is dominated by band features (flatness and degeneracy), which is also supported by the low value of carrier concentration (in the order of 10^{17} cm^{-3}) and can explain why we observe a decoupling of the thermopower and resistivity trends. These results provide experimental and theoretical proof that favorable band structure and the subsequent enhancement of thermoelectric properties can be achieved with an increase in crystal symmetry.

3.2.4 Conclusions

The order-disorder transition of kesterite from ordered *I-4* to disordered *I-42m* crystal structures leads to a beneficial effect on thermopower that presents an increase around the transition temperature of 533K,⁵ conversely to what happens for photovoltaic kesterite for which the transition is deemed detrimental for the performance.¹⁴ In this work, we have demonstrated that the mechanism at the origin of this enhancement of Seebeck coefficient is an improved electronic band structure. DFT calculations show more converged and flatter bands for the disordered polymorph, which lead to an increased carrier concentration and a decreased mobility, confirmed by experimental data. A higher crystal symmetry for the disordered structure is deemed responsible for the improved band degeneracy, which in turn leads to a higher density of states effective mass and enhanced thermopower. Electrical resistivity, differently from what commonly occurs,^{29,30} is not penalized by the low mobility due to the concurrent high carrier concentration originated from band convergence. These results, besides providing a new understanding of the studied material, can cast light on some profitable mechanisms to enhance the thermoelectric performance.

Acknowledgements

This research was funded by the Autonomous Province of Trento, within the framework of the programmatic Energy Action 2015–2017. The computational time was provided by CINECA - Italian Supercomputing Facility, with the project CZTS - HP10CONX70. N.M.P. is supported by the European Commission under the Graphene Flagship Core 2 grant No. 785219 (WP14, “Composites”), the FET Proactive (“Neurofibres”) grant No. 732344, the FET Open (Boheme) grant No. 863179 as well as by the Italian Ministry of Education, University and Research (MIUR) under the “Departments of Excellence” grant L. 232/2016, the ARS01- 01384-PROSCAN and the PRIN-20177TTP3S grants.

3.3 Simultaneous optimization of Thermal Conductivity, Electrical Conductivity and Seebeck Coefficient in Disordered Cubic Cu₂ZnSnS₄

This section is taken from: Isotta, E., Mukherjee, B., Fanciulli, C., Ataollahi, N., Sergueev, I., Stankov, S., Edla, R., Pugno, N.M. and Scardi, P., 2020. Origin of a Simultaneous Suppression of Thermal Conductivity and Increase of Electrical Conductivity and Seebeck Coefficient in Disordered Cubic Cu₂ZnSnS₄. *Physical Review Applied*, 14(6), p.064073.

DOI: <https://doi.org/10.1103/PhysRevApplied.14.064073>

Abstract

The parameters governing the thermoelectric efficiency of a material, Seebeck coefficient, electrical and thermal conductivities, are correlated and their reciprocal interdependence typically prevents a simultaneous optimisation. Here, we present the case of disordered cubic kesterite Cu₂ZnSnS₄, a novel phase stabilized by structural disorder at low temperature. With respect to the ordered form, the introduction of disorder improves the three thermoelectric parameters at the same time. The origin of this peculiar behaviour lies in the localization of some Sn lone pair electrons, leading to “rattling” Sn ions. On one hand, these rattlers remarkably suppress thermal conductivity, dissipating lattice energy via low-frequency optical phonons; on the other, they form electron-deficient Sn-S bonds leading to a p-type doping-like effect and highly localized acceptor levels, simultaneously enhancing electrical conductivity and Seebeck coefficient. This phenomenon leads to a 3x reduced thermal conductivity and doubling of both electrical conductivity and Seebeck coefficient, resulting in a more than 20x increase in figure-of-merit, although still moderate in absolute terms.

3.3.1 Introduction

Thermoelectric (TE) materials, with the possibility of converting heat gradients into electricity, can substantially contribute to the global challenge for a reduced and more sustainable energy demand. But efficient TE energy harvesting and waste heat recovery require improved material performance. This is usually expressed by the

thermoelectric figure of merit, $zT = \sigma S^2 T / k$, which combines three fundamental but conflicting characteristics: electrical conductivity (σ), Seebeck coefficient (S), and thermal conductivity (k), while T is the absolute temperature. TE research has recently led to a thriving of methods to improve zT : nanostructuring^{1–3} reduces k_L (lattice component of k) without excessively penalizing electrical transport; chemical doping improves carrier concentration and conduction, though often to the expense of Seebeck coefficient; crystal and electronic structure engineering^{4–8} mainly enhance the Seebeck coefficient. Many efforts were directed to promoting a phonon-glass electron-crystal behaviour, which aims at increasing the electrical and suppressing the thermal conductivity^{9–11}. Nevertheless, the gain in conductivity, if connected with an increased density of charge carriers, leads to a downturn of Seebeck coefficient. All in all, due to the conflicting interdependence of TE parameters, it has proved hard to improve σ , S , and to reduce k , simultaneously¹².

In this work, we present a physical mechanism capable of optimizing all three thermoelectric parameters at the same time. This is due to the introduction of structural disorder in the quaternary chalcogenide kesterite ($\text{Cu}_2\text{ZnSnS}_4$, CZTS), an earth-abundant, non-toxic, and low-cost material originally proposed for thin film photovoltaics^{13,14}. In the attempt to generalize the concepts presented here, we compare its completely ordered (tetragonal) polymorph with its completely disordered (cubic) one. The low-temperature disordered cubic is a recently discovered phase^{15,16} stabilized with high-energy mechanical alloying. The improvement of all the TE parameters obtained with the introduction of disorder has prompted us to investigate the underlying physical phenomenon. Even if the performance is moderate compared to actual commercial materials for end TE devices, this mechanism leads to the highest reported zT for undoped CZTS. Understanding the origin of this all-round improving phenomenon could open the path to applying similar strategies on other materials to potentially enhance all their TE properties.

3.3.2 Methods

Synthesis

Nanocrystalline kesterite powder was produced via reactive mechanical alloying starting from stoichiometric precursors, as described elsewhere⁷. As-milled powder was cold pressed into 16

mm-diameter disks (~2 mm thickness) applying a load of 5 tons for 3 minutes. The disordered cubic sample was obtained after sintering in a dynamic atmosphere of Ar for 60 min at 160°C (ramp 20 K/min) followed by 20 min at 300°C (ramp 20 K/min up to 260°C and 10 K/min from 260°C to 300°C) and natural cooling down to room temperature. The ordered tetragonal sample was obtained with an identical procedure with temperatures being 300°C for the 60 min step (ramp 20 K/min) and 560°C for the 20 min step (ramp 20 K/min up to 520°C and 10 K/min from 520°C to 560°C).

Structural characterization (XRD, TEM) and thermal analyses

XRD patterns were collected on powder or disk samples at room temperature with Cu K α radiation generated at 40KV and 30 mA (Rigaku PMG diffractometer, graphite bent-crystal monochromator in the diffracted beam). Rietveld refinement of XRD data was performed with TOPAS 7¹⁷, with support of the macros based on Whole Powder Pattern Modelling¹⁸ for crystallite size analysis¹⁹. Transmission Electron Microscopy (TEM) imaging, as well as Selected Area Electron Diffraction (SAED) and high-magnification Energy Dispersive X-ray analysis (EDX) have been performed with a HR-S/TEM instrument (ThermoFischer TALOS 200 s). XRD patterns in temperature were collected using a Panalytical X'Pert pro system equipped with an X'Celerator detector, over the range RT to 550°C, using a HTK1200N facility. The measurements were performed in He atmosphere with a gas pressure of 400 Torr at RT. For each temperature, the patterns were collected performing 10 repetitions on the same angular range (total time per temperature ~60 min with 3 min of equilibration time). Differential Scanning Calorimetry (DSC) was performed with an instrument DSC92 SETARAM on an as-milled powder sample sealed in a crucible under an atmosphere of Ar with 5% H₂ to hinder oxidation processes. Temperature scan from RT to 600°C with a ramp of 10 K/min.

Thermoelectric characterization

Absolute Seebeck coefficient was measured in 4-contact configuration and with Pt standard with a LINSEIS LSR-3 machine. Measurements have been performed under a static He atmosphere in the range RT-480K with heating rate of 10 K/min and a temperature gradient across the sample of approximately 10 K. Three measurement per temperature have been performed to calculate the mean and standard deviation, used in the plots as value and error bar. In addition, a

declared instrumental accuracy of 7% should be considered. Measurements over temperature have been repeated several times and on multiple samples to verify reproducibility. Further discussion on the repeatability of measurements in SN 10.

Carrier density and mobility have been measured with an MMR K-20 and an H-50 measurement systems. Results are obtained by a combined measurement of Hall effect and resistivity as a function of temperature. Resistivity is determined by the Van Der Pauw method using squared shaped samples with side 8 mm and thickness below 1 mm, providing an optimal geometrical ratio between surface and thickness. Hall effect measurements have been performed with a permanent-magnet field of 6270 ± 10 G. The currents for testing have been set to values below 10 mA to prevent any thermal change in the samples. All the measurements are performed in vacuum (4–8 mTorr) in the temperature range 300–450 K. A declared instrumental accuracy of 5% and 10% should be considered for Van der Pauw and hall measurements, respectively. Measurements have been repeated several times to verify reproducibility of results. Further discussion on the repeatability of measurements in SN 10.

Thermal conductivity was calculated as $k = \alpha\rho C_p$, with α thermal diffusivity, ρ density and C_p specific heat. Thermal diffusivity measurements were performed with a laserflash Linseis LFA 500 under vacuum atmosphere on disk samples with a thickness of ~1.5 mm. A declared instrumental accuracy of 3% should be considered for thermal diffusivity. Density ρ was geometrically measured on disk samples and used for thermal conductivity calculations. The measurement with Archimede's method was also performed. Density results are discussed in SN 5. Specific heat measurements have been performed with a Thermal Analysis Q100 DSC instrument in modulated mode (MDSC). A modulation with period 120 s and semi-amplitude 0.5K was applied to isothermal measurements and used to extract the specific heat as a function of temperature. The samples were sealed in Ar atmosphere during the measurement. Discussion on the repeatability of measurements in SN 10.

Ultraviolet-visible spectroscopy

The optical properties were investigated using a Perkin-Elmer spectrophotometer model LAMBDA 750, equipped with a 150 mm integrating sphere. Powder samples (ground disk samples) were dispersed in ethanol and sonicated for 1 h. The optical absorption

spectra were collected in the wavelength range of 300–1000 nm with a step size of 0.5 nm. The Tauc plot was used to extrapolate the bandgap value, operating a linear fit in the range 2.2–2.8 eV.

E. NIS measurements

Nuclear Inelastic Scattering (NIS) measurements were performed at the Dynamics beamline P01 at PETRAIII (DESY, Hamburg) using ¹¹⁹Sn nuclear resonance. A high-resolution monochromator provided an energy bandwidth of 1.4 meV at 23.9 keV. The measurements were carried out on samples with natural enrichment of ¹¹⁹Sn (8.6%), inserted into a closed cycle He cryostat and kept at 43K. The low temperature was chosen to suppress multi-phonon contributions in the inelastic scattering signal, which make difficult the extraction of the one-phonon scattering term and projected vibrational density of states. The nuclear resonance signal was separated in time from electronic X-ray fluorescence and measured using a Si avalanche photodiode detector.

F. DFT and DFPT calculations

The *ab initio* electronic structure calculations have been performed using the plane wave basis set implemented in the Vienna *ab initio* simulation package (VASP)^{20,21}. The electron-exchange correlation functional was approximated using the Perdew–Burke–Ernzerhof (PBE)²² form of the generalized gradient approximation (GGA). All calculations were performed with an energy cutoff of 300 eV. The tetragonal ordered and cubic disordered structures were modelled with 16 and 64 atom supercells, respectively. For the latter, to try to better simulate disorder in the real case, three different configurations were modelled randomly assigning the cation site to Cu, Zn or Sn, respecting the overall stoichiometry (2:1:1). Results for the additional configurations, both of DFT and DFPT, are reported in SN 7 and 11. The geometry was optimized with an $8 \times 8 \times 8$ and $4 \times 4 \times 4$ Monkhorst Pack (MP) k-mesh, respectively for the ordered and disordered cells, centered at the Γ point, with Gaussian charge smearing in the order of 0.01 eV. The electronic degrees of freedom were relaxed until the change in the total free energy and energy eigenvalues were both smaller than 10–6 eV. The bands were calculated along a high-symmetry path in the irreducible Brillouin zone obtained using the SeeK-path²³ tool, while the electronic density of states (DOS) was obtained using a dense $12 \times 12 \times 12$ MP k-mesh for the 16-atom supercell and an $8 \times 8 \times 8$ MP k-mesh for the 64-atom

supercells. The ELF and charge densities are visualized using the VESTA²⁴ visualization tool.

The vibrational properties are obtained using the dynamical matrix calculated using density functional perturbation theory (DFPT). The Phonopy code²⁵ is then used to diagonalize the dynamical matrix to calculate the inter-atomic force constants, from which the phonon dispersion relations and vibrational density of states are calculated.

3.3.3 Results and discussion

Structural: the low-temperature disordered cubic kesterite phase

The stable crystallographic structure of kesterite is the ordered tetragonal (space group *I*-4, Figure 3.3.1a). The structural complexity of this quaternary chalcogenide frequently causes the occurrence of several types of structural defects. The most common one is the Cu_{Zn} substitutional, which is believed to be the cause of the p-type nature of kesterite and possesses the lowest formation energy among the possible defects^{26–28}. Indeed, above 533 K the ordered tetragonal polymorph evolves into a disordered tetragonal (space group *I*-42*m*, Figure 3.3.1b) through the reversible order-disorder phase transition^{7,29–31}, involving a mixed and random occupation of Cu and Zn cations in the 4*d* Wyckoff positions (whereas in the ordered the 2*c* site is occupied by Cu and the 2*d* by Zn)^{7,29}.

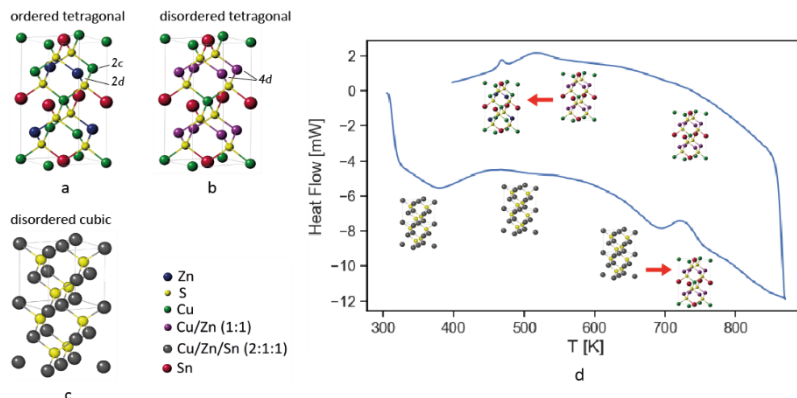


Figure 3.3.1. The different crystal structures of kesterite: a) tetragonal ordered *I*-4, for the sample sintered at 560°C below the order-disorder transition temperature of 533 K, b) tetragonal disordered *I*-42*m*, above the order-disorder transition, and c) cubic *F*-43*m* (ZnS-like), found for the ball-milled powder and for samples sintered up to 300°C. In panel d) a DSC measurement for an as-milled powder sample can be seen, showing the phase evolutions in temperature. On heating, kesterite is cubic *F*-43*m* up to around 650 K, where it transitions to tetragonal disordered *I*-42*m*, the polymorph that is stable at that temperature. On cooling, around 533 K disordered tetragonal kesterite transitions to ordered tetragonal *I*-4, as the transformation is reversible.

When obtained with mechanical alloying in high-energy conditions starting from elemental precursors, the level of structural disorder is so high that the crystal structure is better described by a cubic symmetry. We put forward that atoms arrange in a cubic *F-43m* structure similar to that of sphalerite ZnS, where the Zn site is

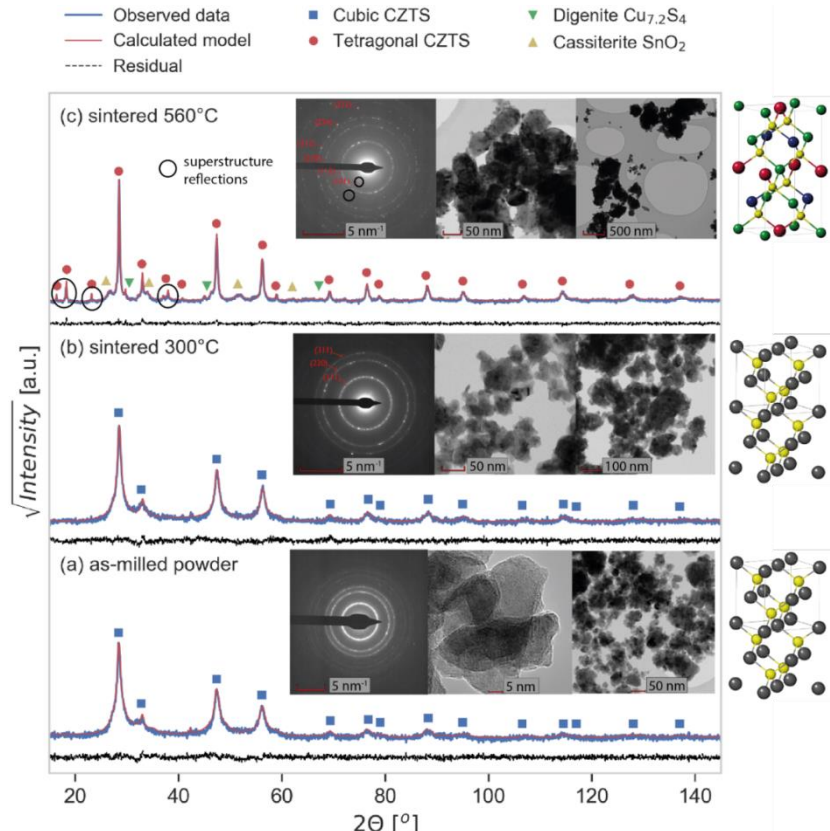


Figure 3.3.2. XRD patterns with phase identification, as well as TEM imaging and SAED, with plane indexing, for a) the as-milled powder, b) sample sintered at 300°C, both with a disordered cubic kesterite crystal structure, and c) sample sintered at 560°C, presenting a tetragonal structure with distinctive superstructure reflections both in the XRD and SAED patterns. The result of the Rietveld refinement modelling made with TOPAS 7 is visible as well as experimental data (blue points), modelled data (solid red line) and difference (solid black line). Part of panel c is reproduced with permission from ref 6. Copyright 2019 MDPI.

occupied by all the kesterite cations (Figure 3.3.1c). X-Ray Diffraction (XRD) and Selected Area Electron Diffraction (SAED) on the as-milled powder both support this statement, as the patterns show reflections of a cubic structure only (Figure 3.3.2a). After cold pressing the powder into a disk sample and annealing at 300°C, the

XRD-peak and SAED-ring positions do not change (Figure 3.3.2b), suggesting that the cubic crystal structure is preserved. Tetragonal kesterite forms instead after a heat treatment at 560°C, as pointed out by the super-structure reflections visible in the XRD and SAED patterns of Figure 3.3.2c. Allegedly the cubic phase, stable at low temperature, transitions to the tetragonal on heating, when the structural defects reduce owing to the activation of cation diffusion. From Differential Scanning Calorimetry (DSC) thermal analyses on as-milled powder (Figure 3.3.1d), we locate the cubic-to-tetragonal phase transition close to 650 K. The same critical temperature is detected with XRD measurements in temperature (see Supplemental Note SN 1). At this temperature and above, kesterite is known to be stable in the disordered tetragonal form, so it is understood that the Sn and S lattice participates the most in this structural rearrangement. Due to the reversibility of the order-disorder transition⁷, the tetragonal ordered form appears at around 533 K during the slow cooling down to ambient temperature, when the XRD pattern reveals the tetragonal nature of CZTS.

By cross-comparing Rietveld refinements of XRD data, Transmission Electron Microscopy (TEM) imaging and Energy Dispersive X-ray analysis (EDX) data (see SN 2), it is possible to assess that sintering at 560°C develops tetragonal kesterite as well as minor fractions of secondary phases, mainly consisting in SnO_2 and $\text{Cu}_{7.2}\text{S}_4$ (Figure 3.3.2c, see also SN 3). Both for the as-milled powder and the sample sintered at 300°C (Figures 3.3.2a and 3.3.2b), instead, an almost pure CZTS phase is found with significantly reduced levels of oxidation and secondary phases. All the samples display nanometric domains (quantitative estimations in SN 3), a feature deemed beneficial for thermoelectricity as it selectively suppresses thermal over electrical conductivity, due to different scattering from the grain boundary region. XRD powder pattern refinements reveal that in the cubic sample the Debye-Waller coefficients for the cation site are comparatively higher, refined as 1.7(3) Å² with respect to an average of 0.75(7) Å² for the tetragonal sample. Large values of these coefficients (proportional to the atomic mean square displacement (MSD) in the crystal structure) can accommodate an effect of high cation disorder, as well as of softer bonds with a wider spectrum of vibrational modes.

Suppressed thermal conduction along with a gain in electrical conductivity and thermopower

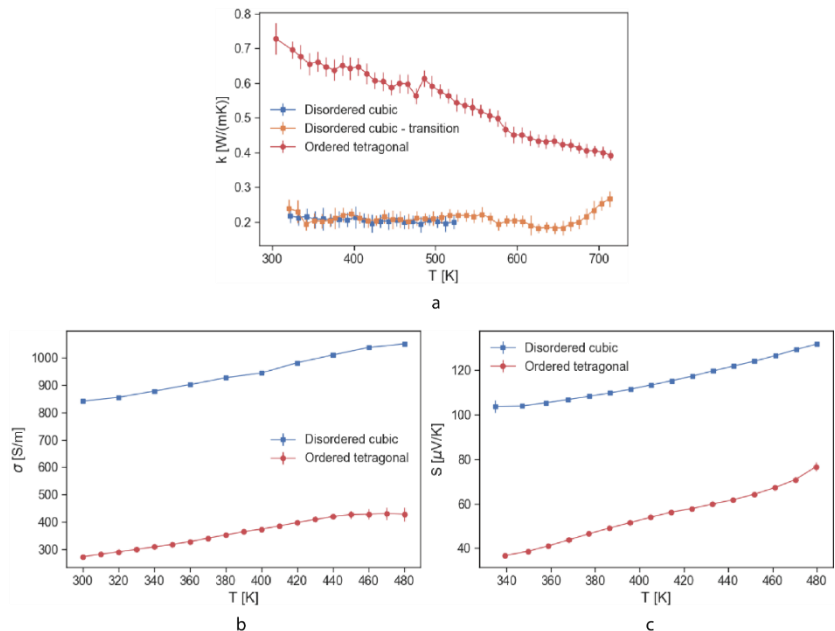


Figure 3.3.3. Thermal conductivity (a), electrical conductivity (b) and absolute Seebeck coefficient (c) as a function of temperature measured for a disordered cubic and an ordered tetragonal CZTS sample.

The disordered cubic sample shows a remarkable reduction in thermal conductivity (Figure 3.3.3a), with room temperature values less than one third of the ordered tetragonal counterpart. It also displays an almost flat curve, a feature that points to temperature-independent mechanisms. Experimental values for the cubic sample are in the order of 0.2 W/(mK) for temperatures between 300 K - 650 K, significantly below the ultra-low limit of high-performance TE materials, typically set as 0.5 W/(mK).¹ The smaller domain size of the cubic sample can play a role in this suppression through an increased phonon scattering from the grain boundary area. Nevertheless, since both the samples are nanostructured and present comparable values of density (see SN 4), we can reasonably assert that a good part of the suppression achieved with the cubic is due to the underlying disorder-induced mechanisms rather than the microstructural properties. Indeed, when measured in a higher temperature range (Figure 3.3.3a, solid orange curve) the cubic sample displays a sudden increase in thermal conductivity around 650 K (see SN 5), coinciding with the cubic-to-tetragonal transition observed by

thermal analyses (Figure 3.3.1d) and XRD measurements in temperature (SN 1).

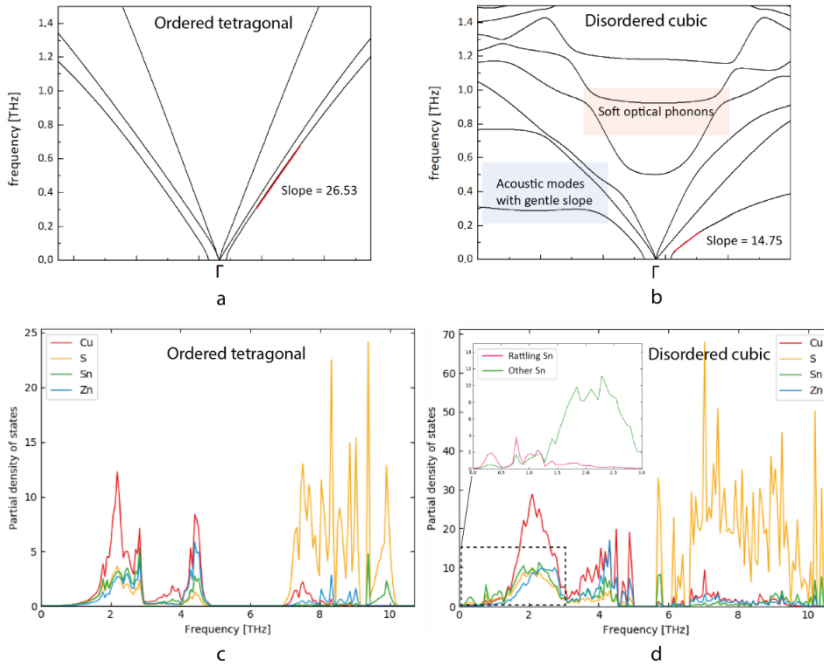


Figure 3.3.4. Phonon dispersion relations for the ordered tetragonal (a) and a disordered cubic (b) supercell. Vibrational density of states with contributions from individual atoms for an ordered tetragonal (c) and a disordered cubic (d). The inset in panel d, commented later on in the text, represents the projected VDOS of two different types of Sn: a “rattling” one (Sn7). and all the others.

In order to understand the origins of the reduced thermal conductivity in the cubic polymorph, the vibrational properties were calculated *ab initio* from density functional perturbation theory (DFPT). By plotting the vibrational density of states (VDOS) as a function of frequency, we observe more available vibrational modes in the high-frequency region (around 5.5–7 THz) of cubic CZTS (Figure 3.3.4d), compared to tetragonal (Figure 3.3.4c), with a significantly reduced gap between higher and lower frequency modes. This promotes Umklapp or diffusive phonon-phonon scattering in the cubic polymorph, leading to a lower thermal conductivity in general. Nevertheless, Umklapp processes increase with temperature, while the low values of thermal conductivity for cubic CZTS remain almost constant over a wide range in temperature. This suggests an additional, temperature-independent contribution to the low thermal conductivity observed in cubic CZTS. Comparing the phonon dispersion relation in the two

polymorphs (Figure 3.3.4a and 3.3.4b), it is evident that the long-wavelength acoustic modes in cubic CZTS have a lower slope than the tetragonal polymorph. This indicates a lower group velocity for phonon wave packets with consequent lowering of the thermal conductivity. More significantly, the acoustic modes in cubic CZTS have a lower frequency cut-off (< 1.1 THz)³², with several optical phonon modes in the low frequency (long wavelength) region below 1.5 THz (~ 50 cm⁻¹). Thermal energy is then dissipated through the activation of these low-frequency optical modes which, by virtue of representing out-of-phase vibrations of ions, do not participate in the conduction of heat. This explanation is supported by recent reports in the literature^{33,34} showing that these soft optical phonon modes are the primary mechanism for reduced thermal conductivity in certain ternary and quaternary chalcogenides.

In terms of electronic properties, the disordered cubic sample exhibits an improvement in both electrical conductivity σ and absolute Seebeck coefficient S (also addressed as thermopower), visible in Figure 3.3.3b-3.3.3c, a coupling that is considered quite unusual in TE materials³⁵. The electronic density of states (DOS, Figure 3.3.5d), from ab initio calculations, reveals the presence of sharp valence-type mid-gap levels above the Fermi energy arising from crystal disorder. Similar trap-states have been reported by Walsh et. Al²⁷ in tetragonal kesterite with introduced defects. These empty levels can act as acceptor states within the gap region, generating holes in the valence band, without a corresponding production of conduction electrons. Experimental observations do indeed show a considerably higher p-type carrier concentration for the cubic sample, (in the order of 10^{19} cm⁻³ compared to 1-2 10^{17} cm⁻³ of the tetragonal sample, Figure 3.3.5c), thus explaining the higher electrical conductivity. This hypothesis is further supported by absorption spectroscopy measurements (see SN 6), which do not show significant differences between the bandgap values of the two samples, suggesting that the improvement in carrier concentration is not connected with a reduction of the gap. Indeed, this is measured as 1.56 eV for the ordered tetragonal polymorph, in accordance with literature reports³⁶⁻³⁸, and as 1.53 eV for the disordered cubic polymorph. Nevertheless, a high carrier concentration is expected to have a negative impact on thermopower, as expressed by Mott's equation³⁹, but the opposite is observed for cubic CZTS.

$$S \approx \frac{\pi^2}{3} \left(\frac{k_B^2 T}{q} \right) \left[\frac{1}{n} \frac{\partial [f(E) DOS(E)]}{\partial E} + \frac{1}{\mu} \frac{\partial \mu}{\partial E} \right]_{E=E_F}$$

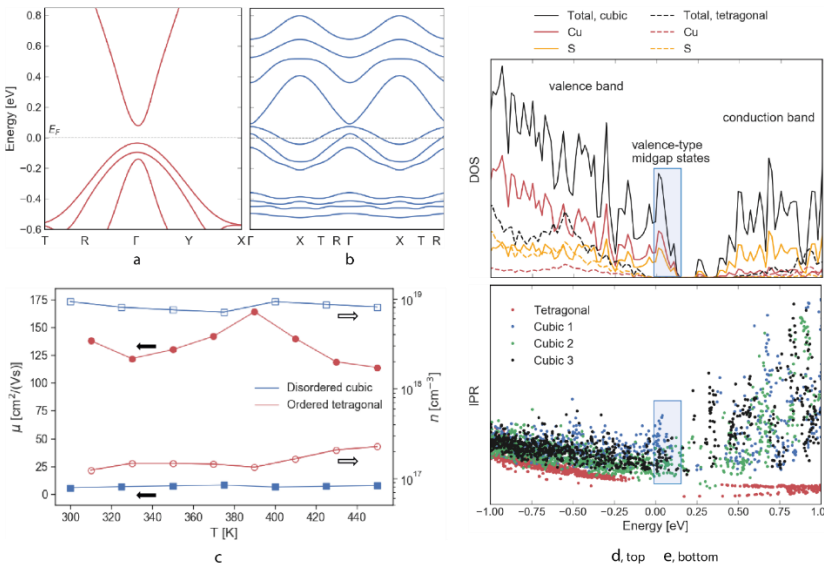


Figure 3.3.5. Electronic band structures for the ordered tetragonal $I-4$ (a) and a disordered cubic $F-43m$ (b) kesterite supercell. (c) Experimental measurements of carrier concentration n and mobility μ for the two samples. Electronic density of states DOS (d) calculated for a disordered cubic and an ordered tetragonal supercell, with partial density of states showing the individual contributions of Cu and S atoms. In panel (e) is the inverse participation ratio IPR , calculated for the ordered tetragonal supercell and three different configurations of disordered cubic supercells. Panels d) and e), where the mid-gap state region is highlighted in blue, show highly localized valence-type states in the bandgap, deemed responsible for the improved electronic behaviour of disordered cubic kesterite.

This is to be attributed in part to the reduced carrier mobility, experimentally measured more than one order of magnitude below tetragonal CZTS (Figure 3.3.5c), and theoretically evidenced in the flatter electronic bands, implying a higher inertial effective mass of charge carriers. In principle, electrical conductivity should be degraded by this low mobility, so it is quite surprising to find such a decoupling of Seebeck coefficient and electrical conductivity trends. Behaviours of this kind often relate to the mechanism of band degeneracy (tendency of electronic bands to converge within an energy range of $\sim 2k_B T$), that can selectively promote the thermopower without penalizing carrier conduction.^{4,6–8,35,40} However, band convergence does not seem to play a significant role in this case, as

little difference is observed in the spacing of bands between the two structures (Figure 3.3.5a-3.3.5b), with the top three bands being separated by more than $2 k_B T$. We therefore put forward that the mid-gap states exert a strong influence in decoupling electrical conductivity and Seebeck coefficient. In fact, these states are seen to be highly localized in energy (as also confirmed by the calculated inverse participation ratio IPR, see Figure 3.3.5e), with steep features in the DOS close to the Fermi energy, enhancing thermopower (see Mott's equation). This leads to a high localization of charge carriers, a feature known for improving thermopower.⁵

The calculated power factor PF (Figure 3.3.6a) is unsurprisingly higher for the disordered cubic sample, of almost one order of magnitude at 480K. Combined with the added benefit of a highly suppressed thermal conductivity, this leads to a remarkable improvement in the figure of merit zT , more than twenty times larger at 480K for the disordered sample (Figure 3.3.6b). Although this value is moderate compared to materials used in highly-efficient TEs, it is, to the best of our knowledge, the highest reported zT for an undoped CZTS.

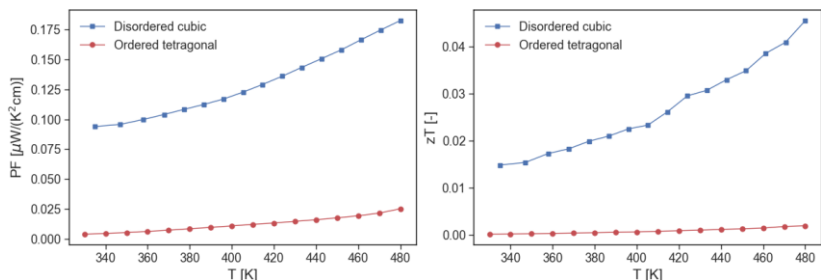


Figure 3.3.6. Power Factor PF (a) and thermoelectric figure of merit zT (b) as a function of temperature measured for a disordered cubic and an ordered tetragonal CZTS sample. A cumulative standard deviation of $\sim 3\%$ should be considered for PF , and ~ 12 for zT .

Nature of bonding and disorder in CZTS

The origin of this peculiar behaviour of disordered cubic CZTS, better performing in terms of both thermal and electronic properties, can ultimately be traced down to the nature of chemical bonding. To understand the charge distribution within the lattice, we calculate the electron localization function (ELF)⁴¹, a measure of the degree of charge localization in a given volume in space (ELF cross-sections, Figure 3.3.7, along with charge density (Figure 3.3.8, SN 8 and SV 2).

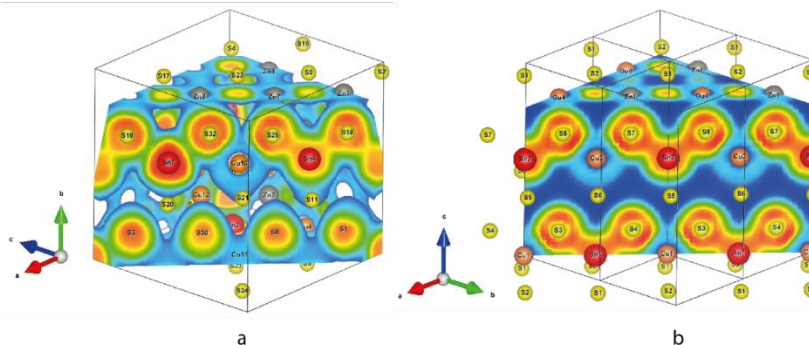


Figure 3.3.7. Electron Localization Function (ELF) for a disordered cubic (a) and an ordered tetragonal (b) kesterite supercell, where the latter, for visualization purposes, is composed of four copies of the cell used in calculations. Sections along a plane including some Sn-S bonds are shown, with colour indicating the likelihood to find an electron close to a reference electron at a given point in space. As visible, in the tetragonal cell (b) Sn atoms form all-similar bonds with sulphur atoms with a high level of electron sharing. In the cubic cell, some Sn atoms behave similarly as in the tetragonal structure (Sn4) while some others behave differently (Sn7) with a significantly higher retention of lone pairs. This is believed to be the cause of the ultra-low thermal conductivity measured for the cubic samples, through an enhancement of phonon scattering caused by the rattling of this type of Sn atoms.

These reveal that cation disorder in the cubic structure leads to different degrees of localization for the $5s^2$ lone pair, for different Sn atoms (see Sn7 and Sn4, Figure 3.3.7a). From the partial charge density of the Sn s electrons (Figure 3.3.8a and S3.3.8a), we observe that Sn in general forms tetrahedral sp^3 hybridized bonds with S in both the cubic and tetragonal polymorphs. This is in agreement with reports of the Sn-S bond being generally covalent in nature, with Sn in a +4 oxidation state⁴².

However, in the case of cubic CZTS, the highly disordered crystal structure gives rise to a correspondingly inhomogeneous crystal field. This in turn leads to a strong localization of the s^2 lone pair in some Sn atoms, as seen around atom Sn7 in Figure 3.3.8a. These lone pairs form a separate nonbonding orbital, with reduced contribution to the bonding sp^3 orbitals, resulting in electron-poor bonds between Sn7 and its coordinating S atoms. From the partial charge density distribution, we attribute to these Sn atoms an approximate oxidation state of +2, in line with theoretical predictions in recent literature⁴².

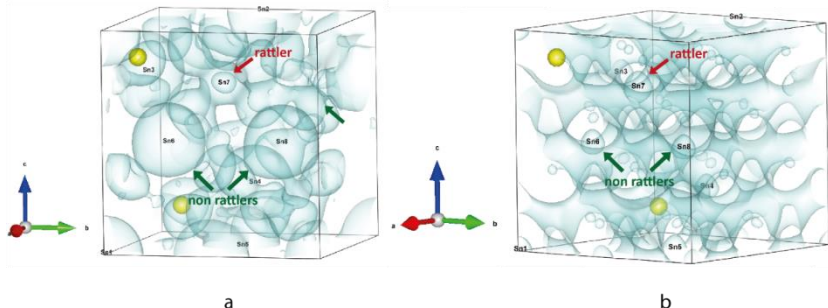


Figure 3.3.8. Partial charge density isosurfaces for a disordered cubic supercell. Picture (a) selectively shows the isosurface corresponding to Sn s electrons while picture (b) is representative of Cu d electrons. As visible, Sn s electrons of the rattling type ions (Sn7 in this case) tend to present a charge density distribution with a different shape, more slender and with a smaller radius, while the charge distribution of Cu d electrons surrounding the rattling Sn has a larger radius. This bonding inhomogeneity is shown to cause both a suppression of thermal conductivity, via promoting the rattling of these Sn atoms, and an improvement of carrier concentration, as the delocalization of Cu-d electrons can behave like a doping agent.

The presence of these atypical Sn atoms then naturally gives rise to inhomogeneity in bonding within the crystal structure. In the presence of thermal vibrations, the movement of atoms brings the lone pair in proximity to orbitals of electrons from neighbouring atoms. The induced overlap of these non-interacting electrons gives rise to a repulsive force⁴³, resulting in a rattling of the Sn7 type atoms within a cage formed by the coordinating S atoms. The rattling mechanism, consisting in the spring-like vibration of an atomic specie that contributes in dissipating phonon transport, has long been known to be responsible for reduced lattice thermal conductivity in binary and ternary compounds^{34,44} including chalcogenides^{45,46}. However, the type of rattling observed here would be different from the generally reported specie-wide rattling, as just a fraction of Sn ions shows this behaviour. By looking closely at the atom-projected VDOS (Figure 3.3.4c-3.3.4d), we observe that while Cu ions generally dominate the vibrational modes in the low-frequency/long-wavelength region, it is in fact Sn which dominates in the frequency range between 1 – 1.5 THz, the region of the low-lying optical modes in the phonon dispersion. Furthermore, by calculating the VDOS projected over individual Sn ions (Figure 3.3.9a), it is clear that the rattling Sn7 ion contributes the most to the formation of the long wavelength optical vibrations. To gain further insights into vibrational properties, Nuclear Inelastic Scattering (NIS) measurements were performed at low

temperature (43K) on a disordered cubic and an ordered tetragonal sample. Experiments were carried out at the Dynamics beamline P01 at PETRAIII (DESY, Hamburg) using a Mössbauer-active isotope, ^{119}Sn , and, therefore, are representative of the vibrational behaviour of Sn. This is a particularly favourable condition to validate our DFPT calculations, showing that Sn dominates the total VDOS below 1.5 THz (see Figure 3.3.4d), where the proposed rattling mechanism manifests.

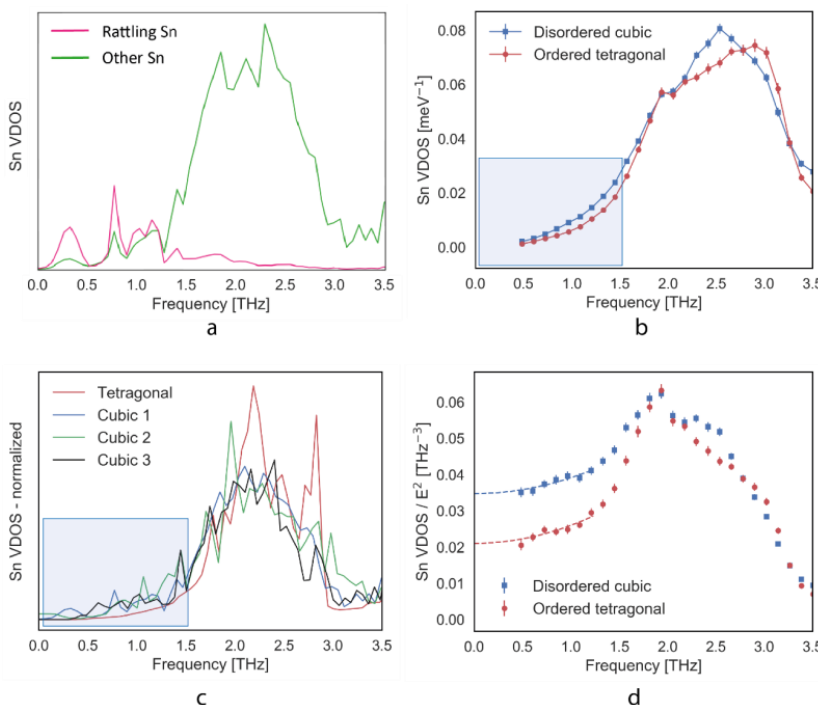


Figure 3.3.9. (a) Theoretical projected VDOS of two different types of Sn: a “rattling” one (Sn_7) and the others. (b) Experimental measurement of the ^{119}Sn projected vibrational density of states for a disordered cubic and an ordered tetragonal sample obtained with Nuclear Inelastic Scattering (NIS). (c) Theoretical Sn projected phonon density of states calculated for three different configurations of disordered cubic supercells and for the ordered tetragonal cell. Panel a corresponds to the curve labelled as Cubic 1. Values are normalized per atom. In the highlighted region it is possible to observe some peaks for the cubic cells corresponding to Sn atoms of the rattling type. Experimental results in (b) could be compatible with DFPT calculations and the rattling interpretation. (d) Reduced ^{119}Sn projected VDOS (divided by E^2) for two samples. The dashed lines show a parabolic fit in the range 0.5-1.23 THz to extrapolate the Debye level value at $E=0$, used to obtain the mean sound velocity (see SN for explanation).

The Sn projected VDOS in Figure S3.3.9b (and Figure 3.3.9b for reduced range) show characteristic features of cation disorder for the cubic sample, with a broadening of the vibrational modes, especially visible at high energy (~4.8 THz and ~11.1THz). NIS results also point out a higher MSD (see SN 9), in agreement with XRD, showing a higher Debye-Waller coefficient for cations in the cubic phase. An even more direct indication of disorder is the softening of the acoustic modes in the cubic sample, clearly seen in the reduced VDOS (VDOS/E²) (Figure 3.3.9d) as an enhancement of the low energy part. Disorder is typically connected with a lower sound velocity v and, indeed, the ratio of mean sound velocities (see SN 9) $v_{\text{cubic}}/v_{\text{tetragonal}} = 0.86$ is in the order of that obtained for the acoustic modes in the phonon dispersion relations (0.66, Figure 3.3.4a-b, see SN 9). But a lower sound velocity alone cannot explain the large suppression of thermal conductivity observed for the cubic sample. We put forward that the rattling Sn atoms are decisive in the reduction of thermal conductivity. Nevertheless, we expect a mild overall contribution from the weakly-bound Sn atoms in the experimental Sn VDOS curve. Figure 3.3.9c shows the theoretical Sn projected VDOS for three configurations of disordered cubic supercells, compared with that of the ordered tetragonal. The mild peaks below 1.5 THz in the cubic Sn VDOS curves are ascribed to rattling Sn ions, their positions varying somewhat for the different configurations (see Figure 3.3.9a and SN 11). Therefore, considering the rare occurrence of rattling atoms, estimated as 8-15 % of total Sn atoms, the overall contribution of rattling is limited to a small enhancement of the experimental Sn VDOS in the energy range between 0.5 and 1.5 THz (Figure 3.3.9b). These weakly-bound atoms also contribute to the enhancement of the reduced Sn VDOS for the cubic sample (Figure 3.3.9d). We thus assert that the introduction of disorder, which we connect with an increase of the rattling phenomenon, is responsible for the marked suppression of thermal conductivity observed in the cubic polymorph with respect to the stable tetragonal CZTS.

For what concerns the effect on electronic properties, the presence of the electron-deficient Sn-S bonds leads to a transfer in charge from Cu d states close to the Fermi surface (within 0.5 eV). These electrons move in to fill the charge deficiency, as shown in Figure 3.3.8b, where the partial charge density of one of the Cu d states is localized around the rattling Sn atom. This process generates free holes in a way analogous to p-type doping, as evidenced by the increased carrier concentration. The presence of the strongly localized s² electrons in

the rattling Sn atoms thus gives rise to the localized acceptor states above the Fermi energy, thereby explaining the observed improvement in electrical conductivity despite the lower mobility of charge carriers. Thus, by closely analysing the electronic structure of cubic CZTS we can ultimately attribute the considerable improvement in thermoelectric properties of this polymorph to the increased localization of Sn lone pairs, resulting from higher disorder and randomness compared to the tetragonal polymorph. This leads both to a suppression in thermal conduction, as well as to an enhancement of electrical conductivity without penalizing the Seebeck coefficient, which is actually increased by the strongly localized states in the DOS.

3.3.4 Conclusion

Disordered cubic is a recently discovered polymorph of kesterite, characterized by complete randomness in the occupation of the cation sites. In comparison to the generally reported ordered tetragonal phase, we demonstrate how the introduction of disorder leads to a significant change in Sn-S bonding. This leads to an optimization of all the thermoelectric properties, suppressing thermal conductivity with a concomitant enhancement of electrical conductivity and Seebeck coefficient, a rather uncommon occurrence in thermoelectricity.

The high density of defects in the cubic polymorph promotes the localization of lone pair electrons in some Sn atoms, which turn into rattlers. These ions suppress thermal conductivity, dissipating lattice energy via low-frequency optical phonon modes. At the same time, they cause a charge deficiency in some Sn-S bonds that turns out to improve the electronic properties. This Sn charge deficiency is compensated by Cu electrons which in turn generate holes. This gives rise to a p-type doping-like effect, improving electrical conductivity, and to highly-localized acceptor states, responsible for the enhancement in Seebeck coefficient.

The unveiled physical mechanism reveals that a single phenomenon connected with structural disorder can provide a concurrent optimization of electronic and thermal properties. Comparing cubic to tetragonal, this leads to a 3x reduced thermal conductivity together with a doubling in both electrical conductivity and Seebeck coefficient, resulting in a more than 20x increase in figure-of-merit.

This emergent paradigm has the potential to be extended to other materials for achieving an all-round improvement of TE performance.

Appendix

Supplemental Note 1: XRD measurements in temperature

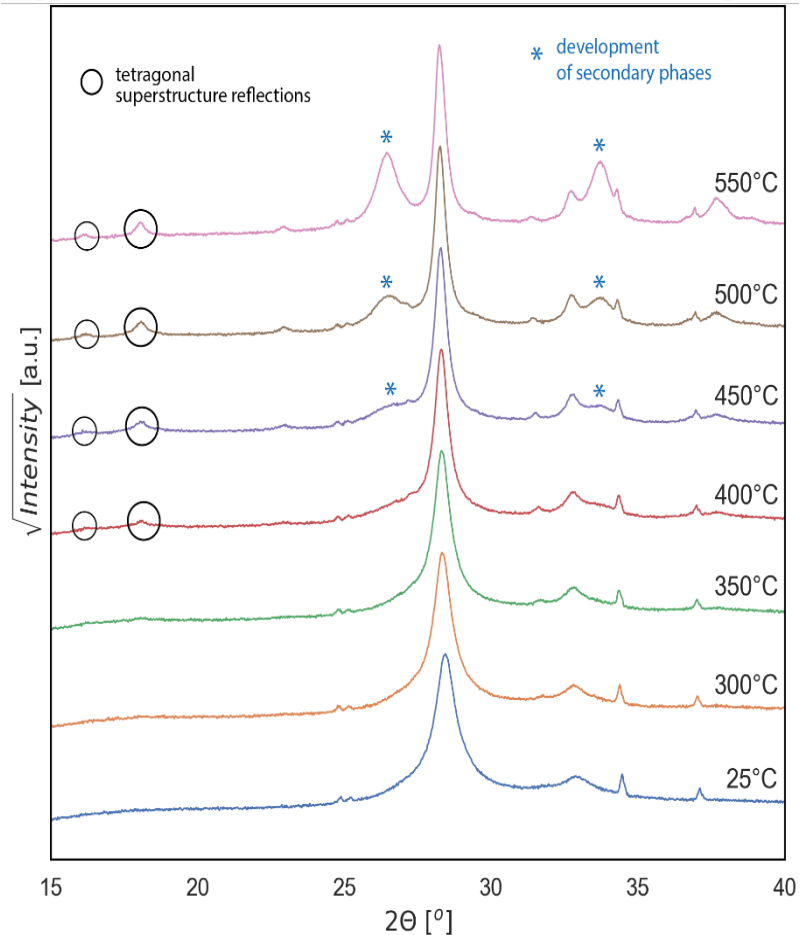


Figure. S3.3.1: XRD measurements in temperature performed on an as-milled and cold pressed sample. The CZTS phase, initially cubic, is seen to evolve into the tetragonal polymorph starting from 400°C.

Figure S3.3.1 shows XRD measurements performed in temperature on an as-milled, cold-pressed CZTS sample. Kesterite presents initially a cubic phase, which evolves into the tetragonal over temperature. Tetragonal superstructure peaks appear indeed to be visible starting

from 400°C, in accordance with the critical temperature observed in thermal analyses (Figure 3.3.1d). High temperature and long measurements times (more than 1h of dwell at each temperature) developed a quite-significant amount of secondary phases (SnO_2 reflections). These were not observed in thermal analysis (Figure 3.3.1d) where the sample was sealed under reducing atmosphere to prevent the occurrence of oxidation.

Supplemental Note 2: Energy Dispersive X-ray analysis (EDX) with TEM

| Disordered cubic | |
|---------------------|---|
| Spot | Stoichiometry |
| Large Area | $\text{Cu}_{2.41}\text{Zn}_{0.96}\text{Sn}_{0.96}\text{S}_{3.66}$ |
| Grain 1 | $\text{Cu}_{1.27}\text{Zn}_{1.87}\text{Sn}_{0.88}\text{S}_{3.98}$ |
| Grain 2 | $\text{Cu}_{1.28}\text{Zn}_{1.48}\text{Sn}_{0.99}\text{S}_{4.21}$ |
| Grain 3 | $\text{Cu}_{2.26}\text{Zn}_{0.94}\text{Sn}_{0.94}\text{S}_{3.86}$ |
| Grain 4 | $\text{Cu}_{2.23}\text{Zn}_{0.93}\text{Sn}_{0.93}\text{S}_{3.91}$ |
| Average | $\text{Cu}_{1.9}\text{Zn}_{1.2}\text{Sn}_{0.9}\text{S}_{3.9}$ |
| Ordered tetragonal | |
| Spot | Stoichiometry |
| Grain 1 | $\text{Cu}_{2.68}\text{Zn}_{1.25}\text{Sn}_{0.80}\text{S}_{3.26}$ |
| Grain 2 | $\text{Cu}_{2.01}\text{Zn}_{1.94}\text{Sn}_{0.80}\text{S}_{3.25}$ |
| Grain 3 | $\text{Cu}_{2.18}\text{Zn}_{1.15}\text{Sn}_{0.88}\text{S}_{3.79}$ |
| Grain 4 | $\text{Sn}_{0.71}\text{O}_{2.29}$ |
| Grain 5 | $\text{Sn}_{1.57}\text{O}_{1.43}$ |
| Average CZTS | $\text{Cu}_{2.3}\text{Zn}_{1.4}\text{Sn}_{0.8}\text{S}_{3.4}$ |

Table I: Results of EDX performed with TEM on some grains of a disordered cubic and an ordered tetragonal CZTS sample.

EDX elemental quantitative analysis, presented in Table I, was performed on some individual grains of a disordered cubic and an ordered tetragonal sample. The stoichiometry approaches that of CZTS ($\text{Cu}_2\text{ZnSnS}_4$) with some fluctuations of stoichiometry between the grains, especially regarding a lack of Sn and S, which can have partially migrated to the secondary phases. This effect is particularly visible for the tetragonal sample, where some grains are identified as Sn oxides (Grain 4 and 5) in accordance with XRD. These are noticed to present a comparatively smaller dimension (~10 nm) than CZTS and are located at the boundary of larger CZTS grains. Standard deviation in stoichiometry is estimated as one unit in the second decimal point.

Supplemental Note 3: Rietveld refinement of XRD data

Phase analysis from Rietveld refinements of XRD data (Figure 3.3.2) reveal that an almost pure CZTS phase is found both for the as-milled powder and the sample sintered at 300°C (Figures 3.3.2a and 3.3.2b), with minor contamination consisting of copper sulphide CuS and brass (estimated mass fractions <1.5%). The sample treated at 560°C and identified as tetragonal (Figure 3.3.2c) shows a slightly less-pure CZTS phase (main impurities are cassiterite SnO₂, weight fraction estimated as 12(1)%, and digenite Cu_{7.2}S₄, 6(1)%). In this sample, XRD peak sharpening and SAED ring spotting point out that grain growth has occurred during sintering. Indeed, from TEM images CZTS appears in nanometric domains of disperse dimension ranging from 10 nm to over 300 nm. A bigger and a smaller fraction of domain sizes were considered in the XRD refinement: for the smaller fraction (41% of total CZTS) the mean domain size is 21(3) nm while for the bigger fraction (59%) it is estimated as 186(15) nm. TEM imaging on the powder and sintered cubic samples (Figures 3.3.2a and 3.3.2b), consistently show smaller domain dimensions, ranging from below 10 nm to over 50 nm. Refinements estimate the mean crystallite sizes as 10(8) nm for the powder and 15(6) for the cubic sintered sample, reasonably in accordance with TEM observation, especially considering that XRD tends to underestimate crystallite sizes.

Supplemental Note 4: density, geometrical and Archimedes'

Kesterite theoretical density estimated from XRD is 4.58(1) g/cm³ for the cubic polymorph and 4.56(1) g/cm³ for the tetragonal. Considering the presence of secondary phases in the tetragonal sample, the overall theoretical density is estimated as 4.79(1) g/cm³. Density has been measured both with Archimedes' method and geometrically. Results using Archimedes' method are 4.1(2) g/cm³ for the cubic sample and 4.5(2) g/cm³ for the tetragonal, respectively 90% and 94% of the theoretical density. The geometrical density has been measured on accurately shaped disk samples as 2.96(9) g/cm³ for the cubic sample and 3.09(9) for the tetragonal, around 65% of the theoretical density for both the samples. From the difference in results between the two methods we can deduce that a large part of the porosity in the sample is open.

Given the fact that for the thermal diffusivity measurement the full sample thickness has been used, the geometrical result is used to calculate thermal conductivity. The geometrical values of density are relatively low, and this might have affected in some amount the

absolute values of transport properties. However, for the sake of the comparison presented in the context of this article this is not of concern, as the comparable densities allow a consistent comparison of properties between the cubic and tetragonal samples. No difference in density has been detected before and after the thermoelectric characterization.

Supplemental Note 5: thermal diffusivity and C_p , further thermal measurements

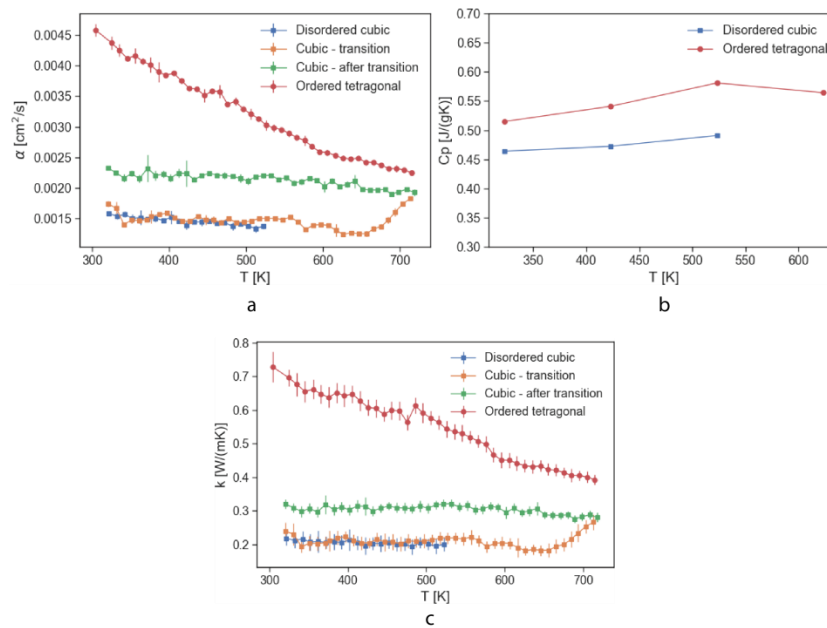


Figure. S3.3.2. Thermal diffusivity α (a), specific heat C_p (b) and thermal conductivity k (c) measured for a cubic and a tetragonal sample. In (a) and (c) the measurements of a cubic sample above the cubic-to-tetragonal transition temperature is performed (orange curve), as well as a second measurement on the same sample (green curve).

Figures S3.3.2a and b show the thermal diffusivity and specific heat data used to calculate thermal conductivity. The green curve in Figures S3.3.2a is a measurement performed on the “cubic” sample after the run until 720 K (after the orange curve), above the cubic-to-tetragonal transition of kesterite. The obtained values remain higher than for the purely cubic sample, as expected, but intermediate with respect to the tetragonal sample. This indicates just a partial ordering towards the tetragonal structure, justified by the relatively short exposure to temperatures just above the critical.

Supplemental Note 6: Absorption Spectroscopy

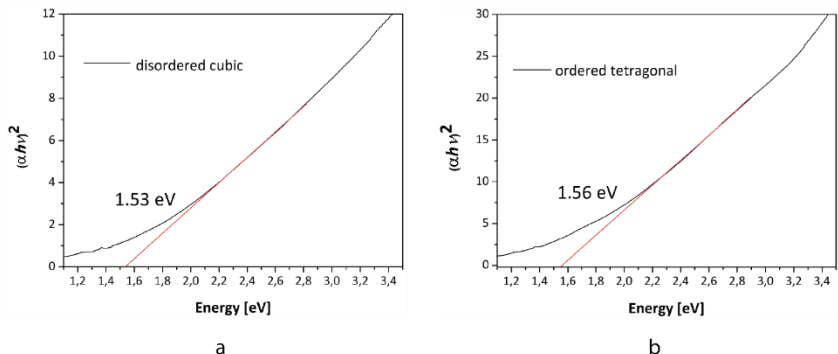


Figure. S3.3.3: Tauc plot obtained from ultraviolet-visible spectroscopy for a disordered cubic (a) and an ordered tetragonal (b) kesterite sample. The value was extrapolated with a linear fit in the range 2.2-2.8 eV.

Supplemental Note 7: ELF isosurfaces (other views and 3D animation)

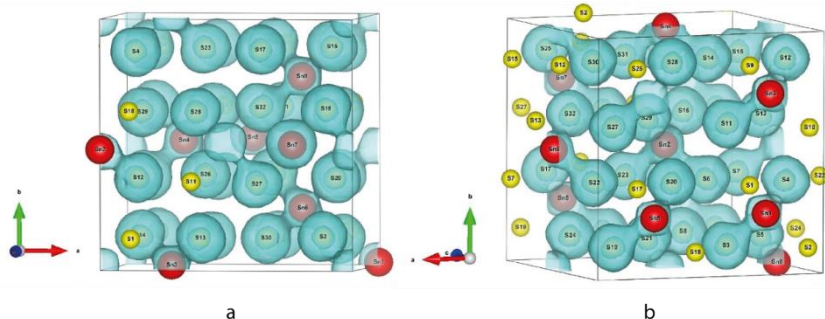


Figure. S3.3.4. ELF isosurfaces for a disordered cubic (a) and an ordered tetragonal (b) kesterite supercell.

For the ordered tetragonal supercell, the shape of the ELF isosurfaces (surfaces at equal values of ELF) appears connected between the atoms (Figure S3.3.4b) with a higher electron localization in the interatomic regions. In the case of the disordered cubic polymorph, instead, some Sn atoms appear to behave in a similar way as for the ordered (see for example Sn6 and Sn8 of Figure S3.3.4a), some other, conversely, (this is the case of Sn7), display an independent bubble-like isosurface and high electron localization in the proximity of the atom. This is associated with the reduced contribution in the bonding of the lone pair and results in the rattling behaviour.

Figures S3.3.5, S3.3.6 and S3.3.7 report the ELF cross-sections of all the Sn atoms for the three different configurations of disordered cubic supercell. As visible, the Sn atoms that display a full rattling behaviour (high localization close to Sn and lower electron-localization in the inter-atomic region with S) vary from 1 to 3 per configuration. Some others seem instead to have an intermediate behaviour. From these observations we put forward that in a sample of disordered cubic CZTS the occurrence of rattling Sn atoms could fall around the 8-15 % of total Sn.

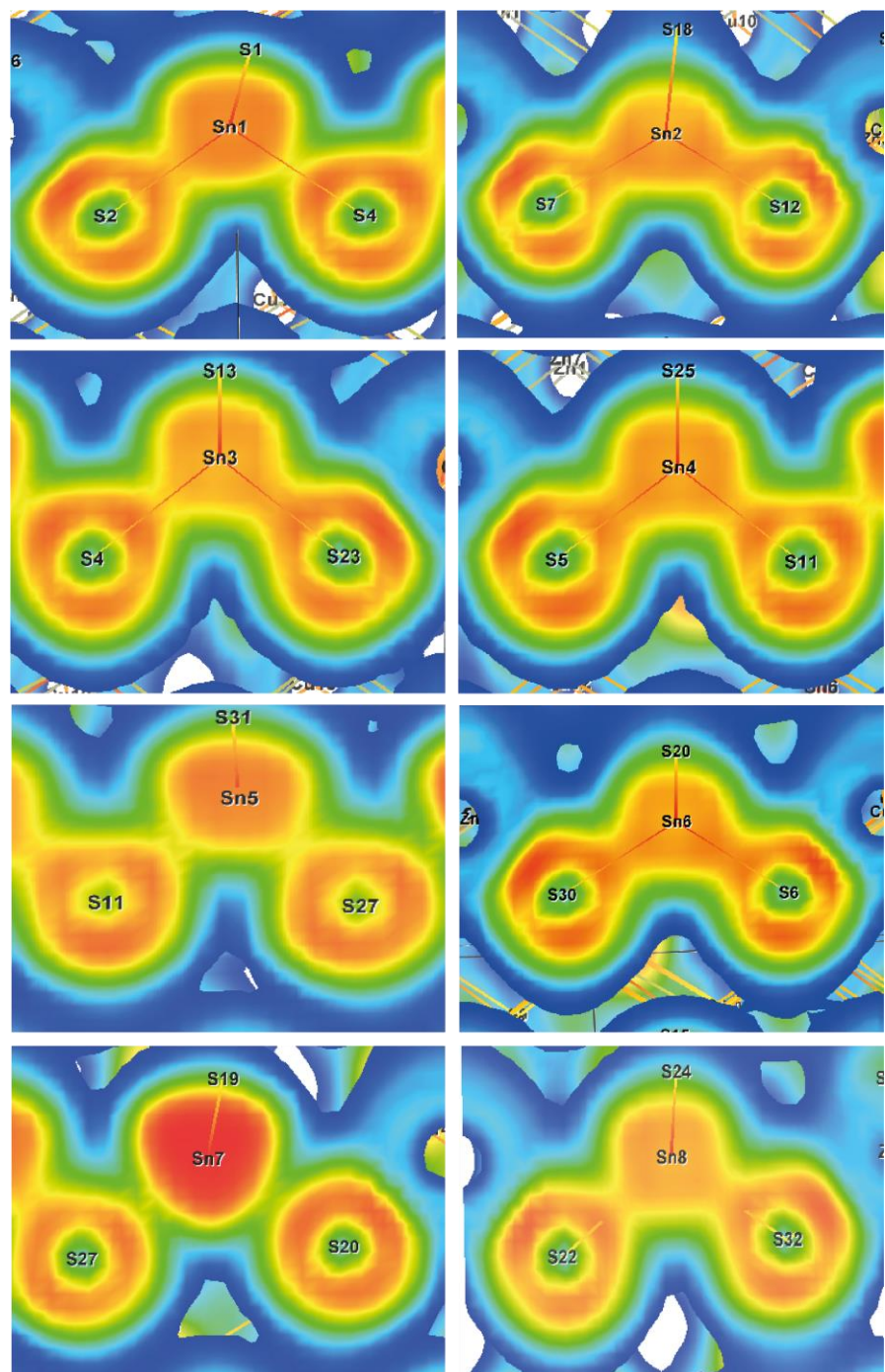


Figure. S3.3.5. ELF cross-sections of all the Sn atoms for the configuration of disordered cubic CZTS that is mainly described in the main text in the main text, labelled as Cubic 1.

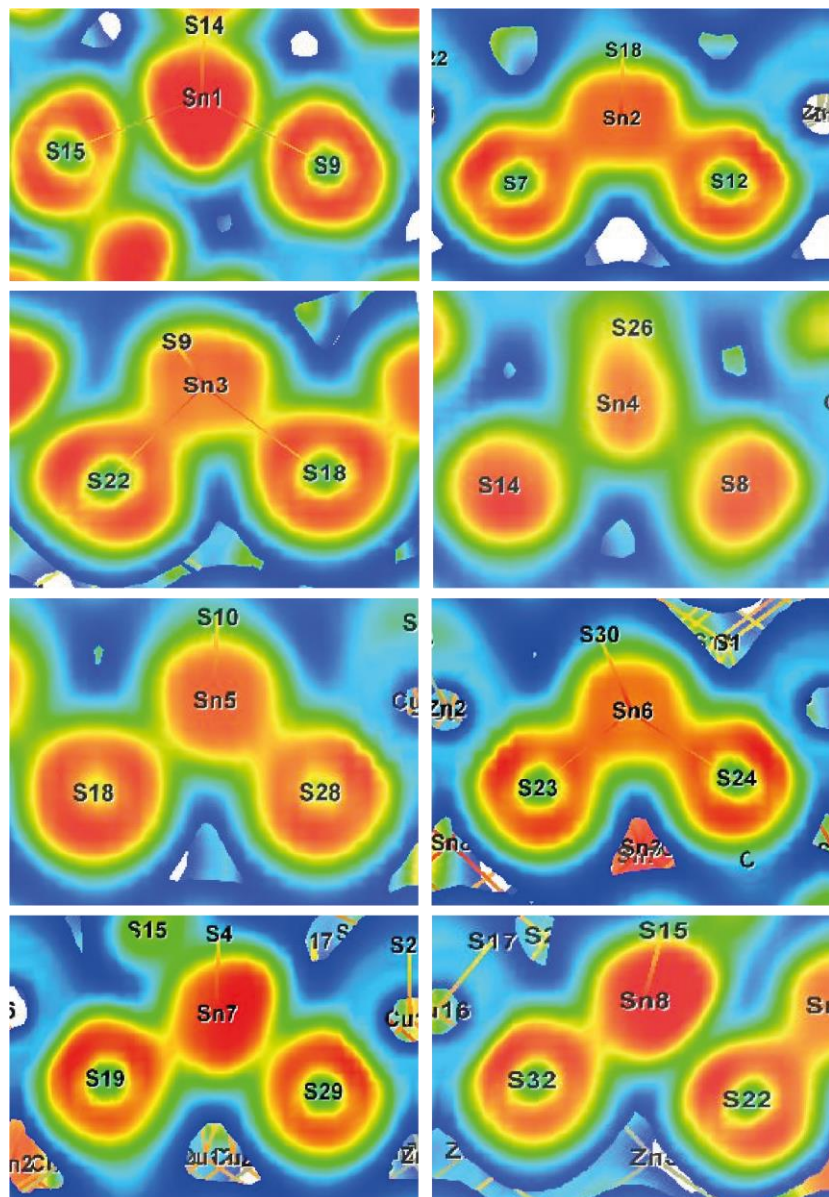


Figure. S3.3.6. ELF cross-sections of all the Sn atoms for the configuration of disordered cubic CZTS that in the main text is labelled as Cubic 2.

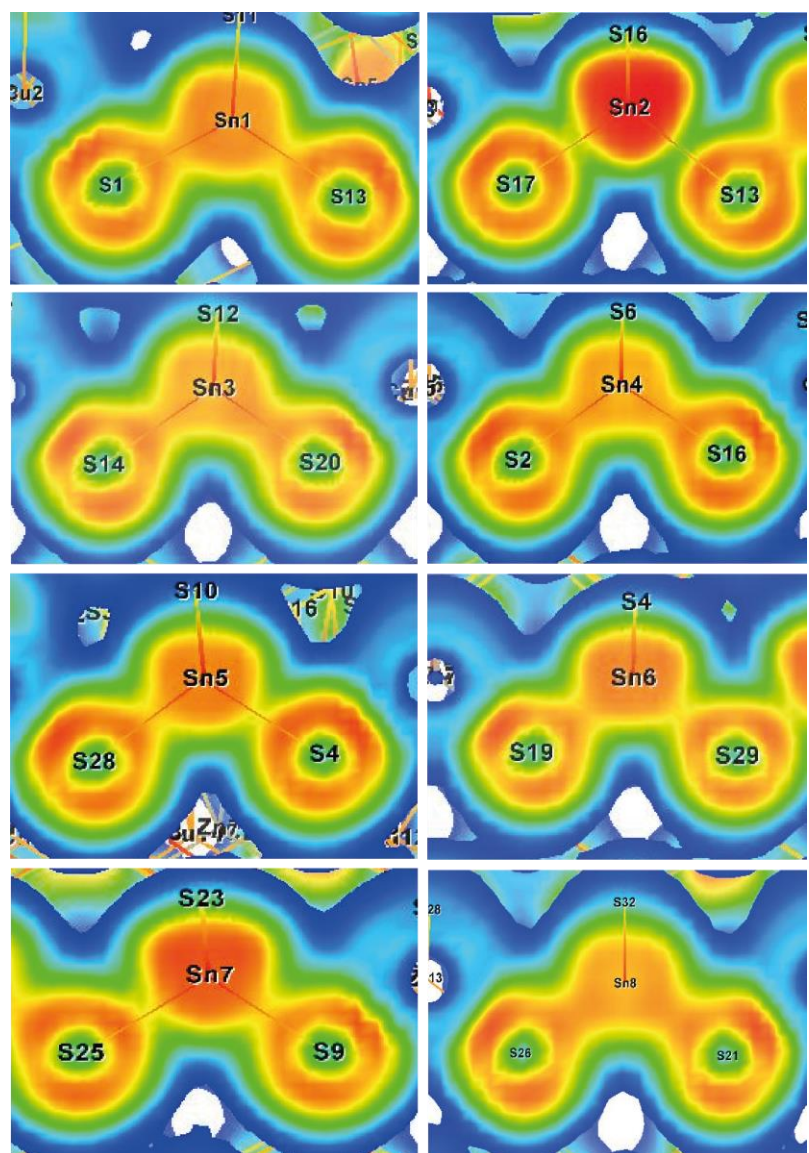


Figure. S3.3.7. ELF cross-sections of all the Sn atoms for the configuration of disordered cubic CZTS that in the main text is labelled as Cubic 3.

Supplemental Note 8: partial charge density isosurfaces (3D animation and ordered tetragonal supercell)

A 3D animation of the Sn s partial charge density isosurfaces for the disordered cubic supercell can be viewed in SV 2, where a higher density of Sn s electrons close to the core can be seen for the rattling type ion.

For comparison, Figure S3.3.8 shows the Sn s (a) and Cu d (b) partial charge density isosurfaces for the ordered tetragonal supercell. As expected, the behaviour of Sn ions in the ordered tetragonal cell is that of non-rattling atoms in the disordered cubic polymorph.

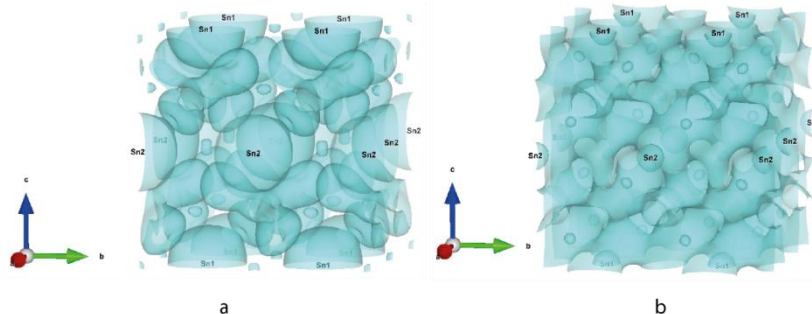


Figure. S3.3.8. Partial charge density isosurfaces for an ordered tetragonal supercell.

Picture (a) selectively shows the isosurface corresponding to Sn s electrons while picture (b) is representative of Cu d electrons. As visible, unlike in the cubic supercell (Figure 3.3.8), no rattling atoms are observed.

Supplemental Note 9: Nuclear Inelastic Scattering measurements and Sn projected VDOS

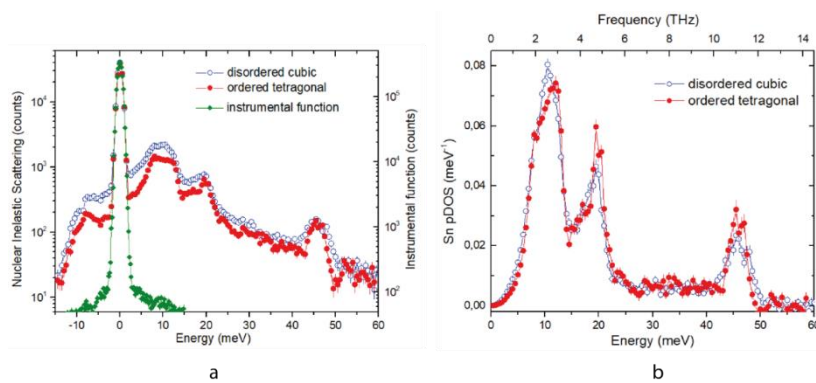


Figure. S3.3.9. (a) ^{119}Sn NIS spectra of the samples measured at 43K. The green diamonds represent the instrumental function. (b) ^{119}Sn projected densities of vibrational states.

NIS spectra are shown in Figure S3.3.10a together with the instrumental function. The Sn projected densities of vibrational states (Sn VDOS), shown in Figure S3.3.9b, were evaluated from NIS spectra using a procedure described elsewhere [48]. The subtraction of the elastic peak affects the NIS spectra in the range [-2:2] meV. The data in this range were interpolated with the Debye approximation. The good quality of the Sn VDOS extraction is confirmed by the deviation of the Sn VDOS area from unity, which is less than 0.1%.

The values of Lamb-Mössbauer factors f_{LM} , atomic displacement parameters U_{eq} and mean force constants F , obtained from the Sn VDOS curves, are presented in Table II, together with Debye energies and mean sound velocities. The Debye energies, E_D , were obtained from the reduced VDOS, $g(E)/E^2$, by fitting the range 2.5-5 meV with a parabolic function, $3/E_D^3 + b \cdot E^2$. The mean sound velocity was calculated as $\langle v \rangle = E_D \cdot \rho^{-1/3} \cdot 0.227$ [km/s], where ρ is the bulk density of the sample.

As discussed in the main text, the ratio of sound velocities from the Debye energy is $v_{cubic}/v_{tetragonal} = 0.86$ and is comparable with that obtained theoretically from the phonon dispersion relations, 0.66. This has been calculated from the group velocity of the three acoustic modes, obtained from the slopes of the phonon dispersion relations (Figure 3.3.4a-b), with the equation $\frac{1}{v_m^3} = \frac{1}{v_L^3} + \frac{2}{v_T^3}$ ⁴⁸, where v_m is the mean sound velocity, v_L is the longitudinal component and v_T the transversal one. While the experimental results exclusively refer to the vibrational properties of Sn ions, the theoretically calculated vibrational modes have contributions from all ions, albeit strongly dominated by Sn within the relevant frequency range (< 1.5 THz).

| Sample | f_{LM} | U_{eq} (Å ²) | F (N/m) | E_D (meV) | v (km/s) |
|--------------------|----------|----------------------------|-----------|-------------|------------|
| Disordered cubic | 0.763(2) | 0.00185(2) | 236(5) | 18.3(3) | 2.50(4) |
| Ordered tetragonal | 0.791(2) | 0.00160(2) | 238(4) | 21.6(4) | 2.91(5) |

Table II. Parameters obtained from the Sn VDOS of the samples measured at 43 K: the Lamb-Mössbauer factor f_{LM} , the Sn atomic displacement parameter U_{eq} , the mean force constant F , the Debye energy E_D , and the mean sound velocity v .

Supplemental Note 10: repeatability of thermoelectric measurements

For what concerns electronic properties, some sample evolution is noticed in the first few cycles of measurement. Typically, after three cycles values become repeatable. Electrical conductivity and Seebeck coefficient curves reported in the text are the repeatable ones. Thermal conductivity measurements show a good reproducibility from the first cycle, as can be seen in the two repeated cycles of Figure 3.3.3a (blue and orange curve). Measurements have been repeated on multiple samples and the obtained results are comparable.

Supplemental Note 11: DFT/DFPT results for other configurations of disordered cubic supercells

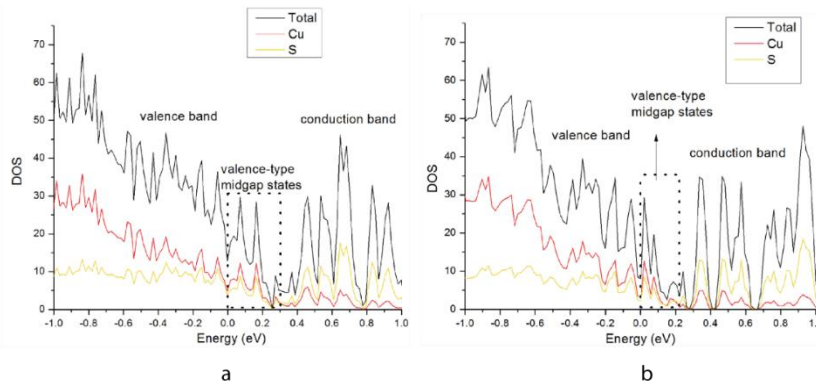


Figure. S3.3.10. Electronic density of states DOS for two additional configurations of disordered cubic supercell, with partial density of states showing the individual contributions of Cu and S atoms. These configurations are labelled in the main text as Cubic 2 (a) and Cubic 3 (b).

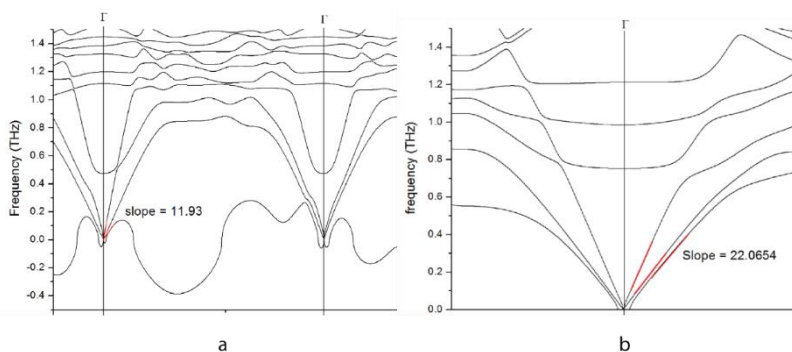


Figure S3.3.11. Phonon dispersion relations for two additional configurations of disordered cubic supercell. These configurations are labelled in the main text as Cubic 2 (a) and Cubic 3 (b). The dynamical instability in (a) is the result of semi-rattling Sn ions (Sn7, Sn8), alongside the fully-rattling ion (Sn1), all visible in the ELF for the corresponding configuration (Figure S3.3.7).

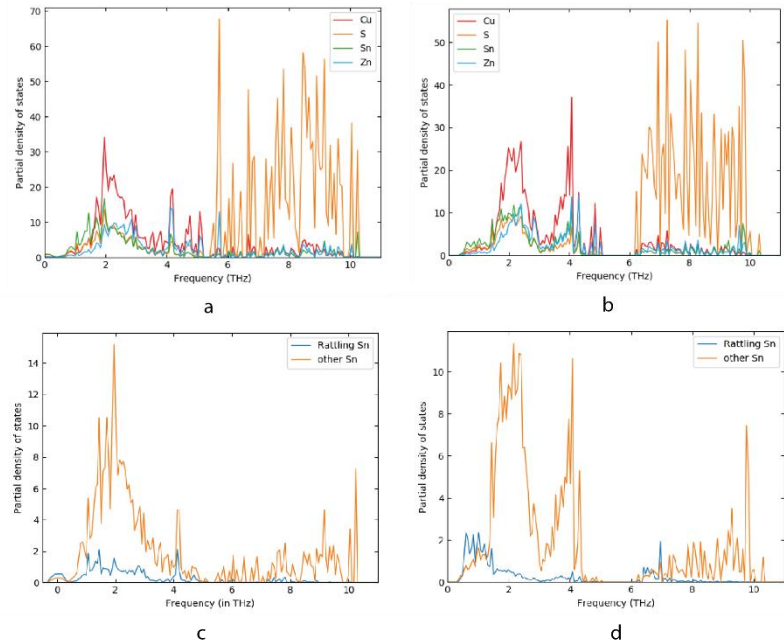


Figure. S3.3.12. Vibrational density of states with contributions from individual atoms for two additional configurations of disordered cubic supercell. These configurations are labelled in the main text as Cubic 2 (a) and Cubic 3 (b). Sn projected VDOS of two different types of Sn, a rattling one and the others, for configuration Cubic 2 (c) and Cubic 3 (d).

Acknowledgements

The authors would like to acknowledge Prof. R. Di Maggio of the University of Trento, Dr. L. Weinhardt and Dr. D. Hauschild of the Karlsruhe Institute of Technology, for helpful discussion and suggestions, as well as the help of Dr. G. Ischia of University of Trento. The computational time was provided by CINECA - Italian Supercomputing Facility, with the Project CZTS - HP10CONX70 and the Modelling and Simulation Project of University of Trento. This

research was funded by the Autonomous Province of Trento, within the framework of the programmatic Energy Action 2015–2017. N.M.P. is supported by the European Commission under the FET Open (Boheme) grant No. 863179.

Author contributions

E.I. contributed with sample preparation, structural and thermoelectric characterization, data interpretation and discussion, main draft preparation. B.M. contributed with DFT and DFPT calculations, data interpretation and discussion, main draft preparation. C.F. contributed with Hall and Van der Pauw measurements, data interpretation and discussion, reviewing and editing of the draft. N.A. contributed with absorption spectroscopy measurements. I. S., S.S. and R.E. contributed with Nuclear Inelastic Scattering measurements and interpretation, reviewing of the draft. N.M.P. contributed with funding acquisition and reviewing of the draft. P.S. contributed with conceptualization of the work, funding acquisition, structural characterization, data interpretation and discussion, reviewing and editing of the draft and supervision of the work.

4 Disorder induced topological Anderson insulator in Cu₂ZnSnS₄

This section is taken from: Mukherjee, B., Isotta, E., Fanciulli, C., Ataollahi, N. and Scardi, P., 2021. Topological Anderson Insulator in Cation-Disordered Cu₂ZnSnS₄. *Nanomaterials*, 11(10), p.2595.

DOI: <https://doi.org/10.3390/nano11102595>

Abstract

We present the first candidate for the realization of a disorder-induced Topological Anderson Insulator in a real material system. High-energy reactive mechanical alloying produces a polymorph of Cu₂ZnSnS₄ with high cation disorder. Density functional theory calculations show an inverted ordering of bands at the Brillouin zone center for this polymorph, which is in contrast to its ordered phase. Adiabatic continuity arguments establish that this disordered Cu₂ZnSnS₄ can be connected to the closely related Cu₂ZnSnSe₄, which was previously predicted to be a 3D topological insulator, while band structure calculations with a slab geometry reveal the presence of robust surface states. This evidence makes a strong case in favor of a novel topological phase. As such, the study opens up a window to understanding and potentially exploiting topological behavior in a rich class of easily-synthesized multinary, disordered compounds.

4.1 Introduction

Topologically non-trivial materials present a novel and exciting field of research in condensed matter¹. They are valued both for their importance to fundamental science as exotic states of quantum matter as well as their inherent potential for application in new and future technologies including thermoelectrics^{2–4}, spintronics^{5–7}, and quantum computation^{5,6,8}. Starting with the discovery of the Quantum Hall Effect (QHE) by von Klitzing et al.⁹, this class of materials has grown to include many candidates in 2-, 3-, and higher dimensional systems, a growing (albeit still small) fraction of which have been experimentally realized. Three-dimensional (3D) topological insulators (TIs) present a sub-class of these exotic materials. They may generally be described as hosting insulating bands in the bulk

with band inversion at high-symmetry points, coupled with symmetry-protected gapless surface states¹⁰. In the absence of symmetry breaking, these surface states support high-mobility electron transport along specific directions on the surface, without backscattering. Large spin-orbit coupling (SOC) was originally understood to be driving the topologically non-trivial behavior^{11–15}. Subsequently, Fu¹⁶ demonstrated that topological surface states can also be protected by crystalline symmetries in the absence of SOC (topological crystalline insulators). This allows for topologically non-trivial materials with a weak SOC¹⁷.

The possibility of TIs in the quaternary chalcogenide class has been investigated by Chen et al.¹⁸, using density functional theory (DFT) band structures. They showed that HgTe, a 3D semimetal with the zinc-blende structure, may be transformed into a TI by introducing a strong crystal field splitting (Δ_{CF}). This can be achieved either by epitaxial straining or by substituting two group-II Hg ions with one group-I ion and one group-III ion. The latter approach results in ordered I-III-VI₂ chalcopyrites. Subsequently, by replacing two group-III cations with one group-I and one group-II cation, the I₂-II-IV-VI₄ chalcogenides are obtained. The non-trivial band gap of these materials could be increased further via a simultaneous increase in Δ_{CF} and the band-inversion strength (BIS). In a contemporaneous study, Wang et al.¹⁹ performed a DFT-based screening of several ternary famatinite and quaternary chalcogenides for TIs and were able to identify several naturally occurring, Cu-based 3D TIs. Unsurprisingly given its weak SOC, Cu₂ZnSnS₄ (CZTS) was found to be topologically trivial, although the authors showed that it could be ‘transformed’ into a TI by changing the atomic number of the cations, which was manifested as a doping effect evolving toward the ternary TI Cu₃SbS₄.

Topological insulators, including the multinary compounds mentioned above, are generally known to host a bulk band gap coupled to gapless surface states, which are robust to weak levels of disorder. Several recent studies have highlighted how TI behavior can exist in aperiodic systems such as quasicrystals²⁰ and can persist in systems with bulk defects such as grain boundaries and vacancies below a certain threshold^{21,22}. Nevertheless, sufficiently strong disorder is expected to close the bulk gap and destroy all topological features^{10,22}. In light of this, a surprising prediction was made by Li et al.²³, who claimed that adding disorder to otherwise trivial systems can lead to the emergence

of topological behavior. The authors showed that disorder-induced Anderson localization may lead to a renormalization of the topological mass of the charge carriers via the band structure, causing a transition from a topologically trivial phase to a TI. This gives rise to the so-called Topological Anderson Insulator (TAI) phase. TAIs have been theoretically shown to be feasible by introducing disorder into trivial 3D systems close to a topological phase^{24,25}. TAI behavior was first demonstrated by Meier et al.²⁶ using quantum simulations in a metamaterial consisting of a 1D chain of ultracold rubidium atoms. Subsequently, in a recent article by Nakajima et al.²⁷, using a Thouless pump realized with ultracold ytterbium atoms on a dynamical optical lattice, the authors demonstrate a disorder-induced pumping, with a topologically trivial phase in the clean limit driven to a non-trivial phase due to quasi-periodic disorder. However, to date, evidence of TAI phases in a real material remains conspicuously absent.

Crucially, the quaternary chalcogenides screened in the aforementioned studies including CZTS are all ordered tetragonal structures. However, it is known that CZTS crystallizes in multiple polymorphs. In a recent study, Isotta et al.²⁸ demonstrated remarkably improved thermoelectric properties in a cubic polymorph of CZTS with complete cation disorder. This polymorph, which was synthesized using high-energy reactive mechanical alloying (ball-milling), shows a simultaneous improvement in both Seebeck coefficient and electrical conductivity, as well as a lower thermal conductivity compared to the ordered tetragonal polymorph. Using the DFT band structure calculations, we argue that introducing full cation disorder in CZTS drives it into a TAI phase; experimental measurements of electrical resistivity and carrier mobility are in agreement with a surface contribution to transport, which such a phase is expected to host. As such, we present the first concrete prediction of a TAI in a material, opening up myriad possibilities to investigate topologically non-trivial behavior in disordered quaternary compounds and their potential effect on thermoelectric performance.

4.2 Computational Methodology

The ab initio electronic structure calculations have been performed using the plane wave basis set implemented in the Vienna ab initio simulation package (VASP), version 5.4.4, Vasp Software GmbH^{29,30}. The electron-exchange correlation functional was approximated using the Perdew–Burke–Ernzerhof (PBE)³¹ form of the generalized

gradient approximation (GGA). It should be noted that the GGA tends to underestimate the band gap for most compounds, which may be corrected using computationally expensive hybrid functionals³². However, a hybrid Hartree-Fock/DFT study³³ has established that the band topology for both computational schemes (hybrid and PBE) are very similar for CZTS. The hybrid functional only shifts the conduction bands to a higher energy, justifying our use of the standard, computationally inexpensive PBE functional. In order to preclude a spurious negative band gap, we have also performed a single-point calculation with the HSE06 functional, with a 25% contribution from the exact Fock exchange energy. All calculations were performed with an energy cutoff of 450 eV and Gaussian charge smearing in the order of 0.01 eV. Calculations for CZTS were performed both with and without spin-orbit coupling, while calculations for CZTSe were made only with SOC. The geometry was optimized with a $2 \times 2 \times 2$ Monkhorst Pack (MP) Γ -centered k-mesh for 64 atom supercells until Hellman–Feynman forces on each atom were converged to below 0.01 eV/Å. SCF calculations were made with a similar $4 \times 4 \times 4$ k-mesh, with electronic degrees of freedom relaxed until the change in the total free energy and energy eigenvalues were both smaller than 10^{-6} eV. Calculations for surface states were performed within a surface slab geometry, with a 10 Å vacuum layer in the Z-direction to minimize the interaction between periodic copies. Only the top three layers of the slab were allowed to relax, with lower layers held fixed. Geometry optimization for the surface slab was made with a $2 \times 2 \times 1$ MP k-mesh, while SCF calculations used a $4 \times 4 \times 2$ mesh. For band structure calculations, the high-symmetry path in the Brillouin zone was obtained using SeekPath³⁴. VESTA³⁵ was used for visualizing atomic geometries. The disordered geometries are constructed by generating a pseudorandom number between 1 and 32 and assigning each cation to the corresponding serially numbered cation site.

4.3 Results and Discussion

Band Inversion in the Bulk

CZTS is a quaternary chalcogenide compound extensively investigated for its potential applications, primarily in photovoltaics^{36–41}, and recently thermoelectrics^{28,42–47}. The most ubiquitous polymorph of CZTS is the kesterite structure (Figure 4.1a), which crystallizes in the tetragonal *I*-4 space group. The structure may be

described as alternating layers of cations and sulfurs, with a further alternation in the cation layers, which are either composed of Cu and Zn or Cu and Sn. Above 533 K, this *I*-4 structure undergoes the so-called order-disorder transition⁴⁸ into a tetragonal *I*-42*m* phase. In this structure, the disorder is manifested through an in-plane randomization of the cations in the Cu-Zn layer (Figure 4.1b). This disorder induces a narrowing of the band gap compared to the ordered tetragonal polymorph (Figure 4.1d, e), while the increase in global symmetry introduces a three-fold degeneracy at the center of the irreducible Brillouin zone (Γ -point) in the valence band maximum (Figure 4.1e). In a recent article, Isotta et al.²⁸ have presented the synthesis of a novel polymorph of CZTS, this time with full cation disorder. This is manifested as a complete randomization of atoms in the cation position (Figure 4.1c). This polymorph was found to crystallize in the cubic zinc-blende/sphalerite structure with space group *F*-43*m* and remain stable up to 673K when it transitions to the tetragonal polymorph. Electronic structure calculations revealed the presence of significant inhomogenous bonding.

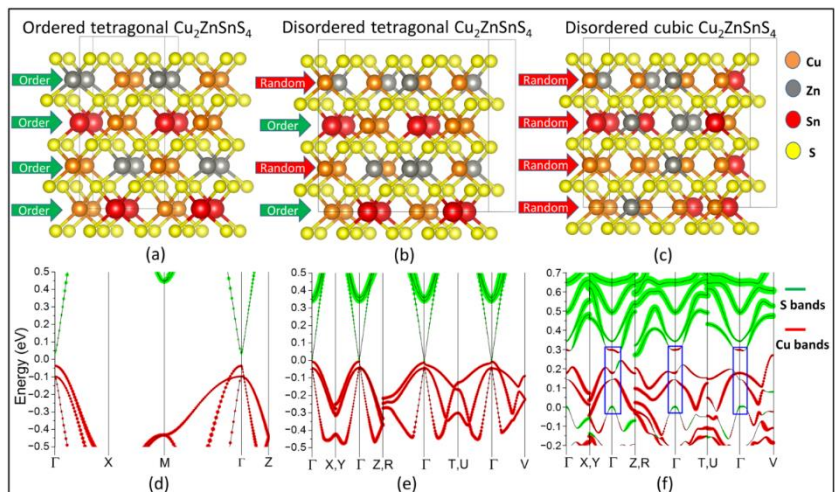


Figure 4.1. Crystal geometries and orbital-projected bands for the different polymorphs of CZTS: (a) the geometry of ordered tetragonal CZTS; (b) a supercell of disordered tetragonal CZTS; (c) a supercell of disordered cubic CZTS; Orange balls refer to copper ions, red balls refer to tin, gray balls refer to zinc, and yellow balls refer to sulfur; green arrows identify the ordered layers, while red arrows show the layers with cation randomization; (d) the bands for ordered tetragonal CZTS; (e) the bands for disordered tetragonal CZTS; and (f) the bands for cubic CZTS; green circles correspond to the dominant contribution from sulfur-p orbitals, while red circles correspond to the contribution from copper-d orbitals; the blue box highlights the region of band inversion in cubic CZTS.

This removes the three-fold degeneracy present in the bands (Figure 4.1f) of the disordered tetragonal polymorph, via strong crystal field splitting, while opening up the band gap somewhat (see Supplementary Note 1). A common feature of all three polymorphs of CZTS is that the states in the valence band maximum (VBM) are dominated by the Cu-d electrons, while those in the conduction band minimum (CBM) are mainly derived from S-p orbitals (Figure 4.1d–f). However, upon closer inspection of the projected bands for cubic CZTS, we observe that the order of the bands is reversed at and around the Γ -point, with an inversion in the Cu-d and S-p orbitals (Figure 4.1f) (see Supplementary note 1, Figure 4.S1 for discussion on band gap). True disorder in ionic positions is of course rather difficult to simulate within the size constraints of a DFT supercell with periodic boundary conditions, which impose a long-range order on the system. In order to ensure that the band inversion is not an accidental artifact but rather a property of the system, we have calculated the band structure for a further nine different configurations of cubic CZTS (Supplementary Figure 4.S2), with Cu, Zn, and Sn ions randomly assigned to each cation position, while maintaining the $\text{Cu}_2\text{ZnSnS}_4$ stoichiometry (see Table S4.1 in the Supplementary Information File) for energies of each configuration. The lowest energy configuration is shown in Figure 4.1c, f. Additionally, in order to discard the possibility that an underestimation of the band gap by the PBE functional leads to a spurious band inversion, a single-point calculation was performed using the computationally expensive HSE06 hybrid functional. This confirms a negative band gap in the order of -0.12 eV.

The features of the bands are necessarily somewhat different from each other. This is because each configuration of disorder generates a different kind of inhomogeneity in the charge distribution, leading to different levels of crystal field splitting. Crucially, however, band inversion is present in every case, which is coupled in most cases with an anti-crossing (camel's back) feature at VBM and CBM. In fact, the band-inversion strength, as defined by the energy difference between the lowest inverted S-p level in the valence band and the highest Cu-d level, is found to be reasonably positively correlated with Δ_{CF} , with a Pearson's r value of 0.84 (Figure 4.2a). While SOC is known to play a driving role in most topologically non-trivial systems, previous studies⁴⁹ have shown that it is negligible for tetragonal CZTS. We confirm that this remains the case in the cubic polymorph. Including SOC in the calculation does not significantly alter the nature of the

bands (Supplementary Figure 4.S3b) at the valence and conduction band extrema compared to the bands obtained without SOC (Supplementary Figure 4.S3a). Band inversion remains intact in both cases, suggesting that SOC might not be the main feature driving the system into a TI phase.

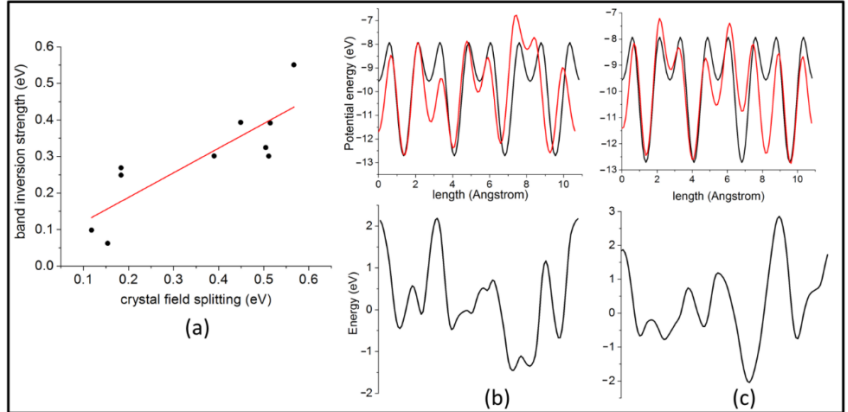


Figure 4.2. (a) Correlation between band inversion strength and crystal field splitting; (b) the local potential in ordered tetragonal (black line) and cubic (red line) CZTS along the x-direction (above) and the difference between the two (below); (c) the local potential in ordered tetragonal (black line) and cubic (red line) CZTS along the y-direction (above) and the difference between the two (below).

Instead, we assert that it is the large Δ_{CF} that causes the inversion and opens up a non-trivial band gap. This is in line with the arguments proposed by Chen et al.¹⁸ in the case of strained HgTe and tetragonal ternary chalcopyrites and quaternary chalcogenides. Here, the Δ_{CF} is a result of inhomogeneous bonding, arising from the full cation disorder in cubic CZTS. In light of this disorder-induced topological transition, we propose cubic CZTS as a candidate Topological Anderson Insulator.

It is well known⁵⁰ that an inverted band structure corresponds to a negative (topological) effective fermion mass, m . In the TAI phase, Groth et al.²⁴ have demonstrated that this inversion is obtained as a result of elastic scattering from a disorder potential, which leads to states with a definite momentum decaying exponentially as a function of space and time. When the effective Hamiltonian of the disordered system acts on the exponentially decaying state, it adds a negative correction δm to the effective mass. This renormalized topological mass $m' = m + \delta m$ can have a sign that is opposite that of the bare mass m , corresponding to a band inversion. The low energy

Hamiltonian H of a general 3D topological Anderson insulator was written by Guo et al.²⁵ as,

$$H = H_0 + \sum_j U_j \Psi_j^\dagger \Psi_j$$

where H_0 is the Hamiltonian of the ordered (trivial) system, Ψ_j is the overall wave function at the j -th lattice site, and U_j is the on-site disorder or Anderson potential. By definition, the Anderson potential must vary randomly within the crystal lattice, and it will correspond to a random component in the local potential energy in addition to the periodic component due to the crystal lattice.

In order to compare the differences in the potential for the different polymorphs, we compute the local potential energy along the X-, Y-, and Z-directions in the CZTS supercells. It is evident from Figure 4.2 b and c (and Supplementary Figure 4.S4a) that the potential in the ordered tetragonal polymorph (black curve) exhibits a highly periodic nature. Instead, the cubic structure (red curve) deviates significantly from this periodicity. This is quite similar to the maximum quasi-periodic disorder of the Thouless pump reported by Nakajima et al.²⁷, which drives a trivial phase into a non-trivial one. As such, we assert that the potential in the disordered polymorphs can be safely approximated to be the potential of the ordered structure plus a modifying potential due to disorder, which is in the spirit of Equation (4.1). Then, this modifying term is given by the difference between the ordered and disordered potentials, as seen in Figures 4.2b and c (and Supplementary Figure S4b).

Critically, it has been demonstrated⁵¹ that bond disorder, which adds random hopping terms to the Hamiltonian, and is present in many material systems, cannot drive a system into the TAI phase. As such, the bonding inhomogeneity prevalent in disordered CZTS cannot be held responsible for the non-trivial nature of the system. Instead, it is an independent by-product of the same random on-site cation disorder potential, which also gives rise to the TAI behavior. This is evident from Figures 4.2b and c, which show the random disorder potential in the x- and y-directions, respectively. These directions are not in fact the bonding directions in CZTS, thus putting our results in agreement with those of Song et al.⁵¹.

Instead, Girschik et al.⁵² have suggested that any long-range correlations in the disorder potential might lead to a strong

suppression of the TAI phase. Such correlations can be reasonably precluded from our system by considering the global nature of the disorder in CZTS. This constitutes a total randomization of atomic species in the cation lattice sites. Thus, the nature of the disorder prevents long-range correlations, instead promoting short-range, random variations of the local potential and allowing for the TAI phase to manifest.

Then, it is clear that the modifying potential is a highly random and aperiodic short-range onsite potential. This makes it a suitable candidate for the on-site disorder potential in the theory of TAIIs. Given the previous predictions of the closely related Cu₂ZnSnSe₄ as a TI¹⁹, and the presence of a strong Anderson potential in the cubic polymorph, we put forward that ordered CZTS is driven into the disordered TAI phase. This is the result of introducing a high level of cation disorder, such as can be achieved through high-energy ball milling.

Adiabatic Continuity

The presence of band inversion in the bulk is considered a necessary but not sufficient condition for the presence of a topological insulator phase⁵³. To this end, adiabatic continuity arguments have emerged as a powerful tool to characterize the topological nature of materials through ab initio calculations, and they have been used to predict new TI phases⁵⁴⁻⁵⁸. The process involves connecting a known topological material to a new structure through a series of adiabatic changes. These include straining the crystalline lattice, tuning the strength of the SOC, and modifying the nuclear charge of constituent atoms within the constraint of overall charge neutrality⁵³. If the Hamiltonian of this new system can be adiabatically connected to that of the known TI via some combination of the aforementioned ways without inducing a band inversion or a closing of the gap, the new material can be considered to be topologically equivalent to the known material and thus also a TI. Previous studies^{18,19} have adiabatically connected quaternary chalcogenides to the known TI HgTe (strained) via both ternary famatinites and chalcopyrites. Of these compounds, the closest to our present case is the proposed TI¹⁹ Cu₂ZnSnSe₄ (CZTSe) with an *I*-42*m* tetragonal stannite structure.

Starting from this structure, we are able to transition to a fully disordered CZTSe with a cubic F-43m lattice by introducing randomization. This is done by interchanging the coordinates of a

single pair of cations at a time. Given that both stoichiometry and charge remain conserved overall, such a transition corresponds to an adiabatic change of the total Hamiltonian of the system (see Table S4.2 in the Supplementary Information File for energies of the intermediate configurations in the transition). Subsequently, we replace selenium ions with sulfur in the anion position, thereby transitioning into our cubic CZTS. This, once more, is an adiabatic transition given that both S and Se are group IV elements with identical s₂p₄ outer-shell electronic configurations. The extra contribution of Se is only through fully occupied core levels that lie well away from the Fermi energy. As Figure 4.3 demonstrates, this entire transition can be made without closing the inverted band gap at the Γ -point. Thus, we can conclude that the disordered cubic polymorph of CZTS is in fact topologically connected to the previously predicted TI CZTSe in the adiabatic limit (see Supplementary Figure S4.5 for band structures of the entire transition). It should be noted that the high degree of cation disorder implicitly increases the global symmetry of CZTS from tetragonal to cubic with two interpenetrating sub-lattices of cations and sulfur anions. This structure lies in the same F-43m space group as HgTe, which is the parent compound of this family of adiabatically connected 3D TIs.

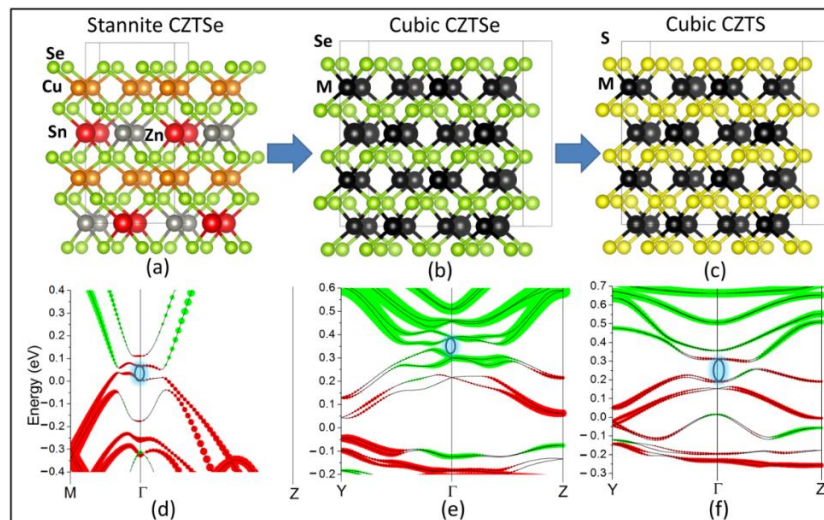


Figure 4.3. Adiabatic continuity between stannite CZTSe and cubic CZTS: (a) the crystal geometry of stannite CZTSe, (b) the geometry of cubic CZTSe, (c) the geometry of cubic CZTS; orange, red, gray, and yellow circles have the same meaning as in Figure 4.1, green circles refer to selenium ions, black circles refer to a

randomized cation; (**d**) the bands of stannite CZTSe, (**e**) the bands of cubic CZTSe, (**f**) the bands of cubic CZTS; red circles correspond to the dominant contribution from Cu-d orbitals, green circles correspond to the dominant contribution from anion-p orbitals; the black arrow shows the open non-trivial band gap.

Topological Surface States

Further evidence to verify the topologically non-trivial nature of a material can be obtained by characterizing the topologically protected gapless surface states, which are guaranteed through bulk-boundary correspondence. The calculation of these states from first principles is computationally demanding, and the results can be distorted by spurious gaps due to interactions between periodic copies⁵³. In order to reduce these artefacts, we calculate the surface states for a 001 surface with sulfur termination within a slab geometry, with a large (10 Å) vacuum introduced in the Z-direction (see Supplementary Figure S4.6 for a simulation cell). Other than the expected quasi-gapless state at the Γ -point, our calculations point to a further two states at the high-symmetry R and V points (Figure 4.4a). This is in agreement with the requirement for an odd number of Dirac points. It must be mentioned that these states tend more toward a parabolic curvature rather than the well-known linearly-dispersing Dirac cones. This “quadratic band touching” was predicted by Fu¹⁶ using a tight-binding model for spinless fermions. In real materials, this corresponds to systems with weak SOC. These so-called “Schroedinger paraboloids” have recently been reported in novel topological semi-metals, namely the Weyl semi-metal candidate SrSi₂⁵⁹ and the so-called Schroedinger semimetal Be₂P₃N⁶⁰. Both these materials, interestingly, show weak SOC similar to cubic CZTS.

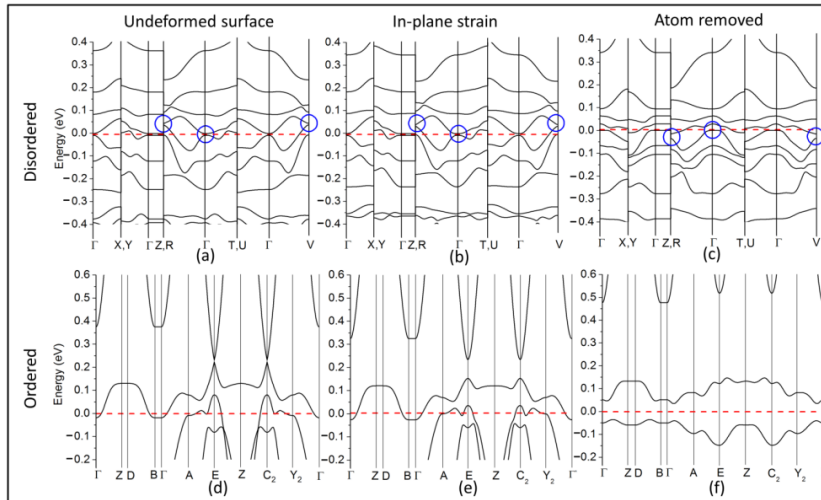


Figure 4.4. Surface states: (a) the surface band structure of cubic CZTS, (b) the corresponding surface bands under 2% expansive strain in the XY plane, (c) the corresponding surface bands with one sulfur atom removed from the surface; blue circles mark the gapless surface states; (d) the surface band structure of ordered tetragonal CZTS; (e) the corresponding surface bands under 1% expansive strain in the XY-plane, (f) the corresponding surface bands with one sulfur atom removed from the surface.

Topological surface states can be sharply distinguished from well-known trivial surface states in semiconductors/insulators. The latter are less robust and can be removed via surface deformation⁵³. Interestingly, we find that the topologically trivial ordered tetragonal CZTS hosts such surface states at the E and C_2 high-symmetry points on the 001 surface (Figure 4.4d). In order to test for robustness, we have deformed the surface by applying a small (1%) in-plane expansive strain (Figure 4.4e) as well as simply removing a single S atom from the surface layer (Figure 4.4f). This leads to an opening of the gap in ordered tetragonal CZTS, causing the trivial gapless states to vanish. In comparison, the surface states in the disordered cubic polymorph are found to be significantly resilient (Figures 4.4c and d) to identical surface treatments, confirming that these states are in fact topologically protected. These robust surface states are expected to support quasi-metallic surface transport. This would contribute significantly to the improved conductivity observed in disordered cubic CZTS²⁸.

Discussion

In general, the evidence presented above, while strongly suggesting that disordered cubic CZTS behaves as a TAI, cannot be considered to be conclusive. Further investigation, both theoretical and experimental, is part of ongoing research. Theoretical calculations using tight-binding models and effective Hamiltonians can be used to calculate the Berry phase and topological invariant, in order to provide a more fundamental understanding of the topologically non-trivial behavior of the material. On the experimental side, conclusive evidence for topological surface states can be obtained with angle resolved photoemission spectroscopy (ARPES). However, the nanopoly-crystalline nature of our samples makes ARPES unfeasible. Preliminary electrical measurements indicate an inverse relation between grain size and carrier mobility, suggesting a strong surface contribution (see Supplementary Note 2, Figures S4.7 and S4.8). However, further transport measurements at ultra-low temperatures and in the presence of magnetic fields might be used to better characterize the nature of the surface states.

4.4 Conclusions

In the present article, we propose a possible candidate for a disorder-induced TI material, the so-called Topological Anderson Insulator. High-energy reactive ball milling has recently been used to produce a low-temperature disordered cubic (*F*-43*m*) phase of the quaternary chalcogenide Cu₂ZnSnS₄, with complete randomization in the cation positions. DFT calculations show that this novel disordered polymorph has an inverted band order in the conduction and valence band extrema at and close to the Brillouin zone center, in contrast to the trivial bands of the ordered tetragonal (*I*-4) counterpart. Furthermore, the band-structure of this phase can be connected adiabatically to the bands for ordered tetragonal (*I*-42*m*) Cu₂ZnSnSe₄, which is known to be a 3D TI, without closing the inverted band gap. Surface slab calculations reveal the presence of an odd number (three) of quasi-gapless surface states, which are remarkably robust to surface deformation such as strain and defects. This is in sharp contrast to the fragile surface states in ordered CZTS.

The DFT calculations presented here offer a strong argument in favor of this novel topological phase in ball-milled cubic CZTS with full cation disorder. While not claiming conclusive proof, this work opens

up a significant possibility for topological matter in the realm of multinary, disordered compounds, where topological behavior is only partially understood. Such materials, which are easily and cheaply synthesized in comparison to perfect crystals for traditional TIs, open up diverse possibilities not just for fundamental research but also the application of topological properties, particularly in the area of thermoelectrics.

Appendix

Supplementary note 1: Band gap in disordered CZTS

Despite appearances to the contrary in Fig 4.1(f), disordered CZTS does in fact have a global band gap, albeit a complicated one. In our previous article (Ref 25), we have experimentally measured the optical gap, which shows a large value of ~ 1.5 eV; notably however, the Tauc plot obtained from UV-vis spectroscopy shows large Urbach tailing, as seen in the image below (Fig S4.1a), Fig S3 from Ref 25 (Isotta et al, Phys. Rev. Applied 14, 064073).

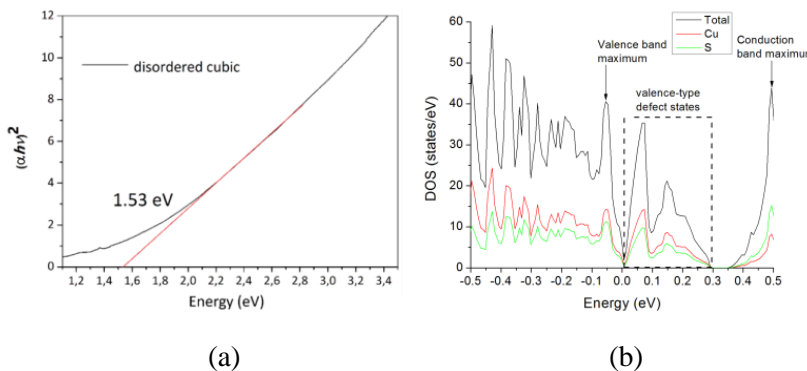


Figure S4.1. The band gap of disordered CZTS seen from (a) Tauc-plot from UV-Visible spectroscopy; (b) density of states calculated using the SCAN meta-GGA functional.

The calculated density of states (above, right) shows that the valence band is dominated by Cu-d electrons, while the conduction band is predominantly composed of S-p electrons, with the presence of large valence type defect states just above the Fermi energy, which is set to 0. The large Urbach tailing in the Tauc plots can be accounted for by these defect states, which of course arise due to the highly disordered nature of the material. For a detailed theoretical discussion on these defect states and how they improve experimentally measured

thermoelectric properties, we refer the reader to Ref 28. These defect states, which originate from the same orbitals as the valence band, but lie mostly above the Fermi energy, also represent the valence band maximum seen in Fig 4.1f, with a smaller gap to the bottom of conduction band, allowing for band inversion. The fact that the Fermi energy lies within the valence band of course is characteristic of p-type semiconductors, and does *not* imply that the system has no global gap, but rather that it has band tailing and a reduced gap.

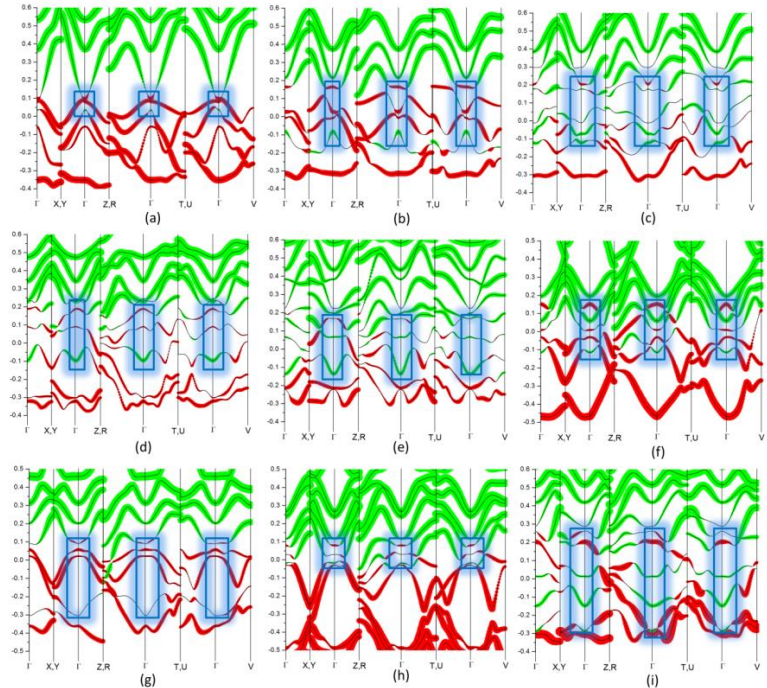


Figure S4.2. Bands for multiple configurations of disordered cubic CZTS. Symbols have save same meaning as in the main text.

| Configuration | Total energy |
|--------------------|---------------|
| Config1 (Fig 1f) | -25723222E+03 |
| Config2 (Fig S1a) | -25487437E+03 |
| Config3 (Fig S1b) | -25700924E+03 |
| Config4 (Fig S1c) | -25462498E+03 |
| Config5 (Fig S1d) | -25416696E+03 |
| Config6 (Fig S1e) | -25364071E+03 |
| Config7 (Fig S1f) | -25547144E+03 |
| Config8 (Fig S1g) | -25522658E+03 |
| Config9 (Fig S1h) | -25509927E+03 |
| Config10 (Fig S1i) | -25400458E+03 |

Table S4.1. Total ground state energies of the multiple configurations of disordered cubic CZTS

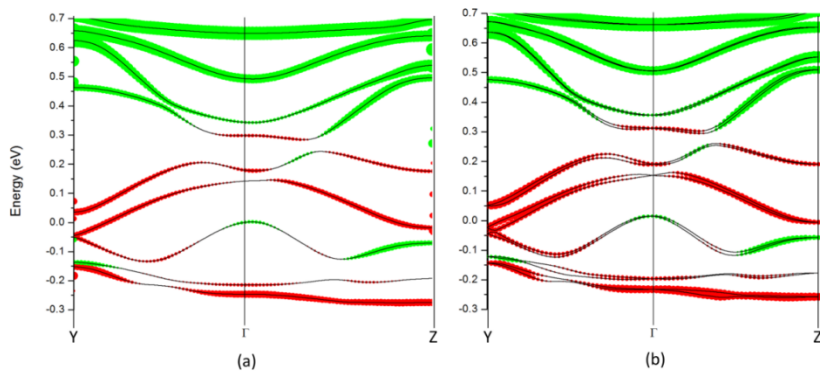


Figure S4.3. Comparison of bands for disordered cubic CZTS (a) without and (b) with spin-orbit coupling. Symbols have same meaning as in the main text.

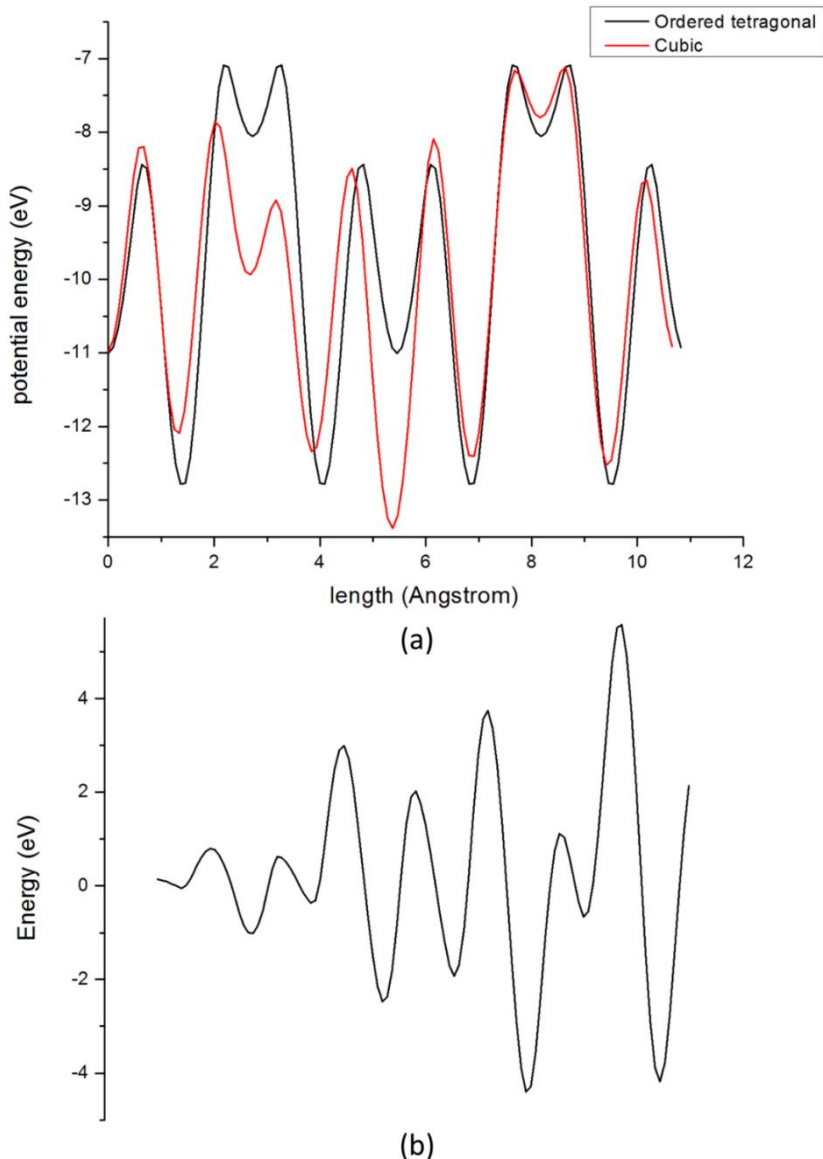


Figure S4.4. (a) Local potential in the Z-direction for ordered tetragonal (black) and disordered cubic (red) CZTS; (b) Difference between the potentials. The lattice mismatch in the Z-direction between the tetragonal and cubic supercells exaggerates the difference.

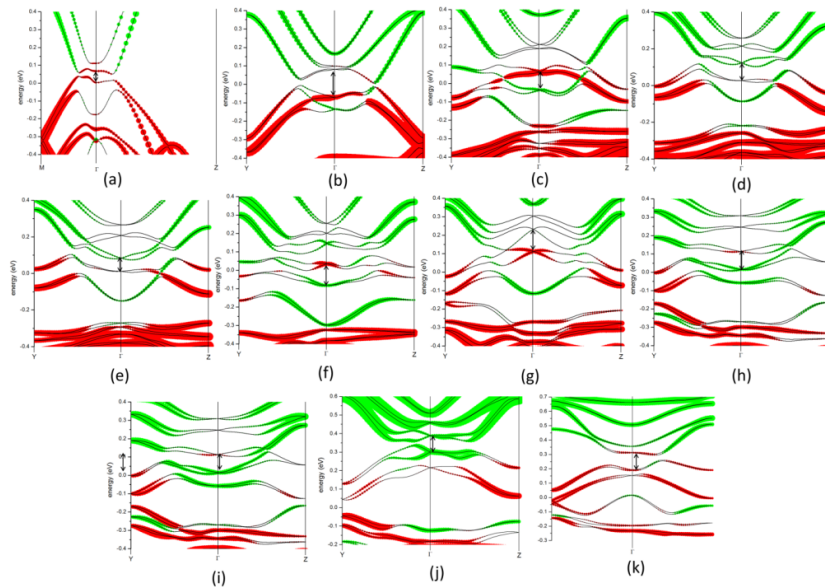


Figure S4.5. Adiabatic transition from (a) stannite CZTSe through (k) cubic CZTS. Intermediate images show the bands for intermediate states. Arrows highlight the open inverted band gap.

| Step | Total ground state energy |
|-------------------|---------------------------|
| Step 1 (Fig S4a) | -23556786E+03 |
| Step 2 (Fig S4b) | -23552479E+03 |
| Step 3 (Fig S4c) | -23484019E+03 |
| Step 4 (Fig S4d) | -23303846E+03 |
| Step 5 (Fig S4e) | -23233460E+03 |
| Step 6 (Fig S4f) | -23221546E+03 |
| Step 7 (Fig S4g) | -23220398E+03 |
| Step 8 (Fig S4h) | -23231033E+03 |
| Step 9 (Fig S4i) | -23122961E+03 |
| Step 10 (Fig S4j) | -23132112E+03 |

Table S4.2. Total ground state energies for the intermediate configurations in the adiabatic transition from ordered to disordered CZTSe

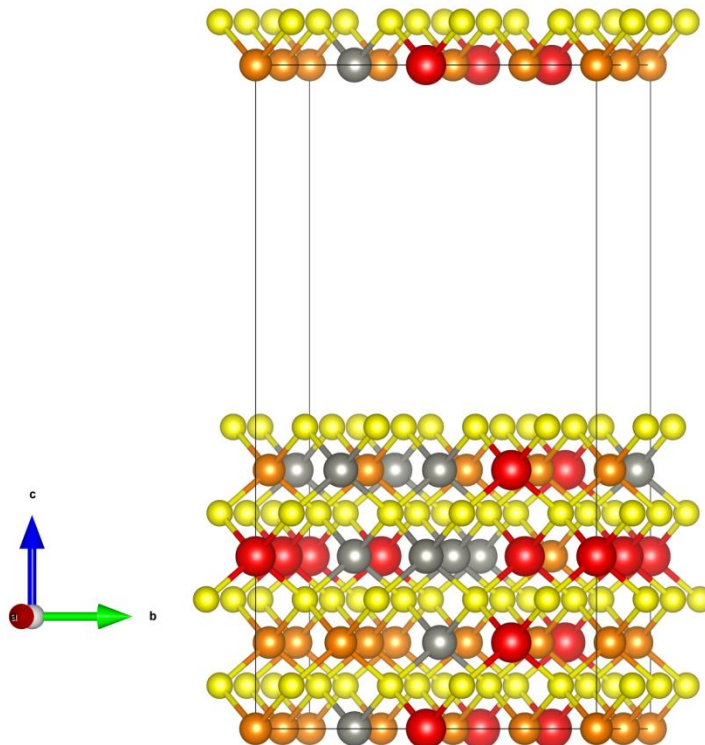


Figure S4.6. Surface slab geometry for the 001 surface of cubic CZTS with S termination. Orange atoms are Cu, grey atoms are Zn, red atoms are Sn and yellow atoms are S.

Supplementary note 2: Grain size dependence of mobility

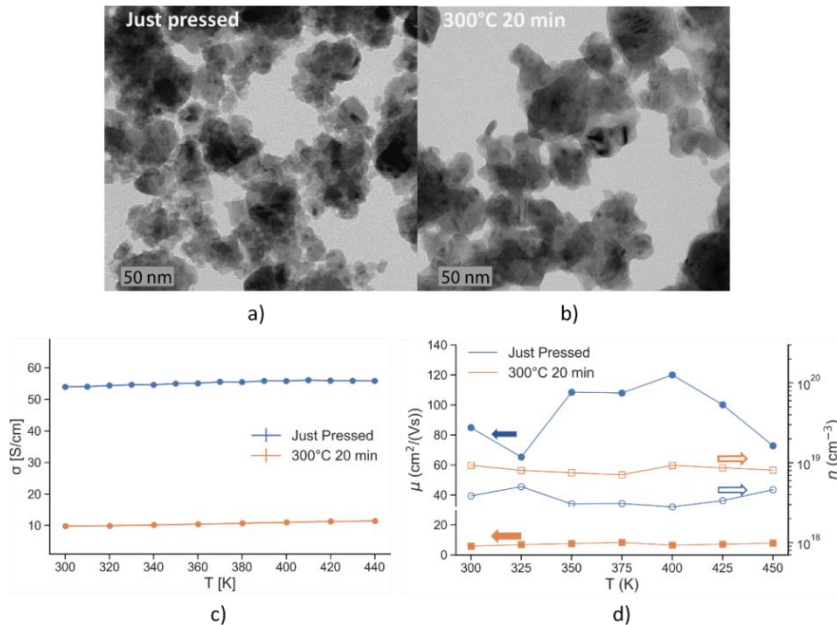


Figure S4.7. TEM imaging (a, b) and electrical transport measurements (c, d) for a just pressed and a thermally treated sample. The smaller grain size observed for the just pressed sample (in panel a and confirmed by XRD, see appendix for details) leads to a higher grain surface area which is thought at the origin of the increased electrical conductivity σ (c). Carrier concentration n and mobility μ measurements (d) demonstrate that the enhancement in σ is coming from a remarkable increase in carrier mobility, while carrier concentration remains in the same order of magnitude (considering the precision of Hall effect measurements). This atypical trend of properties might be due to scattering-resistant transport arising from the topological surface states.

Conclusive evidence in favor of a TI can be obtained via a direct experimental observation of the topological surface states with angle resolved photoemission spectroscopy (ARPES). However, this technique is suitable only for large single crystals with perfectly clean surfaces. Disordered cubic CZTS, synthesized as it is via reactive ball-milling, exists essentially in a metastable, nano-polycrystalline form, and is therefore unavailable for ARPES. Under such circumstances, transport experiments can provide an alternate route to support the presence of the surface states: given a sufficiently insulating bulk, a substantial contribution to conduction is expected from the surface⁶¹. This feature can be verified by observing the grain size dependence of the electrical transport^{62–65}. In particular, this should be seen as an

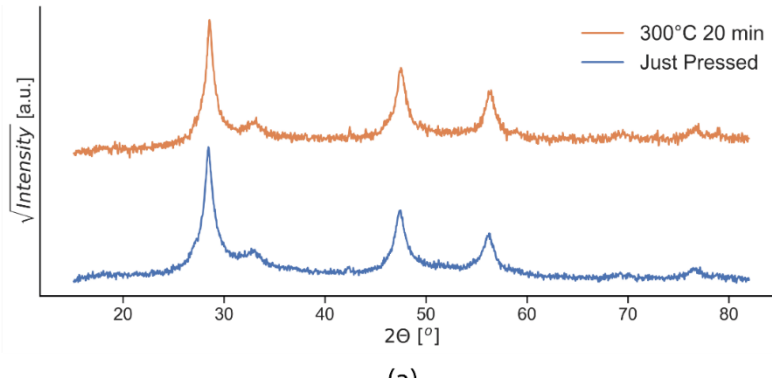
increase in carrier mobility with a reduction of grain size, as a consequence of the topological surface states.

As can be seen in Figure S4.6, the experimental measurements do indeed point to a significant surface contribution to conduction. Two cubic samples have been compared: one has been obtained just with a cold-pressing step, while the other has been thermally treated at 573K. This thermal treatment is performed to promote some grain growth, while keeping the sample below the cubic to tetragonal phase transition (at ~673K). This grain growth is confirmed through TEM imaging (Figure S4.6a, b) and X-ray Diffraction (with, Supplementary Figure S4.6). By modelling the XRD data through the WPPM approach⁶⁶, we estimate the coherent domain size for the just pressed and thermally treated samples as 9.7 nm and 13.4 nm respectively. . Electrical conductivity is found higher for the sample showing smaller grains (Figure S4.6c). This is in contradiction to a general trend in semiconductors⁶⁷: thermal treatments typically lead to higher density, improved connectivity between adjacent domains, and a reduction in carrier scattering from the grain boundary, all of which should improve electrical conduction. In order to identify the origin of this atypical trend in conductivity, we performed mobility and carrier concentration measurements. The carrier concentration is found to be in the same order of magnitude for both the samples (Figure 4.S6d, right axis), with the improved conductivity of the just pressed sample (with smaller grains) originating from an enhancement of carrier mobility (Figure S4.6d, left axis). This is what would be expected from a higher surface area characterized by scattering-resistant charge transport arising from the topological surface states.

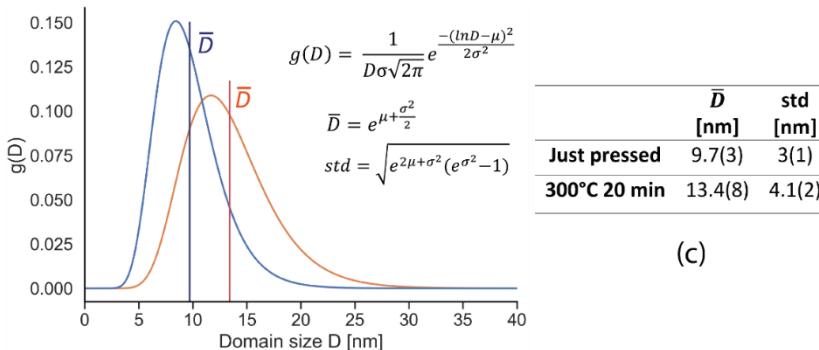
Several sample differences might possibly contribute to the observed variation of transport properties between the samples with different grain size. For example, thermal treatments are expected to trigger some cation ordering. As such, the just pressed sample, by virtue of not being exposed to temperatures above RT, is most probably characterized by a higher cation disorder. However, in a recent study by some of the present authors, it has been demonstrated that cation disorder in CZTS seems to improve conductivity by introducing additional gap states, thereby promoting p-type carrier concentration²⁸. The carrier mobility, on the other hand, was typically found to get depressed with disorder, due to band flattening and increased scattering. This is in direct opposition to our current trends, where the more disordered just-pressed sample shows significantly higher mobility values. Another possible contribution might be from the surface chemistry, which may vary from that of the bulk, although we would expect the changes to be consistent for both the samples. As such, the inverse correlation between mobility and grain size can be best explained by the higher surface-to-volume ratio in the smaller grains, and the correspondingly greater abundance of the topological

surface states⁶¹ predicted from theory. These robust surface states would allow charge carriers to skip around defects at the grain boundary, enabling carrier transport without backscattering, and explaining the experimentally observed increase in mobility in the just pressed sample with smaller grains.

While the experimental evidence provided above falls somewhat short of being sufficient for conclusive proof, it is nevertheless definitely in agreement with the results of the DFT calculations. As such, we can consider it to be satisfying a necessary condition for a topological insulator phase.



(a)



(b)

Figure S8. (a) XRD patterns for a just pressed and a thermally treated sample of cubic CZTS. The purpose of the thermal treatment was to increase the domain size while keeping the phase cubic. Rietveld refinement with the software TOPAS was performed on XRD data using the WPPM model for size broadening. This assumes a lognormal distribution of domain sizes, reported in panel (b) for both the samples. Equations from top to bottom represent a lognormal distribution, the arithmetic mean domain size and the corresponding standard deviation. The thermal treatment leads to a broader and right-shifted distribution, indicating some grain growth, in accordance with TEM observations reported in the main text. Distribution parameters are visible in Table (c).

Author Contributions

B.M. was primarily responsible for making the DFT calculations, theoretical analysis, and writing and editing the manuscript. E.I. was primarily responsible for supplying the samples and making the resistivity measurements. C.F. was primarily responsible for making the Hall effect measurements. N.A. was primarily responsible for the experimental setup and participated in interpreting the results. P.S. was primarily responsible for supervising the research and participated in analyzing theoretical and experimental results and editing the manuscript. Conceptualization, B.M. and P.S.; Data curation, B.M.; Formal analysis, B.M., E.I. and P.S.; Funding acquisition, P.S.; Investigation, B.M., E.I., C.F. and N.A.; Methodology, B.M. and P.S.; Project administration, P.S. Visualization, B.M. and E.I.; Writing—original draft, B.M.; Writing—review and editing, B.M. and P.S. All authors have read and agreed to the published version of the manuscript.

Acknowledgments

The computational time was provided by CINECA—Italian Supercomputing Facility, with the Project CZTS—HP10CONX70.

Conclusions, perspectives, and continuing work

In this thesis, we have carefully studied the nature of disorder and its effects across a range of functional materials, including Palladium nanoparticles used in nanocatalysis, Ag_2O as an antibacterial agent and the primary component of silver oxide batteries, and $\text{Cu}_2\text{ZnSnS}_4$ for thermoelectric applications.

We have characterized disorder *across* this range of materials through the Debye-Waller coefficient B_{iso} , as obtained from the modeling of X-ray powder diffraction data through the whole powder pattern modeling approach; and in each case the corresponding atomic source of disorder has been determined through the mean square displacement computed from molecular dynamics simulations. The measured and computed quantities show generally good agreement, allowing for a reliable description of the material properties based on the computational models.

The types of disorder studied here can be broadly classified into two categories: ‘structural’ disorder, corresponding to the distortion of the ideal, periodic crystalline lattice, and ‘chemical’ disorder, which refers to the compositional disordering of the periodic lattice sites. The case-study of the Pd nanoparticles reveals the strong role of adsorption induced surface disorder at the nanoscale, and its effect on modifying the strain state of these nanoparticles. Both the adsorption of the capping agent CTAB *and* O_2 molecules lead to a softening of the nanoparticle surface. These surface softening effects are found to be stronger than simple surface termination (nanoparticle shape) effects. The adsorption of oxygen and subsequent oxidation of these palladium nanoparticles is found to proceed from corner and edge sites, leading to a rounding of cubic nanoparticles and a consequent release of long-range strain across the nanoparticle. The oxygen activation behavior on different surface terminations is predicted to have opposing trends with surface coverage, with possible implications for the oxygen reduction reaction, an important process at the heart of hydrogen fuel cells and heterogeneous catalysis in general.

Next, we investigated the bulk disorder and large B_{iso} in Ag_2O . The reduction in Bragg peak intensity was associated with a large thermal diffuse scattering background, which was treated using a coordination shell model. While this model fails to account for the sharp features of the thermal diffuse scattering due to long-wavelength phonons, it accounts well for the diffuse features, and provides a reasonable estimate for the B_{iso} . The large value of B_{iso} was found to be the consequence of anisotropic forces and displacements of atoms coupled with dynamical instability from soft phonon modes, resulting in a strong static disorder in the crystalline lattice.

Subsequently, we move on to the chemically complex copper chalcogenide $\text{Cu}_2\text{ZnSnS}_4$, where we study the effects of chemical disorder and polymorphism on the electronic and vibrational properties of the material, and how it affects its thermoelectric performance. From the perspective of electronic band structure, the behavior of the disordered tetragonal and disordered cubic polymorphs is quite distinct. While the flattening of electronic bands are observed as a consequence of disorder in both cases, the tetragonal displays a convergence of bands at the valence band maximum relative to the ordered polymorph, whereas the cubic instead displays a splitting. This is fundamentally connected to the nature of disorder in the two polymorphs: in the tetragonal case this is manifested as a randomization of the Cu and Zn positions only in the Cu-Zn. Since these two species are similar in their electron configuration, the disorder tends towards a homogenization of the local chemical environment of each atom, thus promoting degeneracy of electronic energy levels. On the other hand, the cubic polymorph, which displays full cation disorder, is found to have an inhomogenous charge distribution and bonding, leading to a splitting of the energy levels. These electronic features of disorder have significant consequences for the thermoelectric properties of the material – band convergence in the disordered tetragonal polymorph leads to an increase in carrier concentration at the expense of carrier mobility, with an overall improvement in thermopower compared to the ordered polymorph. In the cubic polymorph instead, the inhomogeneity in the charge distribution leads to the formation of localized trap states *within* the band gap, which induce a simultaneous increase in electrical conductivity (from increased hole concentration due to electrons being ‘trapped’ by the gap states) and the Seebeck coefficient (from a steep

electronic density of states due to the localized nature of the states). Additionally, the inhomogenous bonding and rattling behavior of certain Sn ions in the cubic polymorph manifests as low-lying optical modes which overlap with the heat-carrying acoustic modes. This leads to a dissipation of heat, which, coupled with a flat phonon dispersion corresponding to a low phonon group velocity, leads to an ultra-low thermal conductivity. While the overall thermoelectric performance of these materials is limited, both the disordered polymorphs of CZTS display disorder induced mechanisms which improve their thermoelectric performance vis-a-vis the ordered counterpart. Further improvements to the thermoelectric performance can be achieved primarily by improving the electrical conductivity, by selective dopings and substitutions. Indeed, replacing S with the heavier Se leads to a reduction in the band gap, and ongoing studies deal with the thermoelectric performance of cubic $\text{Cu}_2\text{ZnSnSe}_4$ with full cation disorder.

Finally, we study the atypical electronic band structure of cubic CZTS. The strong disorder in the cubic polymorph was found to have some fundamental consequences for the physics of CZTS. The large crystal field splitting at the band extrema causes a local reversal in the band ordering at the Brillouin zone center, with Cu-d orbitals (valence band) ending up at a higher energy than S-p orbitals (conduction band). This band inversion is a characteristic feature of topological insulators, and the disorder induced nature points to a novel topological Anderson insulator phase in cubic CZTS. Consequently, calculations show the presence of topologically protected surface states, robust to surface disorder. These surface states remain difficult to characterize experimentally, primarily because the metastable, low temperature cubic CZTS phase can only be stabilized in highly nanostructured samples. Nevertheless, they offer the promise of high mobility surface conduction channels, with a significant potential for exploitation within the context of nanostructured and porous thermoelectric materials. Ongoing work focuses on a better understanding of the topological properties of the electronic band structure of the quaternary chalcogenides through the calculation of the Z2 topological invariant, as well as a more complete understanding, both theoretical and experimental, of how these surface states hybridize with adjacent states, and how they affect overall charge transport in the material.

Ultimately, over the course of this thesis, we establish a robust methodology to connect the experimentally measured Debye-Waller coefficient with the atomic mean-square displacement of atomistic models, with good overall agreement. Subsequently calculated mechanical, electrical and vibrational properties provide a good qualitative understanding of the behavior of the studied materials. Nevertheless, the computational methods have certain limitations. Molecular dynamics forcefields, which are quite adequate for the bulk behavior of simple metals, are found to be less so for surface effects, or even the bulk effects in materials with complex structural behavior. Additionally, reactive force fields, which provide a good description of surface adsorption, are found to be less reliable for bulk elastic properties. As such, this necessitates the development of more refined forcefields, possibly with different parameterizations to calculate different properties. The development of machine learned forcefields provides a promising route to partially automate the process- and extend the availability of such forcefields to chemically complex materials.

The underestimation of the band gap of semiconductor materials also poses a significant challenge in the quantitative prediction of the electrical properties of these systems. This stems from a fundamental theoretical inadequacy of density functional theory – the lack of an adequate approximation for the electron-electron exchange and correlation energies. These many-body interactions remain difficult to estimate with single-particle estimations such as the local density (LDA) or generalized gradient (GGA) approximations. Mixing the Hartree-Fock exact exchange energy with the DFT energies leads to an opening up of the band gap, but this gap becomes sensitive to the fraction of mixing, thus lacking predictive qualities. Additionally, the calculation of the many-body exact exchange energy severely affects the computational efficiency of the method, and restricts calculations to relatively small and simple supercells. Nevertheless, the recent acceleration in the development of high performance computing facilities, coupled with the introduction of ‘post-DFT’ methods hold great promise for the accurate modeling of the electronic structure of complex materials.

Besides these systemic drawbacks, materials modeling at the atomic or nanoscale suffers from a further, more fundamental problem – the failure to account for microstructure. Indeed, apart from carefully

grown large single crystals, most real materials contain significant microstructure. Of great consequence for transport properties, whether of electron or phonons, is the role of grain boundaries and interfaces. Particularly in nanostructured complex semiconductor materials, surface states, whether simple or topological, are found to significantly affect electrical conductivity, the former through variations in stoichiometry and carrier concentration, the latter through changes in mobility. However, the way in which these surface states interact with other surface states at grain boundaries and interfaces remains largely unknown, and poses a significant challenge for the future. A better understanding of these interfaces at the atomic and electronic level will open the way for an accurate prediction of material properties, not just for infinite crystals, semi-infinite surface slabs or nanoparticles in a vacuum, but real material samples used in the fabrication of functional devices. Predictions from such reliable computational models hold the promise of significantly reducing experimental overhead, both in terms of time and expenditure, facilitating the efficient optimization and fabrication of high-performance devices.

6 Appendix

6.1 List of publications

1. “Static and dynamic components of Debye-Waller coefficients in the novel cubic polymorph of low-temperature disordered CZTS” Eleonora Isotta, Binayak Mukherjee, Sebastian Bette, Robert Dinnebier, and Paolo Scardi, *IUCrJ*, 9(2), doi.org/10.1107/S2052252522000239, 2022
2. “Topological Anderson Insulator in cation-disordered Cu₂ZnSnS₄”, Binayak Mukherjee*, Eleonora Isotta, Narges Ataollahi, Paolo Scardi*, *Nanomaterials* 2021, 11, 2595, doi.org/10.3390/nano11102595, 2021
*corresponding author
3. “Effect of oxygen adsorption and oxidation on the strain state of Pd nanocrystals”, Binayak Mukherjee, Alberto Flor, Paolo Scardi; *Appl. Surf. Sci.*, Vol 541, 2021 148508, doi.org/10.1016/j.apsusc.2020.148508, 2021
4. “Origin of a Simultaneous Suppression of Thermal Conductivity and Increase of Electrical Conductivity and Seebeck Coefficient in Disordered Cubic Cu₂ZnSnS₄”, Eleonora Isotta*, Binayak Mukherjee*, Carlo Fanciulli, Narges Ataollahi, Ilya Sergueev, Svetoslav Stankov, Raju Edla, Nicola M Pugno, Paolo Scardi*; *Phys. Rev. Applied* 14, 064073, doi.org/10.1103/PhysRevApplied.14.064073, 2020
*corresponding author
5. “Order-disorder transition in kesterite Cu₂ZnSnS₄: thermopower enhancement via electronic band structure modification”, Eleonora Isotta, Binayak Mukherjee, Carlo Fanciulli, Nicola M. Pugno and Paolo Scardi, *J. Phys. Chem. C* 2020, 124, 13, 7091–7096
doi.org/10.1021/acs.jpcc.0c00886, 2020

6. “Surface softening in Palladium nanoparticles: Effects of a capping agent on vibrational properties”, Luca Rebuffi, Binayak Mukherjee¹, Stefano Siboni, Allison P. Young, Benjamin P. Williams, Chia-Kuang Tsung and Paolo Scardi, *Nanoscale*, 2020, 12, 5876-5887, doi.org/10.1039/D0NR00182A, 2020
¹*equal contribution as first author*

Manuscripts under preparation/communicated (tentative titles, authors):

1. “Large Debye-Waller coefficient in negative thermal expansion cuprites Cu₂O and Ag₂O” Binayak Mukherjee, Narges Ataollahi, Stefano Siboni, Paolo Scardi
2. “Thermoelectric performance of cation-disordered Cu₂ZnSnSe₄”, Binayak Mukherjee, Marcelo Malagutti, Ketan Lohani, Eleonora Isotta, Paolo Scardi
3. “Topological insulators in quaternary chalcogenides” Binayak Mukherjee, Giovanni Marini, Matteo Calandra, Paolo Scardi

6.2 Participation in schools and conferences

- Oral presentation at the Giornate sulla Termoelettricità, Italian Thermoelectrics Association, 16th – 17th February, 2022
- Oral presentation at the 12th European Kesterite Workshop, 10th – 11th February, 2022
- Organizer, instructor for LAMMPS MD software at the Scientific and high performance computing school (S/HPC-school 2021) from 30th August – 3rd September, 2021, at the University of Trento, Trento, Italy.
- Topological Matter School (Online) from August 16th – 27th, 2021.
- Oral presentation at the 2021 Virtual Conference on Thermoelectrics, European Chapter, from 20th – 22nd July, 2020.
- Poster presentation at the 11th European Kesterite+ Workshop, 26th – 27th November, 2020.
- Oral presentation at the 2020 Virtual Conference on Thermoelectrics, European Chapter, from 21st - 23rd July, 2020.

- Quantum Espresso summer school (QE-2019) from 15th – 20th September 2019, at the Jozef Stefan Institute in Ljubljana.
- Scientific and high performance computing school (S/HPC-school 2019) from 2nd – 6th September 2019, at the University of Trento, Trento, Italy.
- Instructor for TOPAS XRD software package at the "School on Synchrotron and Free-Electron-Laser Methods for Multidisciplinary Applications", during 9th – 10th May, 2018, at the Abdus Salam International Center for Theoretical Physics (ICTP), Trieste, Italy.

6.3 Grants for computational time

- Class C project for computational time on the Italian high performance computation center CINECA, for a total of 560,000 core-hours. (May, 2019).
- Awarded ~7,833,400 CPU-hrs at the German high performance computation center HLRS Stuttgart, for the project titled “Understanding disorder in kesterite to achieve high thermoelectric performance: from electronic to thermal” (April 2020 – March 2023).

References

1. Kittel, C. *Introduction to Solid State Physics*. (Wiley, 2004).
2. Ashcroft, N. & Mermin, N. *Solid State Physics*. (Holt, Rinehart, Winston, 1976).
3. Fang, H., Dove, M. T. & Phillips, A. E. Common origin of negative thermal expansion and other exotic properties in ceramic and hybrid materials. *Phys. Rev. B - Condens. Matter Mater. Phys.* **89**, 1–6 (2014).
4. Winter, M. R. & Clarke, D. R. Oxide materials with low thermal conductivity. *J. Am. Ceram. Soc.* **90**, 533–540 (2007).
5. Clarke, D. R. Materials selections guidelines for low thermal conductivity thermal barrier coatings. *Surf. Coatings Technol.* **163–164**, 67–74 (2003).
6. Zhao, M. *et al.* Defect engineering in development of low thermal conductivity materials: A review. *J. Eur. Ceram. Soc.* **37**, 1–13 (2017).
7. Heremans, J. P. The anharmonicity blacksmith. *Nat. Phys.* **11**, 990–991 (2015).
8. Ringe, E., Van Duyne, R. P. & Marks, L. D. Kinetic and thermodynamic modified Wulff constructions for twinned nanoparticles. *J. Phys. Chem. C* **117**, 15859–15870 (2013).
9. Marks, L. D. & Peng, L. Nanoparticle shape, thermodynamics and kinetics. *J. Phys. Condens. Matter* **28**, 53001 (2016).
10. Somorjai, G. A. & Li, Y. *Introduction to Surface Chemistry and Catalysis*. (John Wiley & Sons, 2010).
11. Oura, K., Katayama, M., Zotov, A. V., Lifshits, V. G. & Saranin, A. A. *Surface Science*. (Springer, 2003).
12. Somorjai, G. A. Surface reconstruction and catalysis. *Annu. Rev. Phys. Chem.* **45**, 721–751 (1994).
13. Shin, D., Saparov, B. & Mitzi, D. B. Defect Engineering in Multinary Earth-Abundant Chalcogenide Photovoltaic Materials. *Adv. Energy Mater.* **7**, (2017).
14. Wang, F., Bai, S., Tress, W., Hagfeldt, A. & Gao, F. Defects engineering for high-performance perovskite solar cells. *npj Flex. Electron.* **2**, (2018).
15. Park, J. S., Kim, S., Xie, Z. & Walsh, A. Point defect engineering in thin-film solar cells. *Nat. Rev. Mater.* **3**, 194–210 (2018).
16. Hu, L., Zhu, T., Liu, X. & Zhao, X. Point defect engineering of high-performance bismuth-telluride-based thermoelectric materials. *Adv. Funct. Mater.* **24**, 5211–5218 (2014).

17. Li, Z., Xiao, C., Zhu, H. & Xie, Y. Defect Chemistry for Thermoelectric Materials. *J. Am. Chem. Soc.* **138**, 14810–14819 (2016).
18. Hu, Z. *et al.* Two-dimensional transition metal dichalcogenides: Interface and defect engineering. *Chem. Soc. Rev.* **47**, 3100–3128 (2018).
19. Ortiz-Medina, J. *et al.* Defect Engineering and Surface Functionalization of Nanocarbons for Metal-Free Catalysis. *Adv. Mater.* **31**, 1–16 (2019).
20. Bai, S., Zhang, N., Gao, C. & Xiong, Y. Defect engineering in photocatalytic materials. *Nano Energy* **53**, 296–336 (2018).
21. Zhang, Y. *et al.* Defect Engineering on Electrode Materials for Rechargeable Batteries. *Adv. Mater.* **32**, 1–22 (2020).
22. Li, W. *et al.* Defect Engineering for Fuel-Cell Electrocatalysts. *Adv. Mater.* **32**, 1–20 (2020).
23. Simonov, A. & Goodwin, A. L. Designing disorder into crystalline materials. *Nat. Rev. Chem.* **4**, 657–673 (2020).
24. Debye, P. Zerstreuung von Rontgenstrahlen. *Ann. Phys.* **351**, 809–823 (1915).
25. Waller, I. Zur Frage der Einwirkung der Wärmebewegung auf die Interferenz von Röntgenstrahlen. *Zeitschrift für Phys.* **17**, 398–408 (1923).
26. Marder, M. P. *Condensed Matter Physics*. (John Wiley & Sons, 2010).
27. Krivoglaz, M. A. *Theory of X-ray and Thermal Neutron Scattering by Real Crystals*. (Plenum Press, 1969).
28. Scardi, P., Azanza Ricardo, C. L., Perez-Demydenko, C. & Coelho, A. A. Whole powder pattern modelling macros for TOPAS. *J. Appl. Crystallogr.* **51**, 1752–1765 (2018).
29. Scardi, P. & Leoni, M. Whole powder pattern modelling. *Acta Crystallogr. Sect. A Found. Crystallogr.* **58**, 190–200 (2002).
30. Frenkel, D. & Smit, B. *Understanding Molecular Simulation*. (Elsevier B.V, 2002). doi:<https://doi.org/10.1016/B978-0-12-267351-1.X5000-7>.
31. Daw, Murray, S., Foiles, Stephen, M. & Baskes, Michael, I. The embedded-atom method: a review of theory and applications. *Mater. Sci. Reports* **9**, 251–310 (1993).
32. Senftle, T. P. *et al.* The ReaxFF reactive force-field: Development, applications and future directions. *npj Comput. Mater.* **2**, (2016).
33. Wang, J., Wolf, R. M., Caldwell, J. W., Kollman, P. A. & Case, D. A. Development and testing of a general Amber force field. *J. Comput. Chem.* **25**, 1157–1174 (2004).
34. Sun, H. The COMPASS force field: Parameterization and

- validation for phosphazenes. *Comput. Theor. Polym. Sci.* **8**, 229–246 (1998).
35. Vanommeslaeghe, K. *et al.* CHARMM General Force Field: A Force Field for Drug-Like Molecules Compatible with the CHARMM All-Atom Additive Biological Force Fields. *J. Comput. Chem.* **31**, 671–690 (2010).
36. Feynman, R. P. Forces in molecules. *Phys. Rev.* **56**, 340–343 (1939).
37. Fermi, E. Un Metodo Statistico per la Determinazione di alcune Proprietà dell’Atomo. *Rend. Accad. Naz. Lincei.* **6**, 602–607 (1927).
38. Hohenberg, P. & Kohn, W. Inhomogenous Electron Gas. *Phys. Rev.* **136**, 864 (1964).
39. Kohn, W. & Sham, L. J. Self-consistent equations including exchange and correlation effects. *Phys. Rev.* **140**, 1133 (1965).
40. Perdew, J. P. Density functional theory and the band gap problem. *Int. J. Quantum Chem.* **28**, 497–523 (1985).
41. Kohn, W., Becke, A. D. & Parr, R. G. Density functional theory of electronic structure. *J. Phys. Chem.* **100**, 12974–12980 (1996).
42. Perdew, J. P., Burke, K. & Ernzerhof, M. Generalized gradient approximation made simple. *Phys. Rev. Lett.* **77**, 3865–3868 (1996).
43. Heyd, J., Scuseria, G. E. & Ernzerhof, M. Hybrid functionals based on a screened Coulomb potential. *J. Chem. Phys.* **118**, 8207–8215 (2003).
44. Per, M. C. & Cleland, D. M. Roadmap on post-DFT methods for nanoscience. *Nano Futur.* **4**, 1–24 (2020).
45. U.S. Energy Information Administration. *International Energy Outlook 2019 (IEO2019) United States Milestones in Meeting Global Energy Consumption.* (2019).
46. World Energy Council. *World Energy Scenarios: Composing Energy Futures to 2050.* (2013).
47. Oppenheimer, M. & Glavovic, B. C. *2019: Sea Level Rise and Implications for Low-Lying Islands, Coasts and Communities; in IPCC Special Report on the Ocean and Cryosphere in a Changing Climate.* (2019) doi:<https://doi.org/10.1126/science.aam6284>.
48. IUPAC. Compendium of Chemical Terminology, 2nd ed. (the ‘Gold Book’). Compiled by A. D. McNaught and A. Wilkinson. Blackwell Scientific Publications, Oxford (1997). Online version (2019-) created by S. J. Chalk. ISBN 0-9678550-9-8. <https://doi.org/10.1351>.
49. Masel, R. *Chemical Kinetics and Catalysis.* (Wiley-

- Interscience, 2001).
50. Schlögl, R. & Abd Hamid, S. B. Nanocatalysis: Mature science revisited of something really new? *Angew. Chemie - Int. Ed.* **43**, 1628–1637 (2004).
51. Shih, H. D., Jona, F., Jespen, D. W. & Marcus, P. M. Metal-Surface Reconstruction Induced by Adsorbate: Fe(110)p(2×2)-S. *Phys. Rev. Lett.* **46**, 731 (1981).
52. Jona, F., Strozier, J. A. J. & Marcus, P. M. *The Structure of Surfaces II*. (Springer-Verlag, 1988).
53. MacLaren, J., Pendry, J., Rous, P., Saldin, D. & Somorjai, G.A., et al. *Surface Crystallographic Information Service: A Handbook of Surface Structures*. (Reidel, 1987).
54. Somorjai GA. 1991 . *Langmuir* 7: 3 1 76-82.
55. Somorjai, G. A. *Bonding Energies in Organometallic Compounds*. (American Chemical Society, 1990).
56. Haemers Technologies. Industrial waste heat and waste heat recovery systems <https://haemers-technologies.com/industrial-waste-heat-recovery-systems/>.
57. Interreg Central Europe. Low-Grade Waste Heat Utilization in the European Union; 2017.
58. Jouhara, H. et al. Waste heat recovery technologies and applications. *Therm. Sci. Eng. Prog.* **6**, 268–289 (2018).
59. Chaisson, E. J. Long-term global heating from energy usage. *Eos (Washington. DC.)* **89**, 253–254 (2008).
60. Inman, D. J.; Priya, S. *Energy Harvesting Technologies*, Springer U.; 2008.
61. Beeby, S. P., Tudor, M. J. & White, N. M. Energy harvesting vibration sources for microsystems applications. *Meas. Sci. Technol.* **17**, (2006).
62. Vullers, R. J. M., van Schaijk, R., Doms, I., Van Hoof, C. & Mertens, R. Micropower energy harvesting. *Solid. State. Electron.* **53**, 684–693 (2009).
63. Goldsmid, H. J. *Introduction to thermoelectricity*. (Springer, 2010).
64. Takabatake, T., Suekuni, K., Nakayama, T. & Kaneshita, E. Phonon-glass electron-crystal thermoelectric clathrates: Experiments and theory. *Rev. Mod. Phys.* **86**, 669–716 (2014).
65. Bhandari, C. M. in Rowe 2005, pp. 55–65.
66. Snyder, G. J., Christensen, M., Nishibori, E., Caillat, T. & Iversen, B. B. Disordered zinc in Zn₄Sb₃ with phonon-glass and electron-crystal thermoelectric properties. *Nat. Mater.* **3**, 458–463 (2004).
67. Kanatzidis, M. G. Nanostructured thermoelectrics: The new paradigm? *Chem. Mater.* **22**, 648–659 (2010).

68. Minnich, A. J., Dresselhaus, M. S., Ren, Z. F. & Chen, G. Bulk nanostructured thermoelectric materials: Current research and future prospects. *Energy Environ. Sci.* **2**, 466–479 (2009).
69. Morelli, D. T., Jovovic, V. & Heremans, J. P. Intrinsically minimal thermal conductivity in cubic I-V-VI₂ semiconductors. *Phys. Rev. Lett.* **101**, 16–19 (2008).
70. Garg, J., Bonini, N., Kozinsky, B. & Marzari, N. Role of disorder and anharmonicity in the thermal conductivity of silicon-germanium alloys: A first-principles study. *Phys. Rev. Lett.* **106**, 1–4 (2011).
71. Pei, Y., Wang, H. & Snyder, G. J. Band engineering of thermoelectric materials. *Adv. Mater.* **24**, 6125–6135 (2012).
72. Ko, D. K., Kang, Y. & Murray, C. B. Enhanced thermopower via carrier energy filtering in solution-processable Pt-Sb₂Te₃ nanocomposites. *Nano Lett.* **11**, 2841–2844 (2011).
73. Zhang, H. *et al.* Topological insulators in Bi₂Se₃, Bi₂Te₃ and Sb₂Te₃ with a single Dirac cone on the surface. *Nat. Phys.* **5**, 438–442 (2009).
74. Hsieh, T. H. *et al.* Topological crystalline insulators in the SnTe material class. *Nat. Commun.* **3**, (2012).
75. Chen, Y. L. *et al.* Experimental realization of a three-dimensional topological insulator, Bi₂Te₃. *Science (80-.).* **325**, 178–181 (2009).
76. Xing, Y., Zhang, L. & Wang, J. Topological Anderson insulator phenomena. *Phys. Rev. B - Condens. Matter Mater. Phys.* **84**, 1–9 (2011).
77. Müchler, L., Casper, F., Yan, B., Chadov, S. & Felser, C. Topological insulators and thermoelectric materials. *Phys. Status Solidi - Rapid Res. Lett.* **7**, 91–100 (2013).
78. Hsieh, D. *et al.* Observation of time-reversal-protected single-dirac-cone topological-insulator states in Bi₂Te₃ and Sb₂Te₃. *Phys. Rev. Lett.* **103**, 2–5 (2009).
79. Zhang, J. *et al.* Band structure engineering in (Bi_{1-x}Sbx) ₂Te₃ ternary topological insulators. *Nat. Commun.* **2**, (2011).
80. Murakami, S., Takahashi, R., Tretiakov, O. A., Abanov, A. & Sinova, J. Thermoelectric transport of perfectly conducting channels in two- and three-dimensional topological insulators. *J. Phys. Conf. Ser.* **334**, (2011).
81. Takahashi, R. & Murakami, S. Thermoelectric transport in topological insulators. *Semicond. Sci. Technol.* **27**, (2012).
82. Xu, Y., Gan, Z. & Zhang, S. C. Enhanced thermoelectric performance and anomalous seebeck effects in topological insulators. *Phys. Rev. Lett.* **112**, 1–5 (2014).
83. Xu, N., Xu, Y. & Zhu, J. Topological insulators for

- thermoelectrics. *npj Quantum Mater.* **2**, 1–9 (2017).
- 84. Hasan, M. Z. & Kane, C. L. Colloquium: Topological insulators. *Rev. Mod. Phys.* **82**, 3045–3067 (2010).
 - 85. Li, J., Chu, R. L., Jain, J. K. & Shen, S. Q. Topological anderson insulator. *Phys. Rev. Lett.* **102**, 1–4 (2009).
 - 86. Groth, C. W., Wimmer, M., Akhmerov, A. R., Tworzydł o, J. & Beenakker, C. W. J. Theory of the Topological Anderson Insulator. *Phys. Rev. Lett.* **103**, 1–4 (2009).
 - 87. Guo, H. M., Rosenberg, G., Refael, G. & Franz, M. Topological Anderson insulator in three dimensions. *Phys. Rev. Lett.* **105**, 2–5 (2010).
 - 88. Blaser, H. U., Indolese, A., Schnyder, A., Steiner, H. & Studer, M. Supported palladium catalysts for fine chemicals synthesis. *J. Mol. Catal. A Chem.* (2001) doi:10.1016/S1381-1169(01)00143-1.
 - 89. Antolini, E. Palladium in fuel cell catalysis. *Energy Environ. Sci.* **2**, 915–931 (2009).
 - 90. Ataollahi, N. *et al.* A Polyketone-based Anion Exchange Membrane for Electrochemical Applications: Synthesis and Characterization. *Electrochim. Acta* **226**, 148–157 (2017).
 - 91. Ataollahi, N. *et al.* Chemical modification and structural rearrangements of polyketone-based polymer membrane. *J. Appl. Polym. Sci.* **134**, 1–8 (2017).
 - 92. Kishore, S., Nelson, J. A., Adair, J. H. & Eklund, P. C. Hydrogen storage in spherical and platelet palladium nanoparticles. *J. Alloys Compd.* **389**, 234–242 (2005).
 - 93. Shao, M., Yu, T., Odell, J. H., Jin, M. & Xia, Y. Structural dependence of oxygen reduction reaction on palladium nanocrystals. *Chem. Commun.* **47**, 6566–6568 (2011).
 - 94. Xiong, Y., McLellan, J. M., Yin, Y. & Xia, Y. Synthesis of palladium icosahedra with twinned structure by blocking oxidative etching with citric acid or citrate ions. *Angew. Chemie - Int. Ed.* **46**, 790–794 (2007).
 - 95. Xiong, Y. & Xia, Y. Shape-controlled synthesis of metal nanostructures: The case of palladium. *Adv. Mater.* **19**, 3385–3391 (2007).
 - 96. Niu, Z., Peng, Q., Gong, M., Rong, H. & Li, Y. Oleylamine-mediated shape evolution of palladium nanocrystals. *Angew. Chemie - Int. Ed.* **50**, 6315–6319 (2011).
 - 97. Jin, M., Zhang, H., Xie, Z. & Xia, Y. Palladium concave nanocubes with high-index facets and their enhanced catalytic properties. *Angew. Chemie - Int. Ed.* **50**, 7850–7854 (2011).
 - 98. Niu, W. *et al.* Seed-mediated growth of nearly monodisperse palladium nanocubes with controllable sizes. *Cryst. Growth*

- Des.* **8**, 4440–4444 (2008).
- 99. Zhang, Q., Xie, J., Yang, J. & Lee, J. Y. ARTICLE and Superlattice Formation. *Society* **3**, 139–48 (2009).
 - 100. Jin, M., Zhang, H., Xie, Z. & Xia, Y. Palladium nanocrystals enclosed by {100} and {111} facets in controlled proportions and their catalytic activities for formic acid oxidation. *Energy Environ. Sci.* **5**, 6352–6357 (2012).
 - 101. Wang, F. *et al.* Heteroepitaxial growth of high-index-faceted palladium nanoshells and their catalytic performance. *J. Am. Chem. Soc.* **133**, 1106–1111 (2011).
 - 102. Yu, Y., Zhang, Q., Liu, B. & Lee, J. Y. Synthesis of nanocrystals with variable high-index Pd facets through the controlled heteroepitaxial growth of trisoctahedral Au templates. *J. Am. Chem. Soc.* **132**, 18258–18265 (2010).
 - 103. Fan, F. R. *et al.* Epitaxial growth of heterogeneous metal nanocrystals: From gold nano-octahedra to palladium and silver nanocubes. *J. Am. Chem. Soc.* **130**, 6949–6951 (2008).
 - 104. Tian, N., Zhou, Z. Y., Yu, N. F., Wang, L. Y. & Sun, S. G. Direct electrodeposition of tetrahexahedral Pd nanocrystals with high-index facets and high catalytic activity for ethanol electrooxidation. *J. Am. Chem. Soc.* **132**, 7580–7581 (2010).
 - 105. Tian, N., Zhou, Z. Y. & Sun, S. G. Electrochemical preparation of Pd nanorods with high-index facets. *Chem. Commun.* 1502–1504 (2009) doi:10.1039/b819751b.
 - 106. Long, R. *et al.* Surface facet of palladium nanocrystals: A key parameter to the activation of molecular oxygen for organic catalysis and cancer treatment. *J. Am. Chem. Soc.* **135**, 3200–3207 (2013).
 - 107. Bratlie, K. M., Lee, H., Komvopoulos, K., Yang, P. & Somorjai, G. A. Platinum nanoparticle shape effects on benzene hydrogenation selectivity. *Nano Lett.* **7**, 3097–3101 (2007).
 - 108. Crespo-Quesada, M., Yarulin, A., Jin, M., Xia, Y. & Kiwi-Minsker, L. Structure sensitivity of alkynol hydrogenation on shape- and size-controlled palladium nanocrystals: Which sites are most active and selective? *J. Am. Chem. Soc.* **133**, 12787–12794 (2011).
 - 109. Sun, M. *et al.* Sup_Re-engineering the zinc fingers of PRDM9 reverses hybrid sterility in mice. *Nature* **530**, 171–176 (2016).
 - 110. Chen, C. *et al.* Highly crystalline multimetallic nanoframes with three-dimensional electrocatalytic surfaces. *Science (80-.)* **343**, 1339–1343 (2014).
 - 111. Snead, B. T., Kuo, C. H., Brodsky, C. N. & Tsung, C. K. Iodide-mediated control of rhodium epitaxial growth on well-

- defined noble metal nanocrystals: Synthesis, characterization, and structure-dependent catalytic properties. *J. Am. Chem. Soc.* **134**, 18417–18426 (2012).
- 112. Zhao, Y. *et al.* Mesoscopic constructs of ordered and oriented metal-organic frameworks on plasmonic silver nanocrystals. *J. Am. Chem. Soc.* **137**, 2199–2202 (2015).
 - 113. Niu, Z. & Li, Y. Removal and utilization of capping agents in nanocatalysis. *Chem. Mater.* **26**, 72–83 (2014).
 - 114. Sadeghmoghadam, E., Gaïeb, K. & Shon, Y. S. Catalytic isomerization of allyl alcohols to carbonyl compounds using poisoned Pd nanoparticles. *Appl. Catal. A Gen.* **405**, 137–141 (2011).
 - 115. Snelders, D. J. M., Yan, N., Gan, W., Laurenczy, G. & Dyson, P. J. Tuning the chemoselectivity of Rh nanoparticle catalysts by site-selective poisoning with phosphine ligands: The hydrogenation of functionalized aromatic compounds. *ACS Catal.* **2**, 201–207 (2012).
 - 116. Khomskii, D. I. Phonons in crystals. in *Basic Aspects of The Quantum Theory of Solids* 34–53 (Cambridge University Press, 2010). doi:10.1017/CBO9780511780271.005.
 - 117. Bozyigit, D. *et al.* Soft surfaces of nanomaterials enable strong phonon interactions. *Nature* **531**, 618–622 (2016).
 - 118. Sterrer, M. & Freund, H. J. Towards realistic surface science models of heterogeneous catalysts: Influence of support hydroxylation and catalyst preparation method. *Catal. Letters* **143**, 375–385 (2013).
 - 119. Lee, H. *et al.* Morphological control of catalytically active platinum nanocrystals. *Angew. Chemie - Int. Ed.* **45**, 7824–7828 (2006).
 - 120. Lee, I., Delbecq, F., Morales, R., Albiter, M. A. & Zaera, F. Tuning selectivity in catalysis by controlling particle shape. *Nat. Mater.* **8**, 132–138 (2009).
 - 121. Mostafa, S. *et al.* Shape-dependent catalytic properties of Pt nanoparticles. *J. Am. Chem. Soc.* **132**, 15714–15719 (2010).
 - 122. Scardi, P. *et al.* Anisotropic atom displacement in Pd nanocubes resolved by molecular dynamics simulations supported by x-ray diffraction imaging. *Phys. Rev. B - Condens. Matter Mater. Phys.* **91**, 1–8 (2015).
 - 123. Flor, A., Feliu, J. M., Tsung, C. K. & Scardi, P. Vibrational properties of pd nanocubes. *Nanomaterials* **9**, 609–624 (2019).
 - 124. Scardi, P. Microstructural Properties : Lattice Defects and Domain Size Effects. in (eds. Dinnebier, R. & Bilinge, S.) 378–417 (Royal Society of Chemistry, 2008).
 - 125. Vidal-Iglesias, F. J. *et al.* Shape-dependent electrocatalysis:

- Formic acid electrooxidation on cubic Pd nanoparticles. *Phys. Chem. Chem. Phys.* **14**, 10258–10265 (2012).
126. Solla-Gullon, J. *et al.* Structure and morphology of shape-controlled Pd nanocrystals. *J. Appl. Crystallogr.* **48**, 1534–1542 (2015).
127. Wang, J. *et al.* A dedicated powder diffraction beamline at the Advanced Photon Source: Commissioning and early operational results. *Rev. Sci. Instrum.* **79**, 1–8 (2008).
128. Scardi, P. & Gelisio, L. Vibrational Properties of Nanocrystals from the Debye Scattering Equation. *Sci. Rep.* **6**, 1–7 (2016).
129. Beyerlein, K. R., Leoni, M. & Scardi, P. Temperature diffuse scattering of nanocrystals. *Acta Crystallogr. Sect. A Found. Crystallogr.* **68**, 382–392 (2012).
130. Plimpton, S. Fast parallel algorithms for short-range molecular dynamics. *Journal of Computational Physics* vol. 117 1–19 (1995).
131. Daw, M. S. & Baskes, M. I. Semiempirical, quantum mechanical calculation of hydrogen embrittlement in metals. *Phys. Rev. Lett.* **50**, 1285–1288 (1983).
132. Daw, M. S. & Baskes, M. I. Embedded-atom method: Derivation and application to impurities, surfaces, and other defects in metals. *Phys. Rev. B* **29**, 6443–6453 (1984).
133. Sheng, H. W., Kramer, M. J., Cadien, A., Fujita, T. & Chen, M. W. Highly optimized embedded-atom-method potentials for fourteen FCC metals. *Phys. Rev. B - Condens. Matter Mater. Phys.* **83**, 1–20 (2011).
134. Martyna, G. J., Tobias, D. J. & Klein, M. L. Constant pressure molecular dynamics algorithms. *J. Chem. Phys.* **101**, 4177–4189 (1994).
135. Humphrey, W., Dalke, A. & Schulter, K. VMD: Visual Molecular Dynamics. *J. Mol. Graph.* **14**, 33–38 (1996).
136. Giannozzi, P. *et al.* QUANTUM ESPRESSO: A modular and open-source software project for quantum simulations of materials. *J. Phys. Condens. Matter* **21**, (2009).
137. Giannozzi, P. *et al.* Advanced capabilities for materials modelling with Quantum ESPRESSO. *J. Phys. Condens. Matter* **29**, (2017).
138. Perdew, J. P. *et al.* Restoring the density-gradient expansion for exchange in solids and surfaces. *Phys. Rev. Lett.* **100**, 1–4 (2008).
139. Terentjev, A. V., Constantin, L. A. & Pitarke, J. M. Dispersion-corrected PBEsol exchange-correlation functional. *Phys. Rev. B* **98**, 1–12 (2018).
140. Maschio, L., Ferrabone, M., Meyer, A., Garza, J. & Dovesi, R.

- The infrared spectrum of spessartine Mn₃Al₂Si 3O₁₂: An ab initio all electron simulation with five different functionals (LDA, PBE, PBESOL, B3LYP and PBE0). *Chem. Phys. Lett.* **501**, 612–618 (2011).
141. Ahuja, B. L. *et al.* Electronic properties and momentum densities of tin chalcogenides: Validation of PBEsol exchange-correlation potential. *Phys. B Condens. Matter* **465**, 21–28 (2015).
142. Grimme, S. Semiempirical GGA-Type Density Functional Constructed with a Long-Range Dispersion Correction. *J. Comput. Chem.* **27**, 1787–1799 (2006).
143. Stukowski, A. Visualization and analysis of atomistic simulation data with OVITO—the Open Visualization Tool. *Model. Simul. Mater. Sci. Eng.* **18**, 015012 (2010).
144. Warren, B. E. & Averbach, B. L. The effect of cold-work distortion on x-ray patterns. *J. Appl. Phys.* **21**, 595–599 (1950).
145. Scardi, P., Rebuffi, L., Abdellatif, M., Flor, A. & Leonardi, A. Debye-Waller coefficient of heavily deformed nanocrystalline iron. *J. Appl. Crystallogr.* **50**, 508–518 (2017).
146. Iwasawa, Y. *X-Ray Absorption Fine Structure for Catalysts and Surfaces*. (World Scientific Publishing Co. Pte. Ltd., 1996).
147. Scardi, P. & Flor, A. Correlated Debye model for atomic motions in metal nanocrystals. *Philos. Mag.* **98**, 1412–1435 (2018).
148. Zhou, L. G. & Huang, H. Response embedded atom method of interatomic potentials. *Phys. Rev. B - Condens. Matter Mater. Phys.* **87**, 1–6 (2013).
149. Buffat, P. & Borel, J. P. Size effect on the melting temperature of gold particles. *Phys. Rev. A* **13**, 2287–2298 (1976).
150. Stahl, S. S. Palladium-catalyzed oxidation of organic chemicals with O₂. *Science (80-.).* **309**, 1824–1826 (2005).
151. Han, Y., He, Z., Wang, S., Li, W. & Zhang, J. Performance of facet-controlled Pd nanocrystals in 2-ethylanthraquinone hydrogenation. *Catal. Sci. Technol.* **5**, 2630–2639 (2015).
152. Li, Y. *et al.* Recent Progresses in Oxygen Reduction Reaction Electrocatalysts for Electrochemical Energy Applications. *Electrochem. Energy Rev.* **2**, 518–538 (2019).
153. Ciuparu, D., Lyubovsky, M. R., Altman, E., Pfefferle, L. D. & Datye, A. Catalytic combustion of methane over palladium-based catalysts. *Catal. Rev. - Sci. Eng.* **44**, 593–649 (2002).
154. Lee, J. H. & Trimm, D. L. Catalytic combustion of methane. *Fuel Process. Technol.* **42**, 339–359 (1995).
155. Beebe, T. P., Goodman, D. W., Kay, B. D. & Yates, J. T.

- Kinetics of the activated dissociative adsorption of methane on the low index planes of nickel single crystal surfaces. *J. Chem. Phys.* **87**, 2305–2315 (1987).
156. Oh, S. H. & Mitchell, P. J. Effects of rhodium addition on methane oxidation behavior of alumina-supported noble metal catalysts. *Appl. Catal. B, Environ.* **5**, 165–179 (1994).
157. Yarw-Nan, W., Herman, R. G. & Klier, K. Dissociative adsorption of methane on Pd(679) surface. *Surf. Sci.* **279**, 33–48 (1992).
158. Hoflund, G. B., Hagelin, H. A. E., Weaver, J. F. & Salaita, G. N. ELS and XPS study of Pd/PdO methane oxidation catalysts. *Appl. Surf. Sci.* **205**, 102–112 (2002).
159. Zhu, G., Han, J., Zemlyanov, D. Y. & Ribeiro, F. H. Temperature dependence of the kinetics for the complete oxidation of methane on palladium and palladium oxide. *J. Phys. Chem. B* **109**, 2331–2337 (2005).
160. Senftle, T. P., Meyer, R. J., Janik, M. J. & Van Duin, A. C. T. Development of a ReaxFF potential for Pd/O and application to palladium oxide formation. *J. Chem. Phys.* **139**, (2013).
161. Lyubovsky, M. & Pfefferle, L. Complete methane oxidation over Pd catalyst supported on α -alumina. Influence of temperature and oxygen pressure on the catalyst activity. *Catal. Today* **47**, 29–44 (1999).
162. McCarty, J. G. Kinetics of PdO combustion catalysis. *Catal. Today* **26**, 283–293 (1995).
163. Lyubovsky, M., Pfefferle, L., Datye, A., Bravo, J. & Nelson, T. TEM study of the microstructural modifications of an alumina-supported palladium combustion catalyst. *J. Catal.* **187**, 275–284 (1999).
164. Jurzinsky, T., Cremers, C., Jung, F., Pinkwart, K. & Tübke, J. Development of materials for anion-exchange membrane direct alcohol fuel cells. *Int. J. Hydrogen Energy* **40**, 11569–11576 (2015).
165. You, W., Noonan, K. J. T. & Coates, G. W. Alkaline-stable anion exchange membranes: A review of synthetic approaches. *Prog. Polym. Sci.* **100**, 101177 (2020).
166. Shao, M., Liu, P., Zhang, J. & Adzic, R. Origin of enhanced activity in palladium alloy electrocatalysts for oxygen reduction reaction. *J. Phys. Chem. B* **111**, 6772–6775 (2007).
167. Collins, G., Schmidt, M., McGlacken, G. P., O'Dwyer, C. & Holmes, J. D. Stability, oxidation, and shape evolution of PVP-capped Pd nanocrystals. *J. Phys. Chem. C* **118**, 6522–6530 (2014).
168. Mao, Q., Van Duin, A. C. T. & Luo, K. H. Investigation of

- methane oxidation by palladium-based catalyst via ReaxFF Molecular Dynamics simulation. *Proc. Combust. Inst.* **36**, 4339–4346 (2017).
- 169. Zhang, D. *et al.* An: In situ TEM study of the surface oxidation of palladium nanocrystals assisted by electron irradiation. *Nanoscale* **9**, 6327–6333 (2017).
 - 170. Yu, J. *et al.* Fast Gas–Solid Reaction Kinetics of Nanoparticles Unveiled by Millisecond In Situ Electron Diffraction at Ambient Pressure. *Angew. Chemie - Int. Ed.* **57**, 11344–11348 (2018).
 - 171. Sneed, B. T., Young, A. P. & Tsung, C. K. Building up strain in colloidal metal nanoparticle catalysts. *Nanoscale* **7**, 12248–12265 (2015).
 - 172. Kim, D. *et al.* Active site localization of methane oxidation on Pt nanocrystals. *Nat. Commun.* **9**, 1–7 (2018).
 - 173. Rebuffi, L. *et al.* Surface softening in palladium nanoparticles: Effects of a capping agent on vibrational properties. *Nanoscale* **12**, 5876–5887 (2020).
 - 174. Jin, M. *et al.* Synthesis of Pd nanocrystals enclosed by {100} facets and with sizes <10 nm for application in CO oxidation. *Nano Res.* **4**, 83–91 (2011).
 - 175. Coelho, A. A. TOPAS and TOPAS-Academic: An optimization program integrating computer algebra and crystallographic objects written in C++: An. *J. Appl. Crystallogr.* **51**, 210–218 (2018).
 - 176. Humphrey, W., Dalke, A. & Schulten, K. VMD: Visual molecular dynamics. *J. Mol. Graph.* **14**, 33–38 (1996).
 - 177. Van Duin, A. C. T., Dasgupta, S., Lorant, F. & Goddard, W. A. ReaxFF: A reactive force field for hydrocarbons. *J. Phys. Chem. A* **105**, 9396–9409 (2001).
 - 178. Van Duin, A. C. T. *et al.* ReaxFFSiO reactive force field for silicon and silicon oxide systems. *J. Phys. Chem. A* **107**, 3803–3811 (2003).
 - 179. Akimov, A. V. & Prezhdo, O. V. Large-Scale Computations in Chemistry: A Bird’s Eye View of a Vibrant Field. *Chem. Rev.* **115**, 5797–5890 (2015).
 - 180. Hong, S. & Van Duin, A. C. T. Molecular Dynamics Simulations of the Oxidation of Aluminum Nanoparticles using the ReaxFF Reactive Force Field. *J. Phys. Chem. C* **119**, 17876–17886 (2015).
 - 181. Chenoweth, K., Van Duin, A. C. T. & Goddard, W. A. ReaxFF reactive force field for molecular dynamics simulations of hydrocarbon oxidation. *J. Phys. Chem. A* **112**, 1040–1053 (2008).

182. Momma, K. & Izumi, F. VESTA 3 for three-dimensional visualization of crystal, volumetric and morphology data. *J. Appl. Crystallogr.* **44**, 1272–1276 (2011).
183. Bhattacharya, S. & Ghosh, A. Conductivity relaxation in some fast ion-conducting AgI-Ag₂O-V₂O₅ glasses. *Solid State Ionics* **161**, 61–65 (2003).
184. Minami, T. Preparation and properties of superionic conducting glasses based on silver halides. *J. Non. Cryst. Solids* **56**, 15–26 (1983).
185. Iqbal, S. *et al.* Application of silver oxide nanoparticles for the treatment of cancer. *J. Mol. Struct.* **1189**, 203–209 (2019).
186. Li, W. X., Stampfl, C. & Scheffler, M. Why is a Noble Metal Catalytically Active? The Role of the O-Ag Interaction in the Function of Silver as an Oxidation Catalyst. *Phys. Rev. Lett.* **90**, 4 (2003).
187. Gou, L. & Murphy, C. J. Solution-Phase Synthesis of Cu₂O Nanocubes. *Nano Lett.* **3**, 231–234 (2003).
188. Mittal, R., Chaplot, S. L., Mishra, S. K. & Bose, P. P. Inelastic neutron scattering and lattice dynamical calculation of negative thermal expansion compounds Cu₂O and Ag₂O. *Phys. Rev. B - Condens. Matter Mater. Phys.* **75**, 2–9 (2007).
189. Gupta, M. K., Mittal, R., Rols, S. & Chaplot, S. L. Inelastic neutron scattering an ab-initio calculation of negative thermal expansion in Ag₂O. *Phys. B Condens. Matter* **407**, 2146–2149 (2012).
190. Fornasini, P. *et al.* Local behaviour of negative thermal expansion materials. *Nucl. Instruments Methods Phys. Res. Sect. B Beam Interact. with Mater. Atoms* **246**, 180–183 (2006).
191. Beccara, S. a. *et al.* Local Thermal Expansion in a Cuprite Structure: The Case of [Formula presented]. *Phys. Rev. Lett.* **89**, 1–4 (2002).
192. Dapiaggi, M., Tiano, W., Artioli, G., Sanson, A. & Fornasini, P. The thermal behaviour of cuprite: An XRD-EXAFS combined approach. *Nucl. Instruments Methods Phys. Res. Sect. B Beam Interact. with Mater. Atoms* **200**, 231–236 (2003).
193. Sanson, A. *et al.* Negative thermal expansion and local dynamics in Cu₂O and Ag₂O. *Phys. Rev. B - Condens. Matter Mater. Phys.* **73**, 1–13 (2006).
194. Chapman, K. W. & Chupas, P. J. Anomalous thermal expansion of cuprites: a combined high resolution pair distribution function and geometric analysis. *Chem. Mater.* **21**, 425–431 (2009).

195. Dapiaggi, M., Kim, H. J., Božin, E. S., Billinge, S. J. L. & Artioli, G. Study of the negative thermal expansion of cuprite-type structures by means of temperature-dependent pair distribution function analysis: Preliminary results. *J. Phys. Chem. Solids* **69**, 2182–2186 (2008).
196. Artioli, G. *et al.* Negative thermal expansion in cuprite-type compounds: A combined synchrotron XRPD, EXAFS, and computational study of Cu₂O and Ag₂O. *J. Phys. Chem. Solids* **67**, 1918–1922 (2006).
197. Gupta, M. K., Mittal, R., Chaplot, S. L. & Rols, S. Phonons, nature of bonding, and their relation to anomalous thermal expansion behavior of M₂O (M = Au, Ag, Cu). *J. Appl. Phys.* **115**, (2014).
198. Sanson, A. A first-principles study of vibrational modes in Cu₂O and Ag₂O crystals. *Solid State Commun.* **151**, 1452–1454 (2011).
199. Lan, T. *et al.* Anharmonic lattice dynamics of Ag₂O studied by inelastic neutron scattering and first-principles molecular dynamics simulations. *Phys. Rev. B - Condens. Matter Mater. Phys.* **89**, 1–10 (2014).
200. Wada, T. *et al.* Inter-atomic force constants of Ag 2O from diffuse neutron scattering measurement. *Solid State Ionics* **225**, 18–21 (2012).
201. Rebuffi, L. *et al.* Surface softening in Palladium nanoparticles: Effects of a capping agent on vibrational properties. *Submitt. to Nanoscale* (2020) doi:10.1039/x0xx00000x.
202. Mukherjee, B., Flor, A. & Scardi, P. Effect of oxygen adsorption and oxidation on the strain state of Pd nanocrystals. *Appl. Surf. Sci.* **541**, 148508 (2021).
203. Isotta, E., Mukherjee, B., Bette, S., Dinnebier, R. & Scardi, P. Static and dynamic components of Debye–Waller coefficients in the novel cubic polymorph of low-temperature disordered Cu₂ZnSnS₄. *IUCrJ* **9**, 1–14 (2022).
204. Rietveld, H. M. A profile refinement method for nuclear and magnetic structures. *J. Appl. Crystallogr.* **2**, 65–71 (1969).
205. Sakuma, T. Structure and dynamic properties of solid state ionic. *Bull. Electrochem.* **11**, 57 (1995).
206. Kresse, G. & Hafner, J. Ab initio molecular-dynamics simulation of the liquid-metalamorphous- semiconductor transition in germanium. *Phys. Rev. B* **49**, 14251–14269 (1994).
207. Kresse, G. & Furthmüller, J. Efficiency of ab-initio total energy calculations for metals and semiconductors using a plane-wave basis set. *Comput. Mater. Sci.* **6**, 15–50 (1996).

208. Kresse, G. & Furthmüller, J. Efficient iterative schemes for ab initio total-energy calculations using a plane-wave basis set. *G. Phys. Rev. B* **54**, 169–186 (1996).
209. Togo, A. & Tanaka, I. First principles phonon calculations in materials science. *Scr. Mater.* **108**, 1–5 (2015).
210. Saleh, G., Xu, C. & Sanvito, S. Silver Tarnishing Mechanism Revealed by Molecular Dynamics Simulations. *Angew. Chemie - Int. Ed.* **58**, 6017–6021 (2019).
211. Warren, B. E. *Warren, X-ray Diffraction, 1990.pdf.* (Dover Publications, 1990).
212. Schorr, S. The crystal structure of kesterite type compounds: A neutron and X-ray diffraction study. *Sol. Energy Mater. Sol. Cells* **95**, 1482–1488 (2011).
213. Hallt, S. R., Szymanski, J. T. & Stewart, J. M. Kesterite, Cu₂(Zn,Fe)SnS₄, and Stannite, Cu₂(Zn,Fe)SnS₄, Structurally Similar But Distinct Minerals. *Can. Mineral.* **16**, 131–137 (1978).
214. Walsh, A., Chen, S., Wei, S. H. & Gong, X. G. Kesterite thin-film solar cells: Advances in materials modelling of Cu₂ZnSnS₄. *Adv. Energy Mater.* **2**, 400–409 (2012).
215. Siebentritt, S. & Schorr, S. Kesterites—a challenging material for solar cells. *Prog. PHOTOVOLTAICS Res. Appl.* **20**, 1114–1129 (2012).
216. Tanaka, T. *et al.* Preparation of Cu₂ZnSnS₄ thin films by hybrid sputtering. *J. Phys. Chem. Solids* **66**, 1978–1981 (2005).
217. Shockley, W. & Queisser, H. J. Detailed balance limit of efficiency of p-n junction solar cells. *J. Appl. Phys.* **32**, 510–519 (1961).
218. Wallace, S. K., Mitzi, D. B. & Walsh, A. The Steady Rise of Kesterite Solar Cells. *ACS Energy Lett.* **2**, 776–779 (2017).
219. Giraldo, S. *et al.* Progress and Perspectives of Thin Film Kesterite Photovoltaic Technology: A Critical Review. *Adv. Mater.* **31**, 1806692 (2019).
220. Todorov, T. K., Reuter, K. B. & Mitzi, D. B. High-efficiency solar cell with earth-abundant liquid-processed absorber. *Adv. Mater.* **22**, 156–159 (2010).
221. Wang, W. *et al.* Device characteristics of CZTSSe thin-film solar cells with 12.6% efficiency. *Adv. Energy Mater.* **4**, 1–5 (2014).
222. Son, D. H. *et al.* Effect of solid-H₂S gas reactions on CZTSSe thin film growth and photovoltaic properties of a 12.62% efficiency device. *J. Mater. Chem. A* **7**, 25279–25289 (2019).
223. Yan, C. *et al.* Cu₂ZnSnS₄ solar cells with over 10% power

- conversion efficiency enabled by heterojunction heat treatment. *Nat. Energy* **3**, 764–772 (2018).
224. Zhou, J. *et al.* Regulating crystal growth via organic lithium salt additive for efficient Kesterite solar cells. *Nano Energy* **89**, 106405 (2021).
225. Liu, M. L., Huang, F. Q., Chen, L. D. & Chen, I. W. A wide-band-gap p -type thermoelectric material based on quaternary chalcogenides of Cu₂ZnSnQ₄(Q=S,Se). *Appl. Phys. Lett.* **94**, 202103 (2009).
226. Yang, H., Jauregui, L. A., Zhang, G., Chen, Y. P. & Wu, Y. Non-Toxic and Abundant Copper Zinc Tin Sulfide Nanocrystals for Potential High Temperature Thermoelectric Energy Harvesting. *Nano Lett.* (2012) doi:10.1021/nl201718z.
227. Sharma, S. D., Bayikadi, K., Raman, S. & Neeleshwar, S. Synergistic optimization of thermoelectric performance in earth-abundant Cu₂ZnSnS₄by inclusion of graphene nanosheets. *Nanotechnology* **31**, (2020).
228. Jiang, Q. *et al.* Colossal thermoelectric enhancement in Cu_{2+x}Zn_{1-x}SnS₄solid solution by local disordering of crystal lattice and multi-scale defect engineering. *J. Mater. Chem. A* **8**, 10909–10916 (2020).
229. Long, B. D., Van Khanh, N., Binh, D. N. & Hai, N. H. Thermoelectric properties of quaternary chalcogenide Cu₂ZnSnS₄ synthesised by mechanical alloying . *Powder Metall.* **0**, 1–7 (2020).
230. Baláž, P. *et al.* Thermoelectric Cu–S-Based Materials Synthesized via a Scalable Mechanochemical Process. *ACS Sustain. Chem. Eng.* **9**, 2003–2016 (2021).
231. Kosuga, A., Matsuzawa, M., Horie, A., Omoto, T. & Funahashi, R. High-temperature thermoelectric properties and thermal stability in air of copper zinc tin sulfide for the p-type leg of thermoelectric devices. *Jpn. J. Appl. Phys.* **54**, (2015).
232. Kumar, S., Ansari, M. Z. & Khare, N. Influence of compactness and formation of metallic secondary phase on the thermoelectric properties of Cu₂ZnSnS₄thin films. *Thin Solid Films* **645**, 300–304 (2018).
233. Nagaoka, A., Masuda, T., Yasui, S., Taniyama, T. & Nose, Y. The single-crystal multinary compound Cu₂ZnSnS₄ as an environmentally friendly high-performance thermoelectric material. *Appl. Phys. Express* **11**, (2018).
234. Isotta, E., Pugno, N. M. & Scardi, P. Nanostructured kesterite (Cu₂ZnSnS₄) for applications in thermoelectric devices. *Powder Diffr.* **32**, 42–47 (2019).
235. Isotta, E., Fanciulli, C., Pugno, N. M. & Scardi, P. Effect of the

- Order-Disorder Transition on the Seebeck Coefficient of Nanostructured Thermoelectric. *Nanomaterials* **1**–11 (2019).
236. Sharma, S. D., Khasimsaheb, B., Chen, Y. Y. & Neeleshwar, S. Enhanced thermoelectric performance of Cu₂ZnSnS₄ (CZTS) by incorporating Ag nanoparticles. *Ceram. Int.* **45**, 2060–2068 (2019).
237. Isotta, E., Mukherjee, B., Fanciulli, C., Pugno, N. M. & Scardi, P. Order-Disorder Transition in Kesterite Cu₂ZnSnS₄: Thermopower Enhancement via Electronic Band Structure Modification. *J. Phys. Chem. C* **124**, 7091–7096 (2020).
238. Isotta, E. *et al.* Origin of a Simultaneous Suppression of Thermal Conductivity and Increase of Electrical Conductivity and Seebeck Coefficient in Disordered Cubic Cu₂ZnSnS₄. *Phys. Rev. Appl.* **14**, 1 (2020).
239. Zheng, X. *et al.* P-type quaternary chalcogenides of Cu₂ZnSn(S,Se)₄ nanocrystals: Large-scale synthesis, bandgap engineering and their thermoelectric performances. *J. Alloys Compd.* **738**, 484–490 (2018).
240. Isotta, E. *et al.* Thermoelectric properties of CZTS thin films: effect of Cu-Zn disorder. *Phys. Chem. Chem. Phys.* **23**, 13148–13158 (2021).
241. Todorov, T., Gershon, T., Gunawan, O., Sturdevant, C. & Guha, S. Perovskite-kesterite monolithic tandem solar cells with high open-circuit voltage. *Appl. Phys. Lett.* **105**, (2014).
242. Ros, C. *et al.* Turning Earth Abundant Kesterite-Based Solar Cells into Efficient Protected Water-Splitting Photocathodes. *ACS Appl. Mater. Interfaces* **10**, 13425–13433 (2018).
243. Wang, J. J., Hu, J. S., Guo, Y. G. & Wan, L. J. Eco-friendly visible-wavelength photodetectors based on bandgap engineerable nanomaterials. *J. Mater. Chem.* **21**, 17582–17589 (2011).
244. Gurav, K. V. *et al.* Cu₂ZnSnS₄ (CZTS)-based room temperature liquefied petroleum gas (LPG) sensor. *Sensors Actuators, B Chem.* **190**, 408–413 (2014).
245. Shinde, N. M., Deshmukh, P. R., Patil, S. V. & Lokhande, C. D. Development of polyaniline/Cu₂ZnSnS₄ (CZTS) thin film based heterostructure as room temperature LPG sensor. *Sensors Actuators, A Phys.* **193**, 79–86 (2013).
246. Narducci, D. & Lorenzi, B. Economic Convenience of Hybrid Thermoelectric-Photovoltaic Solar Harvesters. *ACS Appl. Energy Mater.* (2021) doi:10.1021/acsam.1c00394.
247. Schorr, S., Hoebler, H. J. & Tovar, M. A neutron diffraction study of the stannite-kesterite solid solution series. *Eur. J. Mineral.* **19**, 65–73 (2007).

248. Schorr, S. & Gonzalez-Aviles, G. In-situ investigation of the structural phase transition in kesterite. *Phys. Status Solidi Appl. Mater. Sci.* **206**, 1054–1058 (2009).
249. Scragg, J. J. S., Choubrac, L., Lafond, A., Ericson, T. & Platzer-Björkman, C. A low-temperature order-disorder transition in Cu₂ZnSnS₄ thin films. *Appl. Phys. Lett.* **104**, 041911 (2014).
250. Paier, J., Asahi, R., Nagoya, A. & Kresse, G. Cu₂ZnSnS₄ as a potential photovoltaic material: A hybrid Hartree-Fock density functional theory study. *Phys. Rev. B - Condens. Matter Mater. Phys.* **79**, 1–8 (2009).
251. Chen, S., Gong, X. G., Walsh, A. & Wei, S. H. Electronic structure and stability of quaternary chalcogenide semiconductors derived from cation cross-substitution of II-VI and I-III-VI₂ compounds. *Phys. Rev. B - Condens. Matter Mater. Phys.* **79**, 1–10 (2009).
252. Yu, K. & Carter, E. A. A strategy to stabilize kesterite CZTS for high-performance solar cells. *Chem. Mater.* **27**, 2920–2927 (2015).
253. Choubrac, L., Lafond, A., Guillot-Deudon, C., Moëlo, Y. & Jobic, S. Structure flexibility of the Cu₂ZnSnS₄ absorber in low-cost photovoltaic cells: From the stoichiometric to the copper-poor compounds. *Inorg. Chem.* **51**, 3346–3348 (2012).
254. Dimitrievska, M. *et al.* Structural Polymorphism in ‘Kesterite’ Cu₂ZnSnS₄: Raman Spectroscopy and First-Principles Calculations Analysis. *Inorg. Chem.* **56**, 3467–3474 (2017).
255. Lu, X., Zhuang, Z., Peng, Q. & Li, Y. Wurtzite Cu₂ZnSnS₄ nanocrystals: A novel quaternary semiconductor. *Chem. Commun.* **47**, 3141–3143 (2011).
256. Li, Z. *et al.* Phase-Selective Synthesis of Cu₂ZnSnS₄ Nanocrystals using Different Sulfur Precursors. *Am. Chem. Soc.* (2014).
257. Mainz, R. *et al.* Phase-transition-driven growth of compound semiconductor crystals from ordered metastable nanorods. *Nat. Commun.* **5**, 1–10 (2014).
258. Singh, A. *et al.* Compositionally Tunable Photoluminescence Emission in Cu₂ZnSn(S_{1-x}Se_x)₄ Nanocrystals. *Angew. Chemie* **125**, 9290–9294 (2013).
259. Singh, A., Geaney, H., Laffir, F. & Ryan, K. M. Colloidal synthesis of wurtzite Cu₂ZnSnS₄ nanorods and their perpendicular assembly. *J. Am. Chem. Soc.* **134**, 2910–2913 (2012).
260. Zhou, B., Xia, D. & Wang, Y. Phase-selective synthesis and formation mechanism of CZTS nanocrystals. *RSC Adv.* **5**,

- 70117–70126 (2015).
261. Azanza Ricardo, C. L. *et al.* Chloride-based route for monodisperse Cu₂ZnSnS₄ nanoparticles preparation. *J. Renew. Sustain. Energy* **7**, 043150 (2015).
262. Syafiq, U., Ataollahi, N., Maggio, R. Di & Scardi, P. Solution-Based Synthesis and Characterization of Cu₂ZnSnS₄ (CZTS) Thin Films. *Molecules* **24**, 3454 (2019).
263. Kattan, N., Hou, B., Fermín, D. J. & Cherns, D. Crystal structure and defects visualization of Cu₂ZnSnS₄ nanoparticles employing transmission electron microscopy and electron diffraction. *Appl. Mater. Today* **1**, 52–59 (2015).
264. Thompson, W. D., Nandur, A. & White, B. E. Thermal transport in Cu₂ZnSnS₄ thin films. *J. Appl. Phys.* **119**, (2016).
265. Engberg, S., Symonowicz, J., Schou, J., Canulescu, S. & Jensen, K. M. Ø. Characterization of Cu₂ZnSnS₄ Particles Obtained by the Hot-Injection Method. *ACS Omega* **5**, 10501–10509 (2020).
266. Schorr, S. & Geandier, G. In-situ investigation of the temperature dependent structural phase transition in CuInSe₂ by synchrotron radiation. *Cryst. Res. Technol.* **41**, 450–457 (2006).
267. Schorr, S., Geandier, G. & Korzun, B. V. Some are different from others: High temperature structural phase transitions in ternary chalcopyrites. *Phys. Status Solidi Curr. Top. Solid State Phys.* **3**, 2610–2613 (2006).
268. Kapusta, K. *et al.* From magnetic cubic pre-kesterite to semiconducting tetragonal kesterite Cu₂ZnSnS₄ nanopowders via the mechanochemically assisted route. *J. Alloys Compd.* **770**, 981–988 (2019).
269. Ritscher, A., Just, J., Dolotko, O., Schorr, S. & Lerch, M. A mechanochemical route to single phase Cu₂ZnSnS₄ powder. *J. Alloys Compd.* **670**, 289–296 (2016).
270. Park, B. I. *et al.* Solvent-free synthesis of Cu₂ZnSnS₄ nanocrystals: A facile, green, up-scalable route for low cost photovoltaic cells. *Nanoscale* **6**, 11703–11711 (2014).
271. Yao, W., Wang, Y., Wang, L., Wang, X. & Zhang, Z. Characterization and preparation of Cu₂ZnSnS₄ thin films by ball-milling, coating and sintering. *Mater. Lett.* **134**, 168–171 (2014).
272. Pareek, D., Balasubramaniam, K. R. & Sharma, P. Reaction pathway for synthesis of Cu₂ZnSn(S/Se)₄ via mechanochemical route and annealing studies. *J. Mater. Sci. Mater. Electron.* **28**, 1199–1210 (2017).
273. Hegedüs, M. *et al.* Mechanochemical approach to a

- Cu₂ZnSnS₄ solar cell absorber via a “micro-nano” route. *J. Mater. Sci.* **53**, 13617–13630 (2018).
274. Baláž, P. *et al.* Photovoltaic materials: Cu₂ZnSnS₄ (CZTS) nanocrystals synthesized via industrially scalable, green, one-step mechanochemical process. *Prog. Photovoltaics Res. Appl.* **27**, 798–811 (2019).
275. Shyju, T. S., Anandhi, S., Suriakarthick, R., Gopalakrishnan, R. & Kuppusami, P. Mechanosynthesis, deposition and characterization of CZTS and CZTSe materials for solar cell applications. *J. Solid State Chem.* **227**, 165–177 (2015).
276. Zhou, Y., Xi, S., Sun, C. & Wu, H. Facile synthesis of Cu₂ZnSnS₄ powders by mechanical alloying and annealing. *Mater. Lett.* **169**, 176–179 (2016).
277. Zhang, X., Fu, E., Zheng, M. & Wang, Y. Fabrication of Cu₂ZnSnS₄ thin films from ball-milled nanoparticle inks under various annealing temperatures. *Nanomaterials* **9**, (2019).
278. Alirezazadeh, F. & Sheibani, S. Facile mechano-chemical synthesis and enhanced photocatalytic performance of Cu₂ZnSnS₄ nanopowder. *Ceram. Int.* **46**, 26715–26723 (2020).
279. Brandl, M. *et al.* In-situ X-ray diffraction analysis of the recrystallization process in Cu₂ZnSnS₄nanoparticles synthesised by hot-injection. *Thin Solid Films* **582**, 269–271 (2015).
280. Ahmad, R. *et al.* A comprehensive study on the mechanism behind formation and depletion of Cu₂ZnSnS₄ (CZTS) phases. *CrystEngComm* **17**, 6972–6984 (2015).
281. Lohani, K. *et al.* Ultra-low thermal conductivity and improved thermoelectric performance in disordered nanostructured copper tin sulphide (Cu₂SnS₃, CTS). *J. Alloys Compd.* **830**, 154604 (2020).
282. Isotta, E., Mukherjee, B., Fanciulli, C. & Pugno, N. M. Order parameter from the Seebeck coefficient in thermoelectric kesterite Cu₂ZnSnS₄. *Proc. TMS* (2021).
283. Scragg, J. J. S., Choubrac, L., Lafond, A., Ericson, T. & Platzer-Björkman, C. A low-temperature order-disorder transition in Cu₂ZnSnS₄ thin films. *Appl. Phys. Lett.* **104**, 2–6 (2014).
284. Scragg, J. J. S. *et al.* Cu–Zn disorder and band gap fluctuations in Cu₂ZnSn(S,Se)4: Theoretical and experimental investigations. *Phys. Status Solidi B* **253**, 247–254 (2016).
285. Rudisch, K., Ren, Y., Platzer-Bjorkman, C. & Scragg, J. Order-disorder transition in B-type Cu₂ZnSnS₄ and limitations

- of ordering through thermal treatments. *Appl. Phys. Lett.* **231902** (2016) doi:10.1063/1.4953349.
286. Valentini, M. *et al.* Effect of the order-disorder transition on the optical properties of Cu₂ZnSnS₄. *Appl. Phys. Lett.* **108**, 211909 (2016).
287. Mendis, B. G., McKenna, K. P., Gurieva, G., Rumsey, M. S. & Schorr, S. Crystal structure and anti-site boundary defect characterisation of Cu₂ZnSnSe₄. *J. Mater. Chem. A* **6**, 189–197 (2017).
288. Chen, W., Dahliah, D., Rignanese, G. M. & Hautier, G. Origin of the low conversion efficiency in Cu₂ZnSnS₄ kesterite solar cells: The actual role of cation disorder. *Energy Environ. Sci.* **14**, 3567–3578 (2021).
289. Mukherjee, B., Isotta, E., Fanciulli, C., Ataollahi, N. & Scardi, P. Topological Anderson Insulator in Cation-Disordered Cu₂ZnSnS₄. *Nanomaterials* **11**, 2595 (2021).
290. Broseghini, M. *et al.* Modeling of the planetary ball-milling process: The case study of ceramic powders. *J. Eur. Ceram. Soc.* **36**, 2205–2212 (2016).
291. Dinnebier, R. E., Leineweber, A. & Evans, J. S. O. *Rietveld Refinement, practical powder diffraction pattern analysis using TOPAS*. De Gruyter (2018). doi:10.1515/9783110461381-201.
292. Kube, C. M. Elastic anisotropy of crystals. *AIP Adv.* **6**, 1–6 (2016).
293. He, X. & Shen, H. First-principles study of elastic and thermo-physical properties of kesterite-type Cu₂ZnSn₄. *Phys. B Condens. Matter* **406**, 4604–4607 (2011).
294. Nye, J. F. *Physical Properties of Crystals*. Oxford University Press (2006).
295. Katagiri, H. *et al.* Enhanced conversion efficiencies of Cu₂ZnSnS₄-based thin film solar cells by using preferential etching technique. *Appl. Phys. Express* **1**, 0412011–0412012 (2008).
296. Ataollahi, N. *et al.* Control of composition and grain growth in Cu₂ZnSnS₄ thin films from nanoparticle inks. *Thin Solid Films* **674**, 12–21 (2019).
297. Isotta, E., Pugno, N. M. & Scardi, P. Nanostructured kesterite (Cu₂ZnSnS₄) for applications in thermoelectric devices. *Powder Diffr.* **0**, 2–7 (2019).
298. Isotta, E., Fanciulli, C., Pugno, N. M. & Scardi, P. Effect of the Order-Disorder Transition on the Seebeck Coefficient of Nanostructured Thermoelectric Cu₂ZnSnS₄. *Nanomaterials* **9**, 762 (2019).
299. Kumar, S., Ansari, M. Z. & Khare, N. Influence of

- compactness and formation of metallic secondary phase on the thermoelectric properties of Cu₂ZnSnS₄ thin films. *Thin Solid Films* **645**, 300–304 (2018).
- 300. Sharma, S. D. & Neeleshwar, S. Thermoelectric Properties of hot pressed CZTS micro spheres synthetized by microwave method. *MRS Adv.* **3**, 1373–1378 (2018).
 - 301. Adachi, S. *Earth-Abundant Materials for Solar Cells*. (2015).
 - 302. Chen, S., Gong, X. G., Walsh, A. & Wei, S. Defect physics of the kesterite thin-film solar cell absorber. *Appl. Phys. Lett.* **96**, 021902 (2010).
 - 303. Chen, S., Walsh, A., Gong, X. & Wei, S. Classification of Lattice Defects in the Kesterite Cu₂ZnSnS₄ and Cu₂ZnSnSe₄ Earth-Abundant Solar Cell Absorbers. *Adv. Mater.* 1522–1539 (2013) doi:10.1002/adma.201203146.
 - 304. Kresse, G. & Furthmüller, J. Efficient iterative schemes for ab initio total-energy calculations using a plane-wave basis set. *Phys. Rev. B - Condens. Matter Mater. Phys.* **54**, 11169–11186 (1996).
 - 305. Hinuma, Y., Pizzi, G., Kumagai, Y., Oba, F. & Tanaka, I. Band structure diagram paths based on crystallography. *Comput. Mater. Sci.* **128**, 140–184 (2017).
 - 306. Malerba, C., Valentini, M. & Mittiga, A. Cation Disorder in Cu₂ZnSnS₄ Thin Films : Effect on Solar Cell Performances. *Sol. RRL* **1**, 1700101 (2017).
 - 307. Kittel, C. *Introduction to Solid State Physics-8th Edition*. (2005). doi:10.1119/1.1934457.
 - 308. Zeier, W. G. *et al.* Band convergence in the non-cubic chalcopyrite compounds Cu₂MGeSe₄. *J. Mater. Chem. C* **2**, 10189–10194 (2014).
 - 309. Zeier, W. G. New tricks for optimizing thermoelectric materials. *Curr. Opin. Green Sustain. Chem.* **4**, 23–28 (2017).
 - 310. Zhang, Q. *et al.* Deep defect level engineering : a strategy of optimizing the carrier concentration for high thermoelectric performance. *Energy Environ. Sci.* **11**, 933–940 (2018).
 - 311. Sun, P. *et al.* Large Seebeck effect by charge-mobility engineering. *Nat. Commun.* **6**, 1–5 (2015).
 - 312. Mott, N. F. & Jones, H. The Theory of the Properties of Metals and Alloys. *Journal of Chemical Education* vol. 14 99 (1936).
 - 313. Pei, Y., Lalonde, A. D., Wang, H. & Snyder, G. J. Low effective mass leading to high thermoelectric performance. *Energy Environ. Sci.* **5**, 7963–7969 (2012).
 - 314. Biswas, K. *et al.* High-performance bulk thermoelectrics with all-scale hierarchical architectures. *Nature* **489**, 414–418 (2012).

315. Zhao, L. D. *et al.* Ultralow thermal conductivity and high thermoelectric figure of merit in SnSe crystals. *Nature* **508**, 373–377 (2014).
316. Morata, A. *et al.* Large-area and adaptable electrospun silicon-based thermoelectric nanomaterials with high energy conversion efficiencies. *Nat. Commun.* **9**, 1–8 (2018).
317. Pei, Y. *et al.* Convergence of electronic bands for high performance bulk thermoelectrics. *Nature* **473**, 66–69 (2011).
318. Isotta, Fanciulli, Pugno & Scardi. Effect of the Order-Disorder Transition on the Seebeck Coefficient of Nanostructured Thermoelectric Cu₂ZnSnS₄. *Nanomaterials* **9**, 762 (2019).
319. Beekman, M., Morelli, D. T. & Nolas, G. S. Better thermoelectrics through glass-like crystals. *Nat. Mater.* **14**, 1182–1185 (2015).
320. Daniels, L. M. *et al.* Phonon-glass electron-crystal behaviour by A site disorder in n-type thermoelectric oxides. *Energy Environ. Sci.* **10**, 1917–1922 (2017).
321. Rowe, D. M. *Thermoelectrics and its energy harvesting*. (2012).
322. Isotta, E., Mukherjee, B., Fanciulli, C., Pugno, N. M. & Scardi, P. Order–Disorder Transition in Kesterite Cu₂ZnSnS₄: Thermopower Enhancement via Electronic Band Structure Modification - Supporting Information. *J. Phys. Chem. C* **2–4** (2020) doi:10.1021/acs.jpcc.0c00886.
323. Lin, S. *et al.* High Thermoelectric Performance of Ag₉GaSe₆ Enabled by Low Cutoff Frequency of Acoustic Phonons. *Joule* **1**, 816–830 (2017).
324. Roychowdhury, S. *et al.* Soft Phonon Modes Leading to Ultralow Thermal Conductivity and High Thermoelectric Performance in AgCuTe. *Angew. Chemie - Int. Ed.* **57**, 4043–4047 (2018).
325. Dutta, M., Pal, K., Waghmare, U. V. & Biswas, K. Bonding heterogeneity and lone pair induced anharmonicity resulted in ultralow thermal conductivity and promising thermoelectric properties in n-type AgPbBiSe₃. *Chem. Sci.* **10**, 4905–4913 (2019).
326. Snyder, G. J. & Toberer, E. S. Complex thermoelectric materials. *Nat. Mater.* **7**, 105–114 (2008).
327. Phaltane, S. A. *et al.* Photocatalytic degradation of methylene blue by hydrothermally synthesized CZTS nanoparticles. *J. Mater. Sci. Mater. Electron.* **28**, 8186–8191 (2017).
328. Ataollahi, N. *et al.* Synthesis and post-annealing of Cu₂ZnSnS₄ absorber layers based on Oleylamine/1-dodecanethiol. *Materials (Basel)*. **12**, (2019).

329. Silvi, B. & Savin, A. Classification of chemical bonds based on topological analysis of electron localization functions. *Nature* vol. 371 683–686 (1994).
330. Kim, S., Park, J. S., Hood, S. N. & Walsh, A. Lone-pair effect on carrier capture in Cu₂ZnSnS₄ solar cells. *J. Mater. Chem. A* **7**, 2686–2693 (2019).
331. Nielsen, M. D., Ozolins, V. & Heremans, J. P. Lone pair electrons minimize lattice thermal conductivity. *Energy Environ. Sci.* **6**, 570–578 (2013).
332. Zhao, L.-D. & Kanatzidis, M. G. Ultralow thermal conductivity and high thermoelectric figure of merit in SnSe crystals. *Nature* **508**, 373–377 (2014).
333. Jana, M. K., Pal, K., Waghmare, U. V & Biswas, K. The Origin of Ultralow Thermal Conductivity in InTe : Lone-Pair-Induced Anharmonic Rattling. *064*, 7923–7927 (2016).
334. Kohn, V. G. & Chumakov, A. I. DOS: Evaluation of phonon density of states from nuclear resonant inelastic absorption. *Hyperfine Interact.* **125**, 205–221 (2000).
335. Vitos, L. *Computational Quantum Mechanics for Materials Engineers. The EMTO Method and Applications* vol. 1 (2019).
336. Pal, K., Anand, S. & Waghmare, U. V. Thermoelectric properties of materials with nontrivial electronic topology. *J. Mater. Chem. C* **3**, 12130–12139 (2015).
337. Moore, J. E. The birth of topological insulators. *Nature* **464**, 194–198 (2010).
338. He, M., Sun, H. & He, Q. L. Topological insulator: Spintronics and quantum computations. *Front. Phys.* **14**, (2019).
339. Pesin, D. & MacDonald, A. H. Spintronics and pseudospintronics in graphene and topological insulators. *Nat. Mater.* **11**, 409–416 (2012).
340. Paudel, H. P. & Leuenberger, M. N. Three-dimensional topological insulator quantum dot for optically controlled quantum memory and quantum computing. *Phys. Rev. B - Condens. Matter Mater. Phys.* **88**, 1–17 (2013).
341. Klitzing, K. V., Dorda, G. & Pepper, M. New method for high-accuracy determination of the fine-structure constant based on quantized hall resistance. *Phys. Rev. Lett.* **45**, 494–497 (1980).
342. Fu, L., Kane, C. L. & Mele, E. J. Topological insulators in three dimensions. *Phys. Rev. Lett.* **98**, 1–4 (2007).
343. Hsieh, D. *et al.* A topological Dirac insulator in a quantum spin Hall phase. *Nature* **452**, 970–974 (2008).
344. Xia, Y. *et al.* Observation of a large-gap topological-insulator class with a single Dirac cone on the surface. *Nat. Phys.* **5**, 398–402 (2009).

345. Jiang, Y. *et al.* Landau quantization and the thickness limit of topological insulator thin films of Sb 2Te 3. *Phys. Rev. Lett.* **108**, 2–6 (2012).
346. Fu, L. Topological crystalline insulators. *Phys. Rev. Lett.* **106**, 1–4 (2011).
347. Alexandradinata, A., Fang, C., Gilbert, M. J. & Bernevig, B. A. Spin-Orbit-free topological insulators without time-reversal symmetry. *Phys. Rev. Lett.* **113**, 2–6 (2014).
348. Chen, S. *et al.* Band structure engineering of multinary chalcogenide topological insulators. *Phys. Rev. B - Condens. Matter Mater. Phys.* **83**, 1–5 (2011).
349. Wang, Y. J., Lin, H., Das, T., Hasan, M. Z. & Bansil, A. Topological insulators in the quaternary chalcogenide compounds and ternary famatinite compounds. *New J. Phys.* **13**, (2010).
350. Huang, H. & Liu, F. Quantum Spin Hall Effect and Spin Bott Index in a Quasicrystal Lattice. *Phys. Rev. Lett.* **121**, 126401 (2018).
351. Huang, H. & Liu, F. A Unified View of Topological Phase Transition in Band Theory. *Research* **2020**, 1–7 (2020).
352. Ni, X., Huang, H. & Liu, F. Robustness of topological insulating phase against vacancy, vacancy cluster, and grain boundary bulk defects. *Phys. Rev. B* **101**, 125114 (2020).
353. Meier, E. J. *et al.* Observation of the topological Anderson insulator in disordered atomic wires. *Science (80-.).* **933**, 929–933 (2018).
354. Nakajima, S. *et al.* Competition and interplay between topology and quasi-periodic disorder in Thouless pumping of ultracold atoms. *Nat. Phys.* (2021) doi:10.1038/s41567-021-01229-9.
355. Lim, D. H. & Wilcox, J. DFT-based study on oxygen adsorption on defective graphene-supported Pt nanoparticles. *J. Phys. Chem. C* **115**, 22742–22747 (2011).
356. Zhou, H. *et al.* CZTS nanocrystals: A promising approach for next generation thin film photovoltaics. *Energy Environ. Sci.* **6**, 2822–2838 (2013).
357. Ravindiran, M. & Praveenkumar, C. Status review and the future prospects of CZTS based solar cell – A novel approach on the device structure and material modeling for CZTS based photovoltaic device. *Renew. Sustain. Energy Rev.* **94**, 317–329 (2018).
358. Ataollahi, N. *et al.* Synthesis and Post-Annealing of Cu 2 ZnSnS 4 Absorber Layers Based on Oleylamine / 1-dodecanethiol. **4**,

359. Syafiq, U., Ataollahi, N., DiMaggio, R. & Scardi, P. Solution-based synthesis and characterization of Cu₂ZnSnS₄ (CZTS) thin films. *Molecules* **24**, 1–13 (2019).
360. Syafiq, U., Ataollahi, N. & Scardi, P. Progress in CZTS as hole transport layer in perovskite solar cell. *Sol. Energy* **196**, 399–408 (2020).
361. Ali, A. *et al.* Enhancement of thermoelectric properties of sulphurized CZTS nano-crystals by the engineering of secondary phases. *Solid State Sci.* **103**, 106198 (2020).
362. Ashfaq, A. *et al.* Tailoring the thermoelectric properties of sol-gel grown CZTS/ITO thin films by controlling the secondary phases. *Phys. B Condens. Matter* **558**, 86–90 (2019).
363. Ashfaq, A. *et al.* Designing of Seebeck coefficient and electrical conductivity in CZTS thin films for giant power factor. *Ceram. Int.* **46**, 9646–9655 (2020).
364. Persson, C. Electronic and optical properties of Cu₂ZnSnS₄ and Cu₂ZnSnSe₄. *J. Appl. Phys.* **107**, (2010).
365. Bernevig, B. A., Hughes, T. L. & Zhang, S. C. Quantum Spin Hall Effect and Topological Phase Transition in HgTe Quantum Wells. *Science (80-.)* **34**, 1757–1762 (2006).
366. Song, J., Liu, H., Jiang, H., Sun, Q. F. & Xie, X. C. Dependence of topological Anderson insulator on the type of disorder. *Phys. Rev. B - Condens. Matter Mater. Phys.* **85**, 1–8 (2012).
367. Girschik, A., Libisch, F. & Rotter, S. Topological insulator in the presence of spatially correlated disorder. *Phys. Rev. B - Condens. Matter Mater. Phys.* **88**, 1–7 (2013).
368. Bansil, A., Lin, H. & Das, T. Colloquium: Topological band theory. *Rev. Mod. Phys.* **88**, (2016).
369. Al-Sawai, W. *et al.* Topological electronic structure in half-Heusler topological insulators. *Phys. Rev. B - Condens. Matter Mater. Phys.* **82**, 1–5 (2010).
370. Chadov, S., Kiss, J., Kübler, J. & Felser, C. Topological phase transition in bulk materials described by the coherent potential approximation technique. *Phys. Status Solidi - Rapid Res. Lett.* **7**, 82–89 (2013).
371. Lin, H. *et al.* Half-Heusler ternary compounds as new multifunctional experimental platforms for topological quantum phenomena. *Nat. Mater.* **9**, 546–549 (2010).
372. Lin, H. *et al.* Adiabatic transformation as a search tool for new topological insulators: Distorted ternary Li₂AgSb-class semiconductors and related compounds. *Phys. Rev. B - Condens. Matter Mater. Phys.* **87**, 1–5 (2013).
373. Feng, W., Xiao, D., Ding, J. & Yao, Y. Three-dimensional

- topological insulators in I-III-VI₂ and II-IV-V₂ chalcopyrite semiconductors. *Phys. Rev. Lett.* **106**, 1–4 (2011).
374. Huang, S. M. *et al.* New type of Weyl semimetal with quadratic double Weyl fermions. *Proc. Natl. Acad. Sci. U. S. A.* **113**, 1180–1185 (2016).
375. Meng, L., Zhang, Y., Ni, S., Li, B. & Wu, W. Unique Schrödinger semimetal state in ternary Be₂P₃N honeycomb lattice. *J. Mater. Chem. C* **7**, 4118–4123 (2019).
376. Ando, Y. Topological insulator materials. *J. Phys. Soc. Japan* **82**, 1–32 (2013).
377. Taskin, A. A., Ren, Z., Sasaki, S., Segawa, K. & Ando, Y. Observation of dirac holes and electrons in a topological insulator. *Phys. Rev. Lett.* **107**, 1–4 (2011).
378. Zhang, X. *et al.* Hybridization, inter-ion correlation, and surface states in the Kondo insulator SmB₆. *Phys. Rev. X* **3**, 1–7 (2013).
379. Kim, D. J. *et al.* Surface Hall Effect and Nonlocal Transport in SmB₆: Evidence for Surface Conduction. *Sci. Rep.* **3**, 1–4 (2013).
380. Wolgast, S. *et al.* Low-temperature surface conduction in the Kondo insulator SmB₆. *Phys. Rev. B - Condens. Matter Mater. Phys.* **88**, 1–5 (2013).
381. Kuo, J. J. *et al.* Grain boundary dominated charge transport in Mg₃Sb₂-based compounds. *Energy Environ. Sci.* **11**, 429–434 (2018).

Disorder is an inherent component of real materials, with significant implications for their application in functional devices. In this thesis, using a combination of computational techniques, primarily density functional theory and ab initio as well as classical molecular dynamics, we investigate disorder in two broad categories – physical and chemical disorder, in three distinct classes of materials: palladium nanoparticles, the negative thermal expansion cuprite Ag_2O and the complex quaternary chalcogenide $\text{Cu}_2\text{ZnSnS}_4$, known commonly as kesterite.

The ‘physical’ disorder discussed in the thesis constitutes shape- and adsorption-induced mechanical softening on the surface of Palladium nanocrystals used for nanocatalysis, and bulk disorder in silver oxide nanoparticles. The disorder was found to be derived from surface effects, due to adsorption of capping agents and oxygen molecules on the Pd nanoparticles, and structural distortion of the bulk coordination tetrahedra in Ag_2O . In each case, disorder was found to increase the Debye-Waller coefficient, as calculated experimentally from X-ray diffraction and correlated with molecular dynamics simulations. This was found to significantly affect the strain state in the materials, and for the case of Pd nanoparticles, potentially alter their catalytic properties.

The ‘chemical’ disorder instead refers to cation disorder in the quaternary chalcogenide $\text{Cu}_2\text{ZnSnS}_4$ studied for its performance as a thermoelectric material. Randomization of only the Cu-Zn pairs was found to promote electronic band degeneracy, with an overall improvement in the power factor. Full cation disorder instead led to inhomogenous bonding and favorable modifications of the electronic and phonon properties, allowing for a simultaneous improvement of the experimentally measured electrical and thermal conductivities as well as the Seebeck coefficients. Finally, the atypical electronic structure of the disordered cubic polymorph was found to correspond to a topological Anderson insulator, the first such prediction in a real material system.

Binayak Mukherjee was born on the 10th of February 1992 in Calcutta, India. He obtained his B.Sc. from the University of Calcutta in 2015 and M.Sc. in Physics from the Hemwati Nandan Bahuguna Garhwal (Central) University, Uttarakhand, India, in 2017. For his master’s thesis work, performed at the, Saha Institute of Nuclear Physics, Calcutta, India, he studied the electronic structure of organic semiconductors using density functional theory. Binayak, started his Ph.D. at the University of Trento in December 2018, studying the effects of disorder on the electronic, mechanical and vibrational properties of metals, metal oxides and chemically complex semiconductors from a computational perspective, using molecular dynamics and density functional theory coupled with the modelling of X-ray diffraction data.